Interaction between site-controlled quantum dot systems and photonic cavity structures

THÈSE N^O 7675 (2017)

PRÉSENTÉE LE 25 AOÛT 2017
À LA FACULTÉ DES SCIENCES DE BASE
LABORATOIRE DE PHYSIQUE DES NANOSTRUCTURES
PROGRAMME DOCTORAL EN PHYSIQUE

ÉCOLE POLYTECHNIQUE FÉDÉRALE DE LAUSANNE

POUR L'OBTENTION DU GRADE DE DOCTEUR ÈS SCIENCES

PAR

Alexey LYASOTA

acceptée sur proposition du jury:

Prof. V. Savona, président du jury
Prof. E. Kapon, Dr B. Dwir, directeurs de thèse
Prof. S. Reitzenstein, rapporteur
Prof. M. Atature, rapporteur
Prof. A. Fontcuberta i Morral, rapporteuse

EPFL

ÉCOLE POLYTECHNIQUE
FÉDÉRALE DE LAUSANNE

Suisse
2017

Acknowledgements

First of all, I would like to thank Prof. Eli Kapon for accepting me as a PhD candidate at the Laboratory of Physics of Nanostructures (LPN) opening me a way for participating in fascinating study shoulder to shoulder with diligent and experienced researches. I am very grateful for Eli's help in many matters, especially in a preparation of conference presentations and an extremely patient and painstaking thesis manuscript reading.

I would like to express my gratitude to Dr. Benjamin Dwir for his guidance of my thesis work as my thesis co-supervisor. His help at clean room significantly enriched my experience in the nanofabrication that was the core of the first two years of my PhD work.

I owe my appreciation to Prof. Anna Fontcuberta i Morral, Prof. Stephan Reitzenstein and Prof. Mete Atature for accepting to be the jury members at my thesis defense and evaluating the manuscript. I am very grateful to Prof. Vincenzo Savona for being the president of the thesis jury.

A special acknowledgment is addressed to Dr. Alok Rudra for turning extremely lethal materials as, for example, arsine into magnificent quantum dots as well as for taking care of the implementation of the safety rules keeping young PhD students alive till the end of their study.

I would like to thank Dr. Pascal Gallo and Dr. Milan Ćalić for introducing me to the site-controlled QD fabrication technology in great details that helped me in getting faster into the LPN work during the first months of my PhD.

I am very grateful to Nicolas Leiser, Damien Trolliet and Yoan Trolliet for keeping the clean-room facilities operating and for the fast response in the case of the hardware failure. I would also like to thank them for the significant improvement of my French thanks to the discussions we had at lunch.

For all quanta of experience I absorbed at LPN I would like to thank present and former members of Kapon's group: Irina Kulkova, Clément Jarlov, Milan Ćalić, Pascal Gallo, Mikhail Lazarev, Romain Carron, Zlatko Mickovic, Vladimir Yakovlev, Alexey Sirbu, Andrei Caliman, Alexandru Mereuta, Alessio Miranda, Christopher Long, Dalila Ellafi, Lydie Ferrier, Alessandro Surrente, Mark-André Dupertuis, Bruno Rigal, Antoine Delgoffe, Elodie Lamothe, Justina Szeszko and Nicolas Volet.

I am very thankful to my office mates Milan Ćalić, Irina Kulkova, Moshe Judelewicz and Alessio Miranda for friendly and enjoyable office atmosphere. A special acknowledgement goes to Milan Ćalić who helped me adapting for the Lausanne life style during my first months in Switzerland. I would also like to thank Irina who is not only a master of nanofabrication but also a very kind person and a good friend.

Abstract

Nanophotonics is the field of physics that summarizes all methods for manipulating light on the nano scale, i.e. below the wavelength of visible light. The goal of this thesis was to investigate light-matter interaction in small systems, in nanophotonic devices based on site-controlled pyramidal quantum dots (QD) embedded in photonic crystal (PhC) cavities. These QDs provide unique position and spectral control, which is hardly achievable by the widely exploited self-assembled QD-based systems, thus allowing almost ideal cloning of differently designed devices in thousands of copies on the same chip. Taking advantage of the high reproducibility of our devices we conducted statistical studies of the optical properties of a large variety of photonic structures without concerns about significant deviations from the targeted layout.

In particular, we addressed the influence of the QD position with respect to the electrical field pattern of the cavity mode (CM) on the optical properties of the QD excitonic transitions. To this end, we integrated a single pyramidal QD in a linear PhC membrane cavity with three missing holes (L3 PhC cavity) at a set of well-defined positions, among which were points corresponding to the first and the second CM lobes as well as a CM node. Taking advantage of the high reproducibility of the fabricated devices, we aimed at providing statistical evidence of the impact of the positioning of a single dipole on the CM-induced Purcell enhancement. Interestingly, we observed a clear Fano-like resonance in the QD emission component co-polarized with a CM that vanished for devices with a QD at the CM node.

Further developing pyramidal QD-based QD-PhC cavity integration technology, we successfully implemented the integration of up to 4 QDs with a linear PhC cavities having seven missing holes (L7 PhC cavity). For several such structures we identified the optical transitions of each QD by means of spatial scanning micro-photoluminescence, accompanied with correlations in spectral wandering traces. Taking advantage of the well identified excitonic transitions, we demonstrated phonon-assisted weak coupling of 4 different QD excitons with the same CM. Using a combination of temperature- and water condensation- induced exciton-CM tuning allowed probing the coupling of the 4 QDs to different CMs, thereby probing the modal spatial profiles.

In parallel, we explored spectral diffusion and spectral wandering processes of QD excitons that could significantly affect exciton-CM coupling, especially its spectral range. As a tool, we developed a correlation technique based on the observation of transitions between different excitonic energy levels induced by the quantum confined Stark effect (QCSE). This technique allowed us to study the nature of charged centers in the vicinity of the QD, leading to spectral jumps between discrete emission energies of the QD excitons. Relating the QD exciton energy to the amplitude of the electric field inducing the QCSE allowed observing unusual spectral response of the QD upon increasing the charge density in its vicinity. Additionally, it allowed probing the ratio between the dipole moments of different excitonic complexes. Scanning spectrally a CM with a single QD exciton tuned by the fluctuations of the built-in electric field, we observed emission intensity enhance-

ment associated with the CM-induced Purcell effect. We also observed an irreversible QCSE-induced giant exciton spectral shift accompanied by the intensity intermittency. Finally, we evidenced a strong dependence of the observed spectral wandering and emission intermittency effects on the sample light exposure history, clearly exhibiting a photon-activated charge trapping in the QD vicinity.

The results of this thesis demonstrate the advantage of site-controlled pyramidal QDs for photonics and highlight the current drawbacks that should be improved for implementation in various photonic devices relevant to QD-based quantum computation and communication as well as low threshold lasers and single photon sources. Longer wavelength pyramidal QDs could potentially allow integration with higher Q-factor photonic cavities that may reach the strong exciton-CM coupling regime, especially if spectral wandering is suppressed leading to nearly Fourier-transform limited linewidth of pyramidal QD excitons. Achieving this step is highly important for many quantum optics experiments, in particular, for optical addressing of QD exciton-based stationary qubit.

Keywords

Résumé

La nano-photonique est une branche de la physique qui englobe les méthodes de manipulation de la lumière à l'échelle nanométrique, bien en dessous des longueurs d'onde visibles. Cette thèse vise à analyser l'interaction entre lumière et matière dans des systèmes microscopiques : des dispositifs basés sur l'intégration de boîtes quantiques (BQ) pyramidales, dont la position est contrôlée, dans des cavités en cristaux photoniques (CP). Contrairement aux BQs auto-assemblées plus répandues, notre technologie procure un contrôle unique sur la position et le spectre des BQs, qui permettent l'implémentation de milliers de structures pratiquement toutes identiques sur un même circuit. Tirant avantage de la reproductibilité de notre technique, nous avons mené des études statistiques sur les propriétés d'une large variété de structures photoniques, sans nous soucier des larges écarts au design initialement planifié.

En particulier, nous nous sommes intéressé à l'influence de la position de la BQ dans une certaine distribution du champ électrique du mode de cavité (MC) sur ses propriétés optiques, c'est-à-dire sur les transitions électroniques. Dans ce but, nous avons intégré à différentes positions une seule BQ pyramidale dans un PC, avec une cavité linéaire définie par l'absence de 3 trous (L3). Dans le premier lobe du MC, dans le deuxième et au niveau d'un nœud. En tirant parti de cette fiabilité à reproduire nos structures, nous avançons les preuves statistiques de l'importance du positionnement d'une BQ par rapport au champ électrique d'un mode par la manifestation de l'effet Purcell. Effet issu de l'interaction entre un dipôle électrique unique et un MC. Il est à noter en particulier que nous observons de manière claire la signature d'une résonance de type Fano pour l'émission de la BQ co-polarisée avec le CM. Cette même signature disparaît quand la BQ est localisée à un nœud du MC.

En continuant à optimiser le processus d'intégration de nos BQs dans des cristaux photoniques, nous avons pu implémenter avec succès jusqu'à 4 BQs dans une cavité L7 (sept trous manquants alignés). Dans plusieurs telles structures nous avons pu identifier les transitions optiques de chacune des BQs en effectuant un balayage spatial pour collecter la lumière émise par ces dernières. Ces mesures sont complétées par des mesures de corrélations des émissions, émissions qui sont marquées par de la diffusion spectrale. En tirant parti de l'identification attestée des transitions excitoniques, nous apportons les preuves d'un couplage faible facilité par les phonons entre 4 BQs et un seul MC. Ce qui nous a permis par la même occasion de sonder le profil spatial du MC.

En parallèle, nous avons exploré les mécanismes de diffusion spectrale et d'élargissement homogène des excitons dans une BQ qui peuvent impacter significativement le couplage des ces derniers avec un MC, en particulier la gamme spectrale où ce couplage est possible.
Nous avons développé une technique de mesure qui établit l'influence de l'effet Stark sous confinement quantique (ESCQ) sur les transitions excitoniques entre différents niveaux d'énergies. Cette technique nous a permis de révéler la nature des impuretés chargées localisées à proximité des BQs. Ces impuretés induisent des sauts spectraux entre des niveaux d'énergie discrétisés des transitions excitoniques. En faisant le lien entre l'énergie d'émission d'un exciton d'une BQ et l'amplitude du champ électrique qui génère l'ESCQ, nous avons pu observer une réponse inhabituelle de la BQ à l'augmentation de la densité de porteurs de charge dans son voisinage. De plus, cela nous a permis d'évaluer les rapports entre les divers moments dipolaires de différents espèces exci-

toniques. Sous l'action d'un tel champ électrique intrinsèque un exciton d'une BQ peut balayer spectralement un MC lorsque son énergie est modifiée par l'ESCQ. Nous rapportons dans ce cas une augmentation de l'intensité lumineuse émise par cette BQ, associée à l'effet Purcell généré par ce MC. Nous faisons aussi mentions du décalage spectral d'un exciton expliqué par l'ESCQ, très marqué, permanent et s'accompagnant d'une modification intermittente de la luminosité. Enfin, nous avons mis en évidence une forte dépendance de ces mouvements spectraux et émissions intermittentes à l'histoire de ces échantillons, en particulier leur exposition à la lumière. Ceci indique clairement l'évidence d'un mécanisme photo-activé de capture de porteurs de charge à proximité des BQs.

Les résultats de cette thèse consolident l'importance loin d'être anecdotique des BQs pyramidales dont on peut contrôler la position pour des applications en photonique. Et mettent en avant les points négatifs qu'il reste à améliorer pour permettre la fabrication de nombreux dispositifs optoélectroniques basés sur des BQs nécessaires à la réalisation d'ordinateurs quantiques et canaux de communication quantique, ainsi qu'autres lasers à faible seuil d'émission et émetteurs de photons uniques. Des BQs pyramidales qui émettent à plus haute longueur d'onde pourraient potentiellement permettre la réalisation de cristaux photoniques avec des facteurs de qualité Q suffisamment élevés pour espérer atteindre le couplage fort et explorer la physique des polaritons. Notamment si nous parvenons à réduire la diffusion spectrale et à obtenir des lignes excitoniques limitées par la transformée de Fourier du temps de vie radiatif. Parvenir à cet objectif est de la plus haute importance pour de nombreuses expériences d'optique quantique, en particulier pour le contrôle optique de qubits stationnaires basés sur les excitons de BQs.

Mots-clés

Nanophotonique, électrodynamiques quantique en cavité, semiconducteur, boite quantique, exciton, effet Stark confiné quantiquement, défaut chargée, errance spectral, intermittence d'émission, cavité à crystal photonique, mode optique, résonance de Fano, effet Purcell, couplage phonon, modèle de Jaynes-Cummings.

Contents

Chapter 1   Quantum-dot-based   semiconductor photonics

1.1   Introduction

During the last 50 years technology progress has gradually decreased the typical length scale limit of structures that can be carved in solids. At some point the lower limit of structure size became comparable with several hundreds of lattice periods (in crystalline materials), opening the way to manufacturing complicated devices confining both electronic and photonic states in the volumes with characteristic lengths below their de Broglie wavelengths. This breakthrough significantly expanded possibilities for studying quantum electrodynamics (QED) that can be achieved in ways different from coupling of a quantized electromagnetic field with a single or just a few trapped atoms, the only source for confined electronic states available in the past for which very complicated equipment is required. As a result, the number of possible QED experiments drastically increased, providing access to many novel fascinating phenomena as well as proposals for possible applications of these new devices having light-matter interaction manipulated on the single quanta level. The physics field that encompasses methods for manipulating light and matter on a scale below the photon wavelength is known as nanophotonics[1].

Photonic crystals (PhCs), that is, dielectric structures with periodic distribution of the refractive index[2] are widely used in nanophotonics, providing a prohibited range of wavelengths close to the period of these photonic structures thus opening a photonic bandgap. Modes with frequencies inside this bandgap have suppressed density except in the specially designed zones (due to channel or point defects) allowing guiding or confining light[3], [4]. Controlling the dispertion of PhC-based waveguides, one can achieve slowing down of light[5], that is, decreasing its group velocity. Properly designed PhC cavities can concentrate electromagnetic fields at prescribed positions thus increasing light-matter interaction with dipole transitions introduced at these points[6], [7]. In the solid state, dipole transitions can be provided by either dopant imbedded in the dielectric lattice or quantum dots (QDs), semiconductor nanostructures that confine electrons in the volumes with dimensions below the Fermi wavelength[8]. Therefore, these nanostructures provide discrete electronic transitions mimicking the behavior of electrons in atomic orbitals. Photonic crystal waveguides allow also light transmission, realizing communication interfaces that can be integrated on chip. Using coupling to photonic cavities, PhC waveguide based structures are promising for information transfer between localized objects, e. g., among QDs by means of guided light quanta[9].

Light transmission on the nanoscale could be also obtained using polaritons, quasiparticles formed by hybridized photonic states and electronic excitations at metal-dielectric interface. These devices form the core of plasmonics, the field that allows shrinking light beams significantly below diffraction limit and strongly enhancing the light-matter interaction while integrated with (nano)structures having non-zero dipole moment. The latter leads to the strong Purcell enhancement effect[10], [11].

Plasmonic nanostructures integrated with active material can serve as a laser[12] while plasmonic-based circuits are proposed for on chip communication although suffering of considerable ohmic losses[13]. Serving as light guides, condensers or filters on the length scale significantly below the Abbe's diffraction limit, metallic or dielectric based nanostructures have significantly changed the paradigm of controlling electromagnetic waves in spectral ranges varying from UV to infrared region. Photonic devices nowadays are the main candidates for successful realization of quantum computation, information processing or nonlinear sources thus entering our day-to-day life.

The goal of this thesis was to investigate light-matter interaction in small systems using the unique position and spectral control of pyramidal QD dipole transitions (excitons) as well as the design flexibility, high spectral control and electrical field confinement of PhC cavity modes. For this purpose we integrated linear PhC cavities with a single QD at a set of different positions or with two, three or four QDs at fixed positions. Taking advantage of the high reproducibility of fabricated devices we aimed at providing statistical studies of the effect of dipole position on the Purcell enhancement and Fano-like resonances induced by exciton-cavity mode coupling. In search for collective effects due to multiple dipole transitions talking through the cavity mode, we studied systems with up to four quantum dots integrated with the same PhC cavity. We focused at the coupling properties of differently positioned QDs with different PhC cavity modes and identified a mode that is suitable for coupling with four differently positioned QD excitonic transitions. In parallel, we looked for spectral diffusion and spectral wandering processes that significantly affect the exciton-cavity mode coupling range. Thus, topics discussed in this dissertation are related to QED and solid-state physics of nanoscale structures.

1.2 Confining charge carriers in semiconductor nanostructures

1.2.1 Semiconductors

Matter in solid state often forms crystalline structures with periodically arranged atoms. This periodicity significantly affects the electron motion in solids, which was historically characterized by material conductivity. It was noticed that solid materials could be categorized as insulators, semiconductors or metals depending on their conductivity value, their response to temperature or doping level variations and light exposure. In particular, insulators have nearly zero conductivity while semiconductors and metals have intermediate and high conductivity values. Metals reveal higher conductivity at low temperature and lower doping layer while semiconductors show the opposite behavior, drastically increasing conductivity with temperature and doping. Among all these properties, semiconductor response to light exposure is a very interesting feature in the framework of light-matter interaction, which is one of the topic presented in this thesis. It should be noticed that conductivity properties of solids were not as clear as described above before fabrication methods of pure crystalline structures were developed. This allowed experiments with pure materials that eliminated the influence of the background doping.

Solids classification described above was gracefully explained by a group of scientists in the 1920's-1930's taking advantage of then recently developed Quantum Mechanics. The band-like structure of electronic spectrum turned out to be responsible for whether the particular crystal is metal, semiconductor or insulator while the periodically arranged atoms were in charge of these

bands formation. Although crystals consist of immense amounts of atoms and electrons, the appropriate physical picture of electron band spectrum can be given in the tight-binding approximation considering each electron mostly interacting with a particular atom and negligibly interacting with neighbor atoms and electrons. Here we also do not consider spin-orbit interaction terms. Then, the following Hamiltonian governs a single electron motion

$$\hat{H} = -\frac{\hbar}{2m}\Delta + U(\vec{r})$$

where $U(\vec{r})$ is an atomic potential term that reflects the electron interaction with atomic nuclei. The atomic potential is a periodic function: $U(\vec{r}) = U(\vec{r} + \vec{T})$ where $\vec{T} = \eta_1 \vec{t}_1 + \eta_2 \vec{t}_2 + \eta_3 \vec{t}_3$ is the lattice translation vector, $\eta_{1...3} \in \mathbb{Z}$ and $\vec{t}_{1...3}$ are the primitive translation vectors. Solution of the Schrodinger equation $\hat{H}\psi = \mathrm{E}_n(\vec{k})\psi_{n,\vec{k}}(\vec{r})$ proposed by Bloch in 1928 is a product of a plane wave and a periodic function with the same periodicity as the atomic potential:

$$\psi_{n,\vec{k}}(\vec{r}) = e^{i\vec{k}\vec{r}} u_{n,\vec{k}}(\vec{r})$$

with the plane wave vector $\vec{k}$ and the periodic Bloch function $u_{n,\vec{k}}(\vec{r}) = u_{n,\vec{k}}(\vec{r} + \vec{T})$. The dispersion relation $\mathrm{E}_n(\vec{k})$ provided by the solution of this equation is a periodic function with period $\vec{G}$ that is a reciprocal lattice vector. For III-V semiconductors $\mathrm{E}_n(\vec{k})$ is nearly quadratic for the $\vec{k}$ values near the bottom of a band valley. Thus, we can define the effective mass of an electron moving in the potential of such a periodic lattice

$$\mathrm{m}_{eff} = \hbar^2 \Big/ \frac{d^2 E}{dk^2}$$

We can then introduce valence and conduction bands that are the highest populated and the lowest unpopulated energy bands at zero temperature. If the Fermi level, that is, the highest level that is occupied by electrons, lies in-between valence and conduction bands, then the material is either dielectric or semiconductor. At nonzero temperatures the energy distance between valence and conduction bands, that is, the band gap, can be use to divide solids into semiconductors or insulators. If the band gap is commensurable with the Boltzmann energy kT at the particular temperature then the material is a semiconductor since the tail of the electron density of states at this energy partly overlaps with conduction band. In other words, fluctuations of crystal lattice (local band gap) can provide single excitation with energy bigger then the band gap, populating conduction band with electrons while leaving positive vacancies in the valence band, that is, holes. Therefore, with increasing temperature more and more mobile electrons are generated in the semiconductor providing increasing conductivity. In insulators the band gap is much bigger than the Boltzmann energy, leading to zero conductivity if an electron does not have a source to borrow energy for overcoming the band gap.

Figure 1:1(a) shows the Zinc-Blende structure of GaAs, representing the III-V group of semiconductors. This is a direct gap semiconductor, that is, the same $\vec{k}$ defines the minimum (maximum) of the conduction (valence) band, as can be seen in GaAs band structure shown in Figure 1:1(b). This allows the vertical (no change in k-vector) recombination of spatially overlapping electrons and

holes providing photon emission, since the momentum conservation is closely satisfied without borrowing missing momentum value as in case of indirect semiconductors. The conduction band of GaAs is formed by the s-orbitals while the valence band is a p-like band. This leads to valence band splitting introduced by the spin-orbital interaction. Since the split-off band is significantly shifted in energy from the conduction band, the main optical transitions are between light and heavy holes that are quasiparticles with total angular momentum $\frac{1}{2}$ and $\frac{3}{2}$, and electrons that are quasiparticles with total angular momentum $\frac{1}{2}$.
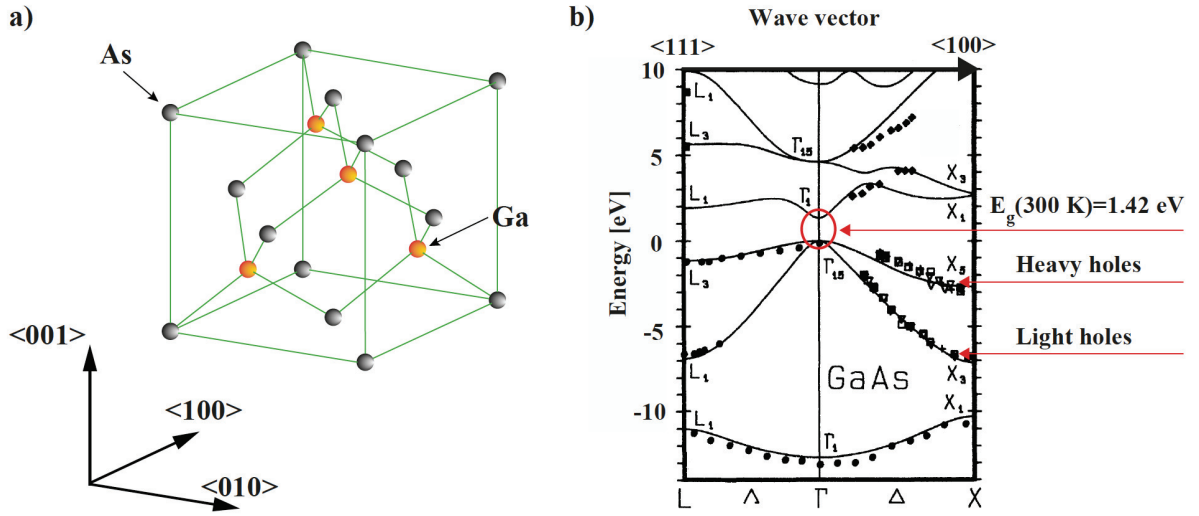
Figure 1:1 a) Zinc-blende lattice of GaAs and b) its band gap structure. Figure in b) is adopted from[14].

Coulomb interaction leads to corrections of the optical transition energy providing two types of observed correlated electron hole pairs. The first is the Frenkel exciton that is a bound electron-hole pair localized on one of the lattice sites, that is, its radius is less then the lattice constant. The second type is the Wannier-Mott exciton that is a delocalized bound electron hole pair with radius much bigger then the lattice constant. Since semiconductors have typically large dielectric constants, the dominant exciton type is Wannier-Mott exciton. The exciton binding energy in bulk GaAs is ~4meV while the Boltzmann energy is around 25 meV at room temperature; therefore, the Wannier-Mott exciton emission line is visible only at cryogenic temperatures, at energies lower than the band gap energy by the exciton binding energy.

1.2.2   Low-dimensional semiconductors

Progress of growth techniques in the second half of the 20th century allowed fabrication of structures with sharp interface transitions between different semiconductors. Thus, fabrication of artificial structures that provide observation of quantum size effect on the single electron level became realistic. Figure 1:2 shows structures with decreasing degree of freedom (dimensionality) due to quantum confinement that also modifies the density of electronic states. Figure 1:2 (a) show the quantum well (QW) structure that consists of a thin semiconductor layer sandwiched between two semiconductor layers with wider band gaps. With suitable bandgap alignment this structure pro-

vides quantum confinement in one direction while in two remaining directions electrons can move freely. Such a structure significantly modifies the density of electronic states in comparison with no confinement (Figure 1:2(a)). The further development of quantum confinement is obtained with quantum wire (QWR) structures where electrons can freely move only in one direction. This affects the electron density of states even more leading to the narrow peaked density of states, independently of the confined electron level. Quantum dots (QD) realize the radical electron confinement in all directions thus providing an analog to the atom (in a solid state material). In such a structure, delta-function-like density of states spectra are formed, providing discrete electronic spectrum.
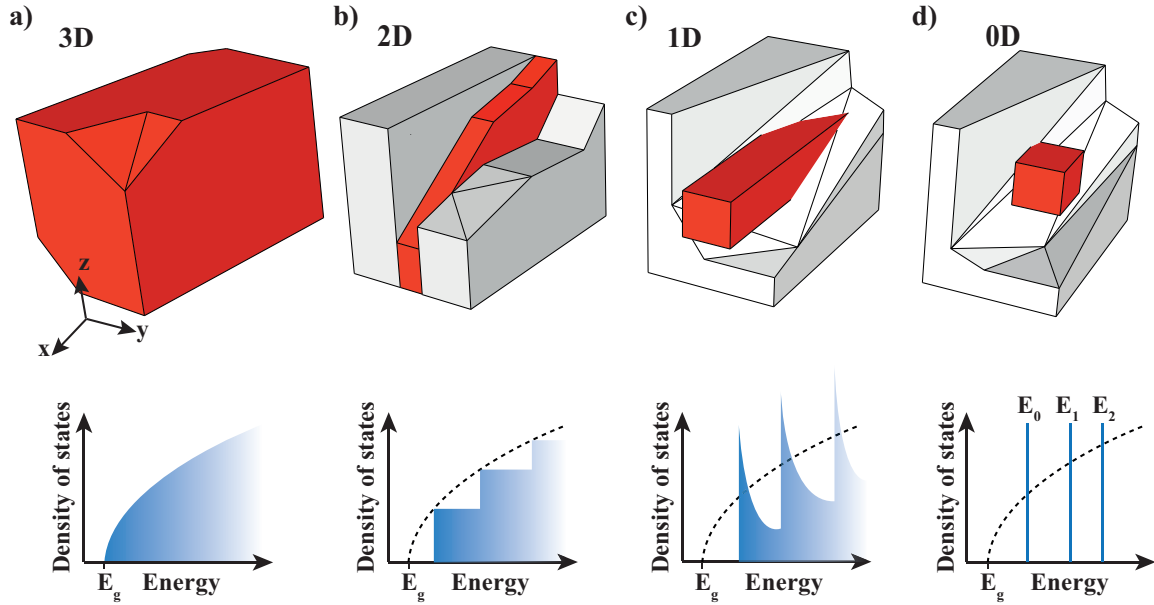
Figure 1:2 a) Bulk, b) quantum well (2D structure), c) quantum wire (1D) and d) quantum dot (0D) structures with corresponding density of states in the bottom. Graphs showing density of states are adopted from[15].

Figure 1:3(a) shows the case of a GaAs/InGaAs/GaAs QW that provides type I band alignment. In this case both electrons and holes are confined inside the QW structure that is typically 1-10 nm thick. In this case the electron energy is quantized, which leads to formation of subbands in the electronic spectrum. These subbands conserve nearly parabolic dispersion at wavevectors close to zero. Due to the quantum confinement, the 1st electron (hole) subband is shifted to higher (lower) energies thus increasing the energy separation between electron and hole levels.
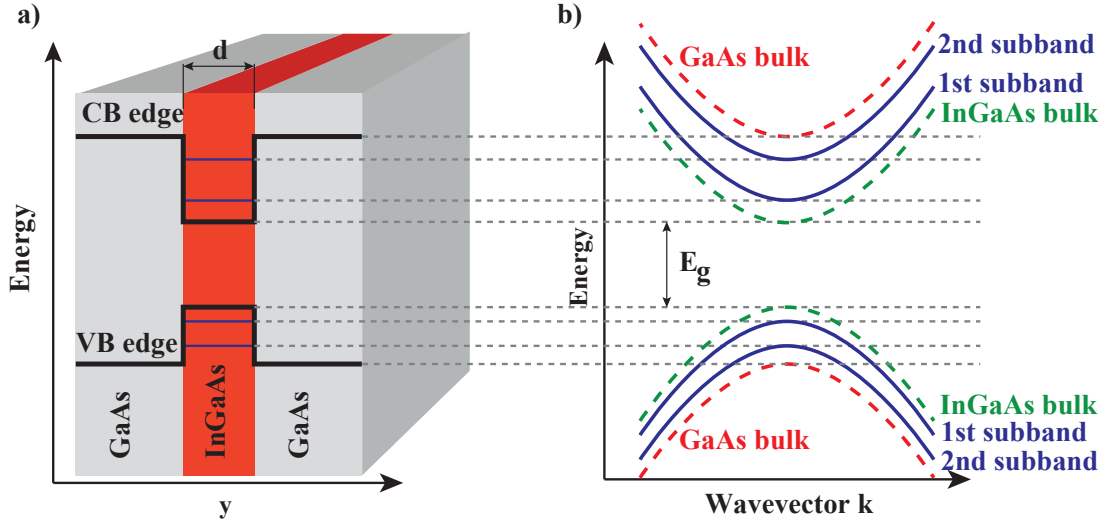
Figure 1:3 Sketch of the GaAs/AlGaAs/GaAs quantum well (a) and its band gap structure (b). Adopted from[15].

1.2.3 Semiconductor QDs

Most of the QD fabrication methods are based on epitaxial growth such as molecular-beam epitaxy (MBE) or metal organic vapor phase epitaxy (MOVPE). One of the most intensively used GaAs/In(Ga)As/GaAs QDs are grown in the Stranski-Krastanow (SK) mode. This method exploits the GaAs and In(Ga)As lattice constant mismatch that leads to more energetically favorable In(Ga)As island formation, rather than the layer by layer deposition. After a thin wetting In(Ga)As layer deposition on the GaAs substrate surface strain relaxes, leading to QD island formation as shown in Figure 1:4(a). These QDs form pyramidal-like structures that turn into truncated pyramids after capping due to material intermixing as shown in Figure 1:4(d). Material intermixing leads to an inhomogeneous strain and indium distributions providing variations in the confinement potential along the growth axis, which moves apart electron and hole envelope function maxima as shown in Figure 1:4(d, e). Spatial separation of electron and hole wave functions forms a static dipole oriented along the growth axis and decreases electron-hole overlap. Although these QDs are of high quality their implementation into photonic devices is challenging due to their arbitrary locations on the sample surface and high inhomogeneity of emission energy[16].

Interface fluctuation QDs, another type of semiconductor QDs, arises from AlGaAs/GaAs QW height fluctuations induced by its growth interruption during the top GaAs interface formation (Figure 1:4(b)). These QDs benefit from lower inhomogeneous broadening in comparison with SK QDs, more predictable wavefunction since the intermixing is absent, narrow linewidth ~30-50 μeV[17] and enhanced oscillator strength that is favorable for photonic application. However, their lateral sizes are much larger (~10-100 nm)[18] and confinement energies much lower than those of SK QDs while integration with real devices is challenging since AlGaAs is sensitive to oxidation processes[16].

Droplet epitaxy is yet another growth technique providing low-density GaAs QDs on the AlGaAs surfaces through saturation of gallium droplets with arsenic (Figure 1:4(b)). These QDs are relatively large with base length and height ~10-20 nm[19], although quantum confinement in these QDs is smaller then expected due to intermixing effect[16] during annealing of the capping layer (Figure 1:4(h, i). Although emission with linewidth as low as ~20-30 μeV[20] has been achieved, droplet QDs have not achieved the optical quality of SK QDs. In particular, for making droplet QDs optically active, high temperature post-annealing process is required after low temperature growth of the AlGaAs capping layer. This leads to lower quantum efficiency in comparison with the SK QDs[16].
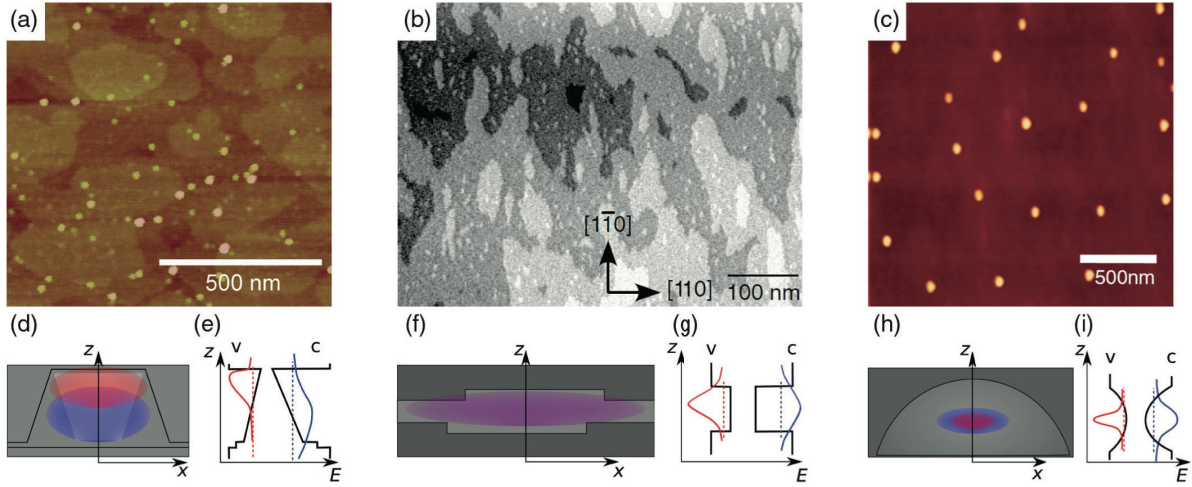
Figure 1:4 Atomic-force microscope (AFM) image of uncapped QDs for a) InAs Stranski-Krastanov QDs, b) GaAs interface fluctuation QDs and c) GaAs droplet epitaxy QDs. d), f) and h) show the confinement potential of the QDs presented in above AFM images. Electron and hole wave functions are shown as blue and red ovals. e), g) and i) illustrate the wave functions along the growth axis z for the respective type of quantum dots. a)-h) are republished from[16].

The methods described above do not provide site control on the QD position. Although several techniques for relative single-QD positioning using optical or cathodoluminescence microscopy provide deterministic integration of single-QDs with nanostructures, spatial and spectral dispersions of QDs is critical for scaling up to multi-QD photonic devices. In particular, integration of multiple QDs with photonic cavities is a virtually impossible task for deterministic multi-QD systems using self-assembled QDs. The first step towards a solution is fabrication of ordered QD arrays where QD positions can be easily identified. Figure 1:5(a) show GaAs surface prepatterned with holes in which SK QDs nucleate during growth procedure as shown in Figure 1:5(b, c). This seeding method provides well-positioned QDs although additional fabrication steps prior to growth significantly reduce the optical quality of QD devices. This can be attributed to impurity incorporation in the crystalline structure of the wafer serving as a potential source of defects or fluctuating electrical fields that significantly broaden the QD emission linewidth. This can be partially solved using GaAs buffer grown on top of patterned surface and increasing purity of the fabrication steps involved. During the recent years several groups successively improved the linewidth of site-controlled QDs[21], [22] although inhomogeneous broadening is more then 10 meV[21].

GaN QDs fabricated on top of site-controlled AlGaN nanowires combine site-control with efficient spatial isolation since these QDs are not necessarily grown in ensembles (Figure 1:5(a)). These QDs emit in the deep-ultraviolet diapason that overlaps with the solar blind region (4.35-6.2 eV) therefore they can be used for short range free-space ultraviolet communication system. Several tenth of meV exciton-biexciton energy of GaN QDs allows separating exciton and biexciton emission even at room temperatures, thus these QDs can be used as single photon sources. However, their integration with complicated photonic devices is unlikely.
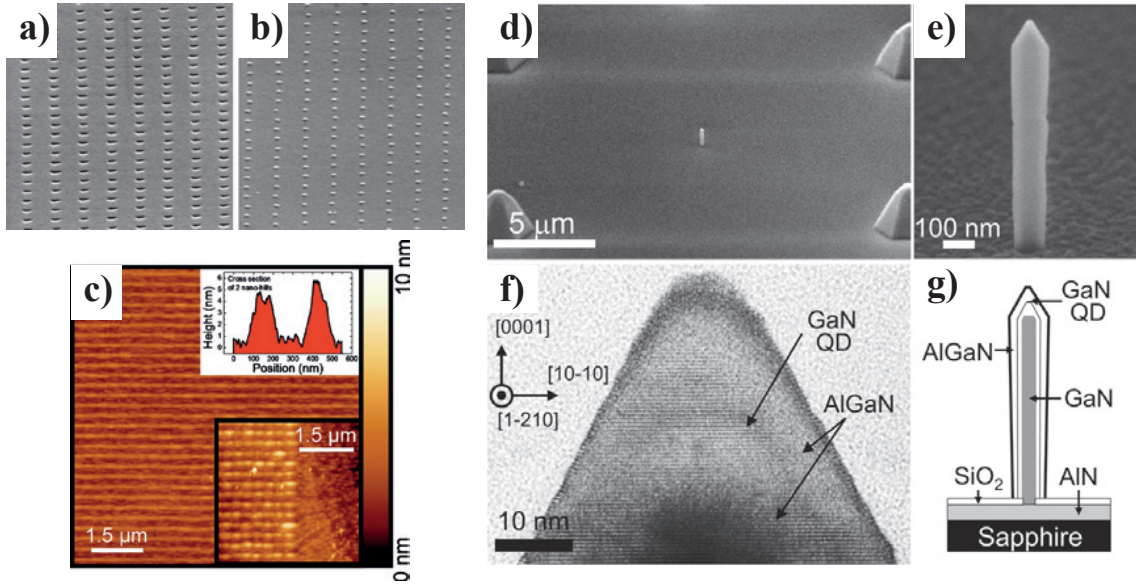
Figure 1:5 Site-controlled QDs.a)-c)[21]; d)-g) [23].

Another way of fabricating site-controlled QDs is MOCVD growth in inverted pyramids etched on (111)B-oriented GaAs substrates. These pyramidal QDs provide excellent position and emission energy control[24], [25]. Allowing integration of pyramidal QDs with photonic structures[26]–[28] this system forms a basis of this thesis. We discuss their fabrication and optical properties in Chapters 2 and 3 correspondingly.

1.2.4 Quantum dot electronic states

GaAs/InGaAs QDs that are relevant for the most of quantum optics experiment can be considered as quantum boxes with electrons and holes confined both in conducting and valence band due to the type I of band alignment discussed above. In small QDs, motion of electrons and holes is dominated by quantum confinement and thus optical states in a QD are always excitonic. That is opposite to the bulk semiconductors and QWs in which an important distinction between an uncorrelated electron-hole pair and an exciton exists. Although there is the hole band mixing, the ground state hole state in QDs is mainly heavy hole like state. Therefore, the major part of optical experiments with QDs can be interpreted in the framework of the two band effective-mass model where only the heavy-hole valence band and the conduction band are included. Since QDs important for quantum optics experiments have energy level spacing much larger than the Coulomb energy, the strong con-

finement approximation is applied including Coulomb effects perturbatively with the motion of the carriers in the conduction and valence band considered independently[16].

A single electron state $|\psi_{c/v}\rangle$ in the conduction (c) or valence band (v) is a superposition of the envelope wave function $|F_{c/v}\rangle$, the electronic Bloch function $|u_{c/v}\rangle$ and the spin state $|\alpha_{c/v}\rangle$: $|\psi_{c/v}\rangle = |F_{c/v}\rangle|u_{c/v}\rangle|\alpha_{c/v}\rangle$. In the equivalent electron-hole picture the valence band states are transformed to the hole states $|F_h\rangle = |F_v\rangle^*$, $|u_h\rangle = |u_v\rangle^*$ and $|\alpha_h\rangle = |\alpha_c\rangle^*$. An optical transition from the conduction to the valence band is considered in this picture as a recombination of the electron and hole with selection rules defined by the total angular momentum of initial and final states. In this formalism we can define the electron and hole pseudospin states reflecting the total angular momentum as a superposition of electron and hole Bloch and spin wavefunctions: $|\uparrow\rangle = |u_c\rangle|\uparrow_e\rangle$, $|\downarrow\rangle = |u_c\rangle|\downarrow_e\rangle$, $|\Uparrow\rangle = |u_h\rangle|\uparrow_h\rangle$ and $|\Downarrow\rangle = |u_h\rangle|\downarrow_h\rangle$. Electrons and heavy holes have pseudospin values $J_e = \frac{1}{2}$ and $J_h = \frac{3}{2}$ forming heavy-hole excitons with two different angular momenta $J_{X0} = 1$ or $J_{X0} = 2$, that is, $|\Uparrow\downarrow\rangle$ ($|\Downarrow\uparrow\rangle$) and $|\Uparrow\uparrow\rangle$ ($|\Downarrow\downarrow\rangle$)[16].

Symmetry breaking of the QD potential removes the twofold degeneracy for each neutral exciton angular momentum value providing four neutral excitonic states with different transition frequencies, that is, two bright excitonic states $|X_b\rangle = \frac{1}{\sqrt{2}}(|\Uparrow\downarrow\rangle - |\Downarrow\uparrow\rangle)$ and $|Y_b\rangle = \frac{1}{\sqrt{2}}(|\Uparrow\downarrow\rangle + |\Downarrow\uparrow\rangle)$ while dark neutral excitonic states are $|X_d\rangle = \frac{1}{\sqrt{2}}(|\Uparrow\uparrow\rangle - |\Downarrow\downarrow\rangle)$ and $|Y_d\rangle = \frac{1}{\sqrt{2}}(|\Uparrow\uparrow\rangle + |\Downarrow\downarrow\rangle)$. This classification to bright and dark states reflects the fact that the ground state of the QD $|g\rangle$ has total angular momentum $J_G = 0$ and therefore only excitonic states with $J_{X0} = 1$ are optically active. Two electron-hole pairs with oppositely oriented angular momentum can be created in the QD forming a biexcitonic complex $|XX\rangle = |\Uparrow\Downarrow\uparrow\downarrow\rangle$ with $J_{XX} = 0$. Due to optical selection rules biexcitons can decay to bright neutral excitonic states[16].

Biexciton and exciton optical transitions form an optical cascade as shown in Figure 1:6(a). Transitions from states $|X_b\rangle$ and $|Y_b\rangle$ to the ground state $|G\rangle$ as well as from $|XX\rangle$ to $|X_b\rangle$ and $|Y_b\rangle$ have linearly polarized, perpendicularly oriented dipoles in respect with the main symmetry axes of the QD confining potential. The energy splitting between the dark and bright excitonic doublets is ~500 µeV, which is smaller than the Boltzmann energy $kT \approx 0.9\ meV$ at $T = 10\ K$. Therefore, the average occupation probabilities of $|X_d\rangle$, $|X_b\rangle$, $|Y_d\rangle$ and $|Y_b\rangle$ excitons are nearly equal. Both the bright and dark excitons reveal a fine-structure splitting of the dark and bright neutral exciton states that are typically ~1 µeV[29] and ~10-100 µeV[17], [30], respectively.
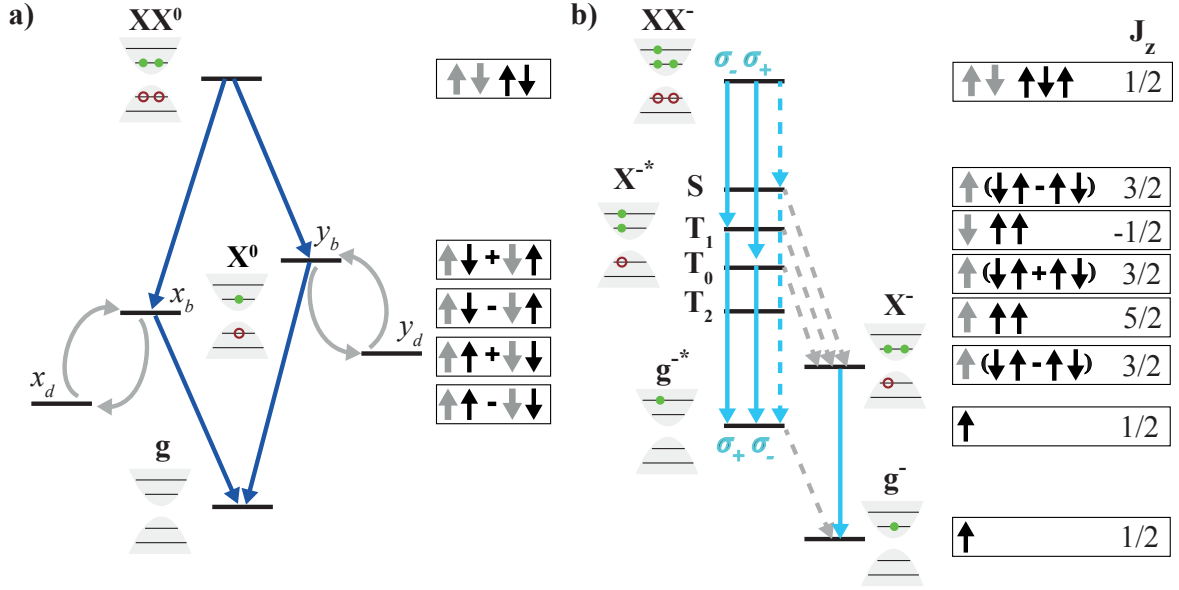
Figure 1:6 Neutral (a) and negatively charged (b) biexcitonic cascades observed in InGaAs/GaAs QDs. Dark and grey arrows correspond to optical and nonradiative transitions while $\boldsymbol{\sigma_-}$ ($\boldsymbol{\sigma_+}$) corresponds to left (right) polarized light emission.

Similarly to the neutral excitonic states one can consider negatively (positively) charged excitonic states with excess electron (hole) in the QD. Since optical properties of both charged exciton types reveal the same properties we review here only the negatively charged excitonic states. It consists of 2 electrons and a single hole. In the simplest case both electronic state belong to the s-subband of the conduction band forming a doubly degenerate state $\frac{1}{\sqrt{2}} |\Uparrow (\uparrow\downarrow - \downarrow\uparrow)\rangle$ with angular momentum $J_{X-} = \frac{3}{2}$. However, 4 more charged excitonic states are possible due to two electrons with the same angular momentum at both s- and p-subbands of the conduction band as shown in Figure 1:6(b). These charged excitonic states optically decay either to the state with single electron on s- or p-subbands. Nonradiative transitions between different charged excitonic states are also possible as shown by the grey dashed arrows in the Figure 1:6(b). It should be noticed that the main nonradiative transitions are expected to be due to relaxation from the p-subband to the s-subband electron state; therefore these transitions are irreversible, which is in contrast to spin-flip induced bright-dark neutral excitonic transitions. The charged biexcitonic counterpart consists of two electron-hole pairs and the excess electron, and decays to $|S\rangle$, $|T_{0,1,2}\rangle$ states with decay paths dictated by optically selection rules. In Figure 1:6(b), σ_- (σ_+) corresponds to left (right) polarized light emission by corresponding transition.

1.2.5   Influence of semiconductor environment

Semiconductor QDs are often considered as "artificial atoms". However, the semiconductor environment significantly affects QD emission properties in comparison with an atomic system. In general, interaction of any kind broadens the system energy spectrum. In atomic systems the emission linewidth is broadened due to radiative processes via interaction with photons, motion of atoms leads to Doppler line shift that affects the atomic ensemble emission linewidth, while elastic and inelastic collisions between different atoms lead to both linewidth shift and broadening and hence to

non Lorentzian lineshape. All these processes, except radiative broadening, are suppressed by cooling atoms to microkelvin temperatures, providing systems for single atom experiments.

In the case of QDs, the main broadening mechanisms come from the solid-state environment in which it is integrated as well as from the QD itself. In particular, the angular momentum of the excitonic transition, combined with that of atoms that form the QD, leads to interesting broadening of the QD linewidth as shown in resonance scattering experiments. Figure 1:7(a) shows the QD optical transition as a two-level system, a typical way to present QD excitonic transitions valid for low QD population values. In this panel, the emission linewidth of the QD is only radiatively broadened, revealing a Fourier transformed-limited linewidth. This scenario should be the goal of any fabrication process that aims at the application of QD systems in fields of quantum computing, information processing, etc.

Impurities or defects in the vicinity of the QD can serve as the source of fluctuating electric fields. Due to the quantum confined Stark effect, the QD emission linewidth can be either broadened or shifted. If the electric field fluctuates faster than the QD emits photons, then the lineshape is expected to be Lorentzian as shown in Figure 1:7(b) with linewidth independent on the integration time used during spectrum measurements. If the fluctuation frequency is much slower than the emission rate of the photon by the QD, than the QD emission spectrum globally shifts. In this case emission linewidth will significantly depend on the measurement integration time. Figure 1:7(c) shows a sequence of spectra measured at different times with spectrometer integration time much smaller than the time between electrical field fluctuations.
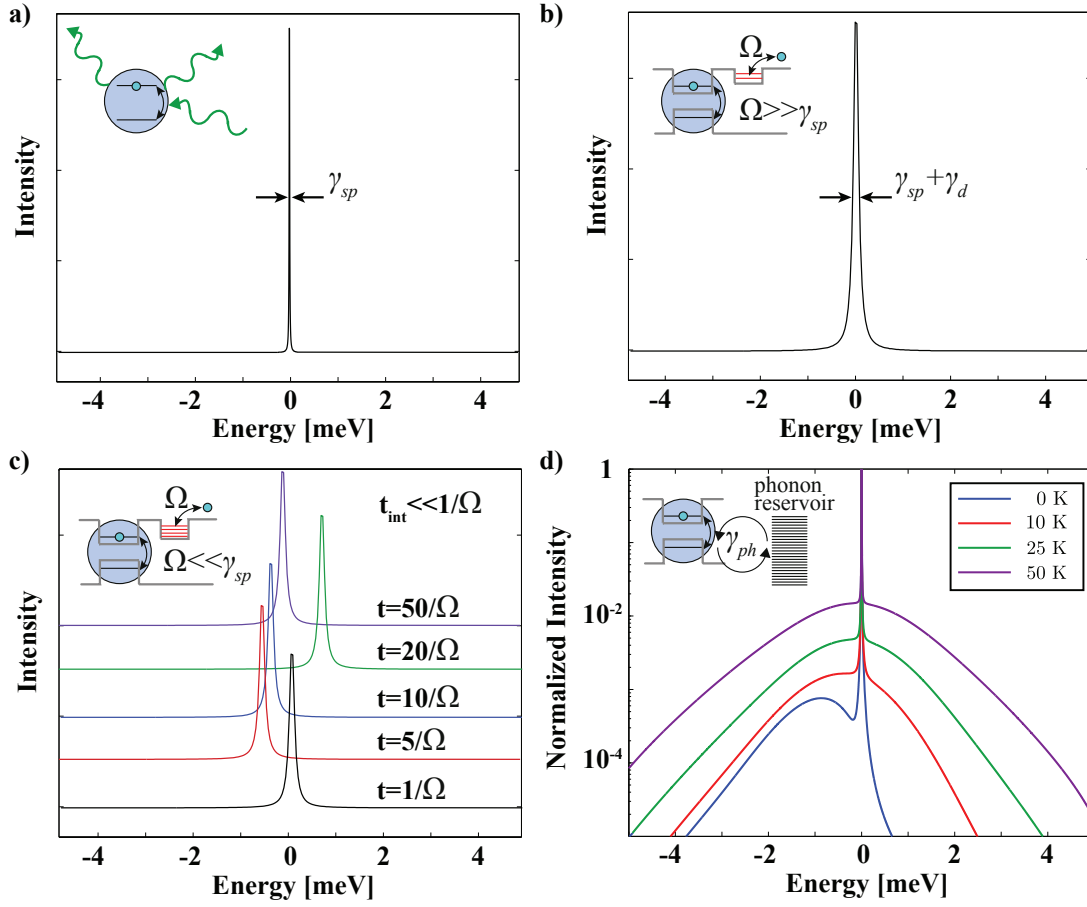
Figure 1:7 Broadening mechanisms for QD emission spectra. Radiative broadening (a), pure dephasing (b), spectral wandering (c) and interaction with phonons (d). Spectra in d) are adopted from[16].

Interaction with crystal vibrations, that is, phonons lead to another broadening mechanism of the QD emission linewidth. Figure 1:1(d) shows the calculated linewidth of a two level system interacting with a phonon reservoir. Phonon broadening leads to very asymmetric linewidth at low temperatures. Indeed, at temperatures lower than some critical temperature excitons can only transfer energy into heat while emitting photons while surrounding crystalline lattice is too cold to donate energy to the excitonic transition.

1.3   Modifying photon density of states

Photonic structures allow tailoring the electromagnetic field, which is extremely important for controlling light-matter interaction on the single photon level. The latter is the core of the quantum electrodynamics experiments. Photonic structures can efficiently control the propagation of targeted optical modes to a level that is of high importance for achieving scalable photonic devices and circuits.

1.3.1 Photonic crystals

Photonic crystals are structures with dielectric constant periodically modulated in space on a length scale comparable with the wavelength of light. Such variations of the dielectric constant lead to Bragg scattering of light. Very sensitive to the modulation amplitude of the dielectric constant, Bragg scattering leads to the significant modification of photon dispersion relations in PhC structures as compared with free space. Variations of the photon dispersion properties are achieved in a very similar way as periodic crystalline lattices affect the motion of electrons. Due to Bragg reflections, stop bands can form for particular wave vector directions. For certain frequencies, stop bands can overlap for all possible orientations of $\vec{k}$-vectors forming a forbidden band gap of photon states inside the PhC structure.

Figure 1:8(a-c) show PhCs with various degrees of freedom for photon propagation. 3D PhCs having refractive index periodic modulation in all 3 directions (Figure 1:8(a)) can completely suppress light propagation for certain range of frequencies. Structures that are periodic only in two or one spatial directions (Figure 1:8(b, d)) affect the light propagation only in the direction of periodicity thus complete band gap cannot be formed.
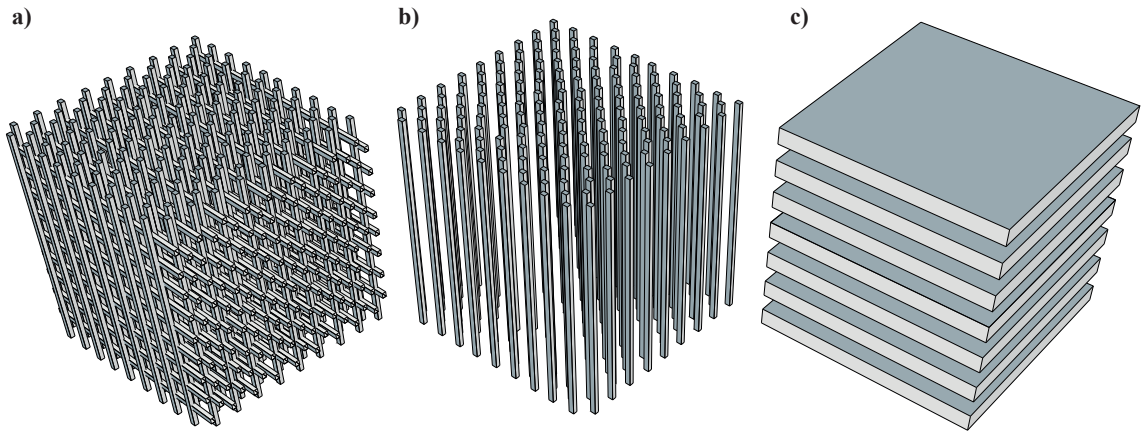
Figure 1:8 a) 3D, b) 2D and c) 1D PhC structures.

The band gap structure of the 3D PhC woodpile-like structure is shown in Figure 1:9(a). Such a woodpile structure is very complicated from fabrication point of view since multiple bottom-up like fabrication steps should be used. More practical PhC structures can be obtained through etching of voids in a slab providing 2.5D like membrane PhC structure as shown in Figure 1:9(c). Membrane slabs confines light due to total internal reflection while holes can suppress the light propagation in the slab plane. Therefore, only optical modes with $\vec{k}$ vectors in a narrow solid angle can enter or leave the PhC structure, forming a light cone. Although the band gap structure is not complete anymore, light cone optical modes can be used for addressing states of QD emitters integrated in the PhC, which is advantageous in comparison with the 3D PhC structures. Figure 1:9(b) show a pseudo band gap of a slab PhC structure with non-confined mode zones shown in blue.

In order to quantify the modification in light-matter interaction provided by a PhC structure, it is useful to introduce the concept of local density of states (LDOS). This value counts the number of photon states at the frequency ω per frequency bandwidth and volume

$$\rho(\vec{r}, \omega, \hat{e}_d) = \sum_{\vec{k}} \left| \hat{e}_d \cdot \vec{u}_{\vec{k}}^*(\vec{r}) \right|^2 \delta(\omega - \omega_k)$$

where $\vec{r}$ is the position of an emitter and $\hat{e}_d$ is a unit vector specifying the orientation of its transition dipole moment. The normalized mode function $\vec{u}_{\vec{k}}(\vec{r})$ constitutes a set of basis functions used to expand the electrical field and obey the wave equation[16]. LDOS is strongly depends on the position and polarization orientation that is expressed by the $\hat{e}_d$ vector.
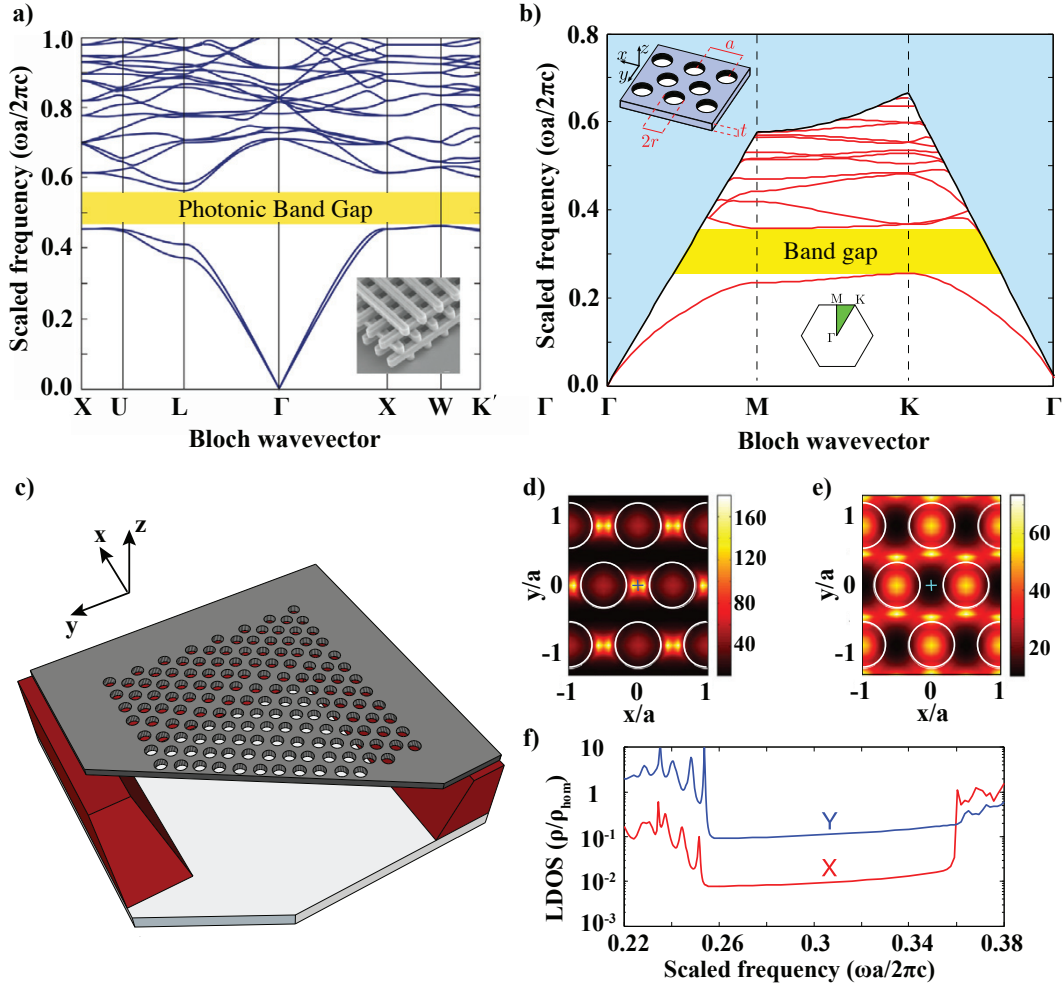
Figure 1:9 a) Band diagram of 3D PhC woodpile structure. Adopted from[31]. b) Band diagram of a triangular-lattice photonic-crystal membrane (shown in the left inset) for TE-like modes with membrane refractive index n=3.5, hole radius to lattice constant ration of r/a=1/3, and membrane thickness t=2a/3. The high-symmetry point of the Brillouin zone is shown in the bottom inset. c) A sketch of the slab PhC structure. d), e) Spatial map in the x-y (z=0) plane of the inhibition factor ρ/ρ_{hom} at a scaled frequency of $\frac{\omega a}{2\pi c} = 0.2838$ for x and y dipoles in d) and e), where $\rho_{hom} = \frac{n\omega^2}{3\pi^2 c^3}$ is the density of states for a homogeneous medium of GaAs. f) Frequency dependence of the LDOS ρ/ρ_{hom} plotted on a logarithmic scale for an x dipole and a y dipole positioned in a photonic-crystal membrane at the crosses shown in d) and e). b),d-f) adopted from[16].

Variations of a dielectric constant in PhC media significantly affect anisotropy of the local density of states (LDOS) of optical modes. Figure 1:9(d, e) show spatial maps of the inhibition factor of LDOS inside the slab PhC in comparison with LDOS in the bulk GaAs, that is, ρ/ρ_{hom} where $\rho_{hom} = \frac{n\omega^2}{3\pi^2 c^3}$. Orientation {x, y, z} axes are shown in Figure 1:9(c). The electromagnetic field distribution significantly varies with field polarization leading to the polarization sensitive LDOS inside the slab PhC band gap. LDOS of the electrical field parallel to the x axes is suppressed by ~1 order of magnitude in comparison with y component as shown in the Figure 1:9(f). The LDOS polarization anisotropy can significantly affect properties of differently polarized emitters integrated with such a PhC structure. Two orthogonal dipole moments oriented along x and y axes would feel very different LDOS leading to significant suppression of one dipole emission in comparison with another. This can significantly affect polarization properties of a light emission. In particular, an emitter with the circularly polarized dipole, that is, with x and y transition dipole moments equal in the absolute amplitude but having nonvanishing phase $\frac{\pi}{2}$ between them could provide strongly elliptically polarized emission while integrated in the environment with such an inhomogeneous LDOS.

1.3.2 Photonic cavities

PhC structures with perturbed dielectric constant periodicity could lead to resonating light at the certain frequencies thus turning into cavities. This effect could be achieved by breaking a dielectric constant periodicity in a small volume of the PhC structure. Figure 1:10(a-c) from left to right show 3D PhC, PhC membrane cavity and μ-pillar cavity. 3D PhC cavity is obtained by introducing a small point defect between sticks thus braking the dielectric periodicity and allowing mode confinement in the defect. PhC membrane cavity is obtained by removing 3 holes from the PhC lattice while two edge holes of the linear defect are slightly shrinking and shifting outside. This PhC design is known as L3 PhC cavity.

The μ-pillar cavity with a strongly confinement ground state mode at wavelength λ is obtained by introducing a λ/n wide layer with refractive index n in-between two super lattices consisting of materials with high contrast in the refractive index. Typically, these layers are $\lambda/4n_{1,2}$ wide where $n_{1,2}$ are their refractive index constants providing bottom and top Bragg reflector structures. Figure 1:10(d) show μ-disk cavity that is another type of photonic cavities that confines electromagnetic field in whispering gallery modes owning to the total internal reflection rather then the Bragg scattering.
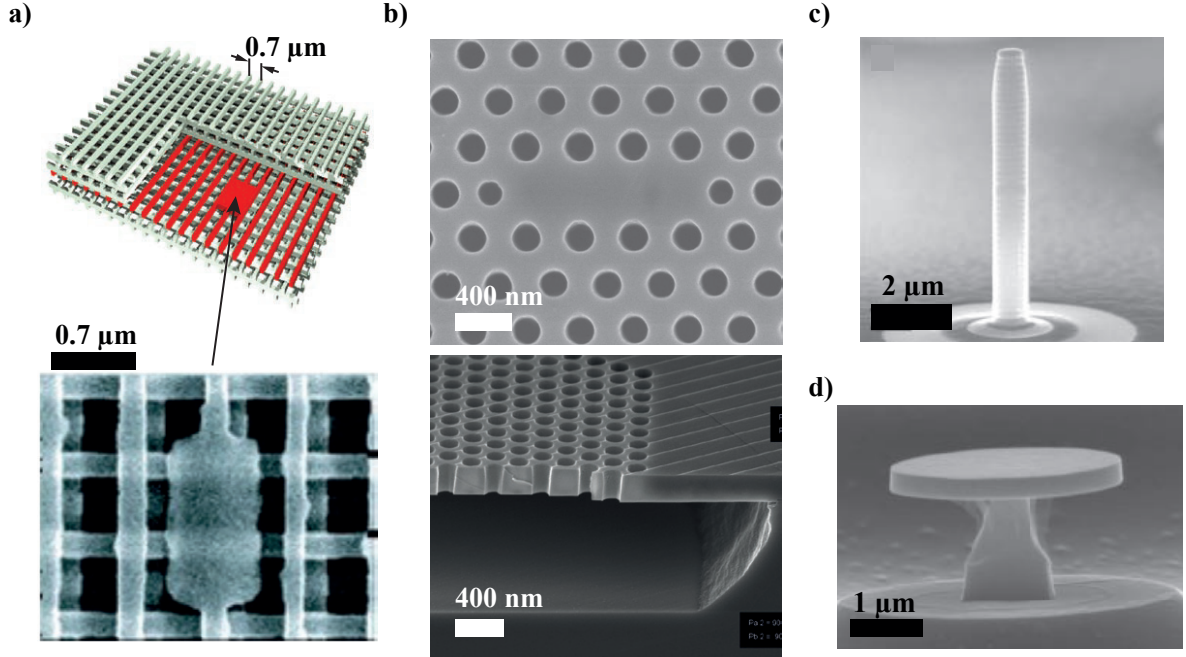
Figure 1:10 3D PhC cavity, b)L3 PhC membrane cavity, c) μ-pillar and d) μ-disk cavities. In a) schematics of a woodpile like 3D PhC is shown (top) with an SEM image of point defect serving for electrical field confinement (bottom). b) Top view of an L3 PhC cavity (top) and side view of a cleaved suspended PhC cavity membrane (bottom) obtained with scanning electron microscopy. PhC cavity was fabricated at LPN. a) is adopted from[4]. c) and d) are republished from[32] and[18] correspondingly.

Photonic crystal cavities allow coupling optical transitions with prescribed mode while sufficiently suppressing coupling with unwanted optical modes. This provides an effective energy and information transfer in-between the electromagnetic field and the stationary system with nonzero transition dipole moment that can constitute for example of QD optical transitions. An ability to transfer the energy and/or information exactly into the targeted mode is the core for multiple quantum experiments and such applications as information processing, communication or nonlinear light sources technology.

The electromagnetic filed confinement strength can be characterized to the certain extent[33] by the effective mode volume that is defined as

$$V_{eff} = \int_V \frac{\epsilon(\vec{r})|\vec{E}_{CM}(\vec{r})|^2}{\max\left(\epsilon(\vec{r})\left|\vec{E}_{CM}(\vec{r})\right|^2\right)} d^3\vec{r}$$

where $\epsilon(\vec{r})$ is the relative permittivity and $\vec{E}_{CM}(\vec{r})$ is a cavity mode electric field. Mode volume significantly varies for different photonic cavities. In particular, $\sim 10(\lambda/n)^3$ effective mode volume was obtained for μ-pillars while specially designed PhC cavities provide mode volume lower then the cubic wavelength[16], that is, less then $(\lambda/n)^3$. Such a low effective mode volume allows significantly enhancing the light matter interaction strength as will be discussed in the following.

Another quantity important for the quantum electrodynamics experiments and photonic cavities applications is the quality factor Q. This quantity is defined as a ratio of the resonant frequency to the damping rate of the optical mode, that is, the relative energy losses per one oscillation period. Thus, quality factor reflects the loss rate of the photonic cavity due to for example scattering on the fabrication imperfections. High-finesse PhC cavities fabricated in SiO_2 reveal as high quality factors as 2×10^6 at l.55 μm emission wavelength[34] although GaAs membrane based PhC cavities suitable for QD integration show much lower quality factors ($\sim1\times10^4$-3×10^4)[16]. That is due to shorter CM wavelength suitable for the integration with QDs leading to the higher CM sensitivity to the fabrication imperfections[35].

While integrated with semiconductor quantum boxes, photonic cavities constitute a platform for various quantum optics experiments. Hybridization of photon states with QD excitonic states has been achieved for membrane PhC cavity[36], μ-pillar[32] and μ-disk cavities[18]. QDs integrated with these cavities can serve as a single photon sources[37] as well as sources of quantum entangled photons[38]. Successful entanglement of stationary excitonic qubit with photon flying qubit[39] have been shown highlighting the potential implementation for quantum information processing of these integrated systems.

1.4   Cavity Quantum Electrodynamics with single quantum dots

1.4.1   Purcell effect in photonic cavities

In most cases optical transitions of the QD at low excitation limit as well as optical modes of photonic cavity are well separated in the energy. Thus, the ground state excitonic transition tuned in the resonance with the CM can be considered as a two level system interacting with the single optical cavity mode. The two level system is described by ground and excited states $|g\rangle$ and $|e\rangle$ that constitute the Fermi modes. The cavity mode is described by the Fock state $|n\rangle$. In the dipole approximation together with the rotating wave approximation the following Hamiltonian governs exciton-CM system behavior

$$\hat{\mathcal{H}}_{JC} = \hbar\omega_0\hat{\sigma}^\dagger\hat{\sigma} + \hbar\sum_{\vec{k}}\omega_{\vec{k}}\hat{a}_{\vec{k}}^\dagger\hat{a}_{\vec{k}} + \hbar\sum_{\vec{k}}(g_{\vec{k}}\,\hat{\sigma}^\dagger\hat{a}_{\vec{k}} + h.c.)$$

where the photon annihilation and creation operators $a_{\vec{k}}$ and $a_{\vec{k}}^+$ obey the boson commutation relation $[\hat{a}_{\vec{k}}, \hat{a}_{\vec{k}}^+] = 1$ while exciton annihilation and creation operators $\hat{\sigma}$ and $\hat{\sigma}^+$ obey the fermion commutation relation $\{\hat{\sigma}, \hat{\sigma}^+\} = 1$. These operators act on the photon and exciton states as $\hat{a}_{\vec{k}}|n\rangle = \sqrt{n_{\vec{k}}}|n_{\vec{k}}\rangle$, $\hat{\sigma}|e\rangle = |g\rangle$ and $\hat{\sigma}^+|g\rangle = |e\rangle$. The vacuum state is the eigenstate of the photon annihilation operator $\hat{a}_{\vec{k}}|0\rangle = 0 \cdot |0\rangle$. The coupling strength between an optical and excitonic modes $g_{\vec{k}}$ is expressed through an electrical field $E(\vec{r}_0)$ at the position $\vec{r}_0$ of the point dipole and dipole moment $\vec{d}$ providing $g_{\vec{k}} = \hbar^{-1}(\vec{d} \cdot \vec{E}(\vec{r}_0))$.

We can obtain dynamics of the system considering the superposition state

$$|\psi(t)\rangle = a(t)e^{-i\omega_0 t}|e, 0_{\vec{k}}\rangle + \sum_{\vec{k}} b_{\vec{k}}(t)e^{-i\omega_{\vec{k}}t}|g, 1_{\vec{k}}\rangle$$

with $a(0) = 1$, $b_{\vec{k}}(t)$. We can formally integrate the equation of motion of probability amplitude $b_{\vec{k}}(t)$ obtained from the Schrödinger equation substituting it into the equation of motion of exciton amplitude probability $a(t)$. This provides the following integral-differential equation

$$\frac{da(t)}{dt} = -\sum_{\vec{k}} |g_{\vec{k}}|^2 \int_0^t d\tau a(\tau) e^{i\Delta_{\vec{k}}(t-\tau)}$$

where $\Delta = \omega_0 - \omega$. In the terms of LDOS of optical modes we obtain[16]

$$\frac{da(t)}{dt} = -\frac{|\vec{d}|^2}{2\epsilon_0 \hbar} \int_0^\infty d\omega \omega \rho(\vec{r}_0, \omega, \vec{e}_{\vec{d}}) \int_0^t d\tau a(\tau) e^{i\Delta(t-\tau)}$$

The above equation fully describes the dipole emitter-photon interaction process for any photonic environment in which the emitter is introduces allowing to take into account any electrical field back action. Here, the local density of states describes the electrical field that is seen by a dipole emitter. We can now introduce the memory kernel that expresses the memory of the radiation reservoir[16] providing

$$K(\vec{r}, t - \tau, \vec{e}_{\vec{d}}) = \frac{|\vec{d}|^2}{2\epsilon_0 \hbar} \int_0^\infty d\omega e^{i(\omega_0 - \omega)(t-\tau)} \omega \rho(\vec{r}, \omega, \vec{e}_{\vec{d}})$$

The memory kernel describes how the electrical field values at the precedent to t time points affect the probability amplitude $a(t)$ at the time t. If $\omega\rho(\vec{r}, \omega, \vec{e}_{\vec{d}})$ varies insignificantly over the emitter linewidth that is the case of Wigner-Weisskopf theory then memory kernel can be approximated with a delta function[16]

$$K_{WW}(\vec{r}, t - \tau, \vec{e}_{\vec{d}}) \approx \frac{\pi |\vec{d}|^2 \omega_0 \rho(\vec{r}_0, \omega, \vec{e}_{\vec{d}})}{\epsilon_0 \hbar} \delta(t - \tau)$$

Thus, the history of the electrical field evolution does not affect the emitter behavior, in other words radiation reservoir is memoryless. In the reservoir theory approach the same approximation is referred to as the Markov one the core of which is the negligible back action of the radiation reservoir. Thus, the excitonic emission decays exponentially with emission rate[16]

$$\gamma_{rad}(\vec{r}_0, \omega, \vec{e}_{\vec{d}}) = \frac{\pi |\vec{d}|^2 \omega_0 \rho(\vec{r}_0, \omega, \vec{e}_{\vec{d}})}{\epsilon_0 \hbar}$$

Therefore, the emission rate of the emitter depends on the photonic environment in which it is introduced through the LDOS $\rho(\vec{r}_0, \omega, \vec{e}_{\vec{d}})$. It is convenient to introduce a ratio between emitter emission rates in the free space and modified photonic environment that is known as the Purcell factor[40]. It should be noticed that in the case of the semiconductor QDs serving as emitter emission rate in the 3D space is sometimes changed by emission rate in the bulk semiconductor that also affects an emission rate due to non unite refraction index (dielectric constant)[41].

$$F_p\left(\vec{r}_0, \omega, \vec{e}_{\vec{d}}\right) = \frac{\gamma_{rad}\left(\vec{r}_0, \omega, \vec{e}_{\vec{d}}\right)}{\gamma_{rad}^{hom}(\omega)}$$

Thus, modifying the photonic environment the emission rate in the photonic cavities can be significantly modified. An emitter inserted in the PhC has the Purcell factor below unity if the emitter frequency matches the optical band gap. In the PhC cavity emission rate can be enhanced providing Purcell factors above unity if the emitter optical transition is coupled with the cavity mode.

1.4.2 Cavity Quantum Electrodynamics with single quantum dots

1.4.2.1 Emitter in Fabry-Perot like cavity

The widely used approach that allows taking into account dissipation processes of an emitter-cavity system is consideration of the dissipative Jaynes-Cumming model. In this model Markov approximation is applied thus different system dissipation processes can be described with dissipation rates. Then the system dynamics is governed by the master equation in the Lindblad form

$$\frac{d\hat{\rho}}{dt} = -\frac{i}{\hbar}\left[\hat{\mathcal{H}}_{JC}, \hat{\rho}\right] + \sum_{\mu} \hat{L}_{\mu}^{\dagger} \hat{\rho} \hat{L}_{\mu} - \frac{1}{2}\left\{\sum_{\mu} \hat{L}_{\mu}^{\dagger} \hat{L}_{\mu}, \hat{\rho}\right\}$$

where $\hat{\rho}$, $\hat{\mathcal{H}}_{JC}$ and $\hat{L}_{\mu}$ are density matrix operator, Jaynes-Cummings Hamiltonian of the closed emitter-cavity system and the Lindblad terms correspondingly. Lindblad terms can describe decay through free space radiation modes, emitter dephasing or interaction with phonon modes.

Figure 1:11 show a typical geometry of an emitter-cavity system that is widely used in the quantum optics experiments. It corresponds to an atom in the Fabri-Perot cavity or QD in the µ-pillar cavity. Here we consider only interaction between an emitter-CM system and radiation reservoir leaving aside other dissipation processes. In this configuration emitter spontaneously decay through the radiation modes with the $\vec{k}$ vectors directed perpendicularly to the main axes of the cavity since the LDOS is significantly suppressed for the $\vec{k}$ vectors along this axes except for the set of resonance frequencies, e. g., CMs.
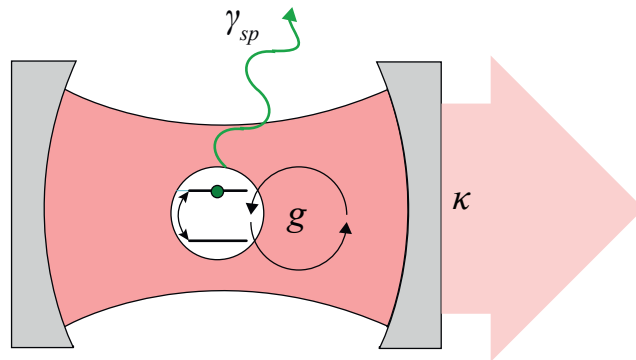
Figure 1:11 Emitter in the Fabry-Perot like cavity structure.

Quite often the CM losses are considered to be through one of the mirrors. Considering µ-pillar cavities it is indeed the case since one of its mirrors is designed in a way to allow collection of the

CM emission while another serves as a nearly perfect mirror. In the Fabri-Perot cavities used for the quantum optical experiments with atoms it is not so obvious since the CM losses happen through scattering on the edges of the mirrors. However, we can assume that in both Fabri-Perot and μ-pillar based system $\vec{k}$ vectors of free space radiation modes excited by an emitter and a CM do not overlap. Therefore, one can expect negligible interference between these radiation modes, in other words emitter and CM couple to the different radiation reservoirs. Then decay rates through radiation modes can be considered independently for an emitter and a CM providing Lindblad terms $\hat{L}_\gamma = \sqrt{\gamma}\hat{\sigma}$ and $\hat{L}_\kappa = \sqrt{\kappa}\hat{a}$ for a two level emitter and a CM.

Considering the low average population of the CM we can solve the Lindblad master equation restricting basis of CM states to the states with no or a single photon, that is, $|0_{CM}\rangle$ and $|1_{CM}\rangle$. The total set of emitter-CM superposition wavefunctions is $|a\rangle = |e\rangle|0_{CM}\rangle$, $|b\rangle = |g\rangle|1_{CM}\rangle$ and $|c\rangle = |g\rangle|0\rangle$. The Lindbald master equation then provides a system of differential equations for the density matrix elements. This system can be solved in the case of a direct resonance, that is, $\omega_{CM} = \omega_0$ and real coupling strength g providing the following expression for the density matrix element evolution of the QD exciton[16]

$$\rho_{aa}(t) = \frac{e^{-(\kappa+\gamma)t/2}}{2}\{\cosh(\Omega_R t)\,[8g^2 - (\kappa - \gamma)^2] + 2\Omega_R(\gamma - \kappa)\sinh(\Omega_R t) + g^2\}$$

where $\Omega_R = \sqrt{4g^2 - \frac{(\kappa-\gamma)^2}{4}}$ is a Rabi frequency. If $g \gg |\kappa - \gamma|/4$ then the emitter population decays exponentialy and the system is in the weak coupling regime. In this regime emission spectrum is Lorentzian. If the condition $g \ll |\kappa - \gamma|/4$ is satisfied then the system is in the strong coupling regime. In this case the emitter population oscillations are observed while the emission spectrum consists of two Lorentzians with equal linewidth. The damping rate of the emitter-cavity system is then $|\kappa + \gamma|/2$ defining the linewidth of these Lorentzian lines.

It should be noticed that the decay rate of the QD governed by the master equation described above is symmetric with respect to the $\Delta \to -\Delta$ variable change. That is since the emission rate can be written as[16]

$$\gamma_{QD}(\Delta) = \gamma + 2g^2 \frac{(\kappa + \gamma)^2}{(\kappa + \gamma)^2 + 4\Delta^2}$$

neglecting phonon interactions and dephasing processes. Interactions with phonons could potentially break the emission rate symmetry in respect with zero detuning point. That is due to different phonon density of states for $\pm\Delta$ detuning. At the same time the phonon assisted exciton-CM emission processes are expected to increase the total emission rate as well as the pure dephasing[42]. Thus, the total QD emission rate is bigger then the spontaneous decay rate of the QD optical transition $\gamma_{QD}(\Delta) > \gamma$. In the following we revise the interference processes that can decrease the total emission rate of the QD below its value in the bulk material.

1.4.2.2   Emitter in membrane PhC cavity

Contrary to the case discussed above, the membrane PhC cavity allows the interference between light excited by a QD optical transition and a CM. Due to the cavity geometry, both emitter and

cavity couple with the free-space optical modes that have the same $\vec{k}$ vectors as schematically shown in Figure 1:12 by the overlap of CM and exciton radiation patterns. In this case, we cannot consider the dissipation of emitter and the CM states through interaction with independent reservoirs only.
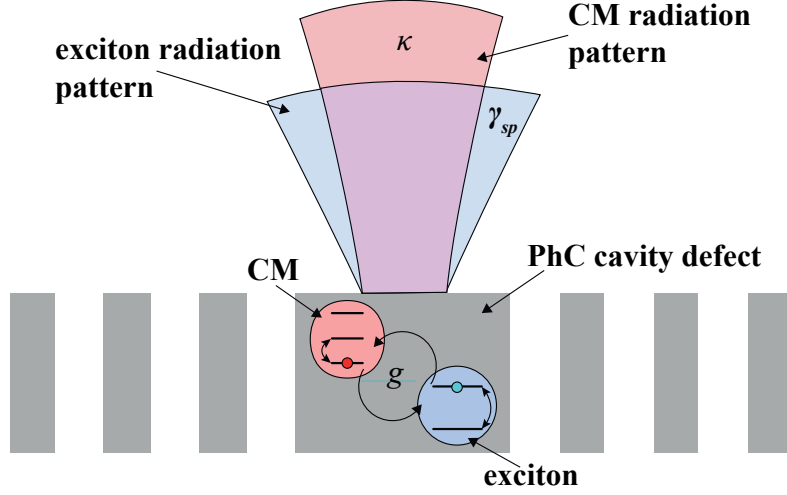
Figure 1:12 Interference between free space emission of an exciton and a CM. Overlap zone of blue and red beams, schematically representing spontaneous decay of the exciton and the CM, respectively, shows the free space modes with the same $\vec{k}$ vectors (violet).

With this geometry one can expect an interference effect between two decay channels: emitter decay through direct excitation of the free space radiation modes and decay through excitation of a CM. This interference significantly affects the spectral symmetry of the QD emission decay rate with respect to the zero detuning point as discussed in [43]. Following this article, we consider the Hamiltonian $\hat{\mathcal{H}} = \hat{\mathcal{H}}_0 + \hat{\mathcal{H}}_{int} + \hat{\mathcal{H}}_R$ that drives the interaction in the exciton-CM system and the common radiation reservoir. $\hat{\mathcal{H}}_0$, $\hat{\mathcal{H}}_{int}$ and $\hat{\mathcal{H}}_R$ are defined as

$$\hat{\mathcal{H}}_0 = \hbar\omega_{QD}\hat{\sigma}^\dagger\hat{\sigma} + \hbar\omega_{CM}\hat{a}_{CM}^\dagger\hat{a}_{CM} + \hbar\sum_{\vec{k}}\omega_{\vec{k}}\hat{b}_{\vec{k}}^\dagger\hat{b}_{\vec{k}}$$

$$\hat{\mathcal{H}}_{int} = \hbar(g\hat{\sigma}^\dagger\hat{a}_{CM} + h.c.)$$

$$\hat{\mathcal{H}}_R = \hbar\sum_{\vec{k}}(\eta_{\vec{k}}\hat{a}_{CM}^\dagger\hat{b}_{\vec{k}} + h.c.) + \hbar\sum_{\vec{k}}(\xi_{\vec{k}}\,\hat{\sigma}^\dagger\hat{b}_{\vec{k}} + h.c.)$$

where $\hat{\sigma}$, $\hat{a}_{CM}$ and $\hat{b}_{\vec{k}}$ are annihilation operators of the QD exciton, CM and free space radiation modes. Complex parameters g, $\eta_{\vec{k}}$ and $\xi_{\vec{k}}$ indicate CM-exciton coupling strength, and CM- and exciton-free space modes coupling strengths. In the case of the Fabry-Perot-like cavity, the imaginary part of g can be set to zero by a proper choice of the CM wavefunction. However, g, $\eta_{\vec{k}}$ and $\xi_{\vec{k}}$ cannot be simultaneously turned into the real numbers except in the case when they have equal complex phases. Here we choose free space mode and CM wavefunctions that provide real dipole coupling strengths g and $\xi_{\vec{k}}$. Since the CM and free space radiation mode wavefunctions are fixed,

we cannot render also $\eta_{\vec{k}}$ a real number. Rather, one should assume an arbitrary complex coupling strength $\eta_{\vec{k}}$ between free space and cavity modes. Now, the dipole phase serves as a reference for the phase of the free space and cavity modes since their phases are linked to the phase of the dipole transition.

Considering the low pumping regime we restrict the photon wavefunction basis to a set of Fock states corresponding to 0 or 1 photons in the CM and free space radiation modes. The two-level QD excitonic transition is between ground and excited states $|g\rangle$ and $|e\rangle$. Then, the superposition wave function is written as

$$|\psi(t)\rangle = a(t)e^{-i\omega_{QD}t}|e, 0_{CM}, 0_{\vec{k}}\rangle + c(t)e^{-i\omega_{CM}t}|g, 1_{CM}, 0_{\vec{k}}\rangle + \sum_{\vec{k}} b_{\vec{k}}(t)e^{-i\omega_{\vec{k}}t}|g, 0_{CM}, 1_{\vec{k}}\rangle$$

Looking for evolution of amplitude probabilities $a(t)$, $c(t)$ and $b_{\vec{k}}(t)$ we solve Schrödinger's equation in the framework of the Weisskopf-Wigner approximation [43] and obtain the following equations of motion:

$$\begin{cases} \dfrac{da(t)}{dt} = -\left(ig + \chi\dfrac{\sqrt{\gamma\kappa}}{2}e^{-i\varphi}\right)c(t)e^{i\Delta t} - \dfrac{\gamma}{2}a(t) \\ \dfrac{dc(t)}{dt} = -\left(ig + \chi\dfrac{\sqrt{\gamma\kappa}}{2}e^{i\varphi}\right)a(t)e^{-i\Delta t} - \dfrac{\kappa}{2}c(t) \end{cases}$$

where γ and κ are dissipation rates of the exciton and CM through radiation modes, while the interference term can be written as $\chi e^{i\varphi} = \dfrac{\Sigma_{\vec{k}}\xi_{\vec{k}}\eta_{\vec{k}}^*}{\sqrt{\Sigma_{\vec{k}}|\xi_{\vec{k}}|^2}\sqrt{\Sigma_{\vec{k}}|\eta_{\vec{k}}|^2}}$ where $0 \le \chi \le 1$ and $\varphi \in [0, \pi]$. Here, the phase φ is the phase difference of the radiation modes excited by the exciton and the CM. Solving the eigenvalue problem of this set of differential equations one can retrieve the emission rate of the exciton. The eigenfrequencies read

$$\gamma_\pm = -\frac{1}{2}\left(\frac{\kappa + \gamma}{2} - i\Delta\right) \pm \frac{1}{2}\sqrt{\left(\frac{\kappa - \gamma}{2} - i\Delta\right)^2 - 4\left(g - i\chi\frac{\sqrt{\gamma\kappa}}{2}e^{-i\varphi}\right)\left(g - i\chi\frac{\sqrt{\gamma\kappa}}{2}e^{i\varphi}\right)}$$

The exciton decay rate can be found as [43]

$$W = \begin{cases} -2Re(\gamma_+), \kappa > \gamma \\ -2Re(\gamma_-), \kappa < \gamma \end{cases}$$

A similar result can be obtained in a similar way but considering equations of motion for polariton wavefunction. Diagonalizing Hamiltonian part $\widehat{\mathcal{H}}_0 + \widehat{\mathcal{H}}_{int}$ we obtain the following set of polariton wavefunctions corresponding to the single excitation in the system

$$|-,1\rangle = \cos\beta\,|e\rangle|0_{CM}\rangle - \sin\beta\,|g\rangle|1_{CM}\rangle$$

$$|+,1\rangle = \sin\beta\,|e\rangle|0_{CM}\rangle + \cos\beta\,|g\rangle|1_{CM}\rangle$$

where $\tan\beta = \frac{2g}{\sqrt{4g^2+\Delta^2}-\Delta}$ and the exciton-CM detuning $\Delta = \omega_{QD} - \omega_{CM}$. The ground state polariton wavefunction corresponds to the zero excitation in the cavity-QD system $|g,0\rangle = |g,0_{CM}\rangle$. Then, the annihilation operators of polariton states $\hat{c}_{\pm}|\pm,1\rangle = |g,0\rangle$ read $\hat{c}_{-} = \cos\beta\,\hat{\sigma} - \sin\beta\,\hat{a}_{CM}$ and $\hat{c}_{+} = \sin\beta\,\hat{\sigma} + \cos\beta\,\hat{a}_{CM}$ while the interaction strengths with the radiation modes are $p_{\vec{k}} = \xi_{\vec{k}}\cos\beta - \eta_{\vec{k}}\sin\beta$ and $f_{\vec{k}} = \xi_{\vec{k}}\sin\beta + \eta_{\vec{k}}\cos\beta$. Thus, the total Hamiltonian assumes the form

$$\widehat{\mathcal{H}}_P = \hbar\omega_-\hat{c}_-^\dagger\hat{c}_- + \hbar\omega_+\hat{c}_+^\dagger\hat{c}_+ + \hbar\sum_{\vec{k}}(p_{\vec{k}}\hat{c}_-^\dagger\hat{b}_{\vec{k}} + h.c.) + \hbar\sum_{\vec{k}}(f_{\vec{k}}\,\hat{c}_+^\dagger\hat{b}_{\vec{k}} + h.c.)$$

Using the similar method as discussed above, we look for equations of motion of the amplitude probabilities $x(t)$ and $y(t)$ of the superposition wavefunction

$$|\psi(t)\rangle = A_-(t)e^{-i\omega_-t}|-,1\rangle|0_{\vec{k}}\rangle + y(t)e^{-i\omega_+t}|+,1\rangle|0_{\vec{k}}\rangle + \sum_{\vec{k}}b_{\vec{k}}(t)e^{-i\omega_{\vec{k}}t}|g,0\rangle|1_{\vec{k}}\rangle$$

obtaining

$$\begin{cases} \dfrac{dA_-(t)}{dt} = -\dfrac{\Gamma_-}{2}A_-(t) - \tilde{\chi}\dfrac{\sqrt{\Gamma_-\Gamma_+}}{2}A_+(t)e^{i(\omega_--\omega_+)t} \\[2mm] \dfrac{dA_+(t)}{dt} = -\dfrac{\Gamma_+}{2}A_+(t) - \tilde{\chi}\dfrac{\sqrt{\Gamma_-\Gamma_+}}{2}A_-(t)e^{i(\omega_+-\omega_-)t} \end{cases}$$

with $\Gamma_\pm = \frac{\kappa+\gamma}{2} \pm \left[\frac{\kappa-\gamma}{2}\cos 2\beta + \chi\sqrt{\gamma\kappa}\cos\varphi\sin 2\beta\right]$. Factor $\tilde{\chi}$ ($|\tilde{\chi}| \le 1$) is a complex number reflecting an overlap and phase shift of radiation modes to which polaritons decay. For $\gamma < \kappa$ ($\gamma > \kappa$), it can be found that $\Gamma_+(\Gamma_-)$ and $\Gamma_-(\Gamma_+)$ have their minimum and maximum values at detuning point

$$\Delta_{ext} = \frac{g}{\chi\cos\varphi}\left(\sqrt{\frac{\gamma}{\kappa}} - \sqrt{\frac{\kappa}{\gamma}}\right)$$

For most cases discussed in the literature the cavity losses exceed the radiation losses of the QD, that is, $\gamma < \kappa$. Taking into account this conditions we found that $\Gamma_+ = 0$ ($\Gamma_- = 0$) is exactly zero for the detuning point Δ_{ext} if $\chi\cos\varphi = 1$ ($\chi\cos\varphi = -1$). Thus, for these conditions, the probability amplitude $A_+(t)$ ($A_-(t)$) of polariton $|+,1\rangle$ ($|-,1\rangle$) does not vary with time at exciton-CM detuning Δ_{ext} since $\frac{dA_+(t)}{dt} = 0$ ($\frac{dA_-(t)}{dt} = 0$). It should be noted that $|+,1\rangle(|-,1\rangle)$ is the QD-like polariton brunch for $\Delta > 0$ ($\Delta < 0$). Since the sign of detuning Δ_{ext} be found from $\Delta_{ext} * g * \cos\varphi < 0$ if $\gamma < \kappa$, we obtain zero QD decay rate for either positive or negative exciton-CM detuning values depending on the phase and sign of the coupling strength. For positive g values and $\cos\varphi = 1$ ($\cos\varphi = -1$) we find that detuning extremum point $\Delta_{ext} < 0$ ($\Delta_{ext} > 0$) provides zero decay rate for $|-,1\rangle$ ($|+,1\rangle$) that is QD like polariton for this detuning sign ($\Delta = \omega_{QD} - \omega_{CM}$).

Figure 1:13(a, c) show QD decay rate for a set of coupling strength values. Even at zero exciton-CM coupling strength QD emission rate is still suppressed due to interaction with the cavity modes through free space modes. Figure 1:13(b) show detuning corresponding to the minimum QD decay

rate as a function of the radiation pattern overlap χ obtained by looking for the minimum of the decay-detuning curve $\Delta_{min}(\chi) = -2 \min \gamma_+(\chi)$ and $\Delta_{ext}(\chi)$ superimposed on top. For $\chi < 1$ and $|\cos \varphi| < 1$ it is not so easy to show that the Δ_{ext} still defines the minimum decay rate of the QD. We find a clear correspondence between the detuning corresponding to the minimum of the simulated detuning-decay rate curve and Δ_{ext} point. The two curves overlap very well especially for $\chi > 0.5$. The same procedure was applied for the phase φ providing again a great correspondence for the most important phase range of $\varphi < \frac{\pi}{4}$ and $\varphi > \frac{3\pi}{4}$. The QD emission rate $W_{QD}\left(\frac{\Delta}{g} \to -\infty\right) > \gamma$ while $W_{QD}\left(\frac{\Delta}{g} \to +\infty\right) < \gamma$ if we assume $\gamma < \kappa$. That is, for sufficiently big detuning Δ emission rate of the QD is bigger for negative detuning and smaller for positive detuning. This observation is also a sign of destructive interference in the CM and QD decay channels.
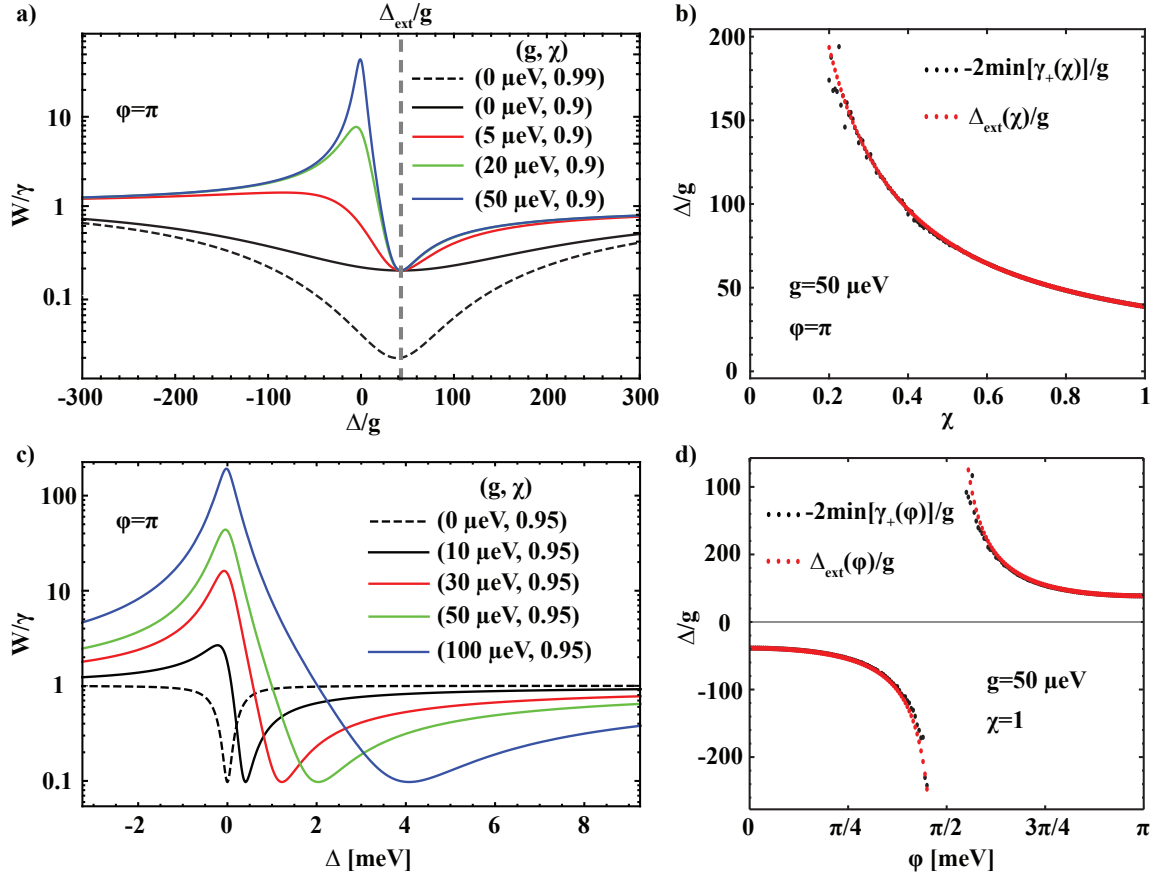
Figure 1:13 QD emission rates as a function of scaled detuning (a) and absolute detuning (c) for different exciton-CM coupling strength. In b) and d) we compare the detuning point of the minimum emission rate curve with extreme detuning point of the polariton state. We use $\gamma = 0.4 \, \mu eV$ and $\kappa = 600 \, \mu eV$ exciton and CM free space decay rates.

It should be noticed that a small inconsistency in the curves appears due to numerical errors during search for the minimum point of detuning-decay rate curve Δ_{min}. Scattering of Δ_{min} points increases for larger values of Δ_{min} corresponding to the less important range of (χ, φ) points. Increasing of

the Δ_{min} detuning value while $\chi \to 0$ and $\varphi \to \frac{\pi}{2}$ reflects the vanishing of the interference between the exciton and CM decay channels as expected for the zero free space mode overlap $\chi = 0$ and the phase $\varphi = \frac{\pi}{2}$.

Such an interference effect could be observed either in the time- or polarization-resolved measurements. While time-resolved measurements are the direct probe of the exciton decay rate, it is time-consuming and suffers from the lack of control of the exciton-CM detuning in a wide energy range that do not affect parameters of the exciton-CM system. In particular, temperature tuning could introduce the nonradiative decay channel that affects the measured excitonic lifetimes while providing only several meV tuning range. On the other side, at certain conditions polarization-resolved measurements allow directly probing the ratio between QD decays through perpendicularly polarized modes as will be discussed in the Chapter 4.

It should be noticed that the interference in the decay channels discussed above could significantly affect the Lindblad formalism that is often used for taking into account pure dephasing and coupling with the phonons. Lindblad terms for exciton and CM are usually set independently as $\hat{L}_\gamma = \sqrt{\gamma}\hat{\sigma}$ and $\hat{L}_\kappa = \sqrt{\kappa}\hat{a}$. However, this definition does not take into account interference in decay channels. In order to take into account this effect one should consider terms of the form $\hat{L}_i = e^{-i\varphi}\cos\vartheta\,(\sqrt{\gamma}\hat{\sigma} + \sqrt{\kappa}\hat{a})$, $\hat{L}_\gamma = e^{-i\varphi}\sin\vartheta\,\sqrt{\gamma}\hat{\sigma}$ and $\hat{L}_\kappa = \sin\vartheta\,\sqrt{\kappa}\hat{a}$ where $\cos\vartheta = \chi$ and $\varphi \in [0, \pi]$. With this definition the Lindblad term $\hat{L}_i$ allow holding the interference between exciton and CM emission in the free space.

Such an interference effect can potentially influence the lifetime of the QD exciton in the PhC cavity. However, it is often affected by the nonradiative losses, spin-flip processes, etc. that can significantly complicate the observation of this effect in detuning-decay curves. Oppositely, such a Fano resonance should be well visible in photoluminescence experiments either as emission/absorption suppression or in polarization-resolved measurements as will be discussed in the following.

1.5   Thesis goals and outline

Several researchers and PhD students working at the LPN during the last decade lay the foundations of this thesis providing the fabrication technology, mature optical setups and sets of theoretical hints necessary for understanding the physics observed. After the first integration of a single pyramidal site-controlled QDs with a PhC cavity [27] several years were spent in order to improve the general quality of the QDs. Pyramidal QD showed flexible energy tuning [24] and low inhomogeneous broadening [25]. The last is highly important for multiple QDs integration with photonic cavities in both spatial and spectral domains. The further improvement of fabrication methods, in particular alignment procedures, led to the integration of a single QD in PhC cavity of higher Q-factors revealing new physics [26]. Subsequently, successful spatial incorporation of two QDs at precise positions inside the L3 PhC cavities was achieved in hundreds of structures providing several devices spectrally coupled with the same CM of an L3 PhC cavity [15].

This thesis has accomplished further progress in the integration and studies of QD systems with PhC cavities, summarized as follows.

Chapter 2 presents the details of the techniques that allow deterministic integration of a single and multiple QDs with linear PhC cavities. It describes the general approach of the fabrication, characterization and designing of the PhC cavities suitable for integration with site-controlled pyramidal QDs. This chapter especially concerns about clean room routines used for QD-PhC cavity structures fabrication, describing in details an electron beam lithography alignment procedure that is an important step in achieving high positioning accuracy. Statistical data presented in this chapter confirm achieving better than 30 nm positioning error on several mm length scales. Finally, we show successfully implemented designs, part of which is further discussed in the subsequent chapters.

Chapter 3 starts with the description of the single QD emission properties that were studied using two QD isolation methods. The first relies on the QDs isolated in PhC cavities while the second uses unique spectral control of our site-controlled QDs providing spectral isolation technique. Subsequently, we focus on the slow dynamic processes observed in the site-controlled QDs integrated with PhC cavities. We discuss a new correlation technique that was used to study the nature of the charge centers leading to the exciton spectral jumps between discrete emission energies. In this chapter we discuss unusual spectral response of the QD exciton to the discretely varying charge density in its vicinity. Probing the Purcell enhancement by means of quantum stark effect is also discussed, as well as the giant spectral wandering effect accompanied by the intensity intermittency.

Chapter 4 first discusses an L3 PhC cavity with a QD incorporated at a set of positions varying from the position of the fundamental cavity mode (CM) antinode to the higher energy CM antinode, with one specific position chosen at the CM electrical field node. After discussion of the charged and neutral exciton coupling with the CM we study the Purcell effect by means of polarization-resolved and time-resolved micro-photoluminescence spectroscopy of a charged exciton positioned near the fundamental CM central lobe. We then discuss the effect of the phonon coupling and non-radiative losses on the exciton emission rate as well as the influence of the interference in exciton and CM decay channels on their emission polarization. Next, we present statistical data related to the exciton-CM coupling using polarization-resolved measurements of structures with QD at positions corresponding to minimum, mean and maximum field amplitudes of the fundamental and the first excited CMs. An influence of the QD position on the interference between the exciton and the CM decay channels is observed.

Chapter 5 deals with the deterministic coupling of 2 and 4 QD optical transitions with different CMs of an L7 PhC cavity. We show results of polarization-resolved measurements evaluated on several hundreds of structures with 2 and 4 QDs providing an estimation of the coupling efficiency of QDs positioned at 2 well-defined points and the four lowest-energy CMs. After identification of each QD optical transitions in the structures with 4 QDs by means of a spatial scanning technique and correlations in spectral wandering traces, we demonstrate a structure with all four QD excitons coupled with the same CM, demonstrated by both polarization-resolved and time-resolved measurements. Finally, we demonstrate how combinations of wide energy range tuning technique through water condensation and temperature variations can be used for probing coupling with different CMs of the L7 PhC cavity using just a single device that contains precisely positioned, site-controlled QDs.

Chapter 6 summarizes results of this thesis and sketches the possible future directions for developing of the site-controlled pyramidal QD-based systems.

Chapter 2 Fabrication of site-controlled QDs integrated with PhC cavities

Quantum dots (QDs) in photonic cavities could serve as a platform for many cavity quantum electrodynamics experiments and related applications. Results obtained with these structures attracted a lot of interest due to novel observations and potential applications, such as the strong coupling regime between a single QD excitonic transition and an optical mode of a photonic cavity [6], [18], [44]. Due to the truly stationary nature of QD qubits in comparison with atom-based systems, integration of several QDs inside a high quality μ-pillar allows a fabrication of solid devices with coherent coupling of several QD transitions with a cavity mode (CM) [45]–[49]. The solid-state environment reveals itself in off-resonant CM emission [36], [44], [50]–[55] and novel collective effects such as phonon-assisted CM-mediated interdot energy exchange [56]–[58]. QD-based photonic devices operate at much higher temperature than atom- or superconductor-based systems and do not need such complicated equipment as ion or atom traps, thus being much more interesting from the application point of view.

The first implementations of these structures were based on integration of photonic cavities on top of a membrane containing randomly distributed self-assembled QDs. Being simple and relatively cheap, at the same time this approach has very low yield due to the high spectral dispersion of QD emission wavelengths and the low probability of finding the desirable number of QDs in the right position in the photonic cavity. In order to identify a single device, thousands have to be optically characterized, excluding scaling up of the approach for either scientific investigations as well as any industrial or commercial applications. From an experimental point of view, there is always a question of how many emitters actually contribute to the measured emission. Even with low QD density, it is not always clear how many QDs couple to a CM, especially taking into account off-resonant coupling effects[36], [44], [50]–[55]. To solve this problem, complex experimental tricks have been used. The influence of spurious QDs not coupled with an optical mode of the photonic cavity can be minimized using QD excitation through resonant or higher energy CMs [47], [59], [60] or precisely tuned optical (quasi-) resonant excitation [58], [61]–[63].

The yield of methods based on self-assembled QDs can be improved by locating the exact QD positions and aligning the photonic cavities with them [6], [51], [64]–[66]. Spectral mismatch between the QD emission and the optical mode can be also eliminated taking into account the particular QD's emission energy. These improvements were successfully implemented, significantly increasing the yield of integration of QDs with photonic cavities i[36], [64], [66]. Taking into account the excitonic structure of an optically located QD, complex μ-pillar designs were implemented providing an entangled photon source with enhanced efficiency [38].

If problems with the positioning and optical coupling of a single QD seem to be solved, all the methods described above are of little use for the integration of several QDs with photonic cavities

or networks. The situation can be significantly improved using self-assembled QDs grown in nano-holes defined by electron beam lithography (EBL)[67]–[70]. However, this type of QDs still suffers from imperfect control of the number of dots per hole and very large inhomogeneous broadening, limiting the potential for QD integration with photonic networks [70].

Here, we describe a unique technology allowing integration of several spectrally- and site-controlled QDs with photonic crystal (PhC) structures. This work is an extension of the work done at LPN-EPFL during the last decade [71]–[75]. Significant progress is achieved in terms of the optical quality of the QDs, their alignment with the optical cavity features and the design and fabrication of various photonic crystal (PhC) cavities. This is of high importance for optimization of the interaction strength between a quantum emitter and an optical mode, as shown in subsequent chapters.

2.1   Design

The design chosen for our structures should fulfill several requirements. First, it should correspond to the physical effect that we want to observe and implement all its elements: the PhC cavity, the QDs, and their coupling. Then, each element should be optimized: The PhC type and quality, the QD emission linewidth and strength, etc. Finally, the matching between the QD emission and the PhC CM should match, both spectrally and spatially. All these should be achieved with the maximum possible yield, in order to be able to measure a significant number of systems with reasonable effort.

2.1.1   Membrane wafer

Designing our devices, we start with the estimation of the appropriate wafer parameters. Figure 2:1(a) schematically shows the starting GaAs/Al$_{0.7}$Ga$_{0.3}$As/GaAs wafer used for the implementation of PhC cavities in a floating membrane. This structure is needed to maintain a single tightly confined optical mode in the vertical (z) direction, which is needed to ensure high cavity Q values. This is achieved by using the high index of refraction of the GaAs surrounded by air on both sides of the floating membrane to produce vertical confinement. Moreover, the vertical distance between the membrane and the GaAs substrate should be large enough, to avoid leakage through the evanescent part of the confined mode (another Q reduction factor). It is also important to have a fundamental optical mode well coupled to the QD, since it gives the higher Q value.

There are several secondary parameters that influence the choice of the membrane thickness. Thicker membranes have the following advantages:

- They are more robust mechanically
- Their surface roughness (inevitable due to the growth of AlGaAs sacrificial layer on {111}B surface) is less harmful for the optical quality of the cavity, as the optical mode is confined more tightly inside the membrane, having thus less overlap with the membrane surface.
- They provide more flexibility in the design of the pyramidal recesses, where we grow the position-controlled QDs, as pyramid size can be increased in thicker membrane. This provides several advantages: first, a certain minimum pyramid depth is required, in order to accommodate the grown buffer and cap layers, as well as the inevitable GaAs diffusion during the deoxidation process before growth. Second, with deeper pyramids we can position the QDs vertically in the center of the membrane, to provide the best overlap with the cavity optical mode. Finally, larger

pyramids are more tolerant to fluctuations during processing, thus producing QDs of better quality and smaller fluctuations in emission energies.

On the other hand, thinner membranes have the following advantages:

- They provide a smaller optical mode volume, thus increasing the Purcell factor
- They can allow higher QD density, by accommodating smaller pyramidal recesses.

Taking into account these limitations, we choose a membrane thickness of around 260±5 nm and therefore pyramid sides equal to 300±10 nm. The AlGaAs sacrificial layer's thickness was chosen as 1000±50 nm to assure enough distance between the floating GaAs membrane and the substrate.

After fixing the membrane wafer layer thickness parameters, we examine the spatial arrangement of our PhC-QD structures on the wafer. First, we grow the QDs on membrane substrate segments of size 1/6 of 2" wafer. On each segment we fabricate two identical structures, grown together, on which the PhC cavities are fabricated separately, to increase versatility and yield. The arrangement of these are shown by dashed lines in Figure 2:1(b), where the division of ½ wafer is shown, first to 1/6 segments, then each segment to two parts.

2.1.2 Alignment marks

The first step in the fabrication is to engrave alignment marks onto the wafer. We have designed special alignment marks, allowing us to precisely position structures with the EBL system. For this purpose, we use 4 groups with 9 identical squares each, simultaneously fabricated on half of the 2" membrane wafer (Figure 2:1(b)). Our EBL system needs only 1 square out of each group for alignment; the others are redundant to assure the availability of high-quality marks. This is important in view of the epitaxial growth steps involved, which might degrade the quality of the alignment marks. Using these alignment marks, we can refer to the exact position of each fabricated QD. Figure 2:1(c, d) show two different designs used for QDs with PhC integration. QDs were grown either in c) 45 independent squares of 330x330 μm^2 size, or d) one square of 2.4x2.4 mm^2 size. Both designs allowed successful QD integration with PhC cavities.

2.1.3 QD arrays

Our experience in the growth of InGaAs/GaAs QDs on patterned (111)B GaAs shows, that the best optical properties in terms of linewidth and inhomogeneous broadening (~6-8 meV) are obtained in QD ensembles grown in large-area (0.3-2 mm) pyramidal recess arrays of moderate density (4-$11 \cdot 10^8$ cm^{-2}, distance between pyramids = 300-500 nm). We subsequently use the etching of the PhC cavities on top of these ensembles to remove all the superfluous QDs, leaving only those inside the PhC cavities. We therefore fabricate the QDs in a triangular lattice that has a period twice that of the PhC hole lattice. Precisely superimposed, through the exact alignment, the holes of the PhC cavity remove all QDs except those designed to be placed in the PhC cavity. In Figure 2:1(f), the red triangles show the positions of the QDs, including those that are eliminated by the PhC holes. To achieve this goal, the maximum alignment error of our procedure should be less than 30 nm, taking into account PhC hole radius and QD lateral size. As discussed in more details below, we verify the alignment accuracy using control marks introduced at the place of some PhC cavities, as shown in Figure 2:1(e). In order to allow for more flexibility in the choice of PhC cavity length, we place the QDs intended for integration with PhC cavities in a narrow 'free' channel, which does not change significantly the growth conditions (Figure 2:1 (f)).
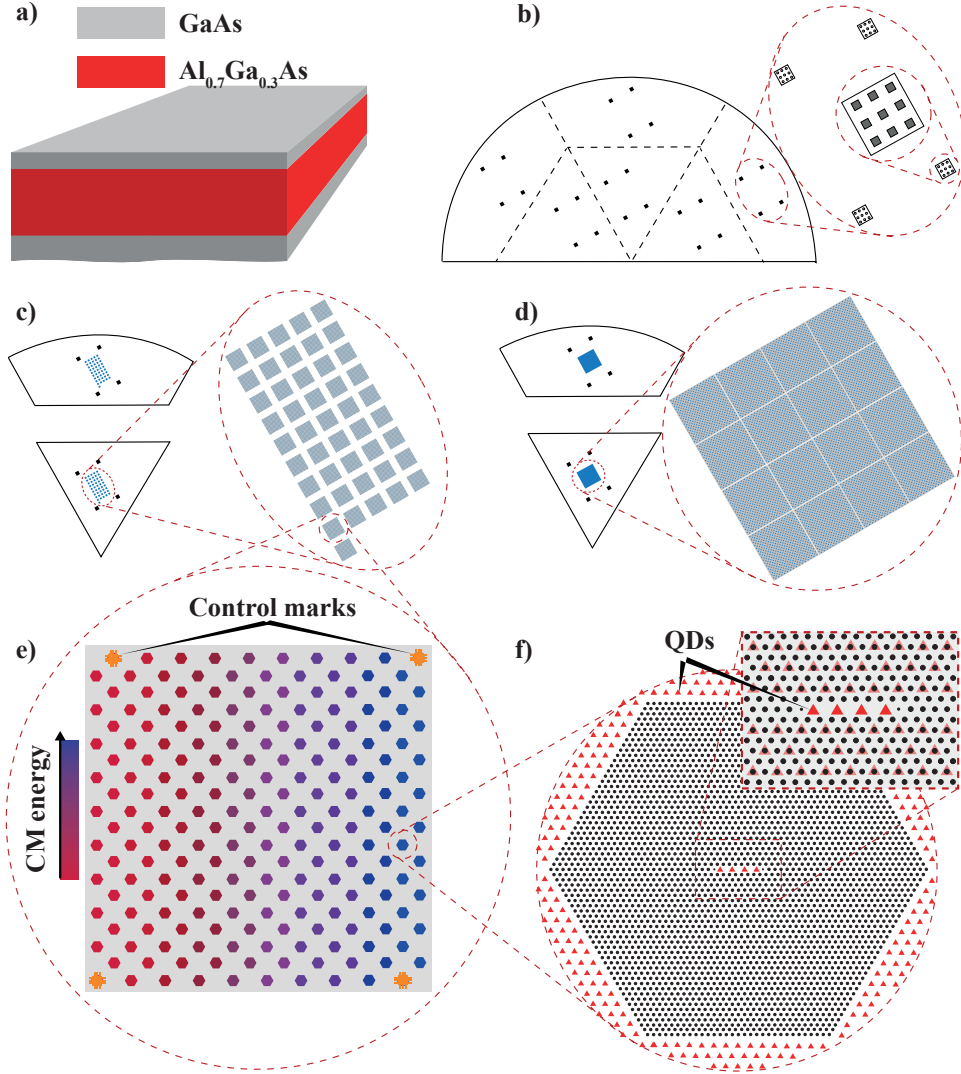
Figure 2:1 Design of PhC cavities with site-controlled QDs: a) Cross-section of the 2" membrane wafer, showing the GaAs/$Al_{0.7}Ga_{0.3}$As/GaAs heterostructure, b) alignment marks etched in one half of the 2" wafer, c) design with QDs grown in separate square regions, d) design with QDs grown in one square region, e) PhC cavities in honeycomb-like lattice and f) an L7 PhC cavity integrated with 4 QDs. Color variation in e) reflects resonance energy of ground state CM.

2.1.4   PhC structures

Our devices are assigned to several physical experiments. In particular, we are interested in the investigation of the coupling between different CMs and QD excitonic transitions, as well as in the influence of CM to QD-exciton detuning. Moreover, even in homogeneous arrays, the QD emission energy fluctuates between QDs, usually by a few meV (inhomogeneous broadening of array emission is on the order of 5 meV per excitonic line). Therefore, we included in our design PhC cavities with (systematic) different resonance wavelengths, spanning the range of measured QD emission

energies. Figure 2:1(e) schematically shows 200 fabricated PhC cavities that fit in a 330x330 μm^2 QD array square (as shown in Figure 2:1(c)). In each line, PhC hole radii increase in ~1 nm steps from left to right, while in each vertical 'zigzag' PhC hole sizes are kept nominally the same. This provides 10 sets of 20 devices with nominally the same PhC cavity parameters in each set. Overall, each piece comprises about 9000 PhCs, containing 9 different PhC-QD configurations and 10 hole radii, each repeated 100 times.

In order to navigate over different devices, we address each square with its row and column number as shown in Figure 2:2(a). In a similar way, we give coordinates to structures in a square. Figure 2:2(c) shows numbering of different PhC sets with 's' and 'p' corresponding to a linear set and a 'zigzag' of PhC cavities. Using this notation, each device can be addressed as RkClsmpn. In each sample, all designs are the same for all columns of the same row (same k), and all PhCs are the same in all rows of the same column (same n). The PhC CM energy increases with PhC column number (n).
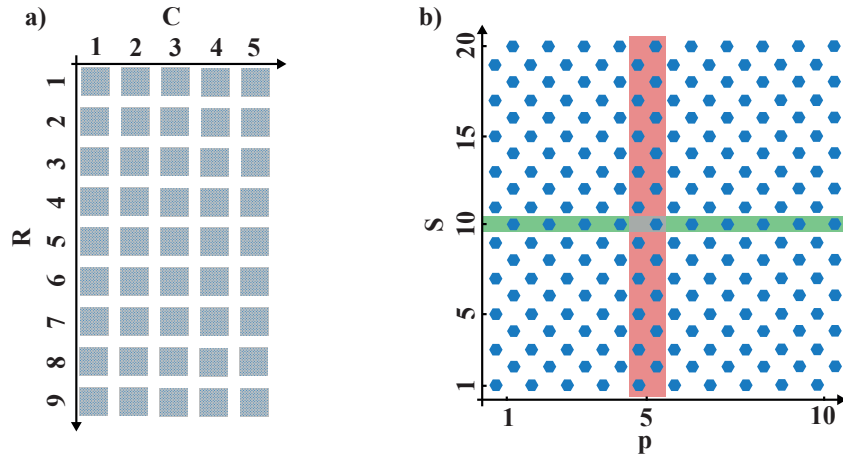
Figure 2:2 Navigation on the sample: coordinates of a) QD squares (330x330μm each) and b) PhC cavities in a square. 'R', 'C', 's' and 'p' stand for row, column, series and PhC number.

Figure 2:3(a) shows an emission spectrum of a QD ensemble (all excitonic lines) at the center of a QD square, obtained with μ-PL setup (see description in 2.3.4). Figure 2:3(b) shows the series of PhC CM resonances designed to fit this center emission wavelength. In this way, we obtain spectral overlap of the PhC optical mode and the QD excitonic transitions. The wide spread of PhC CM wavelengths also increases the robustness of our integration process. We obtain some devices with PhC CM close to resonance with the QD excitonic transition, even in the case of a deviation of the CM wavelength from its targeted value, due to deviations in PhC hole size or membrane thickness.

a)

b)
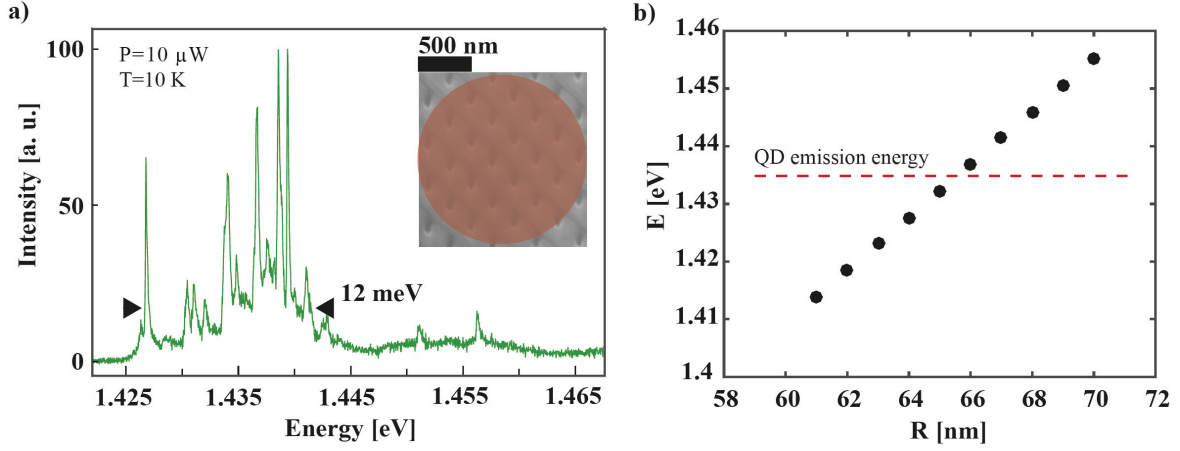
Figure 2:3 Matching of QD emission wavelength with PhC resonance: a) QD ensemble emission and b) PhC cavity resonance energy as a function of PhC hole size. An insert in a) shows a SEM image of a QD ensemble with the red circle sketching the approximate extent of the excitation spot (1.6 μm) for λ=850 nm.

2.1.5 Summary of the process

Figure 2:4 shows the general flow chart of our fabrication process. The process can be divided into several major steps: alignment mark definition, QD growth and PhC cavity fabrication.
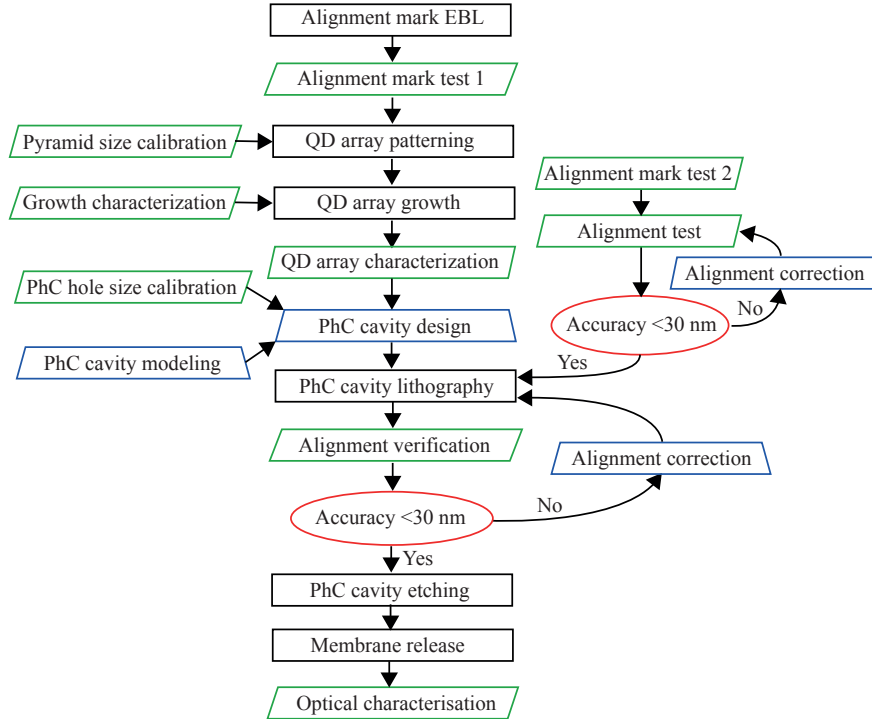
Figure 2:4 Flow chart of the fabrication process, yielding QDs matched spatially and spectrally with a PhC CM.

During all the fabrication processes we run several tests in order to control the quality of our QDs, PhC cavities and alignment precision. The latter is controlled at all major fabrication steps. This procedure allows maintaining the alignment error between QD and PhC cavity positions to below 30 nm, as well as achieving good energy matching between QD excitonic emission and the PhC CM resonance.

2.2 Fabrication and testing of alignment marks

2.2.1 Fabrication

The success of our fabrication procedure depends on an extremely precise alignment of two EBL processes serving for the site-controlled pyramidal QD and the PhC cavity fabrication. In our approach we use special alignment marks (AMs), situated outside the zone of QD growth, so we do not need post-growth location of the QDs, contrary to the alignment techniques used in other laboratories [6], [51], [64]–[66], as the aligned fabrication of site-controlled QDs allows us to know the exact coordinates of all QDs. This is essential for scaling up such integration from single QDs to systems of more than 2 QDs.

The AMs used in our work consist of 4 groups of 3×3 squares; each group is positioned close to the edge of the QD growth area. Our electron beam lithography (EBL) system requires a certain contrast level for AM recognition, usually achieved with metal (e.g. Gold) AMs deposited on the wafer. Because of the epitaxial growth process, we cannot tolerate metal residues on the surface of the wafer (diffusion and contamination), instead we use deeply etched (more than 1 μm) markers. These AMs cannot be directly etched into the membrane wafer, as they would penetrate through the $Al_{0.7}Ga_{0.3}As$ sacrificial layer and would be removed during the pre-growth cleaning process. Therefore we etch them directly in the GaAs substrate, having first removed the GaAs membrane and the $Al_{0.7}Ga_{0.3}As$ sacrificial layer in a square region around the whole AM region. Here follows the full fabrication process of these AMs.

After SiO_2 and PMMA (poly(methyl methacrylate), positive EBL resist) layer deposition on top of the membrane wafer surface, we define square openings of $600x600\mu m^2$ (later $300x300\mu m^2$) size using the EBL system Figure 2:5(a)). Figure 2:5(b) shows these square openings transferred into the SiO_2 hard mask using reactive ion etching (RIE) process [15]. Using an inductive coupled plasma (ICP) process, we then etch away the GaAs membrane and part of the $Al_{0.7}Ga_{0.3}As$ sacrificial layer as shown (without residual SiO_2 layer) in Figure 2:5(c). Using HF solution, we completely remove the $Al_{0.7}Ga_{0.3}As$, as well as the residual SiO_2, mask, exposing the GaAs substrate in these large square areas (Figure 2:5(d)).
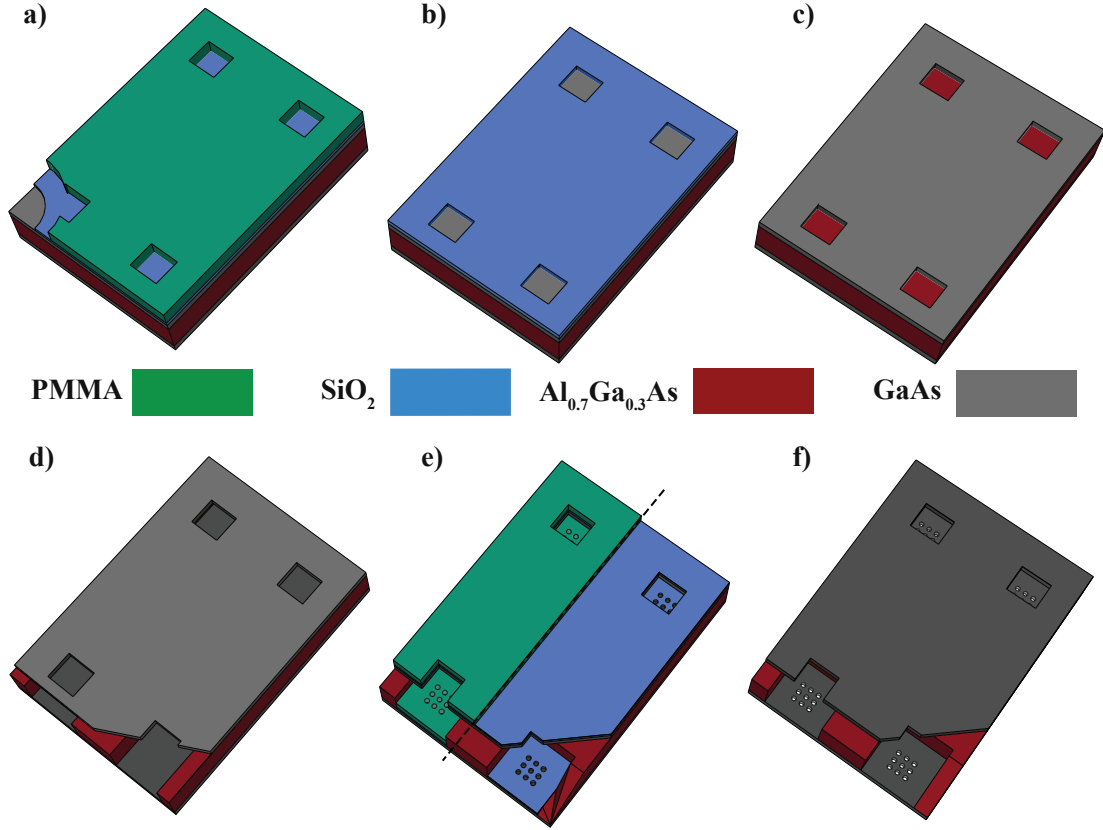
Figure 2:5 Fabrication steps of alignment marks: a) square openings written with EBL in PMMA, b) transfer to SiO_2 mask using RIE, c) square openings etched through GaAs membrane and into $Al_{0.7}Ga_{0.3}As$ layer using ICP process, d) removing of all $Al_{0.7}Ga_{0.3}As$ sacrificial layer in the square openings with diluted HF solution, e) 3x3 alignment mark pattern defined in hard mask using combination of EBL and RIE and f) alignment marks etched in GaAs with ICP.

In the same manner, we etch the AMs (four groups of 3x3 20x20 μm^2 square holes 1.5μm deep) at the bottom of these large square openings as illustrated in Figure 2:5(e, f). After deposition of fresh SiO_2 and PMMA layers, in each square opening we define a pattern of 3x3 squares in PMMA and transfer it to the SiO2 hard mask. Then we remove the PMMA layer and etch the AMs using ICP process. The depth of our AMs was controlled using an Alpha-Step (Tencore Instruments) machine, while etching quality was characterized using scanning electron microscope (SEM). Figure 2:6(a) shows a SEM image of one group of 3x3 squares and an individual square with roughness low enough for good alignment. Having 9 AMs in each group increases the reliability of the system, as each of these squares can be used for alignment purposes, thus providing sufficient redundancy.

The size of the AMs was changed in the course of process development: At first we used 20x20 μm^2 marks, with 200μm spacing (these were used with the samples depicted in Figure 2:1(c)); then we reduced their size to 10x10 μm^2 marks, with 100μm spacing (these were used with the samples depicted in Figure 2:1(d)). The surrounding area, where the membrane was etched down to substrate level, was reduces accordingly, from 600x600μm^2 to 300x300μm^2.
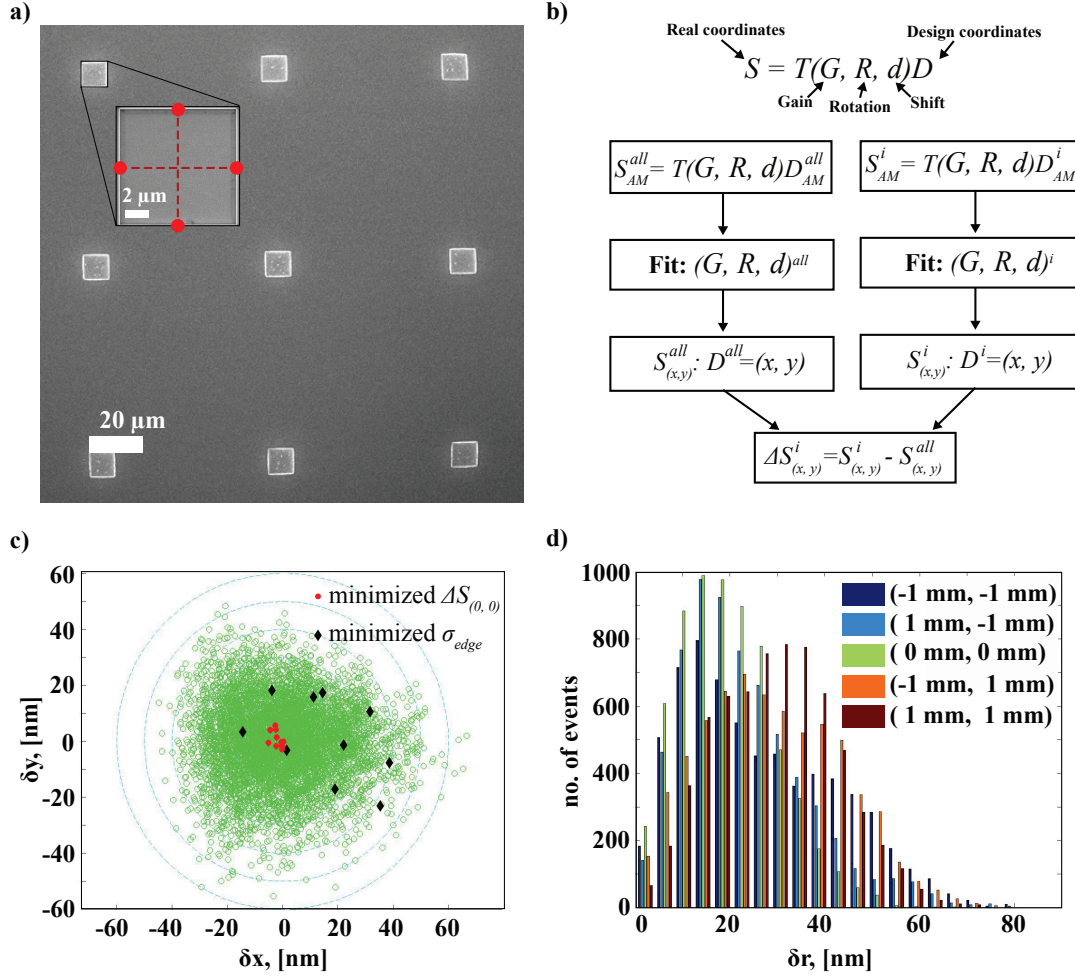
Figure 2:6 Testing of alignment mark (AM) quality: a) SEM of all 3 by 3 AMs in a group (inset: SEM image of one AM), b) diagram of the procedure used to identify the best AM set, c) Results of the procedure: deviation $(\delta x, \delta y)$ of the transformed (0,0) point, from the best transformed (0,0) point, d) Histogram showing the number of AM combinations yielding the value of absolute deviation from the best transformed point.

2.2.2   Testing

Since the accuracy of alignment between QDs and PhCs depends on AMs, we sought ways to test their quality. To that end, we developed two procedures, the first testing the quality of individual marker recognition, the second testing the position accuracy of AMs as used in the alignment process. To obtain the information needed by these procedures, we run a special program (script), which instructs the system to visit systematically all AMs in a sample and report all their parameters.

In order to develop these qualification procedures, one must first understand the alignment process as done by the EBL computer. First, for each AM in a set of four, the electron beam scans the four edges of the square AM, registering their position with high accuracy. The AM center position is thus found, as shown in the inset of Figure 2:6(a). From the measured center position of the four AMs, the system calculates a transformation, using the following parameters:

37

$$\begin{pmatrix} x' \\ y' \end{pmatrix} = \begin{pmatrix} 1 + G_x & R_x \\ 1 + G_y & R_y \end{pmatrix} \begin{pmatrix} x \\ y \end{pmatrix} + \begin{pmatrix} dx \\ dy \end{pmatrix}$$

where (x, y) are the design coordinates, (x', y') are the sample coordinates, G_x, G_y are gain (expansion/contraction) factors, R_x, R_y are rotation factors, and dx, dy are translations. During the writing of the structures, all design points are thus transformed to yield the corresponding points on the sample.

The first procedure tests the quality of each AM by itself: The edge scan process yields not only the mean value (giving the position of the edge), but also a standard deviation value σ_{edge} of the AM edge coordinate, which can be used as a measure of the quality of this edge. We use the sum of the standard deviation value of all four AM edges as a measure of the AM quality. In case of exceptionally high values we exclude the AM. However, the highest quality of each of the AMs does not necessarily assure the lowest final alignment error. Another factor is the position of the AMs: If we use a certain set of AMs to align the QDs, we want the second set of AMs, used to align the PhCs, to yield the same positions. Figure 2:6(b) summarizes the algorithm used in the second procedure for identification of the best set of AMs in terms of alignment precision. Using the coordinates of all AMs, we have to find a transformation T between sample coordinates $S(x', y')$ and design coordinates $D(x, y)$ as shown above:

$$S = T(G, R, d)D$$

This transition matrix can be expressed in terms of a set of parameters G, R, d, corresponding to gain, rotation and shift, respectively. Using the coordinates of all AMs (S_{AM}^{all}, D_{AM}^{all}), we find the best transformation set of paramters $(G, R, d)^{all}$ using a least square fitting procedure. These parameters provide the best transformation of design coordinates $D_{(x,y)}^{all} = (x, y)$ to real coordinates $S_{(x,y)}^{all}$. However, the EBL system does not use all 36 alignment marks, but only a set of four (specified by the user), thus we want to find the set of 4 alignment marks that would give the best transformation (= closest to the transformation obtained by using ALL marks). We find parameters $(G, R, d)^i$ for all possible combinations 'i' of 4 AMs from different groups, using their real S_{AM}^i and design D_{AM}^i coordinates. Then, we calculate the transformation of 5 design points for each AM set and compare the resulting positions with those obtained using the best transformation parameters. As design points we use (0, 0), that is the center of a structure, (-1, -1) mm, (-1, 1) mm, (1, -1) mm and (1, 1) mm, that are the corners of a square with a 2 mm side centered at the point (0, 0). The smallest difference from the best transformation $\Delta S_{(x,y)}^i = S_{(x,y)}^i - S_{(x,y)}^{all}$ points to a set (i) of 4 alignment marks. The results of this procedure are shown in Figure 2:6(c), where green circles show the values of $\Delta S_{(0,0)}^i$ for all combinations of AMs, with the 10 best values indicated by red circles. Surprisingly, the 10 combinations of AMs with the smallest standard deviation of edge position σ_{edge} (black diamonds, Figure 2:6(c)) give moderate deviation from the best transformation point and do not necessarily satisfy our AM selection procedure. Figure 2:6(d) summarizes the alignment errors from all 5 design positions in the form of a histogram, counting the number of AM sets yielding a given absolute alignment error. In this specific sample, we see that design coordinates (-1,1) and (1,1) give worse alignment performance than (0,0). Still, in most samples, we have many AM combina-

tions giving alignment precision better then 10 nm for all design coordinates, as seen by the 10 red points at the center of Figure 2:6(c).

2.3   Fabrication of site-controlled QD arrays

Having remarkably low inhomogeneous broadening, site-controlled pyramidal QDs grown in pyramidal recess arrays are excellent for integration with PhC structures [76]. Full control on QD coordinates not only serves for precise positioning inside the PhC cavity but also for removing redundant QDs as discussed in 2.4.1.

2.3.1   Patterning with pyramidal recesses

We start the fabrication of QD arrays with deposition of SiO_2 and PMMA layers on top of the GaAs membrane surface deoxidized with HF solution. Using the EBL system, we define triangular openings organized in a triangular lattice as shown in Figure 2:7(a). The array base is aligned with the $\{1,-1,0\}$ crystallographic direction with better than 1 mrad precision. The triangular pattern is then transferred to the SiO_2 mask using RIE process, as shown in Figure 2:7(b). The sample is characterized using SEM before and after PMMA removal, as shown in the insets of Figure 2:7(b). At this stage we verify the correct triangular opening sizes, which is important for obtaining the designed emission wavelength of our QDs, as discussed below.
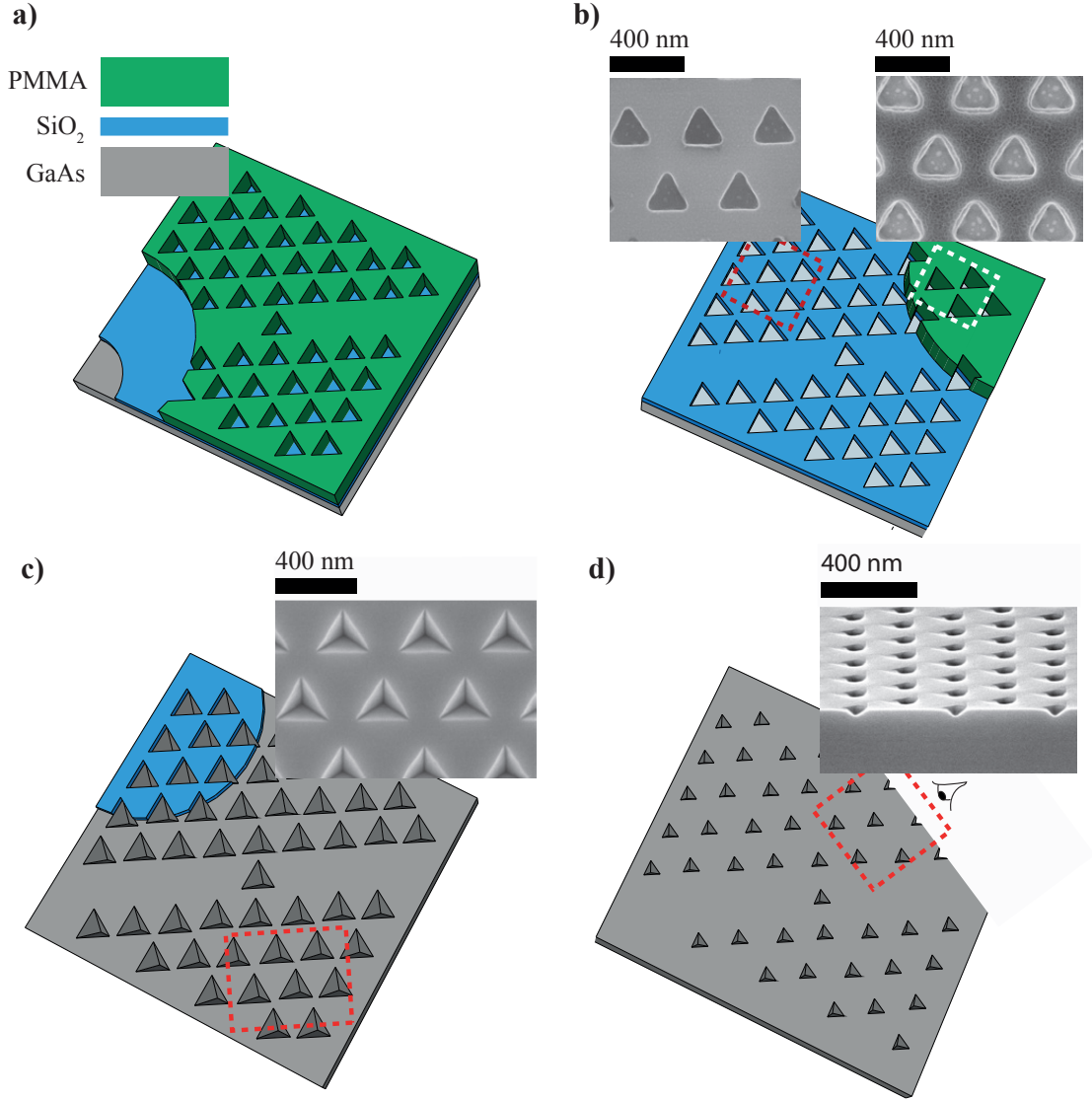
Figure 2:7 Steps of pyramid pattern fabrication process: a) Triangular array pattern of triangles written in PMMA using EBL (note the "channel" with a single triangle in the center), b) RIE of triangular pattern in SiO$_2$ mask (inset: SEM images of etched SiO$_2$ mask before (right) and after (left) PMMA removal), c) pyramids etched in GaAs using Br:Methanol solution (inset: SEM image) and d) substrate after MOCVD growth (inset: SEM inclined image of cleaved sample).

After the triangular pattern transfer to the SiO$_2$ hard mask, we etch pyramidal openings in the GaAs membrane using Br:Methanol solution. Due to the orientation of triangular sides, the chemical etching stops at the border of the triangular openings, producing a pattern of inverted pyramids highly homogeneous in size (Figure 2:7(c)), exposing {111}A crystallographic facets. After pyramid pattern etching, we verify their size using SEM and remove the SiO$_2$ mask using HF solution.

Before growing QDs using metalorganic chemical vapor deposition (MOCVD), we run a cleaning/deoxidation procedure using a sequence of RIE-based O$_2$ plasma ashing, water rinsing, and de-

oxidization with HF solution. After deoxidization, we immediately transfer the sample in nitrogen atmosphere to the MOCVD chamber. Using trimethylgallium, trimethylindium and arsine precursor gases, we grow GaAs/In$_X$Ga$_{1-X}$As heterostructures in the inverted pyramidal recesses as further discussed below. Figure 2:7(d) schematically shows the sample surface with partially planarized surface after MOCVD. The SEM inset shows the cross section of grown QDs with residual, 20 nm deep surface undulations, showing the positions of the QDs.

2.3.2 Optimization of pyramid fabrication.

The emission wavelength of pyramidal QDs depends not only on growth parameters, but also on the length of the pyramid side, as has been reported elsewhere [24], [77]. As a result, we have to optimize all the steps of pyramidal recess fabrication in order to obtain the designed emission wavelength with low inhomogeneous broadening. With our SiO$_2$ RIE process, we observe only small enlargement of the triangular opening size during pattern transfer from PMMA to SiO$_2$. Thus, only EBL and the wet etching steps can affect the size and homogeneity of the resulting pyramidal pattern.

Figure 2:8 shows SEM images of triangular patterns in SiO$_2$ resulting from exposing the PMMA resist layer in EBL with different exposure doses. Figure 2:8(b) shows the size corresponding to the targeted one. In extreme cases of underexposure, some of the triangles are missing, while overexposure leads to rounded patterns and loss of resolution. By systematically taking SEM images of the pattern, we can verify the size and quality of the triangular edges, which reflects the quality of PMMA exposure.
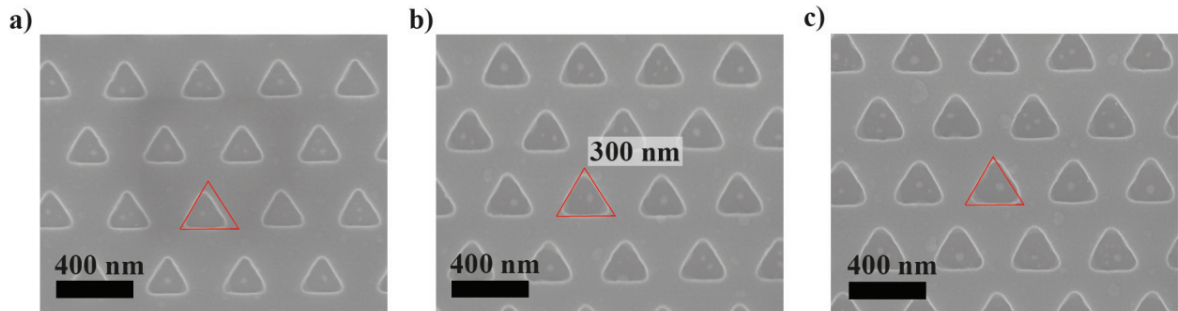
Figure 2:8 Electron beam lithography optimization for QD mask fabrication: a), b) and c) show triangular openings in SiO$_2$ mask obtained with three EBL exposure doses increasing from left to right. Targeted opening size is shown with a red triangle.

The precision of pattern transfer from the triangular opening in the SiO$_2$ mask to the inverted pyramids in GaAs depends on the quality of SiO$_2$ adhesion as well as on the precise calibration of the SiO$_2$ hard mask etching step. Since membrane sample fabrication includes many steps of SiO$_2$ and PMMA deposition and removal, there is potential danger of surface contamination by residues, which could lead to bad SiO$_2$ to GaAs adhesion and thus cause unexpected fabrication problems, such as highly inhomogeneous pyramid pattern.

Figure 2:9 shows SEM images of a correct pyramid array (a) and two common problems. Figure 2:9(b) shows pyramids etched after insufficient cleaning: Residual PMMA layer prevents Br:Methanol solution from interaction with GaAs surface, leading to flat bottoms of the pyramidal

recesses. In other cases, residual PMMA layer after alignment mark fabrication can lead to bad SiO_2 adhesion, causing merging of pyramidal recesses as shown in Figure 2:9(c). There, the Br :Methanol etching process no longer stops at the boarder of the triangular openings. However, simple cleaning procedure with O_2 plasma and water rinsing eliminates all these fabrication problems, leading to homogeneous pyramidal recess pattern (Figure 2:9(a)).

a)

Correct

b)

Flat pyramid tip

c)
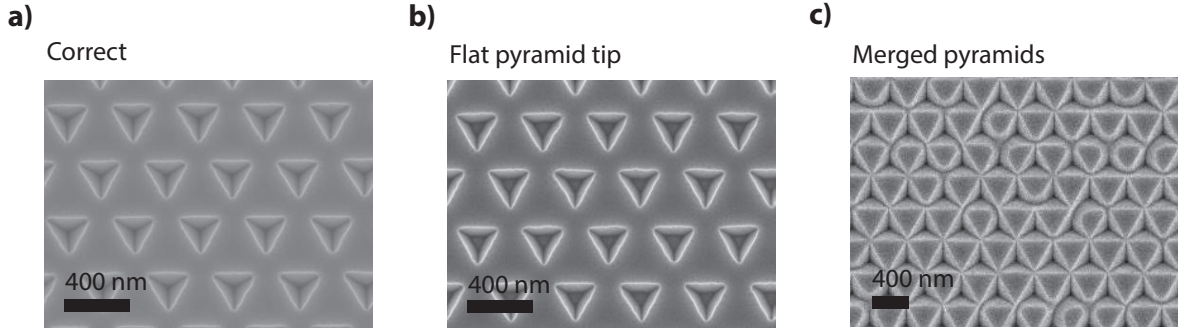
Merged pyramids

Figure 2:9 Optimization of pyramidal recesses wet etching with Br:Methanol solution: a) correctly etched pyramidal recesses, b) pyramidal recesses with flat tip and c) merged pyramidal recesses.

Using RIE time that ensures etching of triangular openings exactly to the SiO_2/GaAs interface, we obtain pyramidal recesses with size corresponding to the target size with precision of better than 10 nm.

2.3.3   MOCVD growth.

The grown InGaAs/GaAs heterostructures consist of a GaAs buffer layer, an $In_XGa_{1-X}As$ QD layer and a GaAs cap layer. We start the growth sequence with a substrate deoxidation process keeping the sample at 570 °C under N_2/AsH_3 flow in order to avoid excessive rounding of the pyramidal recess tips due to Ga surface diffusion, as was confirmed by cross-sectional SEM. The substrate temperature is then adjusted to 600 °C while initializing the growth of the GaAs buffer (Figure 2:10(b)) under a V/III ratio of ≈3000. Decomposition of precursors on the pyramids' {111}A surfaces leads to localized growth in the pyramids, with growth on {111}B plane being almost negligible. During the growth of GaAs layers inside the pyramidal recesses, the crystallographic planes are conserved, maintaining the narrow pyramidal tip at the bottom. This is of high importance for the formation of the $In_XGa_{1-X}As$ QD, which nucleates at the pyramidal tip due to capillarity of the incoming adatoms [78], [79]. The QD layer (Figure 2:10(c)) is made of $In_XGa_{1-X}As$ layer (X=20%) with nominal thickness of 0.6 nm. During the growth of this layer, quantum wire - like structures are also formed by the capillarity at the pyramid edges (Figure 2:10(d)), and thin quantum wells are formed on the pyramid sides. The InGaAs QD array is finally overgrown with a GaAs cap layer to reach near planarization, obtained with a cumulated nominal growth thickness of ≈10 nm. [28]. Planarization increases the distance from the sample's surface to the QD, reducing an influence of surface states and adds to the quality of PhC devices that are fabricated hereinafter.
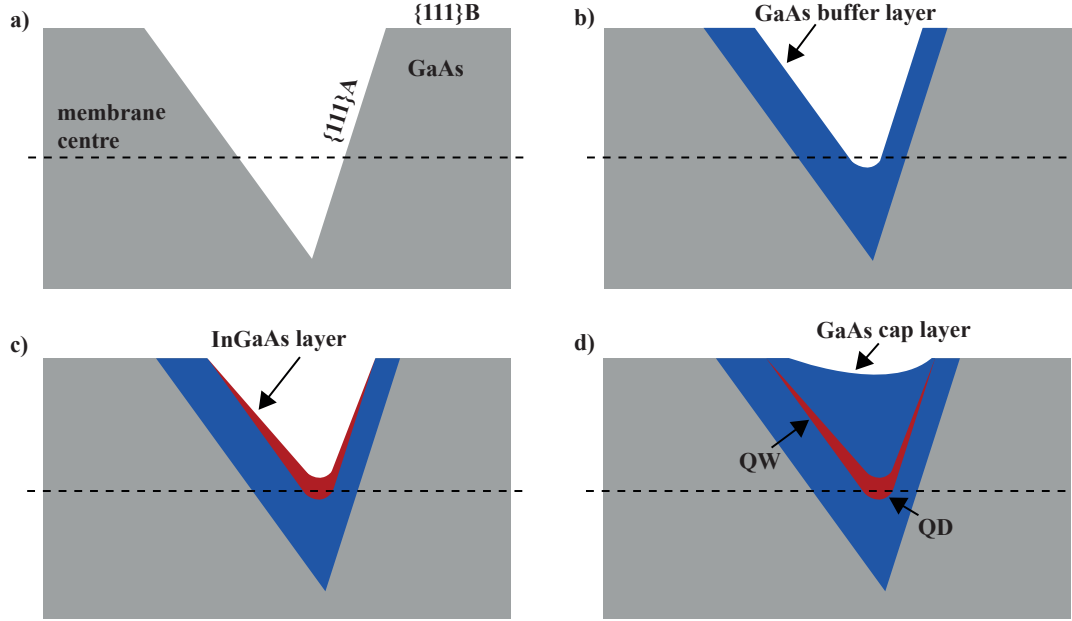
Figure 2:10 Schematics of pyramidal QD growth: a) cross section of GaAs patterned substrate, b) GaAs buffer layer growth, c) In$_X$Ga$_{1-X}$As layer growth and d) covering with GaAs cap layer[79].

Figure 2:11(a) shows a SEM image of a substrate with deep (more than 50 nm) residual recesses after QD growth. Such deep recesses can significantly decrease the quality of the PhC cavities fabricated on top of them. The inset shows misaligned PhC holes that lost their roundness due to the non planarized surface. By increasing the thickness of the GaAs capping layer, we can almost fully planarize the pyramidal recesses, as shown in Figure 2:11(b). In this way we also ensure the round shapes of the PhC holes and decrease the CM losses due to scattering at the residual periodic recess array near the PhC cavity defect.
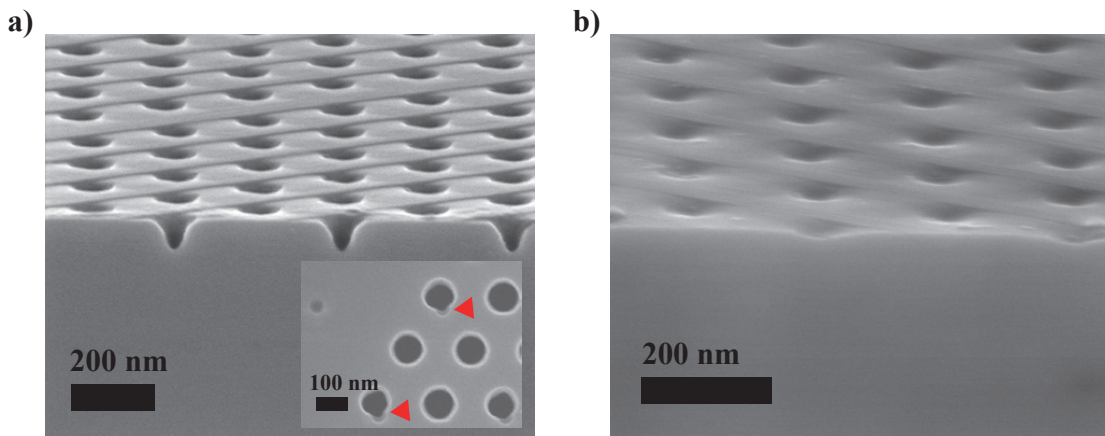
Figure 2:11 Calibration of capping layer thickness for planarization purposes: SEM images of: a) non planarized, and b) almost fully planarized substrates. An insert in a) shows an SEM image of a sample with visible QD fingerprints after PhC etching due to a bad PhC-QD alignment accuracy.

2.3.4 Optical characterization

For optical investigation of our samples we used a micro-photoluminescence (µ-PL) optical setup, shown in Figure 2:12. As an excitation source we use Ti:Sapphire laser pumped with 532 nm Spectra Physics Millenia doubled Nd:YAG (DPSS) laser. Ti:Sapphire laser wavelength is tunable in the range of 700-1000 nm, allowing both above barrier, that is, optical excitation with a photon energy bigger then the GaAs band gap, and (quasi-)resonant excitation regimes. Excitation beam was focused on the sample surface using Zeiss objective with 50x magnification, 0.55 aperture and 3.6 mm working distance, resulting in a ~1.6 µm laser excitation spot size. When the sample is excited at low wavelength (730 nm), carriers are also excited in the GaAs, with typical diffusion length of ~4 µm, and can excite QDs in this range. Low-energy excitation (above the GaAs bandgap) can be used to reduce diffusion. The PL is collected using the same objective lens and then directed using a beamsplitter to an infrared camera and a spectrometer. The infrared camera is used for controlling the position of the excitation spot on the sample surface, which can be varied using a motorized high-precision (50 nm) xy-position stage while the spectrometer is a part of a polarization-resolved spectrum acquisition system. The latter system consists of a polarization analyzer comprising of a λ/2 waveplate and a polarizer; the spectrometer is equipped with a charge coupled device (CCD) detector. We use a 'Jobin Yvon Triax 550' spectrometer with 55 cm focal length and 1200 grooves/nm diffraction grating; and a 'Jobin Yvon Spex Spectrum One' nitrogen-cooled CCD camera, featuring a 2048x512 pixel matrix allowing optical signal detection in the 400-1000 nm wavelength range. With this equipment we obtain a spectral resolution of 80-90 µeV.
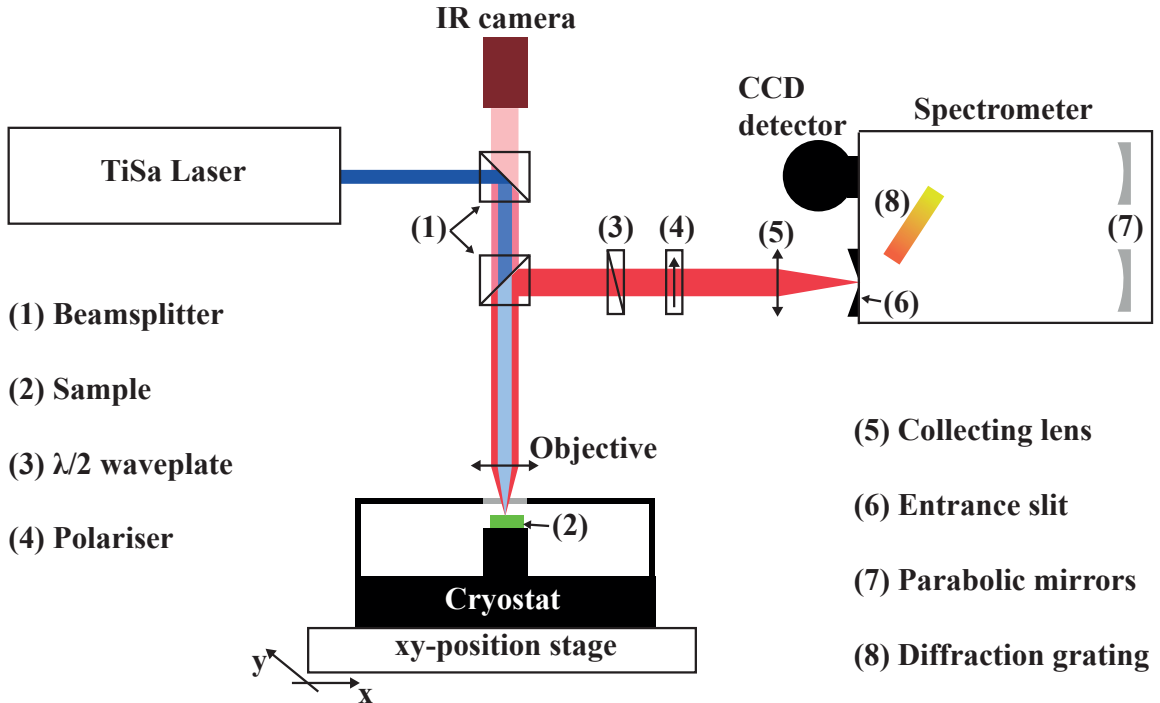
Figure 2:12 Schematics of the µ-PL optical setup. Laser beam used for excitation is highlighted in blue whereas collected photoluminescence is highlighted in red.

PL signal collection efficiency of our optical system is significantly affected by chromatic aberrations of the collecting lens. In particular, we lose ~65 % of the signal if the optical setup is aligned using the reflected laser beam with λ=720 nm, that is, the typical wavelength used in our experiments with above barrier excitation. This is due to different focal lengths of the lenses at λ1=720 nm and λ2=850 nm. This difference leads to PL signal attenuation at the spectrometer entrance slit as schematically shown in the insert of Figure 2:13. Thus, after alignment with the laser beam we further adjust the collecting lens position focusing the GaAs emission beam on the slit surface. The finesse of the focusing is controlled by the intensity of the GaAs PL signal. Using this procedure we increase the collection of our PL system by around 3 times as can be seen in the spectra of Figure 2:13. Note that after alignment with the GaAs PL signal the maximum intensity does not depend on the spectrometer slit size. Spectra measured with 100 µm and 500 µm slit values almost completely overlap, while the spectrum measured with a 50 µm slit is only 25% weaker in intensity.
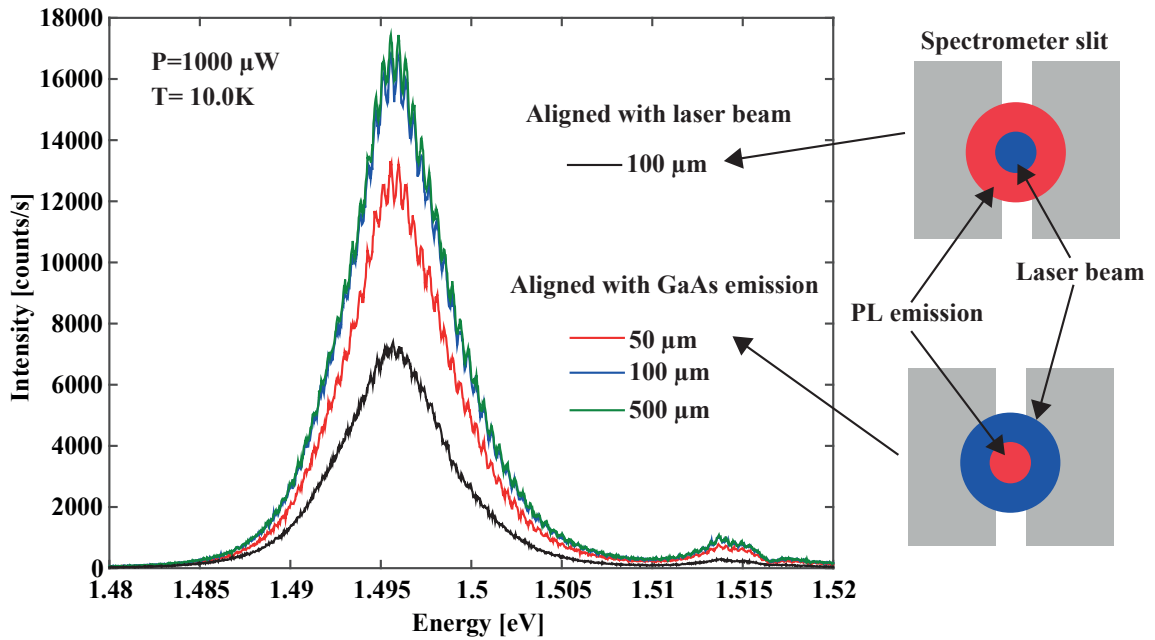
Figure 2:13 Spectra of GaAs emission measured after optical system alignment with reflected laser beam and with GaAs PL emission for several entrance slit widths. Insets on the right show GaAs emission and laser beam spots at the spectrometer slit for two collection lens positions.

After QD growth we optically characterize our samples, focusing on center emission wavelength, inhomogeneous broadening of the QD ensemble and individual QD transition linewidths. These parameters are important for both growth optimization and subsequent integration with the PhC cavities. With growth parameters optimized, we expect QD exciton linewidths of around 100 µeV, inhomogeneous broadening below 10 meV and center emission wavelength around 870 nm. Figure 2:14(a) shows the main spectral features observed in the emission of our structures. Typically, we observe emission of the InGaAs QD ground and excited states, InGaAs quantum wire (QWR) and bulk GaAs emission consisting of carbon impurity and GaAs excitonic lines. The lowest energy part of the spectrum, that is, QD ground state, is formed by multiple narrow lines corresponding to dif-

ferent QDs showing neutral, charged and bi- excitonic transitions. Figure 2:14(b) shows the spectra of the QD ensembles (ground state emission) as a function of excitation spot position inside a given QD "square".
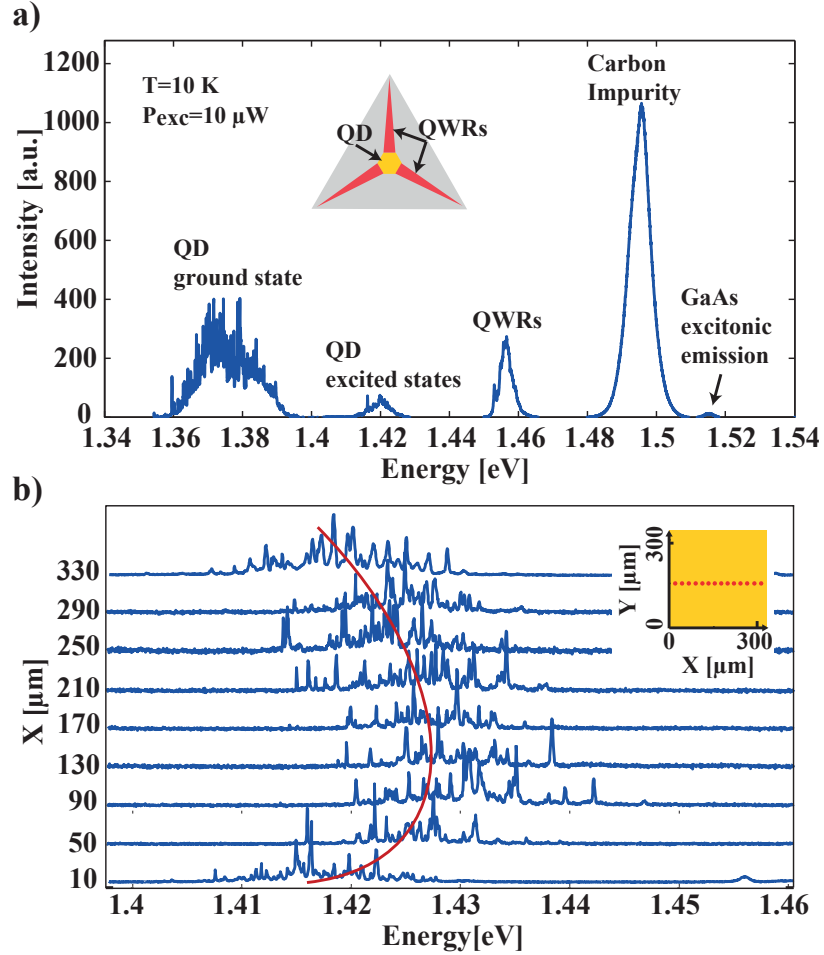
Figure 2:14 Optical characterization of QD ensembles: a) panoramic spectrum showing QD, QWR and GaAs emissions and b) ensemble QD ground state spectra measured for different excitation spot positions in a QD "square" as schematically shown in the insert.

Figure 2:15(a) shows a typical QD ensemble spectrum measured at the center of a QD array square (R5C4). The color map in the inset shows the center emission wavelength of the QD ensembles measured in all 45 squares. We see that the central and top region of the pattern shows a relatively narrow range of wavelengths (around 865±5 nm), while the bottom and outside squares show stronger wavelength dispersion.
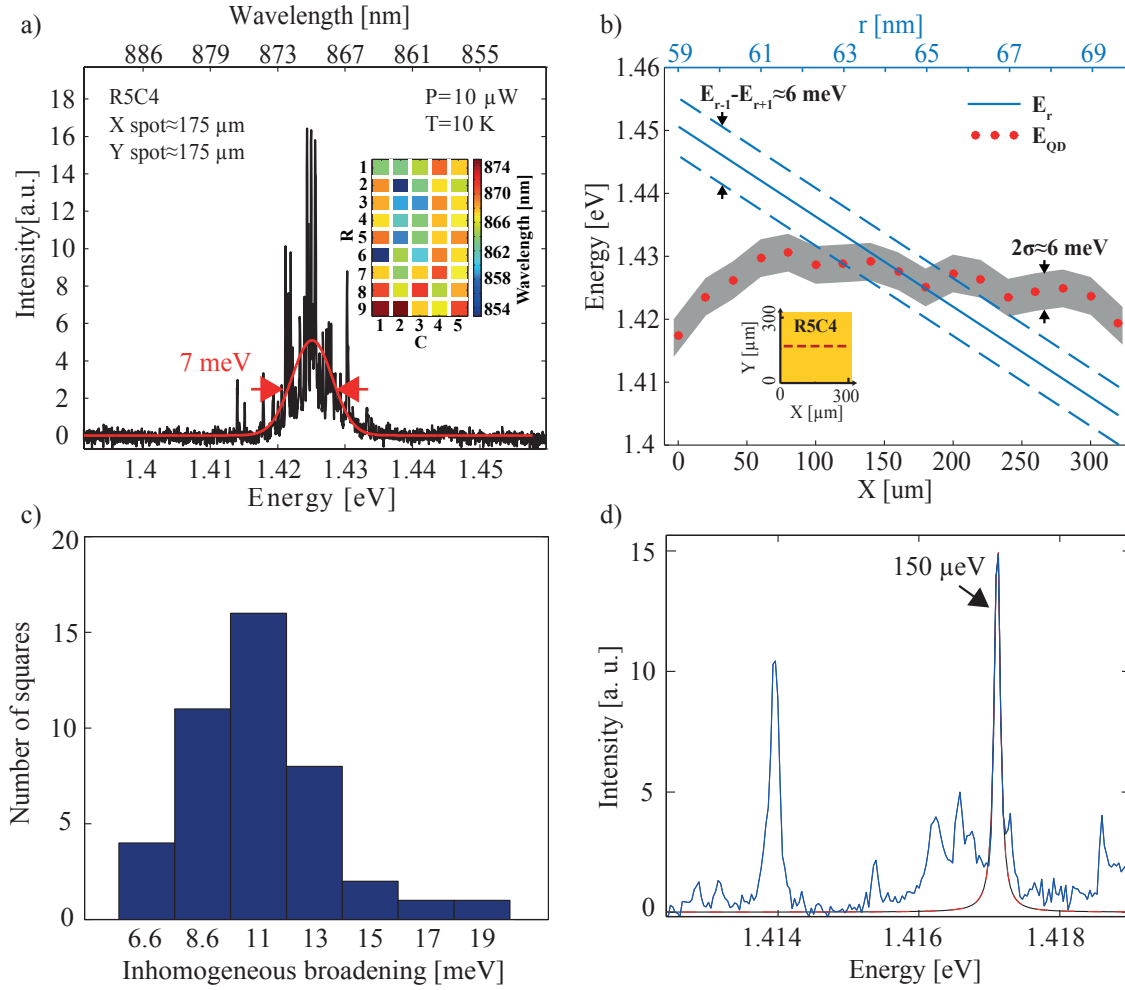
Figure 2:15 Optical characterization of QD ensembles in sample Gio15-3B: a) Typical QD ensemble emission spectrum, measured at the center of square R5C4. The red curve shows a Gaussian fit used to measure the inhomogeneous width. Inset: A color map showing the center emission wavelength of the QD ensembles measured in all 45 squares. b) Spatial dependence of the QD ensemble central wavelength inside a square (R5C4), measured along the red dashed line shown in the inset. The central energy is shown by red dots; the envelope shows the inhomogeneous broadening envelope (±3 meV). The straight blue line shows the CM energies of a series of PhC to be superimposed on these QDs; the dashed lines show the extent of phonon coupling (±3 meV), as discussed in Chapters 4-5. c) Statistics of the inhomogeneous broadening for all 45 squares. d) Expanded emission spectrum of an ensemble of QDs, with a Gaussian fit (black line) to a single excitonic line.

Moreover, when scanning a QD square with the excitation spot, we observe repeating red shift of QD ensemble center wavelength at the edge of QD squares relative to the center of the square (red dots and gray line in Figure 2:15(b)). This wavelength inhomogeneity is due to MOCVD precursor diffusion between regions external to the square (with almost exclusively {111}B surface, where only weak precursor decomposition and almost no growth take place) and the inside of the square (with considerable {111}A surface area, where both precursor decomposition and growth take place). This inhomogeneity is similar in all squares, and is of the same size as the inhomogeneous broadening of QD ensembles. Therefore no special considerations are taken with regard to this in-

homogeneity, as the PhC series are already designed in a way to respond to the inhomogeneous broadening issue (see below). This is demonstrated by the blue line in Figure 2:15(b), showing the expected PhC CM energy variation in a series of PhC that are fabricated with increasing hole diameters along the square. As we can allow for an extra ±3 meV phonon-assisted coupling range[72], we can expect that 4-7 PhC CM will couple to QDs in each row.

Figure 2:15(c) shows the histogram of inhomogeneous broadening collected in all 45 squares of sample Gio15-3B (see Appendix A). The average inhomogeneous broadening is around 11 meV, with several QD squares having inhomogeneous broadening below 7 meV. It should be noted that this broadening reflects not only QD size variations, but also the occurrence of neutral and negatively charged excitons at a given QD, with ~5meV energy separation[76]. Such low inhomogeneous broadening is promising for integration of several QDs with a PhC cavity, as the CM to excitonic transition phonon-assisted coupling range is around ±3 meV. The linewidths of individual QD excitonic lines are around 100-150 μeV, which is equivalent to a cavity quality factor of about 10000. We consider these parameters as satisfying for moving to PhC cavity integration. Using the measured QD center emission wavelengths, we calculate and implement the correct PhC hole size for each QD square area independently.

2.4   Fabrication of PhC cavities

The fabrication of PhC cavities is the final and very delicate procedure, as all PhC parameters should be correctly realized to match the previously fabricated QDs. Using the knowledge obtained previously at LPN-EPFL during integration of site-controlled QWRs and QDs [71], [72], [80] with PhC cavities, we successfully demonstrated integration of multiple QDs with PhC cavities [28].

2.4.1   Process description

After QD growth, we deposit a SiO_2 hard mask and PMMA resist layer on top of the grown membrane surface. Then we run an alignment test, followed if needed by alignment error compensation, as discussed in detail below. These tests are carried out using only the PMMA layer, conserving the same SiO_2 layer on top of the sample's surface as a protective layer. In this way, we do not increase the defect density that could reduce the quality of our devices. After these tests, we redeposit a new PMMA layer and start PhC fabrication. Using EBL, we define the PhC cavity patterns as shown in Figure 2:16(a). After PMMA development, we transfer the PhC patterns onto the SiO_2 mask using RIE and remove PMMA. Figure 2:16(b) schematically shows the superposition of the QD and the PhC pattern triangular lattices. At this point, we can finally verify alignment accuracy between the QDs and PhC cavity. QD residual recesses are well visible through the holes etched in the SiO_2 mask. The SEM in the inset to Figure 2:16(b) shows a device with alignment error of less then 30 nm, ensuring the removal of all redundant QDs and precise positioning of the target QDs in the PhC cavity.
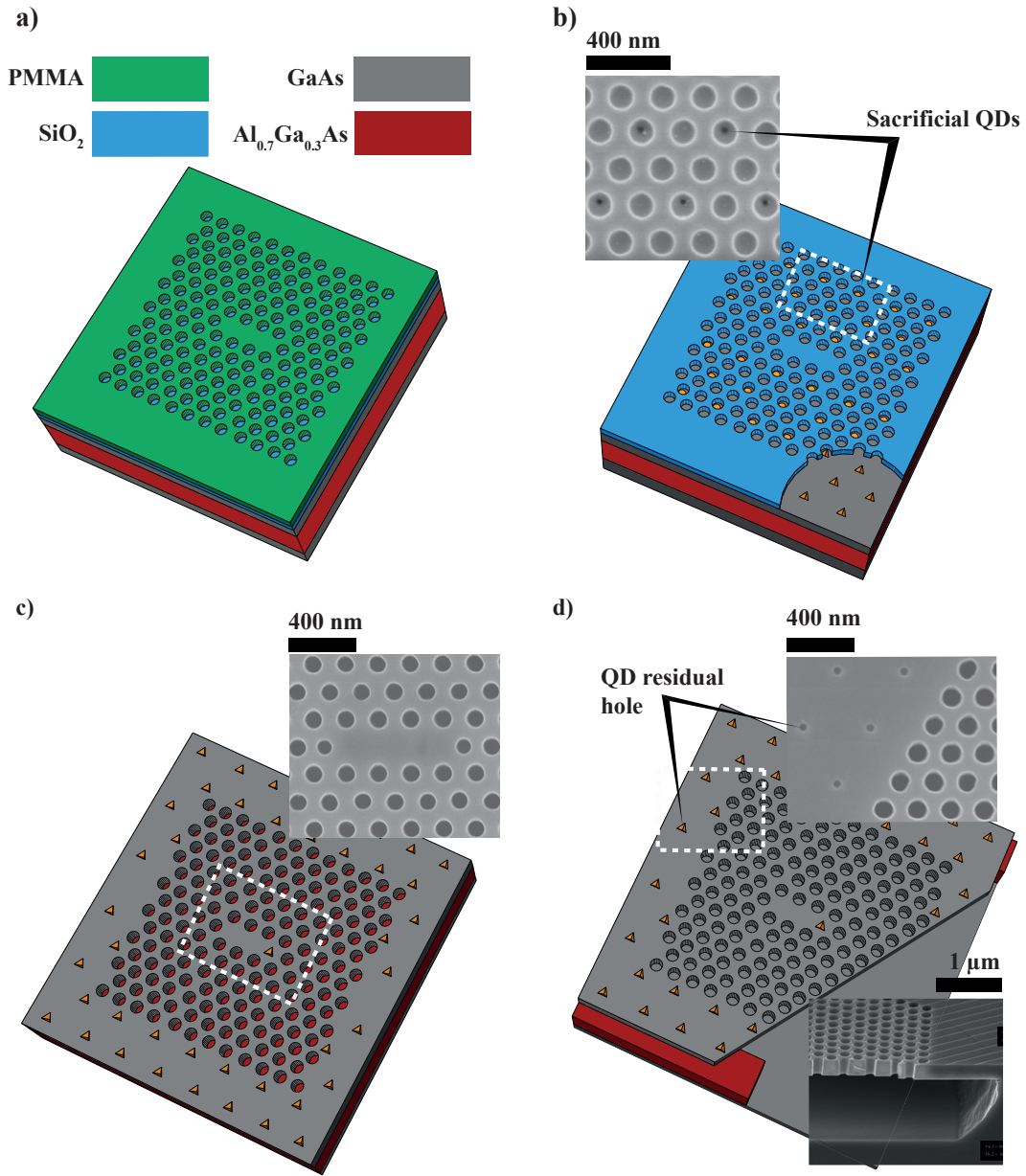
Figure 2:16 Steps of the PhC cavity fabrication process: a) PhC cavity written in PMMA using EBL, b) PhC pattern in the SiO_2 hard mask (underneath: the QDs). Inset: SEM top view of the PhC holes, where the QD centers can be seen, c) PhC structure after ICP process, etched down to the $Al_{0.7}Ga_{0.3}As$ sacrificial layer. Inset: SEM top view (a single QD pyramid can be seen at the right part of the PhC cavity). d) PhC after membrane release. Top inset: SEM top view at the edge of the cavity. Bottom inset: SEM cross-section after membrane release, showing the floating membrane and the holes.

After this final verification of alignment accuracy, we etch the PhC holes in the GaAs membrane using ICP process[81]. Figure 2:16(c) schematically shows an L3 PhC cavity with a single QD designed to probe the electric field at the edge of the PhC cavity. A SEM image of a real device is

shown in the inset. After etching of the PhC holes, we release the GaAs membrane by etching away the $Al_{0.7}Ga_{0.3}As$ sacrificial layer with diluted HF solution. This last processing step also removes any residual SiO_2 mask and deoxidizes the GaAs sample surface. In Figure 2:16(d) insets show the top view and the cross section of a device with released PhC. With our membrane release process, the sacrificial layer is over-etched by about 1μm around the PhC cavity.

2.4.2 Calibration of PhC hole etching

In order to obtain good matching between the PhC CM resonance and the QD emission wavelength, we need to control the PhC hole sizes with precision below 5 nm as can be seen in Figure 2:16(b). In PhC cavities, the CM wavelength depends strongly on hole pitch and size[78]. In our structures, written by EBL, the hole pitch is fixed by interferometric control with 1 nm precision. This leaves the hole size as the most important parameter to control, as the CM wavelength (in nm) depends on the hole size (in nm) as $d\lambda/dr \approx 4$. Therefore, we established tight control over the design hole radii, with precision of ~1 nm. However, as these patterns pass from the design to PMMA mask to SiO2 mask and finally to GaAs, their size changes through many processing parameters. Thus, before writing the actual PhC structures, we verify that EBL parameters result in correct PhC hole sizes at the end of the processing chain, namely in GaAs. For this purpose, we fabricate calibration pieces, containing a series of PhC cavities with different nominal hole sizes on a GaAs wafer. These go through the same processing steps as the final PhC structures on the membrane wafer, thus serving to calibrate the process. Figure 2:17 shows actual PhC hole versus nominal hole diameters used as EBL system input. On the right, several SEMs of PhC cavity patterns etched in GaAs wafer with different hole sizes are shown.
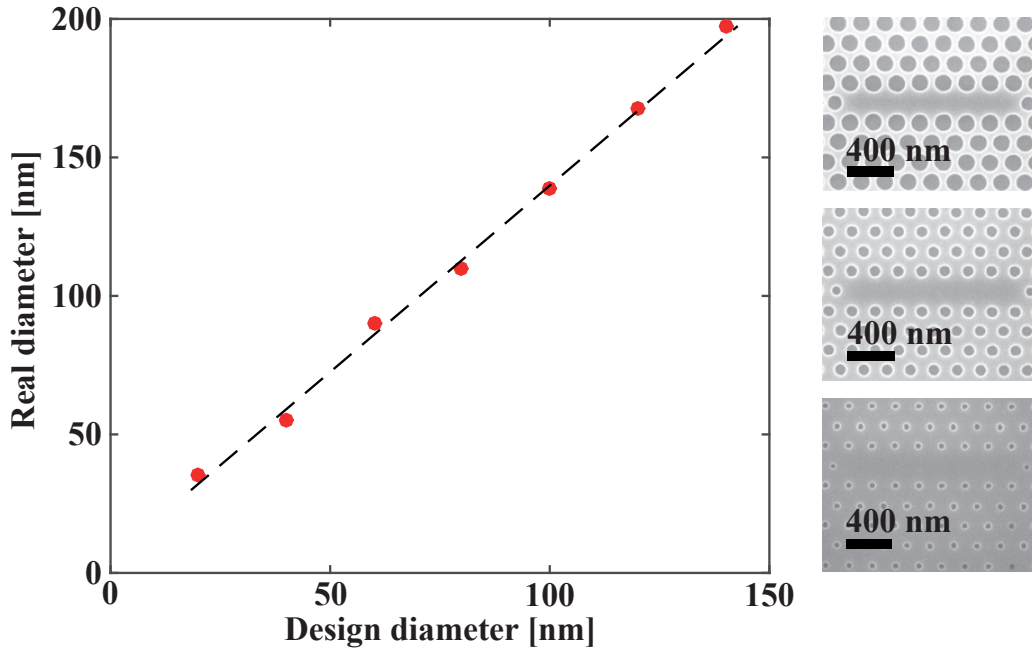
Figure 2:17 Actual PhC hole diameters versus design (nominal) hole diameters. On the right: SEM images taken of PhC cavities of different hole sizes, used for hole size calibration.

Apart from wavelength, which depends on hole size and membrane thickness, hole shape is also important, especially for achieving high Q values. The demands on shape include both hole round-ness (as determined by SEM top view) and verticality (as determined by SEM cross-section). Out of all processes, RIE etching of the hard mask and ICP etching of the PhC holes are the most important ones for achieving the required PhC quality. Figure 2:18(a, b) shows a SiO_2 mask etched during different times. In Figure 2:18(a), the SiO_2 mask is over-etched, leading to deeper etching into the GaAs layer. This leads to extended lateral etching of GaAs at the beginning of ICP etching, which distorts the shape of the PhC holes (Figure 2:18(c)). At the same time, PhC holes have sharp round shape if the etching of the SiO_2 hard mask stops exactly at the GaAs surface (Figure 2:18(b)), as confirmed by top view SEM shown in Figure 2:18(d).
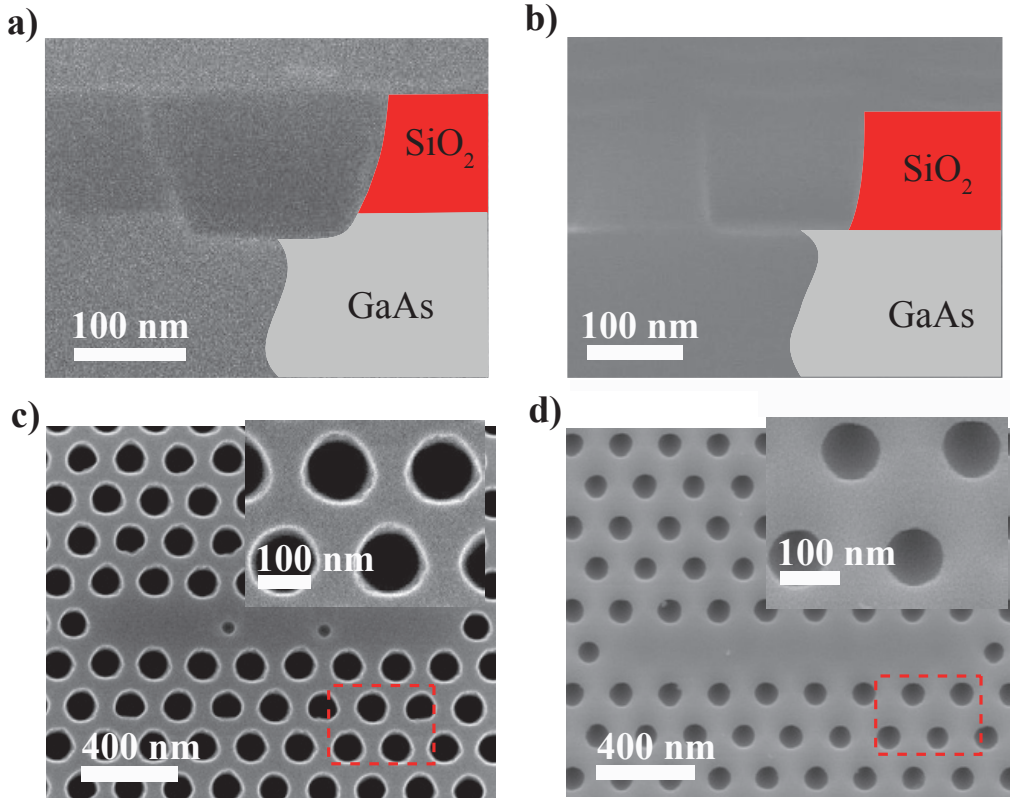
Figure 2:18 Optimization of SiO_2 RIE step: a) Over-etching the SiO_2 mask, as seen by SEM cross-section. The etched hole in the SiO_2 layer extends into the GaAs. b) Etching the SiO_2 layer precisely down to the GaAs surface, no over-etch. c) Top view SEM of the PhC cavity (after ICP etching, with mask removed) corresponding to the mask in a) The holes have skewed shapes at their tops, as is better seen in the enlarged inset. d) Same for the mask in b), showing near-perfect hole shapes.

After SiO_2 mask etching optimization, we tune the verticality of the PhC holes by changing the ratio between the ICP gas etching mixture ($BCl_3:N_2$). BCl_3 chemically etches GaAs, while N_2 passivates the walls of the PhC holes and removes chemical products [82]. Figure 2:19 shows a cross section of the PhC cavity etched in a membrane wafer. The PhC holes penetrate the $Al_{0.7}Ga_{0.3}As$ layer by 50 nm, allowing easy membrane release with high yield. In Figure 2:19(b) one can see the PhC

holes at higher magnification, showing their good verticality (deviation from the vertical below 0.03 rad, corresponding to the SEM resolution limit).
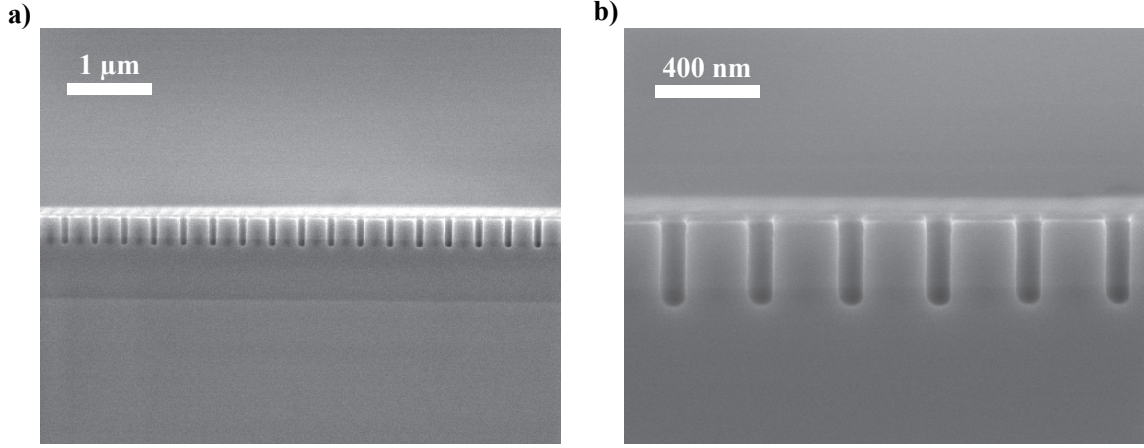
Figure 2:19 SEM images of PhC holes etched in a 260 nm GaAs membrane grown on 800 nm $Al_{0.7}Ga_{0.3}As$ layer. In a) PhC holes are seen together with the sacrificial layer. b) Magnified SEM image, showing holes penetrating into the sacrificial layer and the SiO_2 residual layer on the top.

After PhC hole etching we remove the $Al_{0.7}Ga_{0.3}As$ layer with diluted HF solution, releasing the GaAs membrane and removing any residual SiO_2 mask material from the sample surface. The devices with suspended PhC structures are first characterized by optical microscopy in bright and dark field modes (Figure 2:20). The latter allows efficient localization of defects, such as broken PhC membrane or contamination with etching products, as shown in Figure 2:20(c). Blue lines passing through the centers of the PhC cavities show the positions of the QD free channels in the QD square array. In a), b) the control marks used for alignment verification are also visible.
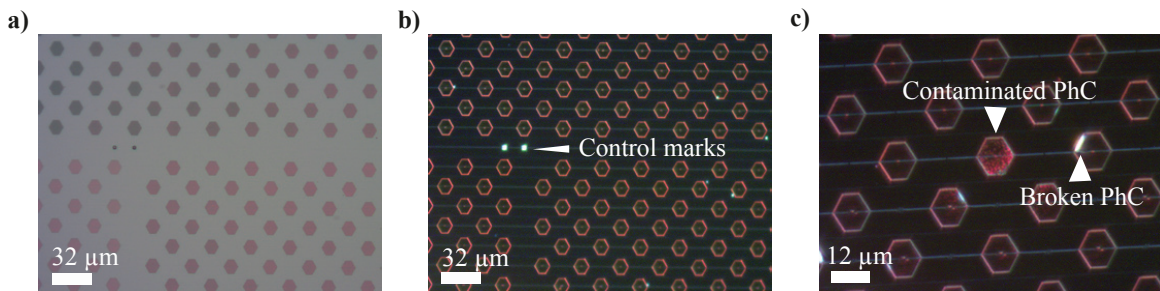
Figure 2:20 Optical microscope images of PhC cavities after membrane release. In a) and b) released PhC cavities are seen in bright and dark field, correspondingly. In c) (higher magnification image in dark field) we can distinguish the PhC cavities, as well as several defects (white arrows).

2.5   Verification of QD to PhC alignment

Position control of our QDs and PhC cavities is limited by the precision of the EBL system, which is sensitive to various parameters, such as temperature fluctuations (leading to drift), magnetic fields or vibrations, as well as to the quality of the alignment marks. While the first three are sys-

tem-dependent, quality of the alignment marks is sample-dependent and its influence can be independently assessed. We developed test procedures in order to assess the quality of the alignment marks through the different processing steps, as was shown in section 2.2, as well as methods to measure and compensate for positioning errors appearing during pattern writing discussed below.

2.5.1 Methods of alignment accuracy control

The high-temperature epitaxial growth process and other fabrication steps (e.g. etching) can lead to distortions of the borders of the alignment marks, thus affecting the precision of PhC cavity to QD positioning. As a first measure to minimize the effect of these distortions, we choose the best-quality sets of alignment marks to be used at each EBL writing (see section 2.2). Additionally, in order to minimize the effects of thermal sample drift, long (1-2 h) sample thermalization delay was introduced before writing, and the alignment procedure was repeated every ~2 min. during the pattern writing. In spite of these precautions (some of which were developed during the last parts of this thesis work), some samples still showed position errors. In order to compensate for these errors, we developed a procedure of alignment verification, which was carried out between the QD and PhC fabrication processes ('Alignment test' in the flow chart of Figure 2:4). For this purpose, after SiO_2 hard mask and PMMA resist deposition on the grown membrane sample, we exposed (using a very rapid writing process, to minimize drift) in PMMA 4 control marks in each QD square. Each control mark is placed at the position of a corner PhC cavity as shown in Figure 2:1(f). Figure 2:21(a) shows a SEM image of a control mark with QD fingerprints visible through the SiO_2 layer. Alignment accuracy is thus checked by comparing the position of the center QD fingerprint (highlighted with a red arrow) and a center of the control mark. Usually the measured error is similar for the 4 control marks of a square, and varies gradually across the sample, due to its source which is usually thermal drift. If the obtained alignment error is smaller than ~100 nm, then we compensate this shift by correcting the coordinates of the PhC cavities in each QD square independently. We repeat this test with different alignment mark sets in case of bigger positioning error. After choosing the set with the smallest positioning error, we compensate for it as explained above by introducing the necessary shift in the PhC cavity coordinates. It should be noticed that control marks are written in PMMA only, so it can be redeposited for each test run with the underlying SiO_2 hard mask kept in place. Thus, we prevent any contamination of our sample and protect the alignment marks from further distortion.
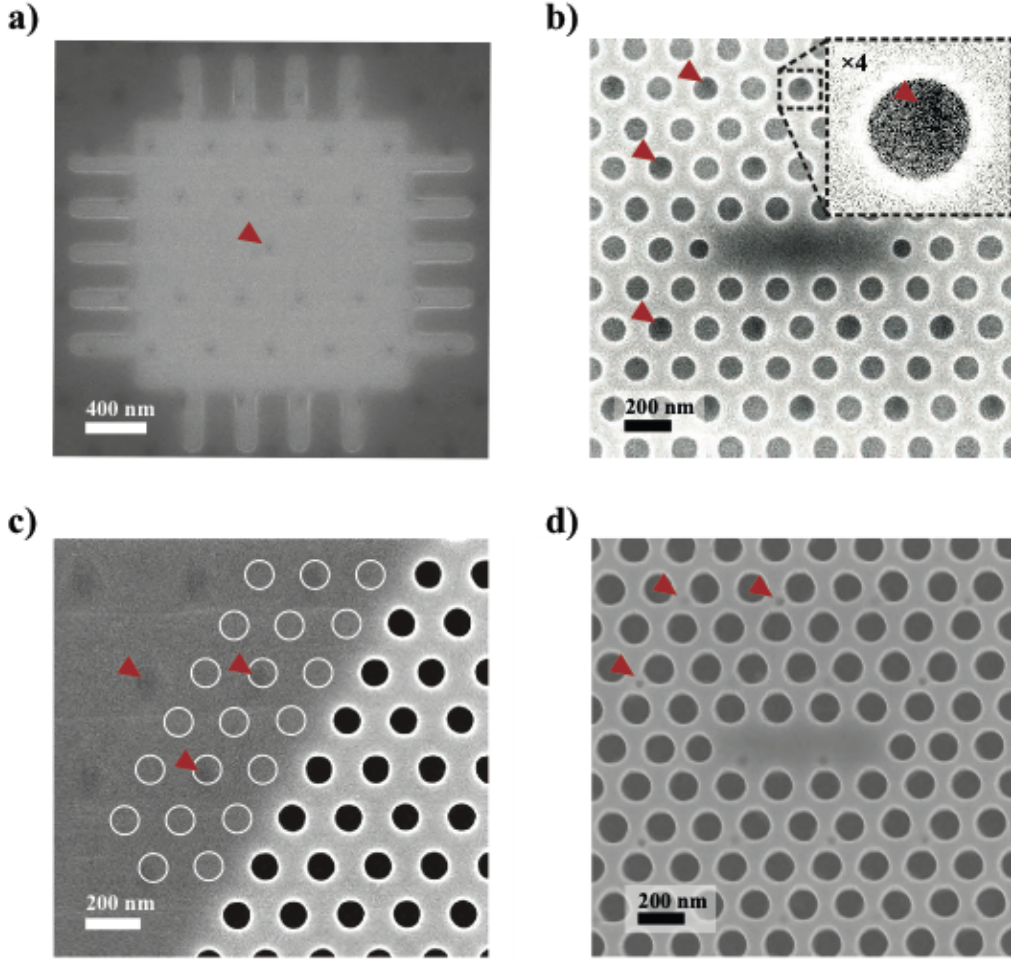
Figure 2:21 Alignment accuracy tests: a) SEM image of a test pattern (exposed in PMMA) used for alignment accuracy check after QD growth ('Alignment test' in the flow chart), the arrow points to the trace of a QD pyramid, which should be at the center. b) SEM image of a PhC pattern etched in the SiO_2 hard mask, with QD pyramids visible through the PhC holes (marked by arrows) c) SEM image of the edge and d) of the center of a PhC cavity, with QD pyramids marked by arrows, as used for post processing alignment measurements. Important misalignment can be seen in (d).

If the final coordinate system shift is successful, that is, misalignment becomes less than 30 nm, we start fabrication of the PhC structures, using the same coordinate shifts as found with the test patterns. After SiO_2 etching, we re-verify the alignment precision by comparing the positions of the QD fingerprints visible through the PhC holes in the SiO_2 mask (Figure 2:21(b)). This final verification is reflected in the flow chart as 'PhC-QD alignment test'.

We also measure the alignment error after the fabrication process to confirm QD isolation. For this purpose, we compare the matching of the QDs and imaginary PhC positions on the side of the devices (drawn on a SEM image), or measure the positions of QDs in the PhC cavity, as shown in Figure 2:21(c, d). The former method is more precise in case of almost completely planarized QDs,

as measurements of QD positions inside the PhC cavity are possible only with relatively deep QD fingerprints.

2.5.2 Compensation of alignment error

We successfully compensate the alignment errors due to their reproducibility. Distortion of the co-ordinate system associated with a fixed set of alignment marks remains the same throughout different EBL processes, if the same alignment marks are used and are permanently protected with the SiO_2 hard mask. Figure 2:22 shows the alignment errors before and after applying the alignment corrections. The former were measured with control patterns, while the latter were measured in the processed PhC structures. Initial alignment errors exceeded 60 nm, as can be seen in Figure 2:19(a). After alignment error compensation, we finalized the fabrication of our devices and confirmed that the alignment errors were reduced below 20 nm for almost all the structures (Figure 2:22(b)).
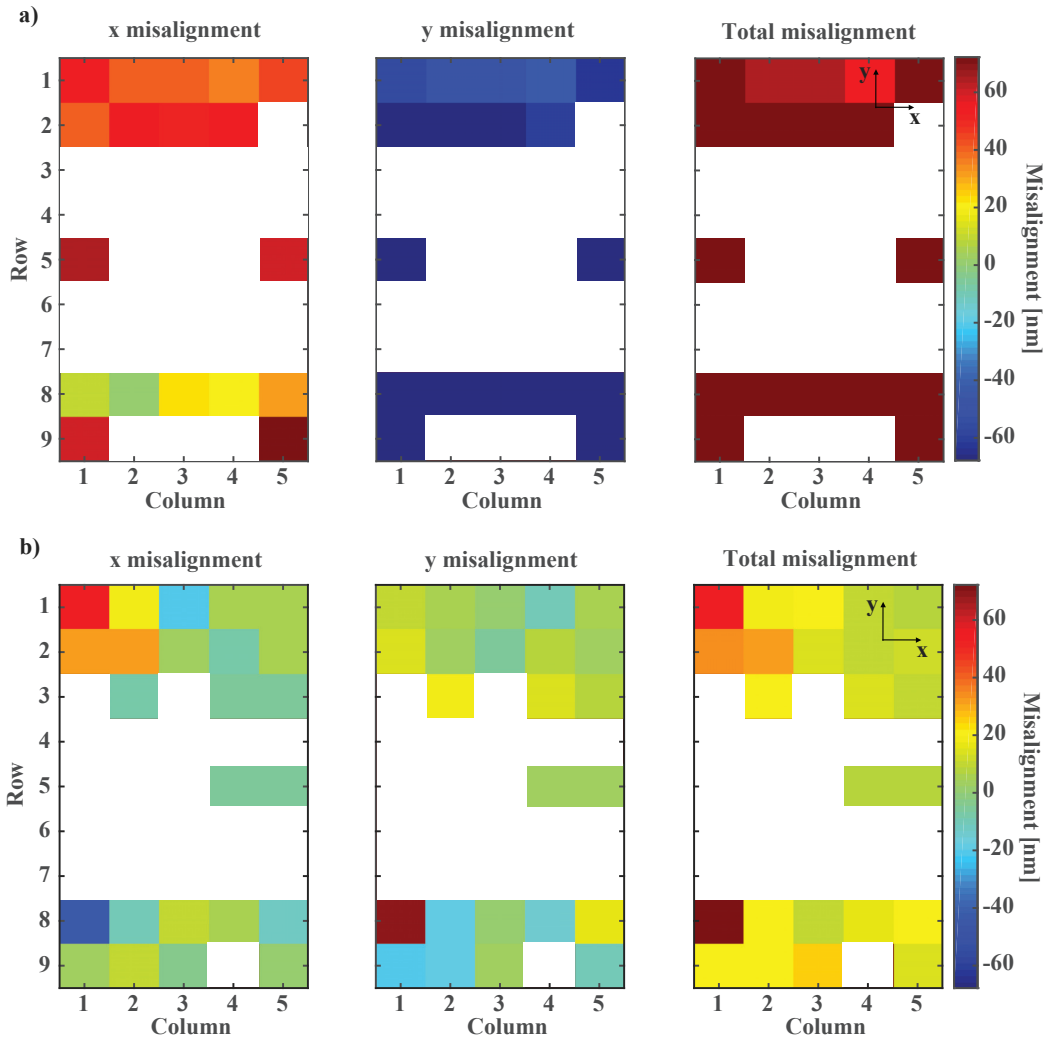
Figure 2:22 Positioning error compensation process for sample Gio15-2B: a) Mapping of the initial positioning error, measured with control marks in several squares. Total misalignment is the length of the alignment error vector. b) Same mapping of alignment accuracy, measured after PhC writing using the corrected coordinates. Squares shown in white were not checked for alignment accuracy.

2.5.3   Probing the alignment drift

So far we have treated alignment errors on the level of entire squares. Concerning possible drift during the EBL writing process inside a single QD square (see Appendix B), we check the alignment accuracy for several PhC devices lying on the same horizontal or vertical line inside the same square, that is, 's' or 'p' coordinate is kept constant. Alignment accuracy of different PhC cavities did not deviate significantly from its mean value inside a square, as one can see in Figure 2:23. We observed no significant alignment dependence on position inside the individual square, less than 20 nm in almost all cases. This shows that the relatively short EBL writing time of an individual square does not contribute to any significant drift.
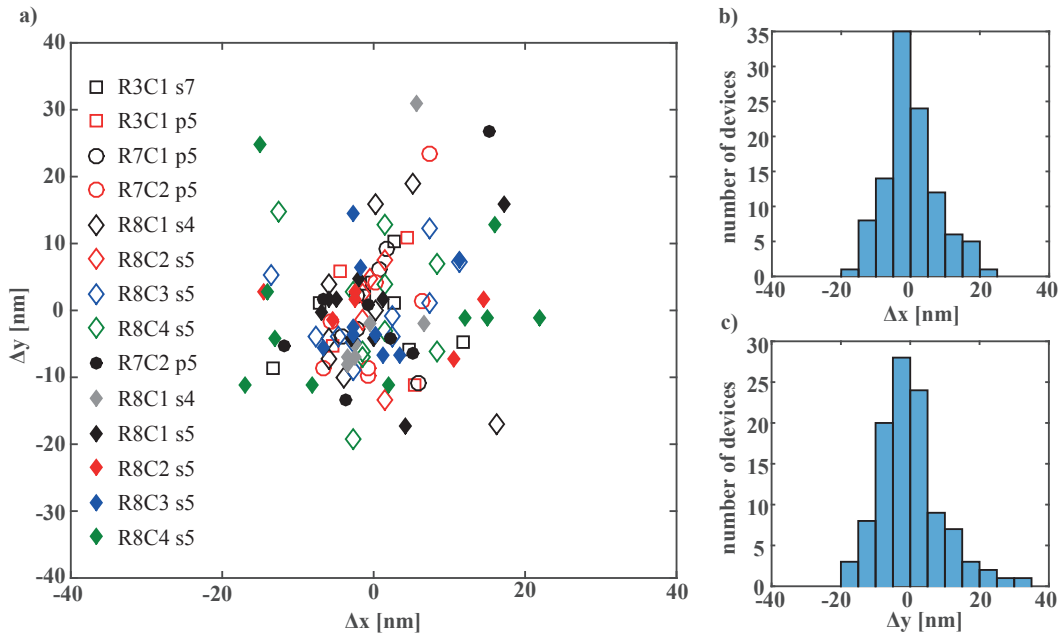
Figure 2:23 Alignment accuracy of QD with PhC cavity inside a square: a) For each square (denoted by a different symbol), the difference between X-axis and Y-axis measured alignment errors of different devices, all in the same square, from the mean value in this square. 'R' and 'C' stand for row and column, that is, coordinates of a square while 's' and 'p' stand for coordinates of a device inside the square as described in section 3.1.4. b) and c) Histograms of X and Y alignment error deviation from its mean value (data from all squares, several devices per square).

Another method for verifying that the QDs are aligned with the PhC structures is to consider the elimination of all QD in the arrays by the PhC holes. Using μ-PL spectroscopy, we search for luminescence signals at zones outside the PhC cavity, as indicators that some QDs were not eliminated. This simple procedure, is not as precise as SEM, and can only confirm that alignment of the PhC to the QD array is within the PhC hole radius, namely 50-70 nm, without giving any further indication on the magnitude or direction of the alignment error. However, because of its simplicity, this procedure was always used as a double-check on all samples.

Out of 4 samples that reached the final stage of processing, 3 had reasonable optical quality and will be discussed in more details later. Figure 2:24 shows the summary of alignment accuracy measured

for these samples. Misalignment was significantly less than PhC radii, ensuring confident QD isolation for at least 60% of all structures.
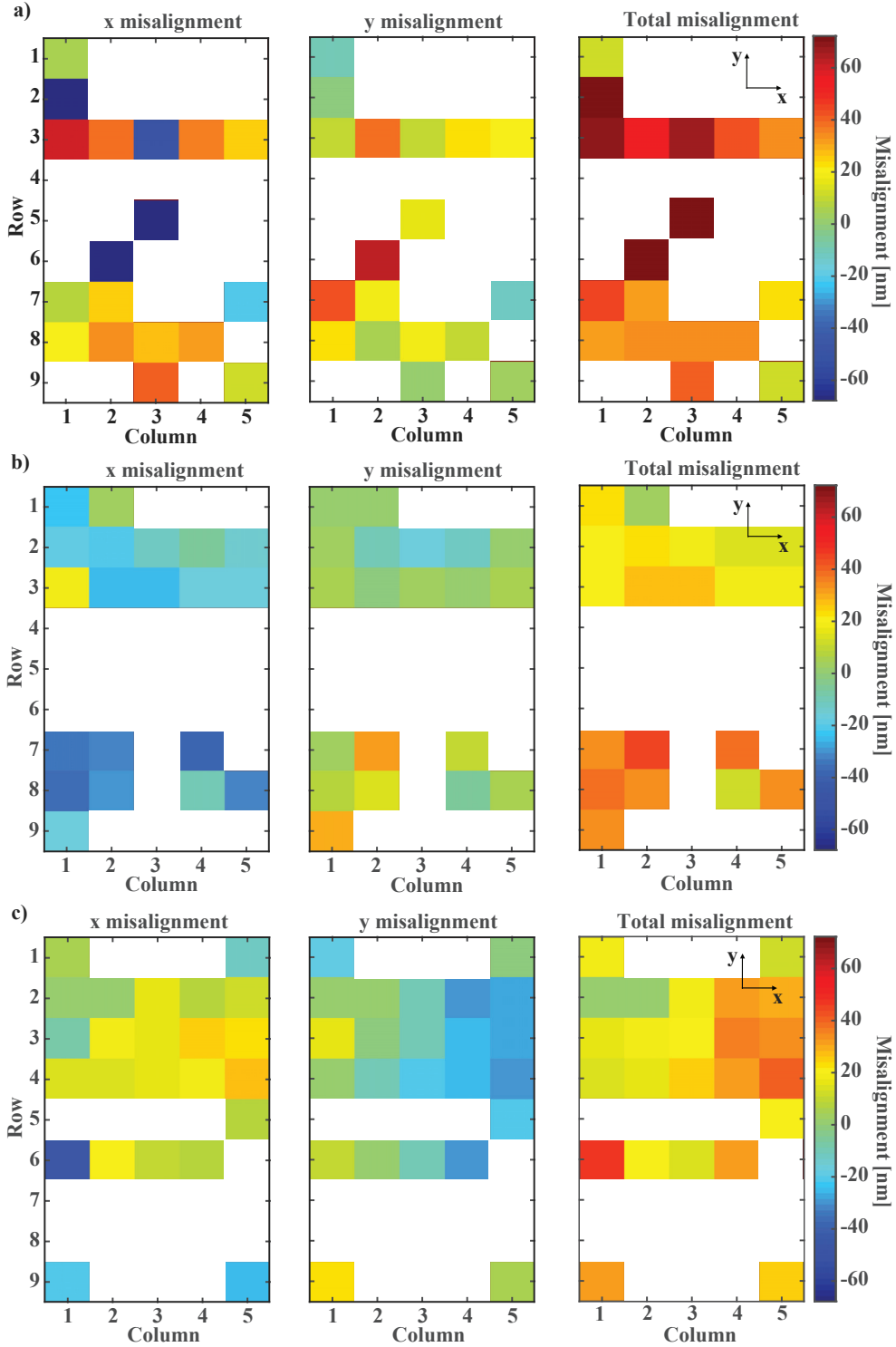
Figure 2:24 Mapping of alignment errors, measured after PhC fabrication, for x, y coordinates and absolute deviation for 3 different samples: a) Gio15-1A, b) Gio15-4A and c) Gio15-3B. Squares shown in white were not checked for alignment accuracy.

Further generation of samples were fabricated with deeper 2 μm alignment marks giving even better alignment results. Figure 2:25 shows structures obtained with deeper alignment marks. QD to PhC cavity alignment showed errors below 15 nm for a mm wide region allowing, e.g., a perfect integration of 2 QDs with coupled PhC cavities.
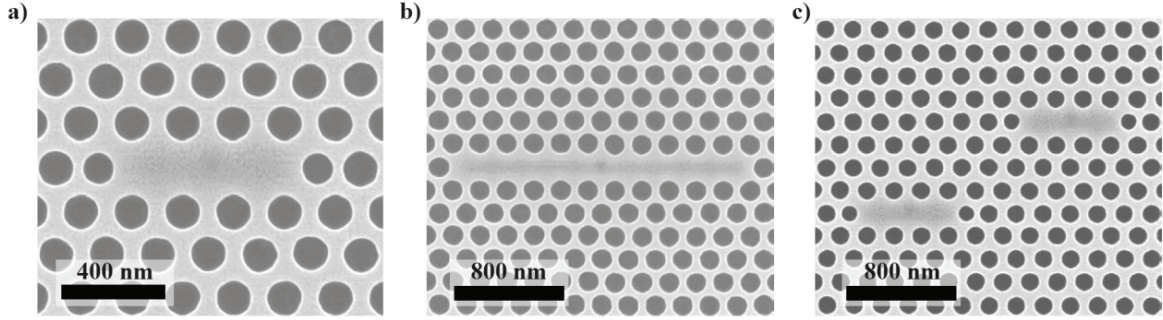
Figure 2:25 SEM of L3 (a), L11 (b) and coupled L3 (c) PhC cavities with QDs placed at the center with negligible (< 15 nm) alignment error.

2.6   Fabricated devices: examples

Using our approach, we implemented several experiments focused on the investigation of light-matter interaction in a QD-PhC system. For integration of several QDs, we used linear PhC cavities as shown in Figure 2:26(a-c). These cavities provide linearly polarized CMs with high quality factor (exceeding 10000 in our devices for wavelength above 900 nm) to mode volume ratio. Figure 2:26(d) shows a "vertical" PhC cavity that is an alternative to L3 PhC cavity for single QD integration with a CM having different polarization properties. In order to couple a single QD or two QDs with a "photonic molecule" (two coupled PhC cavities), we also fabricated devices containing 2 coupled L3 PhC cavities as shown in Figure 2:26(e-f). The different spacing between L3 PhC cavities is used to control the coupling strength between their CMs[83]–[85].
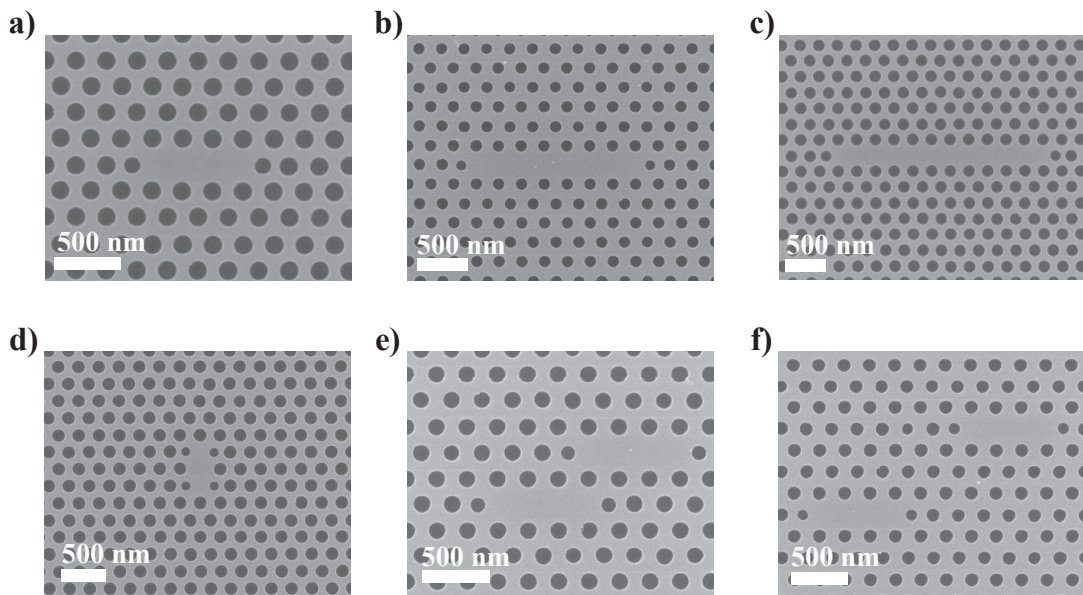
Figure 2:26 Fabricated devices: a), b) and c) linear PhC cavities with 3, 7 and 11 missing holes, d) vertical cavity with 2 skipped holes, e) and d) two (modified) coupled L3 PhC cavities with different spacing between them.

2.7   Conclusions

In this chapter we discussed a fabrication method that allows integration of several pyramidal QDs in PhC cavities. The excellent spatial and spectral control obtained with pyramidal QDs significantly increases production yield of obtaining almost identical devices. This is important for significant statistical investigation of light-matter interaction of QD excitons and cavity photons that will be the core of the following thesis chapters. Together with the advantages of pyramidal QD system, we also gain here from flexibility of PhC design that potentially allows using our method for fabrication of photonic systems containing multiple QDs integrated with any number of PhC cavities. This achievement is important more generally, for building a platform for quantum information technologies as well as for novel light emitting devices.

Chapter 3   Slow dynamics in the emission of pyramidal QDs integrated with PhC cavities.

3.1   Introduction

Although a QD system is often considered as an atomic object, its interaction with a surrounding solid environment may lead to significant complications of its physical behaviour. This is well visible in the photoluminescence features of such "quantum box". The QD excitonic emission line has a nontrivial shape due to the QD interaction with surrounding vibration modes of the semiconductor matrix, while the coherence time of an electron trapped in the QD is significantly affected by magnetic field fluctuations due to nuclear spin noise of the QD constituting atoms. Due to the QD charging, multi-carrier transitions are typical spectral features of the QD emission. Another striking effect observed in the QD photoluminescence are spectral diffusion and emission intermittency (blinking). These effects appear due to the quantum confined stark effect (QCSE) induced by a fluctuating electric field. The source of this field could be an impurity trapped in the vicinity of the QD, fabrication-induced defects or an inhomogeneous charge density near heterointerfaces.

In this chapter we briefly discuss the optical properties of site-controlled pyramidal QDs and then focus on the slow dynamics processes: spectral diffusion and emission intermittency effects, observed in our site-controlled pyramidal QDs integrated in PhC cavities.

3.2   'Typical' and 'non typical' single QD emission

After etching of PhC cavities, we can observe the emission from a single QD isolated within the PhC matrix. Figure 3:1 shows an example of a structure used in such study of a single QD emission, that is, a single QD in an L3 PhC cavity shifted in the horizontal direction. Although the polarisation properties of a QD in PhC cavity could be significantly modified (Chapter 4), these devices are very useful for studying many features of the excitonic structure of a single pyramidal QD.
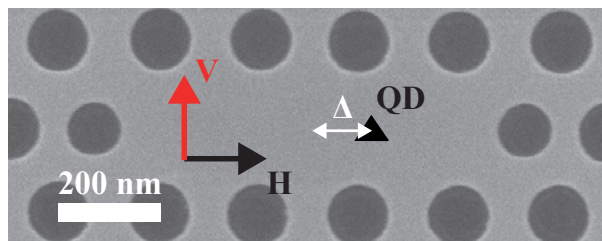
Figure 3:1 A shifted pyramidal QD in an L3 PhC cavity. The QD position is schematically indicated on a SEM image of a fabricated structure.

Typical spectrum of a QD integrated with an L3 PhC cavity consists of neutral and charged excitons separated by around 5 meV [15]. Figure 3:2 shows polarization resolved PL spectrum (bottom) and

corresponding degree of linear polarization (DOLP) spectrum (top) of a QD whose charged excitonic transition is coupled with a ground state optical cavity mode CM0 of the L3 PhC cavity. This mode is linearly polarized along the main axis of symmetry of the cavity (V-direction in Figure 3:1). Excitonic transitions that spectrally overlap with the CM reveal strong co-polarization (Figure 3:2), as analysed in detail in Chapter 4.
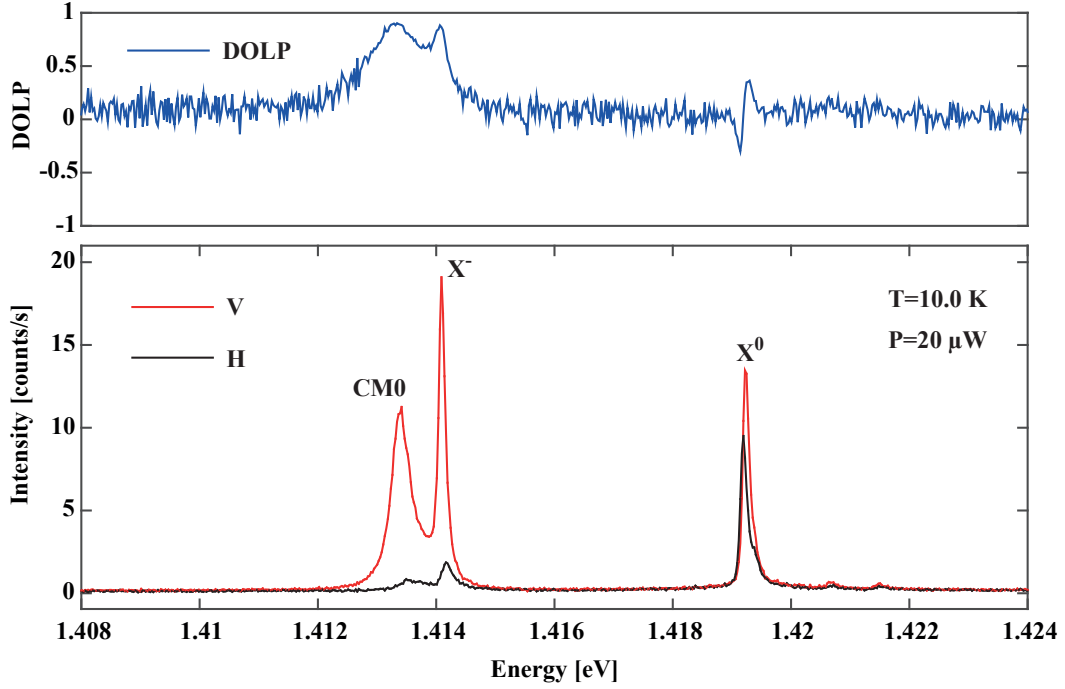
Figure 3:2 Polarization-resolved (bottom) and DOLP (top) spectra of a QD in an L3 PhC cavity (sample Gio15-3B, see Appendix A for details).

If the cavity mode is tuned out of resonance, then only excitonic transitions are visible in emission spectra of a single QD in PhC cavity devices. In Figure 3:3, two sets of measured PL spectra are shown for two different samples containing InGaAs QDs grown with a) Trimethyl-Ga (TMGa) and b) Triethyl Ga (TEGa) (and trimethyl-In in both) precursors. The GaAs membrane substrates used during the fabrication of these two samples were provided by different MBE growers. All other parameters, such as PhC design and fabrication process, membrane thickness, etc., were identical. Both sets of spectra show the same electronic structure with negatively charged and neutral excitonic transitions independent of precursor types. These spectral features are separated by around 5 meV [15]. In both samples the spectra were measured with the excitation conditions corresponding to saturation of the neutral excitonic transition.

Interestingly, the exciton saturation power level for the sample grown with TMGa (a) was P=300 µW, that is, one order of magnitude higher than that for the sample grown with TE-Ga (b). Comparing the GaAs line intensity in these two samples, we found that the difference in the saturation levels corresponds to the carrier generation efficiency and relaxation processes in the substrate. In the sample grown with TMGa the GaAs emission intensity was around 5-7 times smaller than for the TEGa sample, that is, close to the difference in the saturation power levels. Thus, QD carrier

feeding at a particular excitation power significantly depends on the quality of the GaAs membrane substrate as well as on the density of the impurities integrated in the semiconductor matrix during the different QD growth processes. The higher impurity density obtained with TMGa leads to additional channels of carrier recombination, reducing the QD feeding efficiency and increasing the saturation power level, although the maximum QD ground state excitonic intensity is not affected.
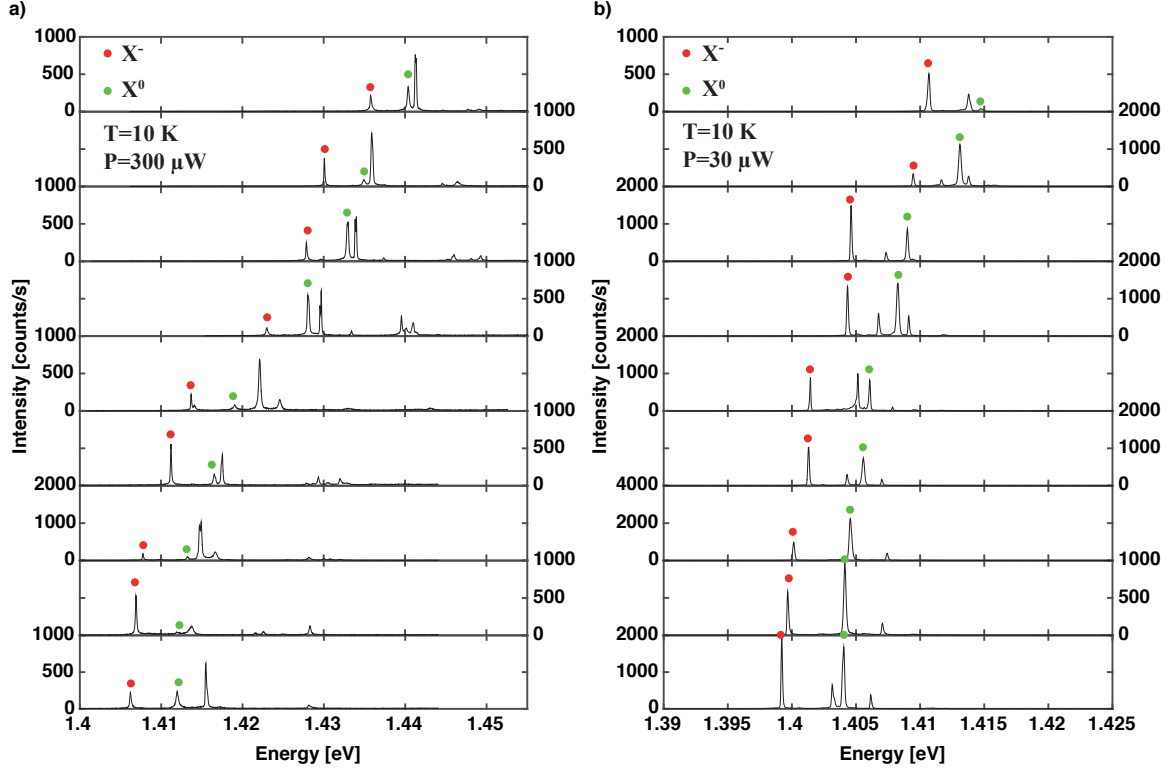
Figure 3:3 PL spectra of QDs isolated with an L3 PhC cavity. QDs were grown using a) Trimethyl-Ga (sample Gio15-3B) and b) Triethyl-Ga (sample TA-2-5) precursors.

As has been already reported[76], spectral fluctuations of an excitonic line energy could be as small as 1 meV due to dot-to-dot size and composition variations. At the same time, the QD ensemble emission in our samples shows inhomogeneous broadening around 10 meV at low excitation power. Using QDs isolated with PhC cavities we found that this apparent inconsistency is not only due to different excitonic transitions presented in the QD ensemble emission spectra, but also due to fluctuating electric field at the QD position.

We measured a set of V3 (Figure 2:26(d)) QD-PhC cavities that do not have a CM coupled with QD ground state transitions (Figure 3:4). Out of 10 spectra we were able to assign the QDs to two types. The 'typical' QDs have usually several reproducible transition lines, the neutral (heavy hole) exciton and the charged exciton, separated by ~5 meV, the biexciton, and a higher energy line that is probably an excited (light) hole excitonic state (Figure 3:4(a)). Spectra of non-typical QDs do not have this clear structure as can be seen in Figure 3:4(b), but reveal additional broad lines that could appear due to interaction with residual impurities and/or defects. Among these 10 devices we find an equal number of 'typical' and 'non typical' QDs.
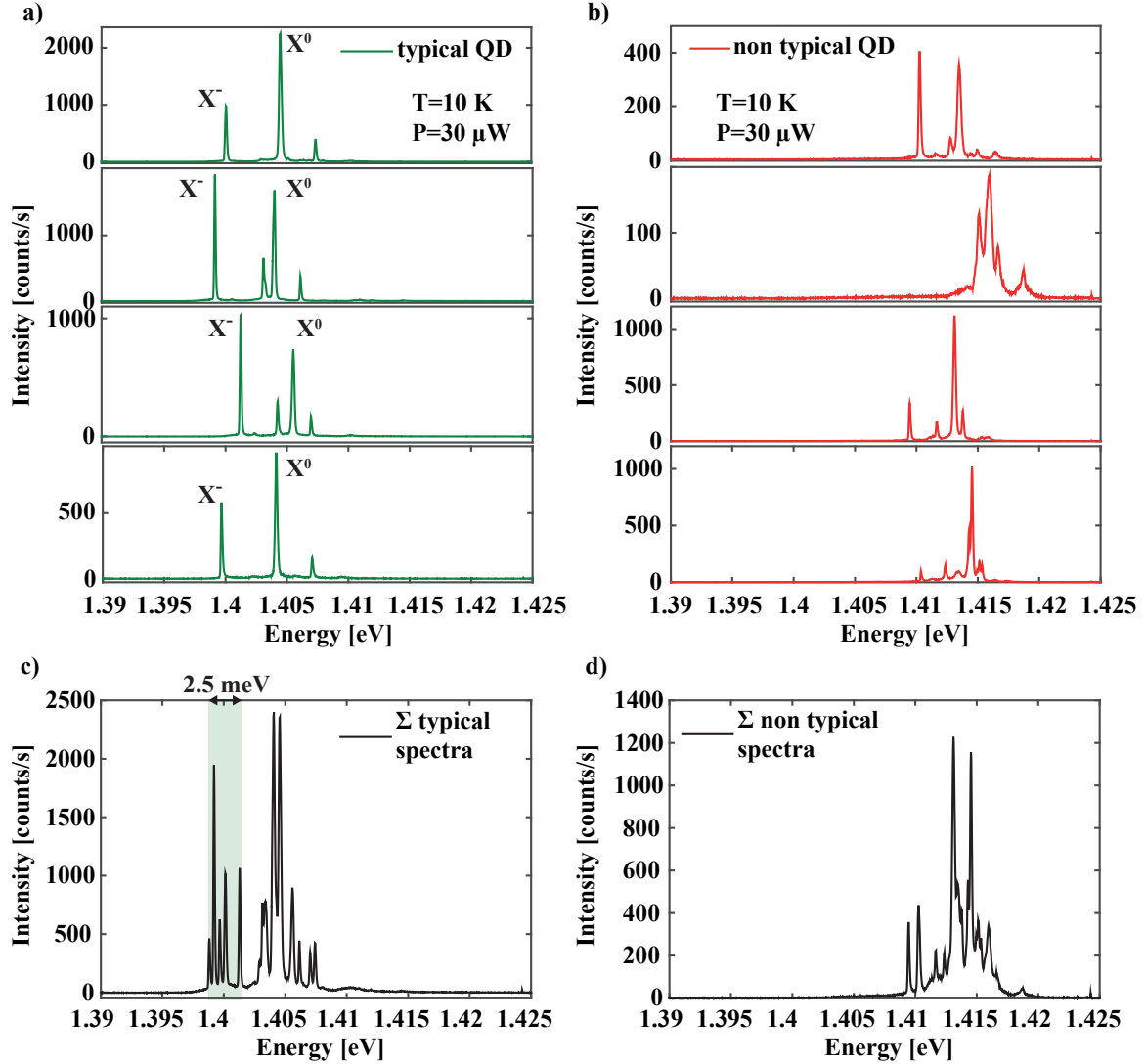
Figure 3:4 Spectra of QDs isolated with V3 PhC cavity (sample TA-2-5-5, grown with TEGa). In a) and b) spectra of 2 QD types, that is, 'typical' (a) and 'non typical' (b) QDs, are shown, obtained by scanning of 10 V3 PhC cavities. In c) and d), emission spectra of QD ensembles are simulated by summing of the 'typical' (c) and 'non typical' (d) individual QD spectra.

The emission energy of particular lines in 'typical' QDs fluctuated by ~2.5 meV as can be seen in Figure 3:4(c), showing QD ensemble emission reconstructed using spectra of 5 'typical' QDs. The inhomogeneous broadening of this "artificially constructed" ensemble is of the order of 8 meV due to the presence of neutral and charged excitons. Figure 3:4(d) shows ensemble emission constructed using the 'non-typical' QD spectra. 'Non-typical' QD emission energy is much more dispersed, by ~10 meV. We thus see that in general growth conditions and substrate quality can affect the QD optical quality in terms of spectral reproducibility and inhomogeneous broadening.

3.3 Spectroscopy of single pyramidal QDs using spectral isolation

Single QD spectroscopy is typically implemented by isolating a single dot out of an ensemble, e.g., by adding PhC holes around the dot or by etching a mesa that contains the dot. However, the PhC holes in the membrane (as well as the mesa etching) create multiple surfaces around that QD, which can significantly affect the capture of carriers, emission linewidth[86] and dynamics[87]. Additionally, the PhC cavities significantly modify local density of optical states at the QD, thus modifying the QD emission. The bare emission properties of a single QD, free from modified dielectric environment, can be investigated using spectrally isolated QDs grown on special seeded pyramidal patterns[77]. An example of such pattern is depicted in Figure 3:5, which shows an array of pyramidal recesses of homogeneous size with smaller-size pyramidal recesses introduced on a sublattice (pitch of about 4.5 μm).
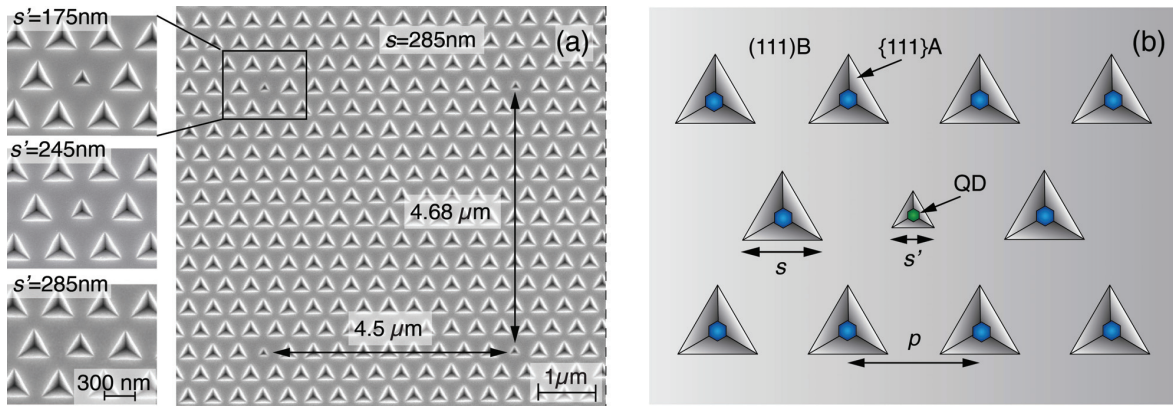
Figure 3:5 (a) SEM images of the QD pyramidal arrays consisting of smaller pyramids with $s' = 175$ nm, 245 nm and 285 nm embedded in a matrix of larger pyramids with $s = 320$ nm ($p = 450$ nm). (b) Schematic of QD growth in the pattern used for "spectrally isolated" QDs. Adopted from [77].

QDs grown in pyramids of different sizes have different emission wavelengths [24]. Figure 3:6(a) shows PL spectra of QDs grown in ensembles with the 3 different sizes of smaller pyramids s' (175, 245 and 285 nm) and the same size of surrounding bigger pyramids $s = 320$ nm. Excitation spot was centred at an s' pyramidal QD thus providing efficient excitation of a single s'-QD only. The emission spectra consist of typical emission of s-QD ensembles appearing at a higher emission energy, in addition to the single s'-QD spectrum. The relatively large separation of the emission energy of the s- and s'- QDs provides the spectral isolation of the s'-QD emission lines. Figure 3:6(b-d) show zoomed views of the 3 spectra of individual s'-QDs obtained using this technique.
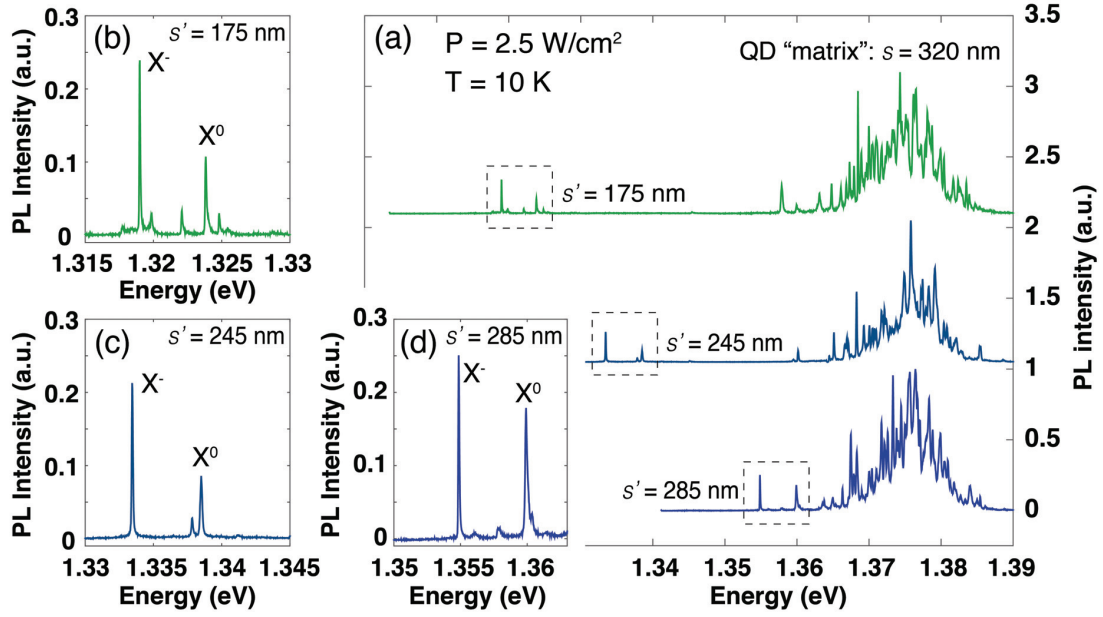
Figure 3:6 (a) Micro-PL spectra of QD arrays with pyramid size s = 320 nm, which include spectrally isolated QDs with various pyramid size s' = 175, 245 and 285 nm. (b)-(d) Zoomed-in spectra in the spectra vicinity of the isolated QD lines, for s' = 175, 245 and 285 nm, respectively. Adopted from [77].

Spectrally isolated QDs allow investigation of properties of a single pyramidal QD without adding any additional surfaces (hole or mesa isolation) or perturbation of nearby potential (e.g. deposition of metal layer). Figure 3:7 (a, b) shows spectra of spectrally isolated QDs at several excitation powers. Grown in s'=200 nm in Figure 3:7 (a) and s'=150 nm in Figure 3:7 (b) pyramidal recesses, these QDs have typical excitonic structure with 2 main lines corresponding to neutral and charged excitons separated by ~5 meV as visible at medium excitation powers. At low excitation power, the neutral exciton dominates over other spectral features revealing negligible QD charging with excess carriers. This suggests low impurity density in the environment of these QDs. At higher excitation power we observed biexcitonic transition with several additional lines. QDs grown in the s'=150 nm pyramidal recess exhibit more rich spectral structure at high excitation power (Figure 3:7(b)) that could be explained by smaller distance to substrate/air interfaces and higher charging with excess carriers. Figure 3:7(c, d) shows power dependence of several emission lines observed in the spectra. The neutral exciton has nearly linear power dependence while the biexciton has quadratic power dependence, as expected.
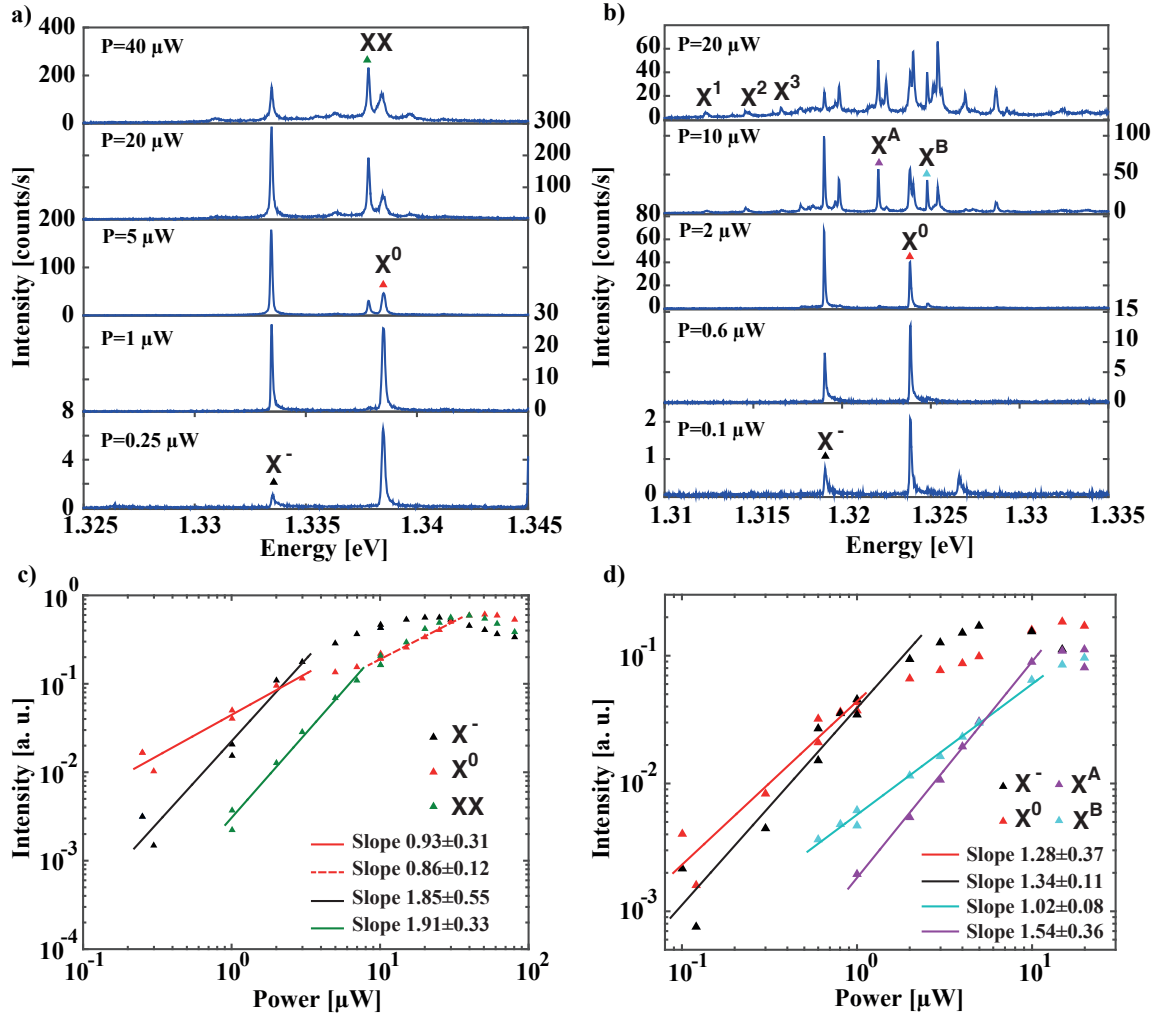
Figure 3:7 PL spectra of ground state and intensity of several excitonic transitions of spectrally isolated QDs. In a) and b) the QDs were grown in pyramids with s'=200 nm and s'=150 nm, respectively. In c) and d) power dependence of several emission line intensities are shown.

We observed wide emission background at higher excitation power around the single-QD emission lines, as can be seen in Figure 3:7(a, b). Figure 3:8 shows expanded spectra of the neutral and charged exciton lines extracted from Figure 3:7(a). Measured at 4 excitation powers, these spectra are normalized by the maximum intensity of either the neutral or the charged exciton transitions. At low power, only emission lines of neutral and charged excitons are visible, while at higher excitation powers, many additional peaks appear together with wide emission background.
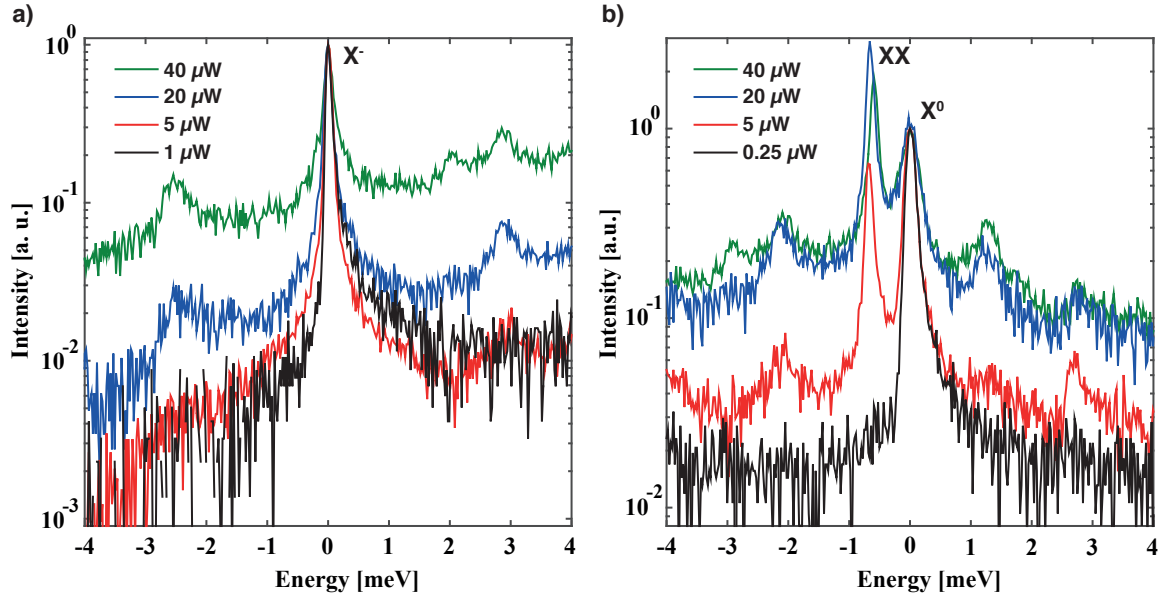
Figure 3:8 PL spectra of a) negatively charged exciton and b) neutral exciton transitions, normalized by maximum intensity (structures as in Figure 3:7(a)).

3.4   Slow dynamics in pyramidal QD emission spectra

3.4.1   Dynamical processes in low dimensional structures

Quantum communication and information processing request QDs with atom-like behavior, providing Fourier transform limited linewidth and near unity quantum efficiency. However, this requires negligible influence of the surrounding environment on the QD confinement potential and its electronic structure. During the last 20 years, different groups have reported observations of emission intermittency (blinking) in single molecules[88], [89], nanowires[90], nitrogen-vacancy[91] and semiconductor QDs[92]–[100]. Intensity intermittency reveals random telegraph signal (RTS) like behavior with 'on'/'off' states persisting from microsecond to hundreds of seconds with power-law probability density[101]–[105].

New theories had to be developed to explain these effects, taking into account the surrounding QD media[106]. Almost all theories explained the blinking behavior by fluctuating electric fields at the location of the emission source due to charges trapped at defects or surfaces. The influence of the QD environment was already clear in [92] where colloidal CdSe QDs capped with ZnS shell revealed higher 'on' to 'off' state ratio in comparison with uncapped ones. Undesirable for applications, such blinking was suppressed in later works by removing charge traps from the solution[107] or by engineering appropriate shell thickness of CdSe/CdS QDs thereby reducing Auger recombination of charged excitons[108]. Recently, correlation between blinking and charging of a CdSe/ZnS nanocrystal was directly probed by a carbon nanotube[109] showing RTS of current with power-low statistics. For epitaxial QDs, surface defects play the dominant role in the observation of blinking[96], [99], [100]. However, epitaxial QDs very rarely reveal blinking behavior thanks to high quality fabricated semiconductor structures that avoid defects.

Spectral diffusion is another interesting effect observed in nanostructures and caused by mechanisms similar to emission intermittency. Useful as a single charge electrometer[110]–[112], QD emission energy is very sensitive to charge fluctuations due to the quantum confined Stark effect (QCSE). Thus, variations of charge density trapped at defects or nearby surfaces change the QD emission line energy. Values of a such energy shift vary between several µeV on µs timescale[113]–[115] to tenth of meV up to hundreds of seconds[116]–[119] as summarized in Figure 3:9. Due to the similar nature of emission intermittency and spectral diffusion, these effects could appear simultaneously as reported in [118]. Spectral diffusion even reveals similar power-law behaviour to blinking[120].
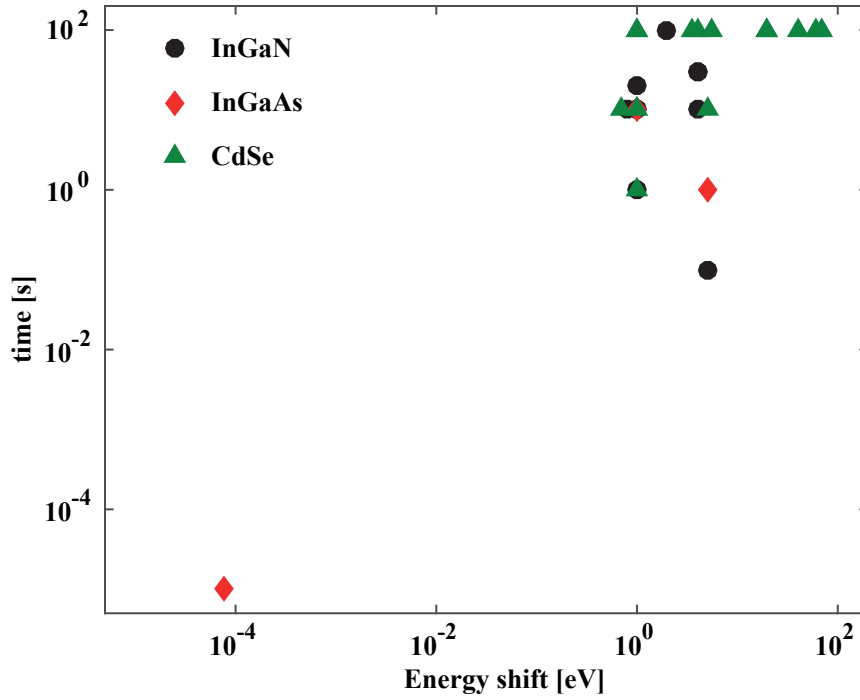
Figure 3:9 Maximal time and energy parameters of spectral diffusion. Energy shifts and time parameters were taken from text or estimated from presented figures in the references mentioned in the text.

Emission intermittency and spectral diffusion can be supressed by using sufficiently pure materials with low-defect fabrication processes. Consulting many articles presenting spectral diffusion in CdSe, In(Ga)N and InGaAs QDs, we did not find clear dependence of these phenomena on the growth method of these nanostructures. Spectral diffusion was observed in colloidal CdSe QDs[92], [116], [121], in CdSe QDs grown by MOCVD[122]–[124] and MBE[125], In(Ga)N QDs grown by MOCVD[126]–[131] and MBE[132]–[134] and in InGaAs QDs grown by MBE[135] and MOCVD[136]. More recent articles reported very small energy shifts of several µeV[113], [114] evidenced by several µeV linewidth of In(Ga)As self-assembled QDs.

As reported in [122], [137], [138] the same build-in electrical fields can create very different shifts depending on their position with respect to the QD axes. In particular, for CdSe QDs deposited on GaAs, 0.26 meV and 1.8 meV energy shifts were estimated for 100 kV/cm electrostatic field in

growth and lateral direction correspondingly[122]. In the same article, an average electric field ~45 kV/cm at the QD position was estimated for 3 charges separated ~10 nm from the QD. This energy shift estimation is consistent with calculations reported in [137]. Thus, ~0.3 meV neutral exciton energy shift observed in this structure is consistent with the charging of an impurity or a defect separated by ~10 nm from the QD center. This 10±5 nm separation is of the order of the QD size, therefore a very inhomogeneous field is created at different QD points.

Among different types of In(Ga)As QDs investigated, site-controlled QDs should be more sensitive to spectral diffusion or emission intermittency as they are typically grown on a pre-patterned surface. The latter is exposed to wet or dry etching steps, removal and deposition of different materials, de-oxidation processes, etc. Depending on the distance between the regrown interface and the QD, all these fabrication steps can increase the defect effects, reducing the emission intensity and increasing the linewidth due to spectral diffusion[112], [137]. Interestingly, for the site-controlled QDs grown in nanoholes or in pyramidal recesses, we did not find reports on slow emission dynamics. Moreover, narrow emission linewidth down to 18 μeV was observed in QDs grown in pyramidal recesses[139] separated by more than 100 nm thick buffer layer from the regrown surface. Linewidth of site-controlled QD grown in the nanoholes was reduced from 2.3 meV down to ~110 μeV at large distances from the regrown surface[140]. In another work the linewidth of site-controlled QDs grown in nanoholes was independent of the GaAs buffer layer thickness ranging from 15 nm to 35 nm as an ultra-clean re-growth process was used[22]. In the course of emission quality improvement of these site-controlled QDs, the best linewidth obtained with above-barrier excitation was ~40 μeV[67], [141], [142] and even down to 7 μeV[143]. This narrow linewidth is comparable with the state of the art values for self-assembled In(Ga)As QDs grown by MBE[144], [145] or MOCVD[146], [147].

Thick buffer layers of high purity between the substrate and the QD cannot be implemented in our QDs grown in pyramidal recesses, which in the context of the current work need to be small enough for integration in the PhC membrane cavities. Only a few tens of nanometers (Δ_1) separate the QD from surfaces that experienced different processing steps as discussed in Chapter 2. These surfaces can serve as sources of charged defects if the surface cleaning procedure is not perfect. We should also point out that MOCVD-grown GaAs typically exhibits higher residual background doping as compared with MBE material, even for thick buffer layers.

Another source of charge fluctuations in our devices are PhC holes that introduce GaAs/air surfaces. QD emission linewidth significantly depends on the distance from these interfaces, even under quasi-resonant excitation conditions through QD p-shell[144]. Figure 3:10(a) shows a schematic cross section and top view of our structures. The QD is shifted by as much as ~30 nm from the 265 nm thick membrane center, which corresponds to the precision of our QD positioning. Thus, the QD is distanced by around 100 nm from the membrane surface (Δ_2). Considering standard devices with 200 nm PhC hole pitch and 80 nm PhC hole radius, Figure 3:10 (b) shows 2 QD positions providing 90 nm and 120 nm QD-to-PhC hole surface distances. In our devices the shift of the QD due to spatial misalignment can reduce the QD to PhC hole surface distance further, by ~15 nm. The PhC structures discussed below have 200 nm pitch and hole radii varying from 60±5 nm to 70±5 nm.
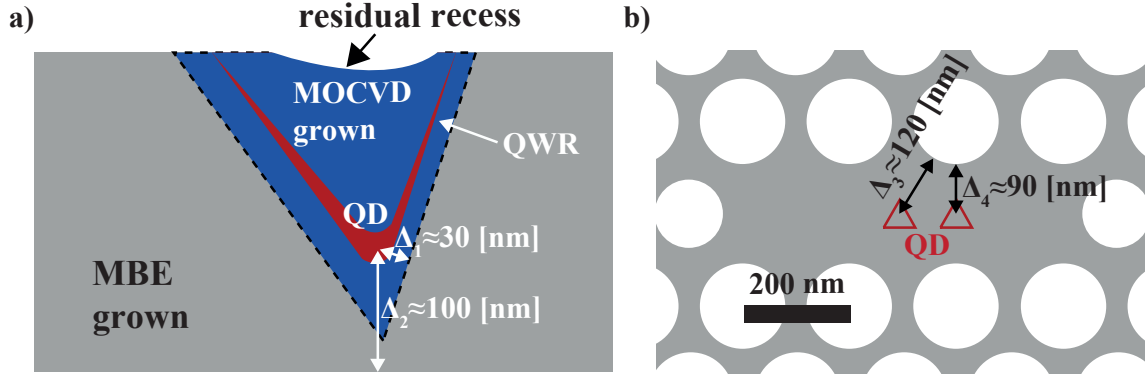
Figure 3:10 Surfaces and interfaces around a pyramidal QD. In a) (side view) approximate distances from QD to pyramidal interfaces and membrane surfaces are shown. In b) (top view) typical distances from PhC hole surface to QD are shown for 2 QD positions. In b) schematics shows QDs displaced by Δ=0 nm and Δ=90 nm from the PhC cavity center.

Another issue relevant to QD spectral shifts is the lateral QWRs formed in our pyramids. Since the distance between these QWRs and the surface is of the order of several nm, charges can be trapped at one edge of these QWRs, significantly affecting the confinement potential of our QD.

3.4.2 Spectral diffusion of QD excitonic transitions.

Here we present a detailed investigation of spectral diffusion of single InGaAs/GaAs pyramidal QDs integrated with L3 PhC cavities. These structures contain QDs nominally shifted by Δ=0 nm, Δ=120 nm and Δ=180 nm from the L3 PhC cavity center, as shown in Figure 3:10(b) (see also Chapter 4). We choose this system instead of the spectrally isolated QDs in bulk GaAs because it's more relevant to our main subject, namely the study of integrated QD-PhC systems, and due to the enhancement of the collection efficiency through light redirection in narrower solid angles. Thus, significantly shorter integration times could be used for spectral measurements. All measurements correspond to the sample Gio15-3B that contains QDs grown using TMGa.

We knew from previous PL experiments with quantum wells that slow processes in emission significantly depend on the details of the cooling down process. In particular, any light that can cause above-GaAs band gap excitation should be suppressed during cooling, thus all preparations of the experiments were done in advance during the day before measurements. Then, the sample was cooled down in almost complete darkness, i.e. we switched off computer monitors and laboratory light. The objective of the µ-PL setup was positioned above the sample edge far from the region of interest (see Chapter 2, schematics).

After cooling to 10 K we positioned the objective above a PhC device situated at least 100 µm away from the device to be probed for slow dynamics. After maximizing the excitation efficiency, we blocked the laser beam and moved the objective to the targeted PhC device. Finally, we simultaneously unblocked the laser beam and started recording a continuous sequence of spectra taken at fixed time intervals.

Figure 3:11 shows spectra of 2 structures measured in this way during several tens of seconds. In the top panels, the first and the last spectra obtained during measurements are shown, with complete

sets of time-resolved traces presented at the bottom. These images of spectral dynamics are plotted in pseudo 3D manner with colour code showing the spectral line intensity. These structures do not present any spectral diffusion or emission intermittency, at least with our spectral resolution of ~80µeV and time resolution of 1 s. The time interval between two spectral measurements is the sum of integration time and the spectrometer dead time, in this case t_{int}=1 s and t_{dead}=1 s. The smallest spectrum integration time used in our measurements is 1 s, therefore the fastest dynamics that we are able to measure has approximately 2 s characteristic time. The behaviour represented by Figure 3:11 is typical for 90 % of all measured devices (~100 devices were measured).
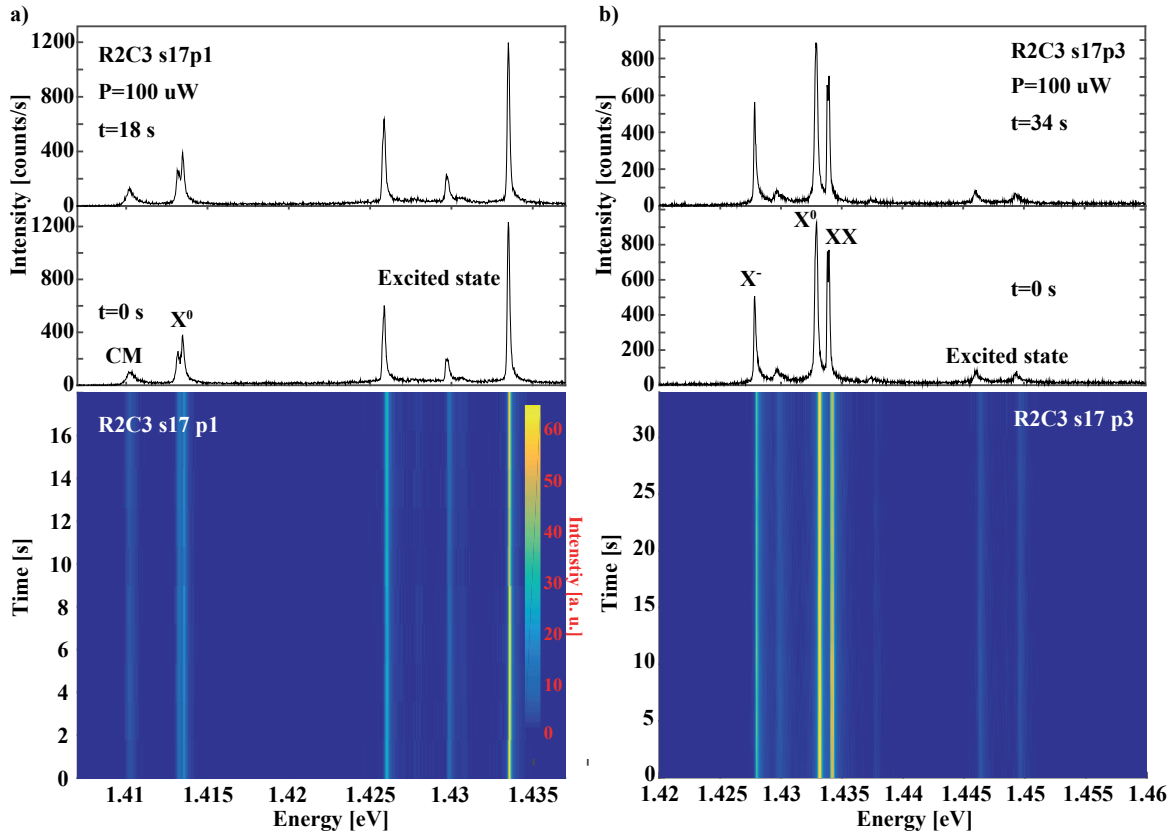
Figure 3:11 In a) and b) spectra (top) and images of spectral dynamics (bottom) for 2 different structures. Spectra are shown for 2 times, corresponding to the first and the last measurement points. Excited states in top panels of a) and b) are probably p states of our QDs.

However, around 10 % of the structures revealed very pronounced temporal changes in the energy of the emission lines. Figure 3:12 shows examples of two types of the spectral diffusion observed in our structures. In some structures, exciton energy fluctuated only during finite periods and then stabilized, while in other structures spectral diffusion continued during hours. "Stabilizing" slow dynamics is shown in Figure 3:12(a). After energy fluctuations during several tens of seconds, the emission lines converged to well-defined energy positions. Varying excitation level or keeping this sample for several hours in the darkness did not resume spectral diffusion. In order to observe again these spectral fluctuations, the sample should be heated up to nearly room temperatures and then cooled down again. Figure 3:12(b) shows spectra and image of emission dynamics acquired from

another structure. In this case, chaotic spectral fluctuations persist during several tens of minutes and show around 10 meV energy shifts.
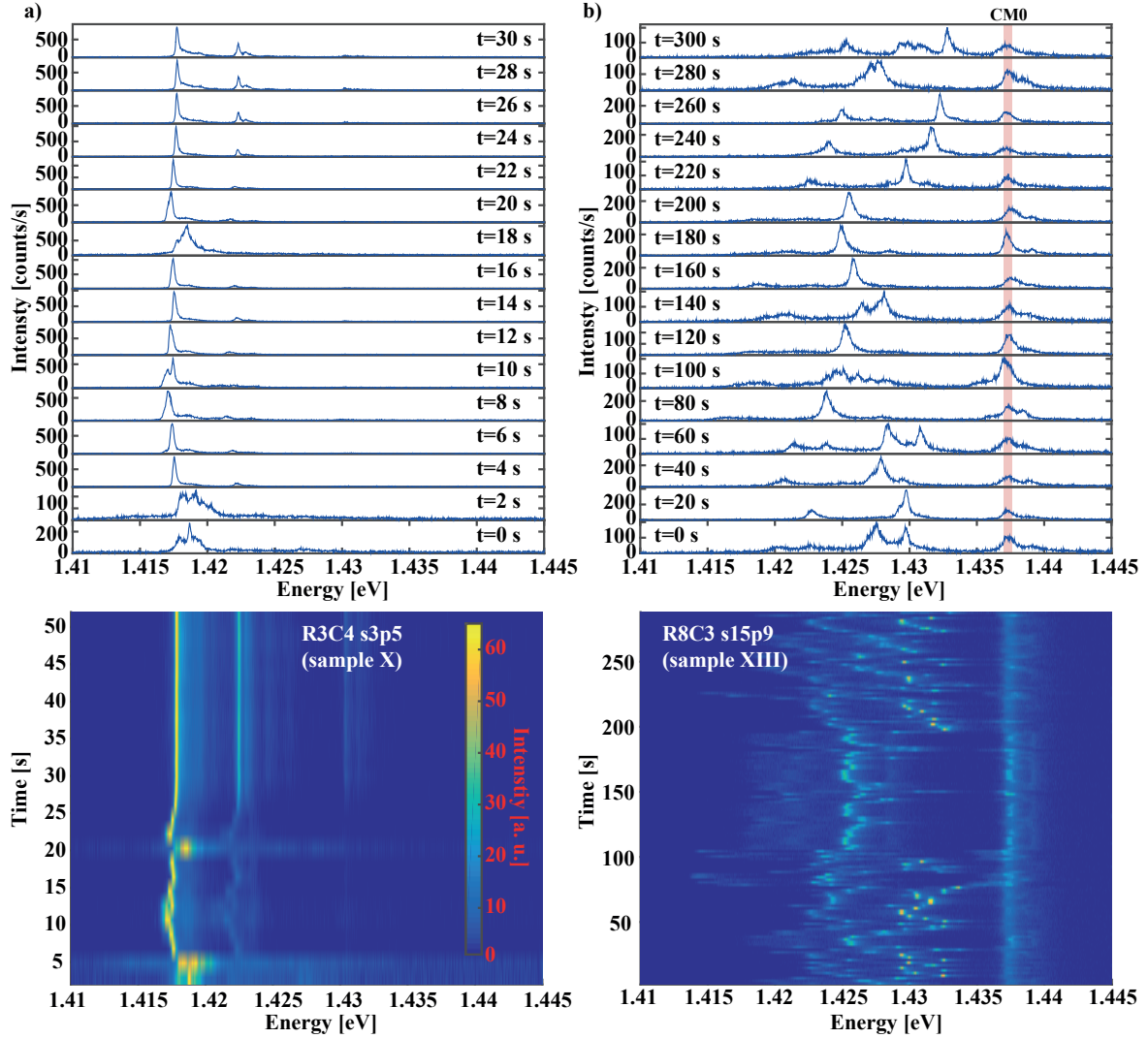
Figure 3:12 Time-resolved PL measurements of 2 devices containing a single QD in an L3 PhC cavity shifted by Δ=120 nm (a) and Δ=120 nm (b) from the PhC cavity center. Spectra (top) and images of spectral dynamics (bottom) clearly reveal several meV fluctuations in line energies. All measurements were obtained at 10 K under 300 µW excitation power.

Interestingly, after re-measuring this sample with the same excitation power and at the same temperature we found that spectral diffusion also stabilized after some time in the darkness during the time when the excitation beam was blocked. As can be seen in Figure 3:13(a), instead of spectral diffusion behaviour we obtained emission spectra with properties identical to ones of the QDs without spectral diffusion. Spectral diffusion of this QD can be recovered only through sample heating to room temperature with consequent cooling down to the temperatures adequate for our QD spectral measurements. Figure 3:13(b) shows image of recovered spectral dynamics obtained in this structure during another day of measurements at the same excitation power as in Figure 3:12(b). In the top of Figure 3:13(b) statistics of emission energy shows only a few pronounced peaks. One of

these peaks corresponds to a cavity mode (CM) and another to a QD excited state emission line that is also evident in the spectrum after stabilization. Irreversible stabilization with changing of excitation conditions was also observed in other samples. It should be noted that a few other devices showed spectral diffusion that did not stabilize even after ~10 hours and was insensitive to modification of excitation conditions and temperature.

Thanks to stabilization of the spectral diffusion of this structure we can compare emission properties of the same QD during the spectral diffusion and during the stable mode. Figure 3:13(c) shows the power dependence of this sample after stabilization. Significantly, at low excitation power only the charged exciton is present in contrast with 'non fluctuating' samples having only neutral excitonic transition visible at low excitation power. This difference highlights the presence of some charging centers in the vicinity of this particular QD. These centers modify local carrier balance leading to the negative charging of this QD at low excitation power.

At higher excitation power, additional transitions appear including the neutral exciton and a CM pumped by the QD excited state. Another significant difference from 'non fluctuating' samples is the very wide tail appearing at the lower energy shoulder of the charged exciton line at higher excitation power. This is a sign of spectral fluctuations of excitonic transitions, although too fast to be recorded with our spectrometer time resolution. This wide background is typical for structures with spectral fluctuations, as will be discussed at the end of this chapter. Correlations between this lower energy tail and spectral diffusion will also be clearly shown in section 5.4.2, describing 4 QDs in an L7 PhC cavity.
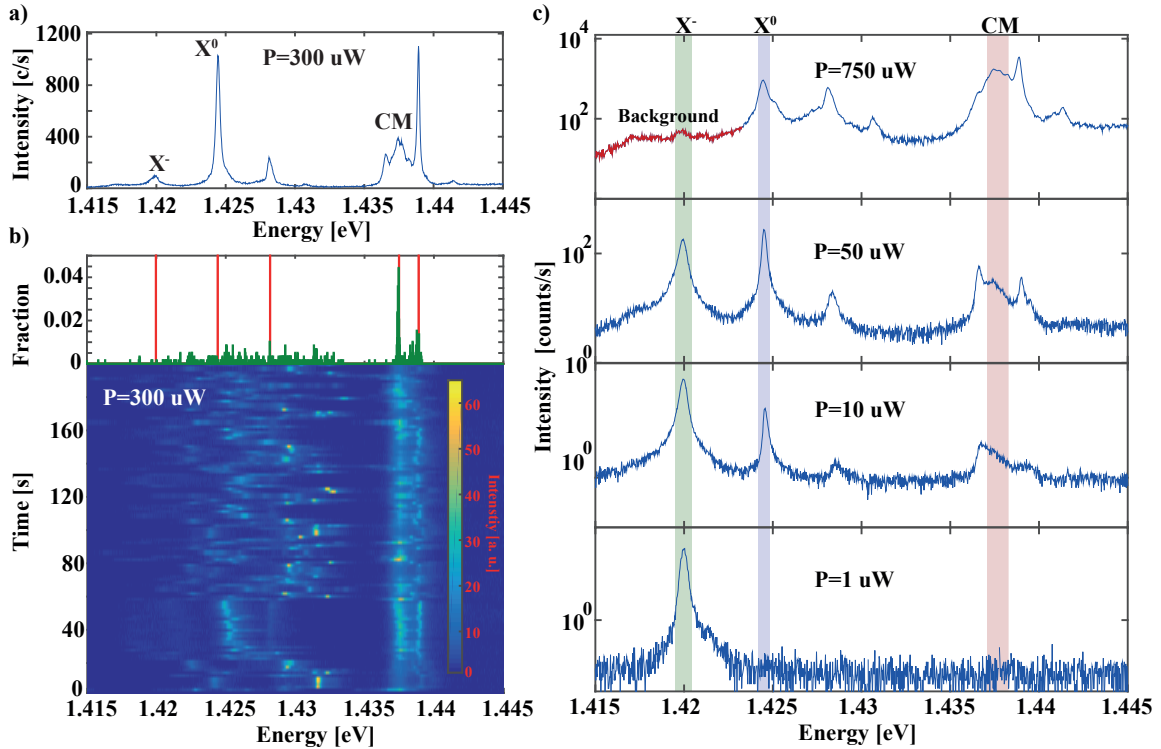
Figure 3:13 Emission of a single QD in an L3 PhC cavity before and after stabilization of spectral fluctuations (sample XIII, see also Figure 3:12(b)). In a) spectrum shows QD emission after stabili-

zation. In b) image of spectral dynamics shows emission fluctuations before stabilization. Statistics of excitonic emission energy (top panel) highlights positions of the main spectral lines shown in a). In c) spectra are taken at several excitation powers after fluctuation stabilization.

Remarkably, during the spectral diffusion shown in Figure 3:13(b), the emission of the lower energy lines corresponding to QD ground state emission is significantly quenched, whereas in the stable configuration, at the same excitation power, the neutral exciton has the same intensity as the excited state line enhanced by the presence of a CM. This tendency was observed in several devices with the spectral diffusion behaviour and can be attributed to reduction in the transition rate of the dipole moment of the ground state excitons due to a strong intrinsic electric field at the QD position.

Such slow dynamics of our exciton emission lines should provide very broad lines in spectra with more than 10 s integration time. Figure 3:14 shows polarization-resolved spectra measured in several devices containing single QDs in PhC cavities with 10 s integration time. The emission lines have non-Lorentzian line shapes while two polarization-resolved consecutive spectra show several meV wide lines. Statistically, using 10-30 s integration time during quality characterisation of QDs incorporated in PhC cavities, we observed similar broad (>1 meV) low intensity lines in 10 % of the samples. Thus, we selected the structures with pronounced broad emission features from such spectra specifically for probing the slow dynamics processes. Measuring consecutive set of spectra in these structures we found slow dynamics in around 90% of these samples.
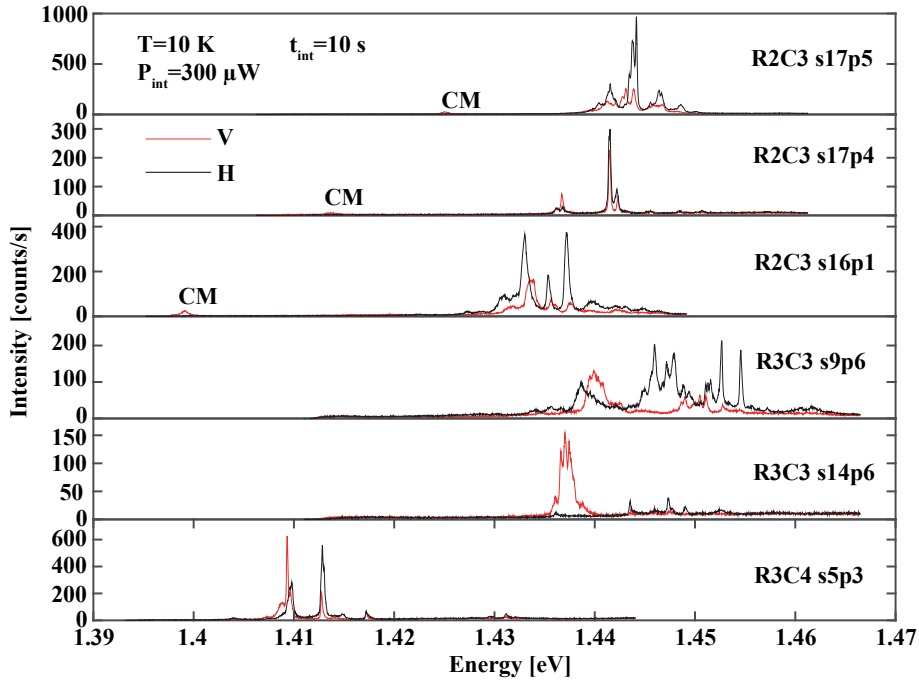
Figure 3:14 Spectra with seemingly wide emission lines measured in devices containing a single QD in an L3 PhC cavity, acquired with integration time of 10 s.

Using the procedure described above, we identified 15 structures revealing the spectral diffusion. Looking for the correlations between QD distances to the PhC hole surface, we probed 7 devices 'p1-7' in a single raw 'R2C3 s17' according to the notification described in Chapter 2. Each of these devices contains a QD horizontally shifted by ~180 nm from the L3 PhC cavity center. PhC hole

sizes linearly increase from the first device in row 'p1' to the last device in row 'p10'. The last 3 structures in the row with the biggest PhC hole sizes 'p8-10' were not measured due to contamination or cracks of the PhC hole matrix. Observing no slow dynamics in structures 'p1-3' corresponding to the smaller PhC hole radii (Figure 3:11), we found slow dynamics in structures 'p4-7'. Thus, in this particular series we indeed observed a preference of slow dynamics occurrence near larger PhC holes, although we do not have enough statistics for confirming it. We did observed slow dynamics in the structures with the smallest hole sizes (sample II and IX, Table 3:1), although not as pronounced and of long duration as for larger holes.

Sample number	Structure ID	Stabilization	QD nominal shift [nm]	PhC nominal size [nm]	QD to PhC hole surface distance [nm]
I	R2C3 s13p7	>5 min	180	66	110
II	R2C3 s16p1	~1 min	180	60	116
III	R2C3 s17p4	>30 min	180	63	113
IV	R2C3 s17p5	>30 min	180	64	112
V	R2C3 s17p6	~10 s	180	65	111
VI	R2C3 s17p7	~10 s	180	66	110
VII	R3C3 s9p6	~30 min	120	65	94
VIII	R3C3 s14p6	~2 min	120	65	94
IX	R3C4 s5p3	~12 min	120	62	97
X	R3C4 s3p5	~30 s	120	64	95
XI	R3C4 s7p9	>14 hours	120	68	91
XII	R3C4 s7p11	~1 min	120	70	89
XIII	R8C3 s15p9	>5 min	0	68	117
XIV	R8C4 s12p7	~1 min	0	66	119
XV	R8C4 s20p7	~1 min	0	66	119

Table 3:1 Devices with slow dynamics behavior. Text color indicates structures corresponding to the same QD shift delta. QD-to-PhC hole surface distance is calculated taking into account the possible misalignment of ~15 nm (see Figure 3:10).

3.5   Jumps across just a few discrete emission states

Depending on the charge trap density, an emission line energy was observed to change discretely[120], [121], [127], [132], [148] or quasi-continuously[126], [128]–[131], [133]–[135], [149] with clear correlation between energy shifts and different excitonic complexes. Emission line jumps across several energy levels are explained by QCSE due to a finite number of charge configurations in the vicinity of a QD. Thus, the number of charge configurations is directly projected to a number of different spectra observed in the temporal measurements of the same structure. These spectra can be considered as different emission configurations reflecting the particular internal field at the QD position.

During investigation of the slow dynamics process in the QD-PhC cavity system we have also found several structures with such discrete change of emission line energy. Figure 3:15 shows a structure with emission line jumps across only 4 energy levels. Since this structure contains a single QD all spectral features change their emission energies simultaneously. Two emission configurations of the QD emission line can be explained by a single impurity/defect in the vicinity of the QD

having two charge states. Four emission configurations can be explained by either two impurities/defects having two charge states each, or a single impurity/defect having four charge states.
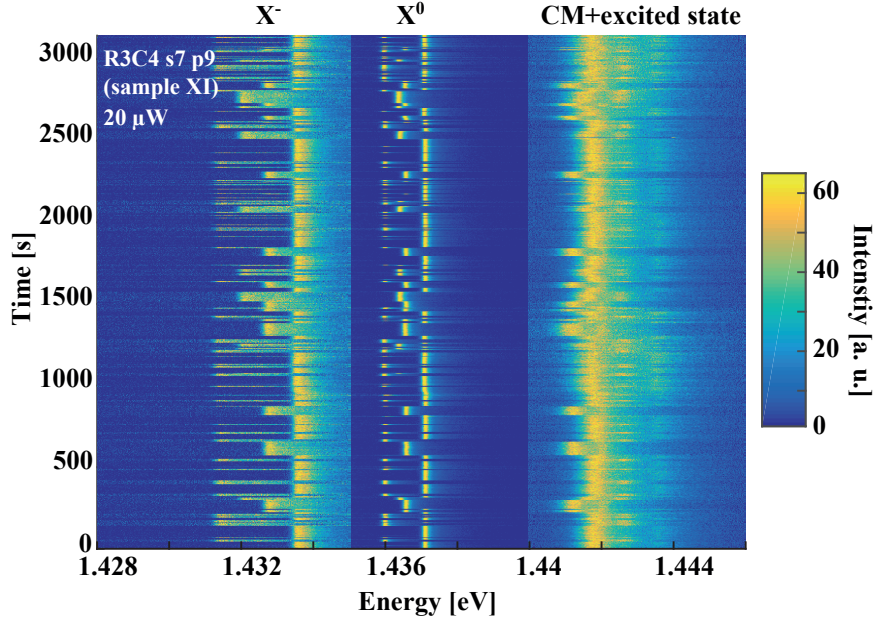
Figure 3:15 Images of spectral dynamics of sample XI(Table 3:1) showing jumps between four discrete emission states.

The structure with four emission configurations revealed non-stabilizing slow dynamics over tens of hours with clear spectral features and repeatable temporal parameters among different days of measurements. The temporal parameters of slow dynamics were not affected by history of measurements. In particular, characteristic time parameters of the emission line jumps were not affected by previous illumination with a high intensity laser beam or by temperature variations. Thus, this structure allows a solid study of the QD charge environment temporal evolution and the influence of the local electrical field on the QD emission.

Figure 3:16 shows the spectra of the four emission configurations at two different excitation powers observed in this structure. These spectra are extracted from the measurements of slow dynamics shown in Figure 3:16(c, d). Measured at excitation power lower than the saturation power level (Figure 3:16(a)), the spectra consist of 2 main lines, which are charged $X^-(y)$ and neutral $X^0(y)$ excitons, where 'y' denotes the emission configuration number, arbitrarily chosen according to denote increasing energy. At higher excitation power, higher energy lines ES_1 and ES_2 corresponding to an excited QD state appear. These lines are ~6 meV above the neutral exciton, typical to the separation of excited hole states. At higher excitation power an additional line XX appears at the higher energy shoulder of the charge exciton X^-. This line could be either a biexcitonic QD transition or other multiparticle complex. In the following we keep the XX notification for this optical transition.

Histograms on the top of the images of the slow dynamics in Figure 3:16(c, d) show the fraction of different lines in the temporal measurements. The peak position of the narrowest measured lines fluctuates by less than the width of a single histogram bin (27 μeV) corresponding to the distance between two energy points measured with two adjacent pixels on the CCD camera. Thus, it is pos-

sible that spectral diffusion processes additional to the observed discrete energy jumps across the four emission states cannot be resolved in our measurements.
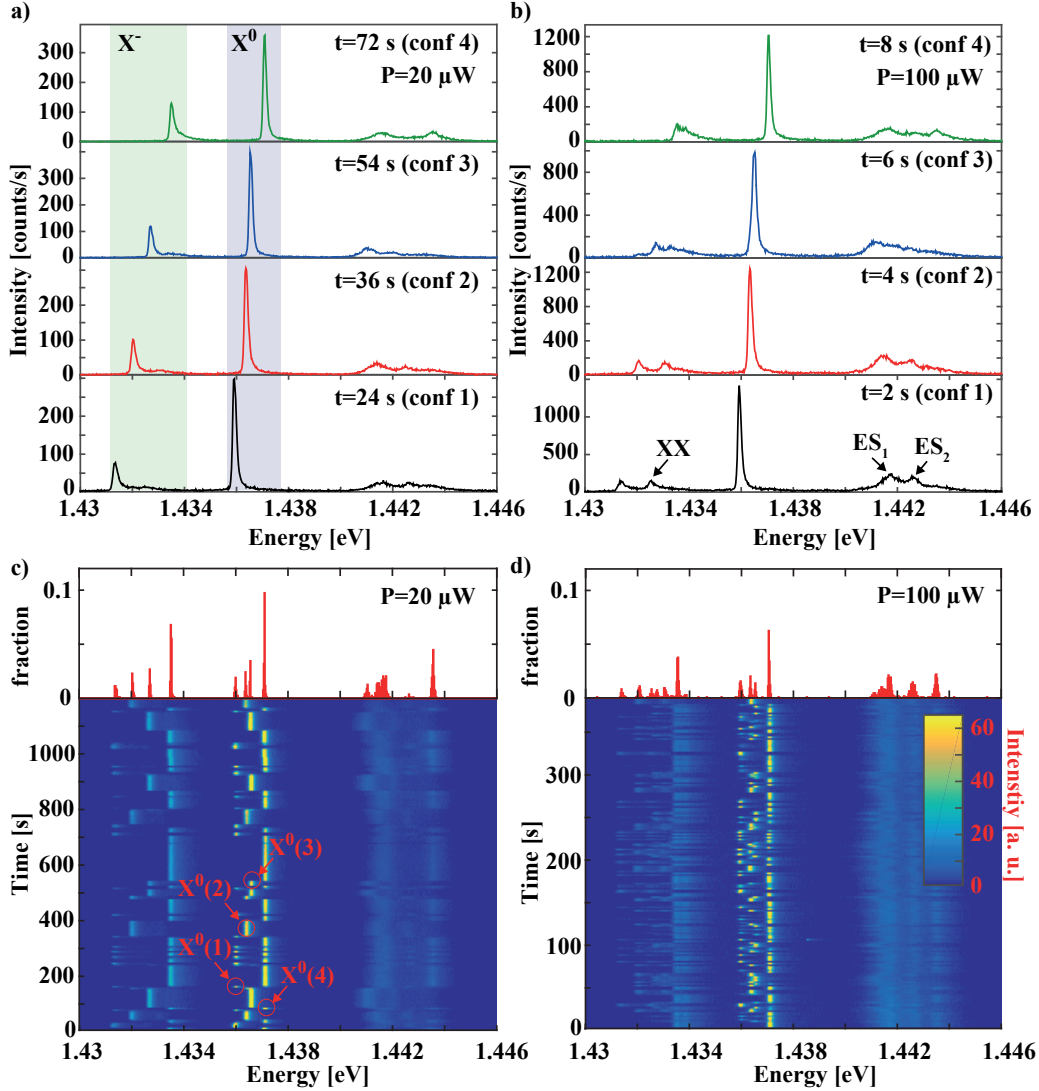
Figure 3:16 Spectra and images of spectral dynamics showing jumps between 4 emission configurations of sample XI(Table 3:1). Spectra show 4 emission configurations at 20 µW (a) and 100 µW (b) excitation powers. Images of spectral dynamics measured at the same powers as in a) and b) are shown in c) and d) correspondingly. Statistics of observed emission energies are shown on top of images. Measurements were done at 10 K.

Integrating intensities of X^-(1-4) and X^0(1-4) lines in ~100 µeV spectral windows centered at their peak energies, we constructed their intensity traces for each configuration (Figure 3:17). Integrated intensity of X^-(1-4) (Figure 3:17(a)) and X^0(1-4) (Figure 3:17(b)) lines fluctuate near two possible values, reflecting either occupied or non-occupied emission configurations. If the system is in 'y' state then the integrated intensities of both X^-(y) and X^0(y) lines take their maximum values, otherwise their integrated intensities are nearly zero (Figure 3:17).

The intensity fluctuations visible in the time traces are due to fluctuations in the QD position with respect to the excitation spot, which happened due to the drift of the cryostat by ~50 nm/min. Correcting cryostat position each 10 minutes without aborting measurements, we supressed the effect of this drift on long enough time scale, although on a short time scale ~20% emission intensity fluctuations are still visible. Fluctuations of the zero value of the intensity traces are due to the vicinity of $X^-(y)$ and $X^-(y\pm1)$ ($X^0(y)$ and $X^0(y\pm1)$) lines corresponding to the adjacent emission configurations 'y' and 'y±1'. For example, $X^0(2)$ and $X^0(3)$ lines are separated by less than 200 μeV leading to overlap between their tails with spectral windows centered at their peak energies.
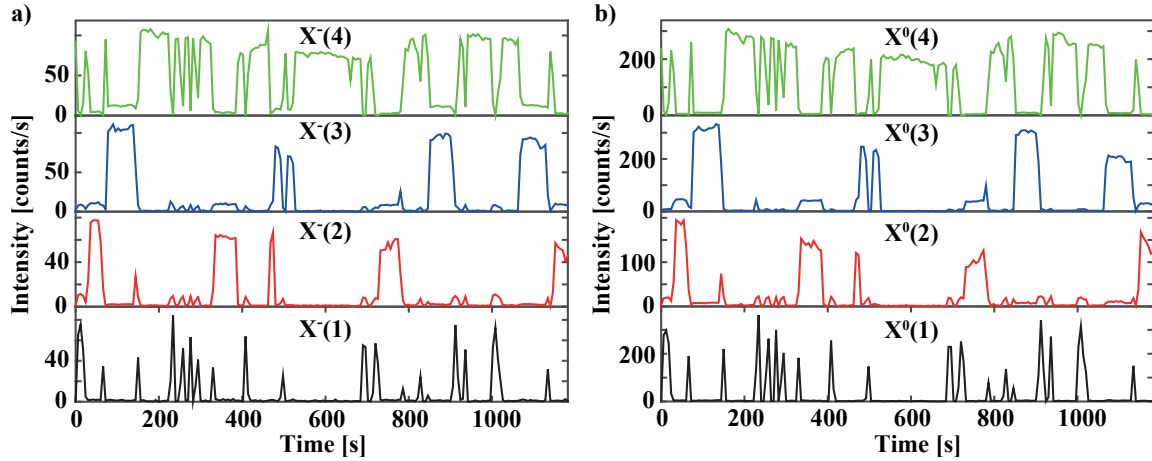
Figure 3:17 Intensity of transitions X(1-4) (a) and X^0(1-4) (b) for all 4 emission configurations at 20 μW excitation power (T=10K) of sample XI(Table 3:1). See Figure 3:16 for the definitions of the exciton states displayed.

Figure 3:18 shows correlation coefficients calculated using the intensity traces of lines $X^-(y)$ and $X^0(y)$. Figure 3:18 (a, b) shows correlation coefficients calculated between the different configurations of $X^-(y)$ and $X^0(y)$ intensity traces, correspondingly. The anti-correlations of intensity traces of different configurations reveal that during our measurements only a single emission configuration appears during the spectral integration time. In c) correlation coefficients are measured between intensity traces obtained for the two exciton types. Near unity correlation coefficients were observed for intensity traces $X^-(y)$ and $X^0(y)$ corresponding to the same mission state 'y'. This confirms that $X^-(y)$ and $X^0(y)$ lines appear always in pairs.
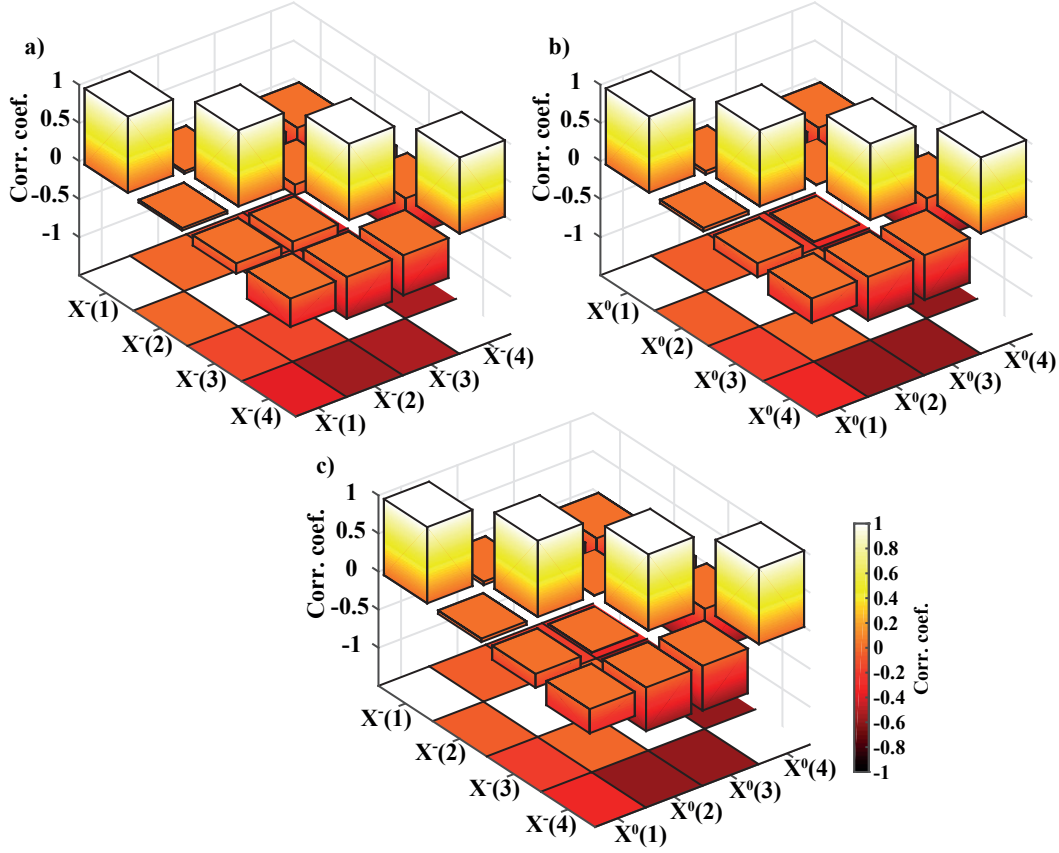
Figure 3:18 Correlation between different configurations of the same exciton X(y) (a) and X^0(y) (b) of sample XI(Table 3:1). Correlation coefficients between different configurations of different excitons X^-(y) and X^0(y) are shown in c).

We found that all spectral lines are more V-polarized due to the presence of a CM coupled to the excited state. As expected[72] the DOLP of the emission lines decreased with increasing detuning from the CM. The neutral excitonic nature of the X^0(1-4) transition observed in the slow dynamics process was proved by polarization-resolved measurements a shown in Figure 3:19(a). X^0(1-4) transitions have FSS ~55 μeV as can be seen in the inset of Figure 3:19(a). Observation of FSS for all four emission configurations confirms that the energy shift of emission lines happened due to QCSE but not as a result of a QD charging with an excess carrier.
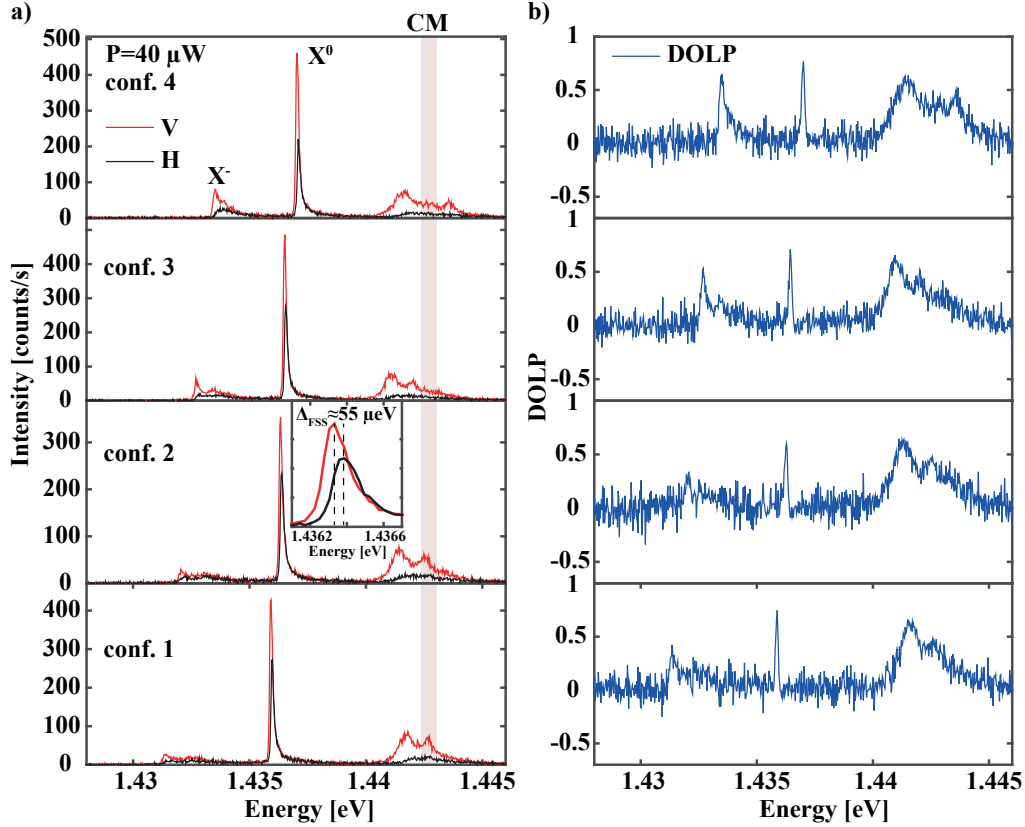
Figure 3:19 Polarization-resolved PL (a) and DOLP spectra (b) of the 4 discrete states of Figure 3:16. The inset shows neutral exciton X^0 FSS splitting. In b) DOLP spectra show V-polarization for all emission lines.

The energy of each excitonic emission line is shown in Figure 3:20(a). With increasing configuration number from 1 to 4, emission lines X^-, XX and X^0 shift to higher energies. Assuming the influence of the QCSE, we suppose that the electric field at the QD position decreases with increasing configuration number. Interestingly, we observed nontrivial energy shifts of the higher energy lines that are attributed to the excited state excitonic transitions. The energy of these lines did not increase monotonically with increasing the configuration number that corresponds to the decreasing electrical field. Thus, the energy trajectory of the excited state transitions is not linear, while the ground state trajectory depends almost linearly on the emission configuration number (electric field).

This behaviour can be explained in the following way. Similar energy shifts are very pronounced in structures with multiple emission state configurations and will be discussed below. Although opposite energy shifts of charged and neutral excitons were observed during spectral diffusion[148], we did not find any report of opposite energy shifts of the ground and excited state energies. It should be noted that the similarity in the energy shifts of different lines during spectral diffusion process are widely used for identification of the emission lines corresponding to the same QD[122], [123]. This approach can lead to the wrong identification of the spectral diffusing QD spectral structure as emission lines that belong to the same QD can shift very differently. However, this problem can be

solved looking at cross-correlations between different excitonic lines energy shifts during spectral diffusion[150].
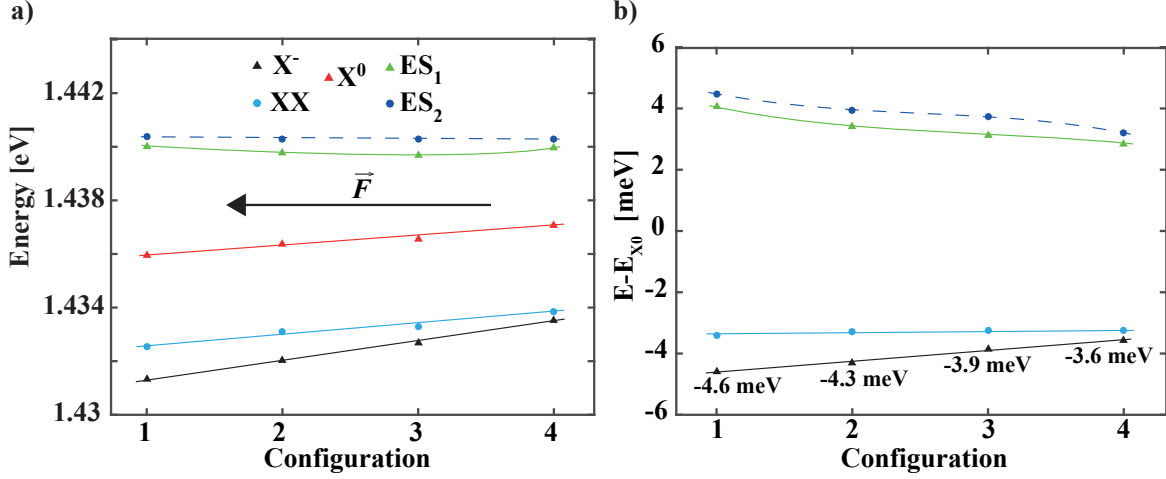
Figure 3:20 Absolute (a) and relative to X^0 (b) energy position for the first 5 excitonic transitions observed at 100 µW excitation (structure of Figure 3:15). In b) the relative energy position of excitonic complexes is shown above the data points in units of meV. The arrow in a) schematically shows the direction of increasing electric field $\vec{F}$, assuming the influence of the QCSE.

The negatively charged exciton 'X^-' has higher energy response to the electrical field of the local charge center then the neutral exciton 'X^0'. Taking into account the nearly linear dependence of the charged and neutral excitonic energies on the configuration number, we estimated the ratio between their permanent dipoles. As was mentioned above, the transition from one configuration to another happens due to the charging of an impurity or a defect by a single electron or hole. Thus, the linear dependence on the configuration number reflects a linear Stark effect. Thus, the ratio between the permanent dipoles of the charged end neutral excitons $r_{X^-X^0} = \frac{\mu_{X^0}}{\mu_{X^-}} = \frac{\alpha_{X^0}}{\alpha_{X^-}}$ where α_{X^0} and α_{X^-} are slopes of the linear fits of the neutral and charged exciton energy traces shown in Figure 3:20(a). We obtain $r_{X^-X^0} \approx 2$ that is slightly smaller than the value obtained for another QD structure (see Table 3:2 below).

Figure 3:20(b) shows the energies of the excitonic complexes with respect to the neutral exciton energy for different configuration numbers. Energy separation between negative and neutral excitonic transitions varied by ~1 meV. Interestingly, the energy separation between the charged and neutral excitons reached the typical value ~4.6 meV for configuration 1 although it corresponds to the highest electric field. The energy separation between neutral and charged exciton exhibited a smaller value of ~3.6 meV for configuration 4 that corresponds to the smallest electric field at the QD position.

3.5.1 Temperature dependence of QD spectral diffusion

Spectral diffusion in the sample showing jumps across four discrete emission configurations was found to be stable in the measured temperature range, between 10 K and 40 K. Independently of the

emission configuration, and therefore the local field strength, the QD excitonic transitions showed very similar temperature dependence of the emission intensity. Figure 3:21 shows the integrated intensity as a function of temperature for the neutral X^0 and charged X^- excitonic transitions. The temperature dependence of charged excitonic intensity is very close to typical Arrhenius intensity behavior $I(T) = \dfrac{I_0}{1 + \alpha e^{-E_0/kT}}$ previously observed in other QD structures[130], [151], [152]. Parameters E_0 and α are the activation energy and the efficiency of thermal activation.
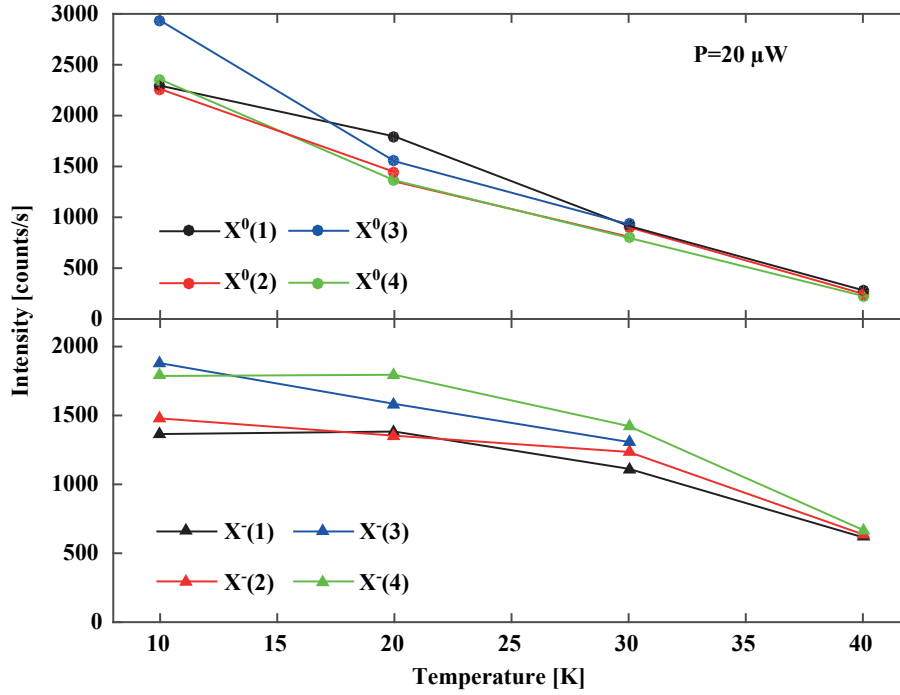
Figure 3:21 Temperature dependence of the neutral X^0 and charged X^- excitonic transitions of the sample XI (Table 3:1) for all four electronic configurations (see Figure 3:16 for definitions of the configurations).

The neutral exciton intensity decreases with increasing temperature much faster than the charged exciton transition as can be seen in Figure 3:21. We attribute the neutral excitonic intensity reduction to thermal population of the higher energy levels. In this structure the excited state (ES) is just ~5 meV apart from the neutral exciton transition, leading to very efficient thermal population of the excited state (ES).

Averaged over 50 sequential PL measurements with 1 s integration time, the spectra in Figure 3:22 show the temperature dependence of the QD spectral diffusion observed in the sample XI for two excitation powers, that is, 20 µW (a) and 100 µW (c). Figure 3:22(b, d) shows the integrated intensity of the charged exciton X^-, neutral excitons X^0 and the excited state (ES). A significant reduction of the neutral exciton X^0 intensity is visible at higher temperatures, while the intensity of the excited state transitions increases. This hints to the thermal population of excited states. Another proof of this transfer is the fact that the sum of the neutral and excited state intensities ('X^0+ES') follows the same temperature dependence as the charged excitonic transition. We can also see that in a plot of the (normalized) total integrated intensity ('X^-+X^0+ES'), that is, the sum of intensities of all three

QD spectral features, which almost exactly overlaps the (normalized) sum ('X^0+ES'), showing their same temperature dependence.
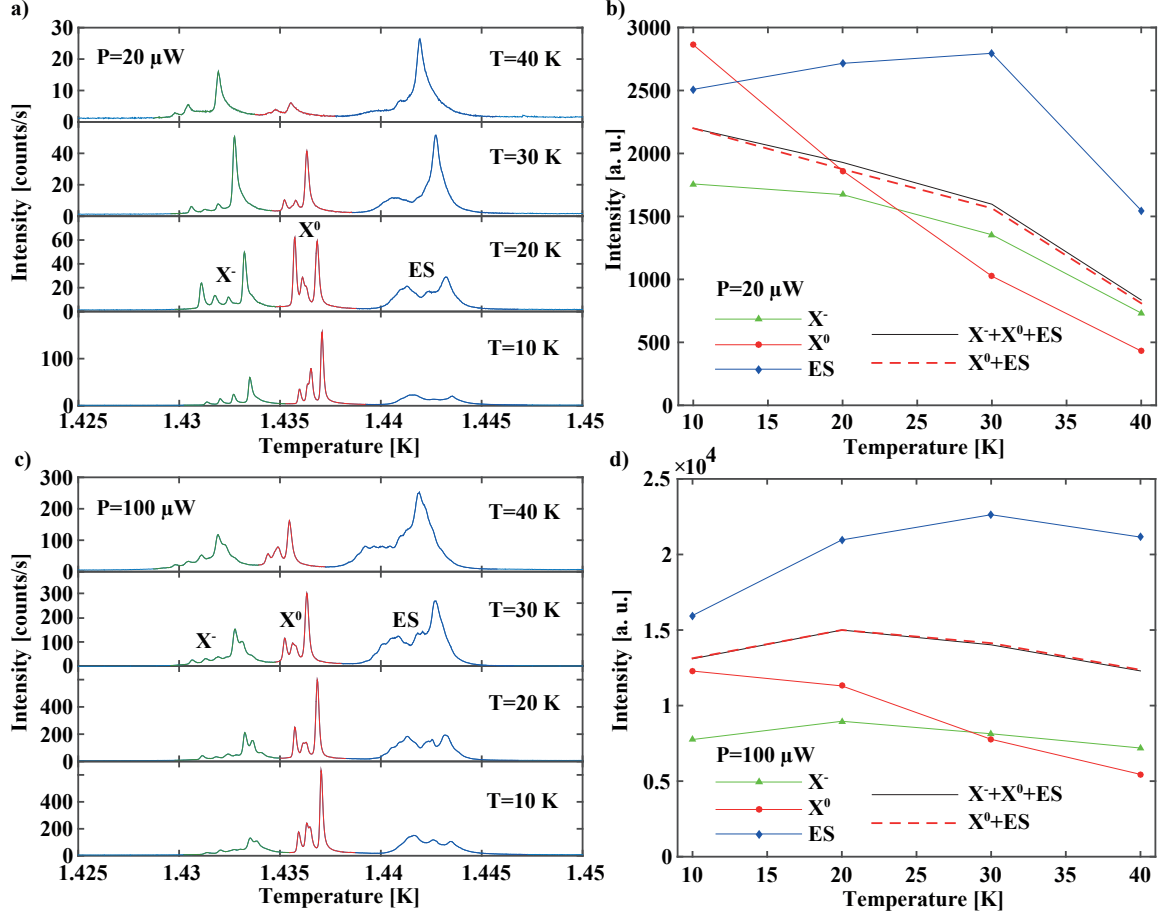
Figure 3:22 Time averaged spectra (a, c) and the intensities of different excitonic transitions (b, d) at a set of temperatures of sample XI (Table 3:2) at two excitation powers of 20 µW (a, b) and 100 µW (c, d). In b) and d) are displayed the intensities of the neutral X^0 and charged X^- excitons and excited state (ES) transitions (integrated over all configurations), as well as their sums. The sums ('X^0+ES') and ('X^-+X^0+ES') are normalized by a factor $\frac{2000}{\max_T I(T)}$.

At 100 µW excitation power, (Figure 3:22(d)), the temperature dependence of the X^-, X^0 and ES integrated intensities follow a more complicated trend than at 20 µW, although the charged exciton integrated intensity and sums of the integrated intensities 'X^-+X^0+ES' and 'X^0+ES' again have identical behaviour. We assume that this deviation from a simple Arrhenius behaviour at higher excitation power is due to the influence of several-particle states, such as biexcitonic transitions, appearing both at the charged exciton and excited state transition energies.

In the temperature dependence we also observed reduction of the total integrated intensity, that is, 'X^-+X^0+ES'. We did not observe other QD emission lines outside the presented spectral region. As a consequence population of higher energy QD states at higher temperature cannot explain this in-tensity reduction. Thus, the only reasonable explanation for the total intensity reduction is non radi-

ative recombination processes or a lower QD pumping efficiency appearing at higher temperatures. The latter is important for temperatures above 100 K[152]. Besides, pumping efficiency reduction would lead to the relative decrease of excited state intensity (Figure 3:22(d)), which is not observed. Thus, we explain the reduction of the total emission intensity ('X^-+X^0+ES') as well as of the charged exciton integrated intensity by higher non radiative recombination rate at higher temperatures. This process was confirmed by time-resolved measurements as reported elsewhere[153].

3.5.2 Time constants of interstate transitions

The structure showing jumps across just a few emission configurations is a useful platform for the investigation of spectral diffusion time constants. Figure 3:23 shows spectra measured at four excitation powers during several thousands of seconds. The excitation power levels employed provide the occurrence times of all emission configurations, which are much longer than the spectral integration time used. Thus, typically no more than two emission configurations were observed in spectra measured at instants corresponding to the transitions between different emission configurations. In other words, the probability of observation of 3 and more inter configuration transitions during the integration time employed, and more importantly during the dead spectrometer time, is negligible.
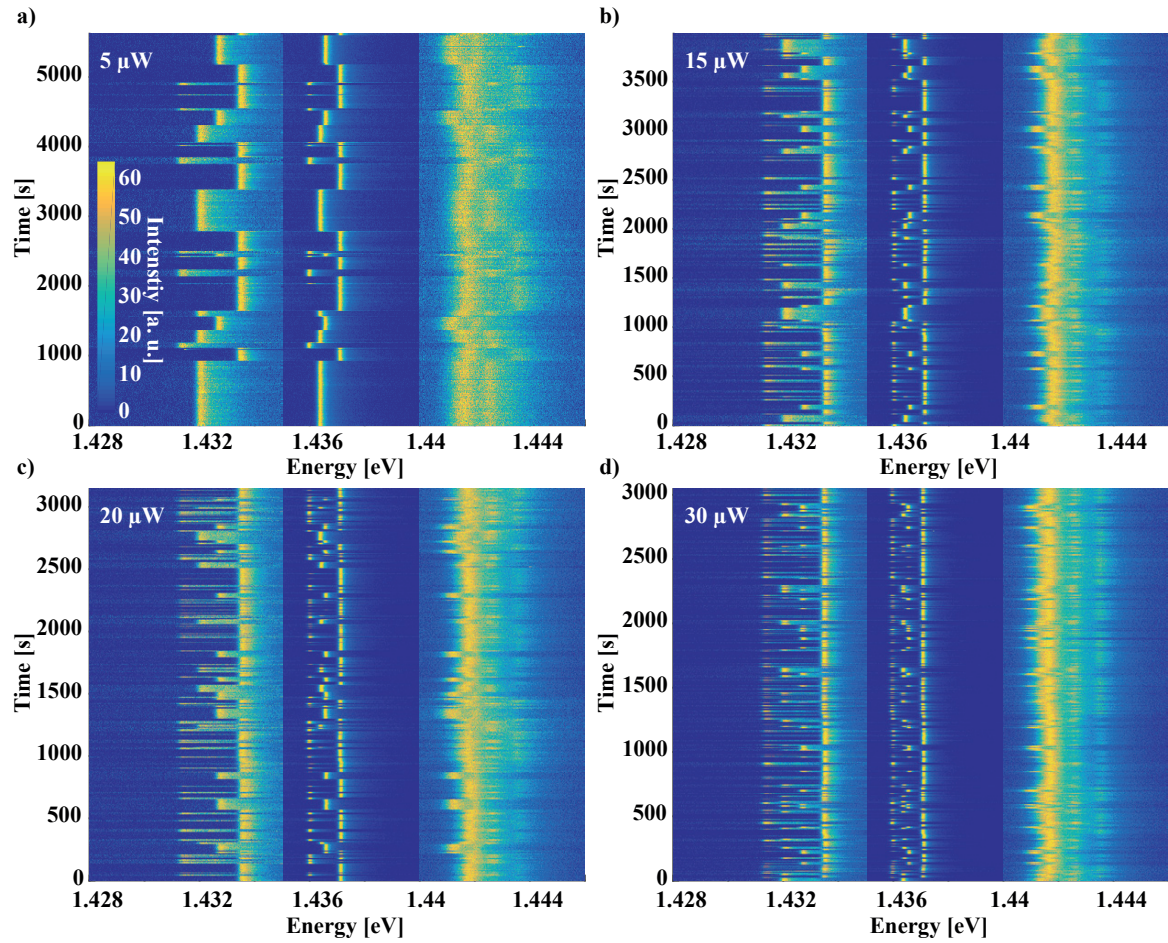
Figure 3:23 Images of spectral dynamics of sample XI (Table 3:1) measured during ~1-2 hours. In a), b), c) and d) measurements were done at 5 µW, 15 µW, 20 µW and 30 µW excitation power,

correspondingly. In each image of slow dynamics colour scale was normalized by the maximum intensity for three separate spectral regions covering charged exciton, neutral exciton and excited state transitions.

If emission lines jump across a finite number of energy levels, it is possible to introduce an emission state population parameter for each emission state. The parameter value can be either 0 or 1, corresponding to the absence or occurrence of the particular emission configuration in the measured spectrum. For the structure revealing 4 emission configurations we reconstructed population parameters identifying the neutral excitonic complex 'B'. If the line energy at time t_i belongs to the energy interval $(E_X - \delta E, E_X + \delta E)$, where E_X is the peak energy of state $X \in \{1, 2, 3, 4\}$ and $\delta E = 50\ \mu eV$, the population parameter $I_X(t_i) = 1$ while the other population parameters are $I_Y(t_i) = 0, Y \neq X$. It never happened that the energy of the neutral exciton did not fit one of the four energy intervals defined above.

Figure 3:24(a) shows the population parameters for emission configurations 2 and 3 retrieved from the slow dynamics measurements shown in Figure 3:23(b). At several instants, the population parameter of configuration 2 transits from 1 to 0 simultaneously with the transit of population parameter 3 from 0 to 1. These instants correspond to transitions from emission configuration 2 to emission configuration 3. The transition points are clearly visible in the differential parameter $dI_X(t_{i+1}) = I_X(t_{i+1}) - I_X(t_i)$ shown in Figure 3:24(b). The differential parameter can assume one of three values $dI_X \in \{-1, 0, 1\}$. The emission state X was depopulated (populated) at the moment t_i if $dI_X(t_i) = -1$ ($dI_X(t_i) = 1$). For each transition point between these two emission states (2->3 or 3->2) there is a clear coincidence of the positive and negative peaks of their differential signals (Figure 3:24(b)).
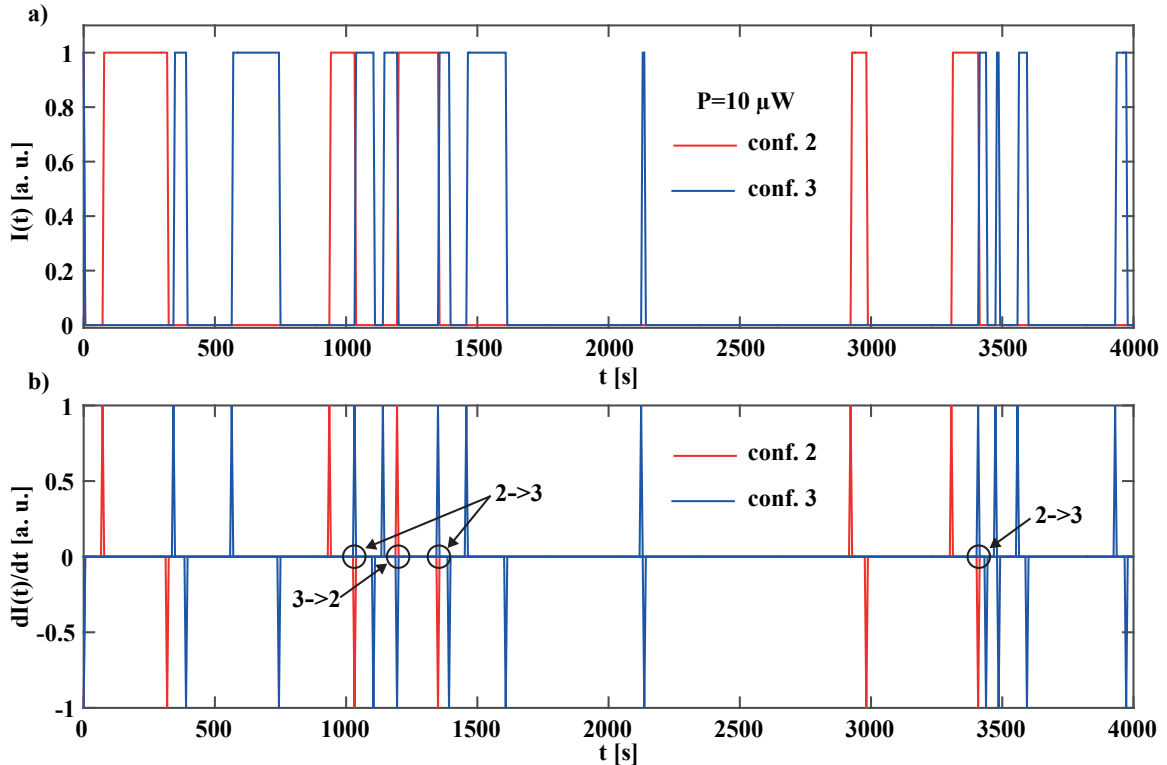
Figure 3:24 a) population traces of emission configurations 2 and 3 and b) corresponding differential parameters (sample XI, see Table 3:1). Arrows show transitions from configuration 3 to 2 or vice versa.

We identified occurrence time periods of each emission configuration X by defining time positions t_k^- and t_s^+ of negative and positive peaks in the differential parameter, that is, $dI(t_k^-) = -1$ and $dI(t_s^+) = 1$. Then the occurrence time period T_i is simply the difference between the closest time points t_k^- and t_s^+, that is, $T_i = t_k^- - t_s^+, \nexists k1, s1 : t_{k1}^-, t_{s1}^+ \in (t_s^+, t_k^-)$. Figure 3:25 shows histograms of time periods obtained using this approach. It can be seen that the time constants significantly depend on the emission configuration and excitation power.
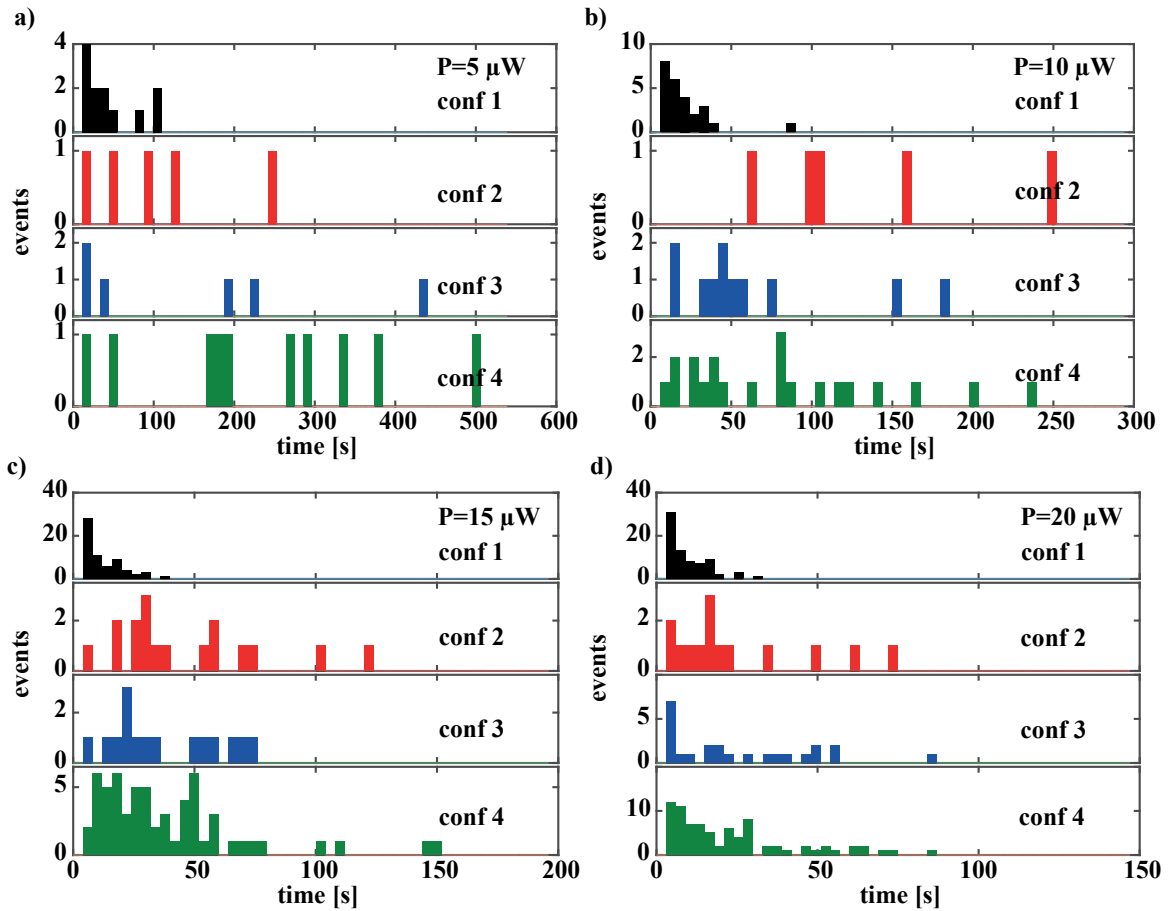
Figure 3:25 Measured life times of all 4 excitonic emission configurations for a) 5 µW, b) 10 µW, c) 15 µW and d) 20 µW excitation powers (sample XI, see Table 3:1).

Figure 3:26 shows the average occurrence time as a function of excitation power for each configuration. The emission configuration '1' corresponding to the biggest red shift revealed the shortest occurrence time while emission configurations '2'-'4' had very similar time constants. Magenta curves in Figure 3:26 show the total spectrometer time delay $t_{tot} = t_{int} + t_{dead}$, that is, the resolution of our spectrometer temporal measurements. While the average occurrence time approaches t_{tot}, the error of the occurrence time measurements significantly increases, as several transitions can happen during the measurement or during the spectrometer dead time t_{dead}. The latter can lead

to the higher time constants obtained. We consider these effects negligible for data measured at excitation powers smaller than 50 µW as the average occurrence time for each transition was at least 3 times bigger than the spectrometer total time and at least 1 order of magnitude longer than the spectrometer dead time. Comparing the average occurrence times measured at two different days, we found that these measurements were very reproducible as can be seen in Figure 3:26. Excitation power dependences of the average occurrence time obtained from data measured in 2 different days are reproducible for all emission configurations.
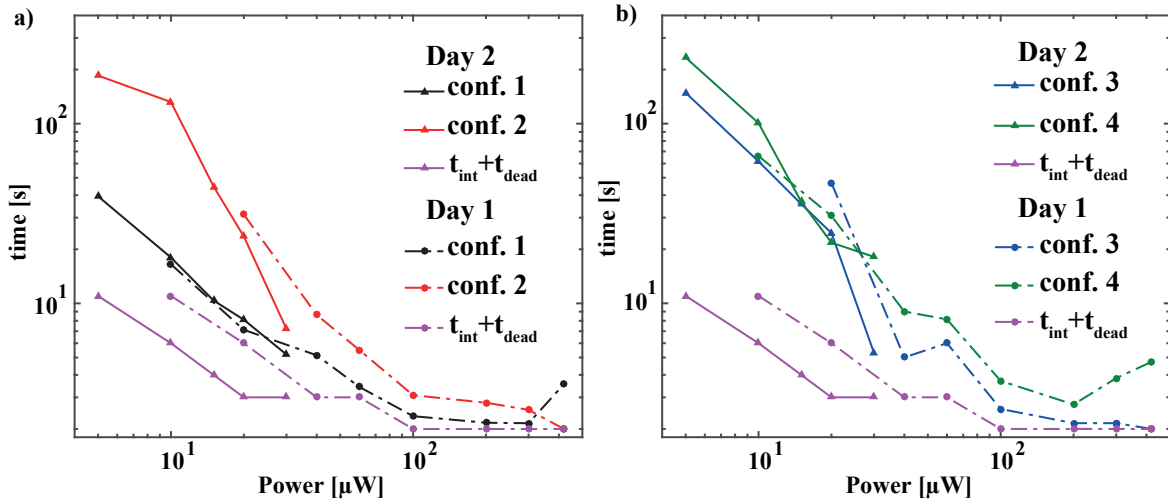
Figure 3:26 Average life times of all 4 excitonic emission states. Lifetime is shown in a) for configuration 1 and 2 and in b) for configuration 3 and 4 (sample XI, see Table 3:1). Dashed and solid lines correspond to different days of measurements. Sum of spectrometer dead and integration time (indicating the precision of this measurement) are shown by magenta curves for each day.

Fourier transforms of the population traces are shown in Figure 3:27 for the three excitation powers. The higher frequency shoulder of the spectral density decays as $\frac{1}{f^{0.7}}$ while at lower frequencies power the spectral density flattens. With increasing excitation power the flat spectral region moves to higher frequencies. Unfortunately, the duration of measurements was not enough to identify a clear frequency dependence of the spectral power density on the low frequency side. In [113] similar spectral density behaviour is obtained through convolution of a Lorentzian spectrum and a noise spectrum with a power-law like spectral density dependence. The Lorentzian spectrum is attributed to charge fluctuations of a two level system, whereas the nature of the power-law spectrum is not explained.
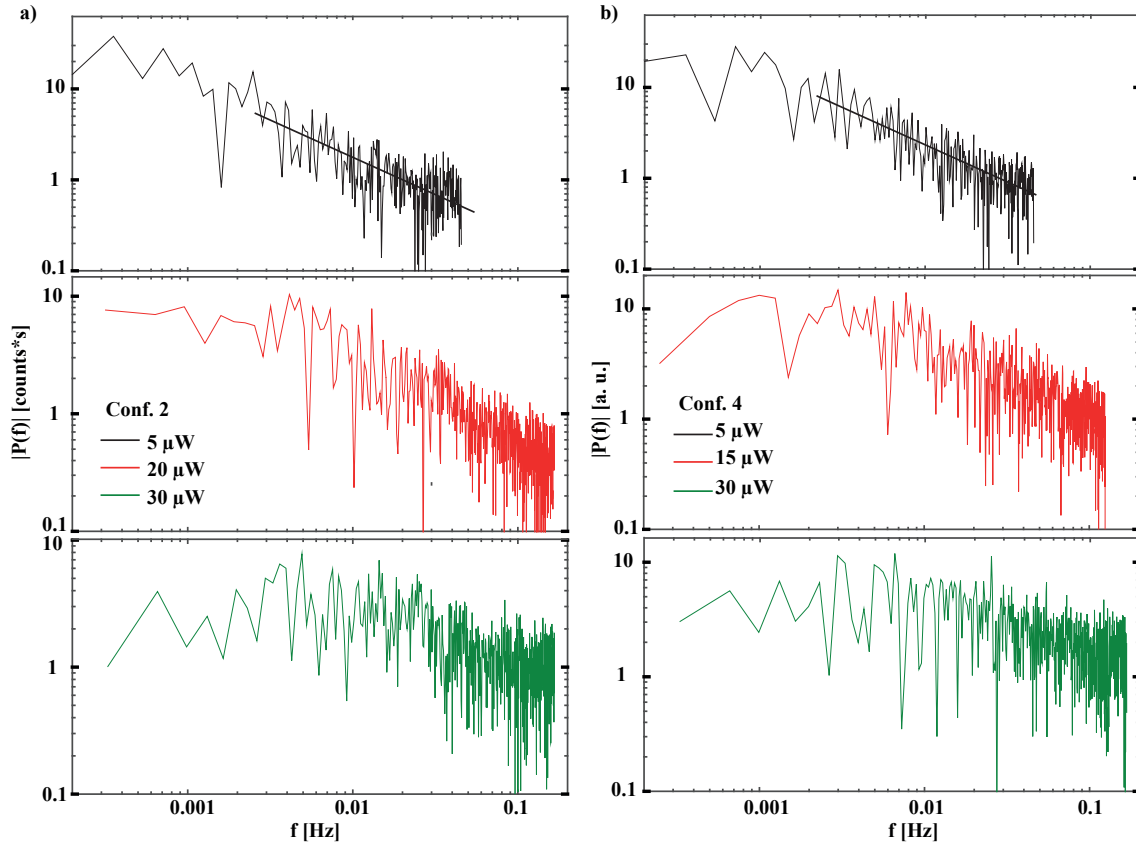
Figure 3:27 Fourier transforms of slow dynamics parameters for configuration 2 (a) and 4 (b) at several excitation powers (sample XI, see Table 3:1).

3.5.3   Transitions between different emission configuration

Both intermittency and QCSE are very sensitive probes of the QD local environment. Using dots consisting of a CdSe core in an elongated CdS shell, a single charge location was detected using difference in the quantum jitter of such a single nanocrystal[119]. In a recent work[154], a study of two different blinking mechanisms allowed to distinguish between QD electron capture mechanisms. Here we demonstrate how a QD jumping over several discrete energy states can open the way to observe the charging processes in the surrounding media.

Only two mechanisms can explain the observation of four emission states of a QD. Either there are two charge centers that can be only in two charge states each, for example, $q_{1,2} \in \{0, e\}$ where e is a single electron charge; or there is a single charge center that can be in four charge states, for example, $q \in \{0, e, 2e, 3e\}$. It is very unlikely that these two cases can be distinguished by the values of the Stark shift. This is due to numerous variants of charge centers positioned in 3D around the QD. In particular, highly inhomogeneous electrical fields created by two close charge centers can add constructively or destructively depending on the sign of charges trapped in each center and their mutual position with respect to the QD. QD energy can be either red or blue shifted depending on the electric field orientation with respect to the QD symmetry axes[137], [138]. The latter effect was also observed in the case of a QD in a homogeneous lateral electric field created by two external electrodes[155], [156].

Although we are not able to distinguish between these two cases, we can study the charging process of the QD-environment system using additional information hidden in the temporal dynamics of the excitonic energy. In our experiment, we tracked transitions between different charge configurations gaining from their influence on the observed QD excitonic emission energy. Looking at allowed transitions between different charge configurations of the system we were able to discriminate if linear or nonlinear processes drive the charge trapping in the QD environment. Here, the linear (nonlinear) charge trapping process means uncorrelated (correlated) trapping of multiple charges.

All possible charge configurations of a system formed by two charge centers can be described with a pair of numbers $[x, y]$ where x and y can be either 0 or 1. Change from 0 (1) to 1 (0) in this notation corresponds to trapping of a single charge by the single charge center. Thus, the most probable transitions between different charge configurations are $[0,0] \leftrightarrow [0,1]$, $[0,0] \leftrightarrow [1,0]$, $[1,0] \leftrightarrow [1,1]$ and $[0,1] \leftrightarrow [1,1]$ corresponding to the trapping of a single charge per single charging event. If the two charge centers are independent, that is, the charge state of one of then does not influence the charge state of another, then transitions $[0,0] \leftrightarrow [1,1]$, $[1,1] \leftrightarrow [0,0]$, $[1,0] \leftrightarrow [0,1]$ and $[0,1] \leftrightarrow [1,0]$ are highly unlikely as the two independent charge centers simultaneously change charge configurations with very low probability. Moreover, there are two possible transition pathways for each charge configuration. For example, charge configuration $[1,0]$ can either change to $[0,0]$ or $[1,1]$ charge configurations, corresponding to no charges trapped in the system or two charges trapped by both centers.

The system formed by a single charge center with the four states can be described in a similar way with a single number $x \in \{0, 1, 2, 3\}$ that reflects the amount of charge maintained by the charge center. As the probability of trapping of more than a single electron (hole) is low, we get the following chain of allowed transitions: $[0] \leftrightarrow [1] \leftrightarrow [2] \leftrightarrow [3]$. Transitions $[0] \leftrightarrow [2]$, $[1] \leftrightarrow [3]$ or $[0] \leftrightarrow [3]$ have much lower probability and can be considered as forbidden since they require trapping of more than a single charge per single charging event. Therefore, configurations $[1]$ and $[2]$ have two possible transition pathways while configurations $[0]$ and $[3]$ have only a single transition pathway.

For excitation powers lower than 30 µW, the total spectrometer measurement time was around one order of magnitude smaller than the average lifetime of any emission configuration (Figure 3:26). Thus, we were able to exclude events with several transitions happening during the sum of the integration and dead spectrometer times. Due to QCSE, changes in the QD charge environment were directly reflected as changes between different emission configurations. Therefore, transitions between different charge configurations are in direct correspondence with the transitions happening between different emission configurations that can thus be recorded spectrally. Figure 3:28 shows the number of observed transitions N from an initial emission configuration i to a final emission configuration f (denoted by $i \to f$ on the horizontal axes). These data are obtained by multiplying the negative part of differential signal of the emission configuration i by the positive part of the differential signal of the emission configuration f (see Figure 3:24): $N = -(dI_f^p)^T * dI_i^n$ where

$$dI_f^p(t_j) = \begin{cases} 1, dI_f(t_j) = 1 \\ 0, dI_f(t_j) \neq 1 \end{cases} ; \quad dI_i^n(t_j) = \begin{cases} -1, dI_i(t_j) = -1 \\ 0, dI_i(t_j) \neq -1 \end{cases}$$
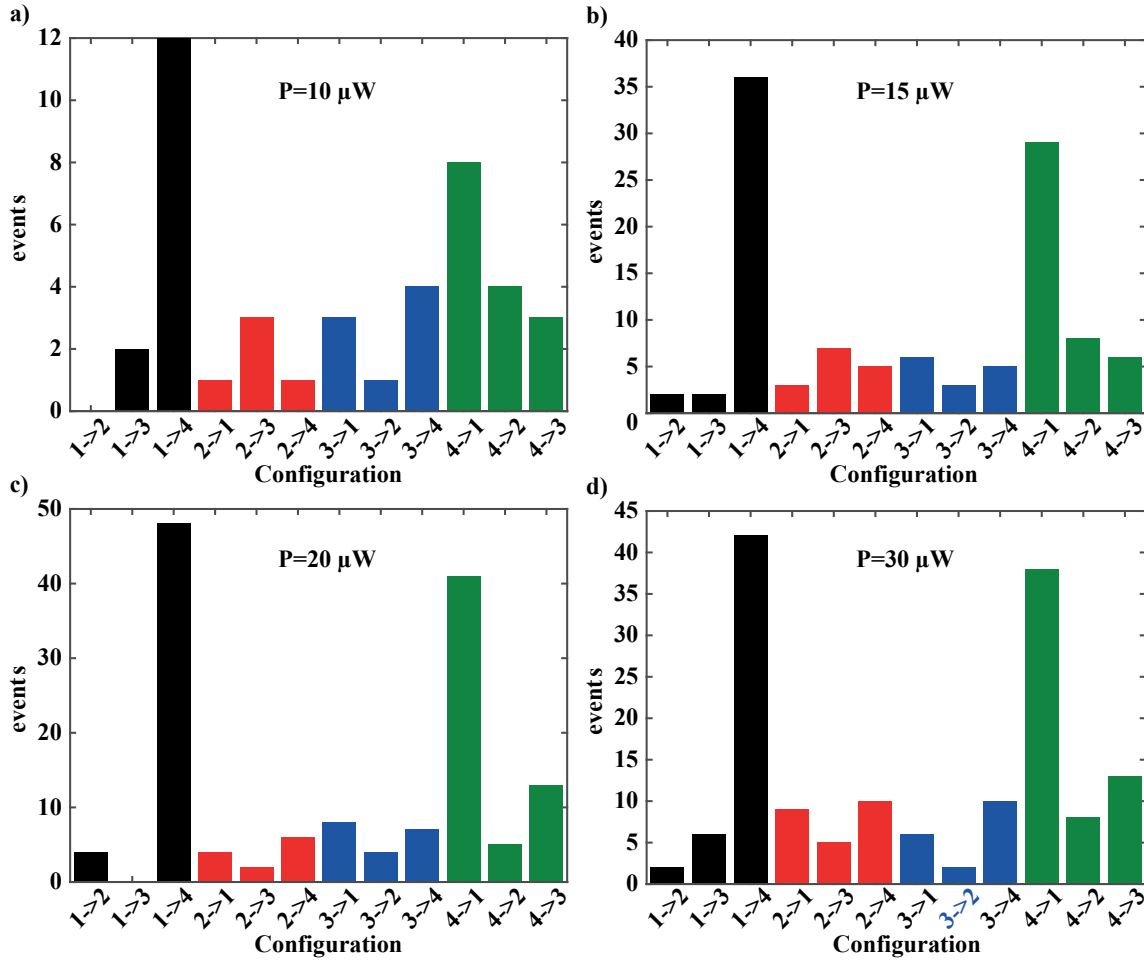
Figure 3:28 Number of transitions between all possible emission configurations. In a), b), c) and d) statistics are shown for 10 μW, 15 μW, 20 μW, and 30 μW, correspondingly.

As can be seen in Figure 3:28, the most frequent transitions are the ones between configuration '1' and '4' (see Figure 3:16). Three out of the four emission configurations, namely, '2', '3' and '4', are unlikely to be interconnected in the case of QCSE induced by two independent two level charge centers. Indeed, in Figure 3:28 they appear with low probability. Figure 3:29 shows the probability of transition from an initial configuration i^- to a final configuration f^+ obtained from the data presented above (Figure 3:23). In this figure, it is clearly seen that the emission configurations '2', '3' and '4' can transit to any other configuration, while configuration '1' transits preferentially to configuration '4'. This observation is a sign of comparable possibilities of observing single and multicharging effects that is only possible if the charge trapping is nonlinear.

Obtained result is very solid as transitions during the dead time of our spectrometer are very unlikely for the employed excitation powers because of much longer characteristic inter-configuration transition times. It is further confirmed by the fact that we did not observe any single spectrum with simultaneous 3 emission configurations. The latter would reflect a set of transitions happening between more than 2 emission configurations during the integration time employed, which is several times longer than the spectrometer dead time ($t_{dead} = 1\ s$).
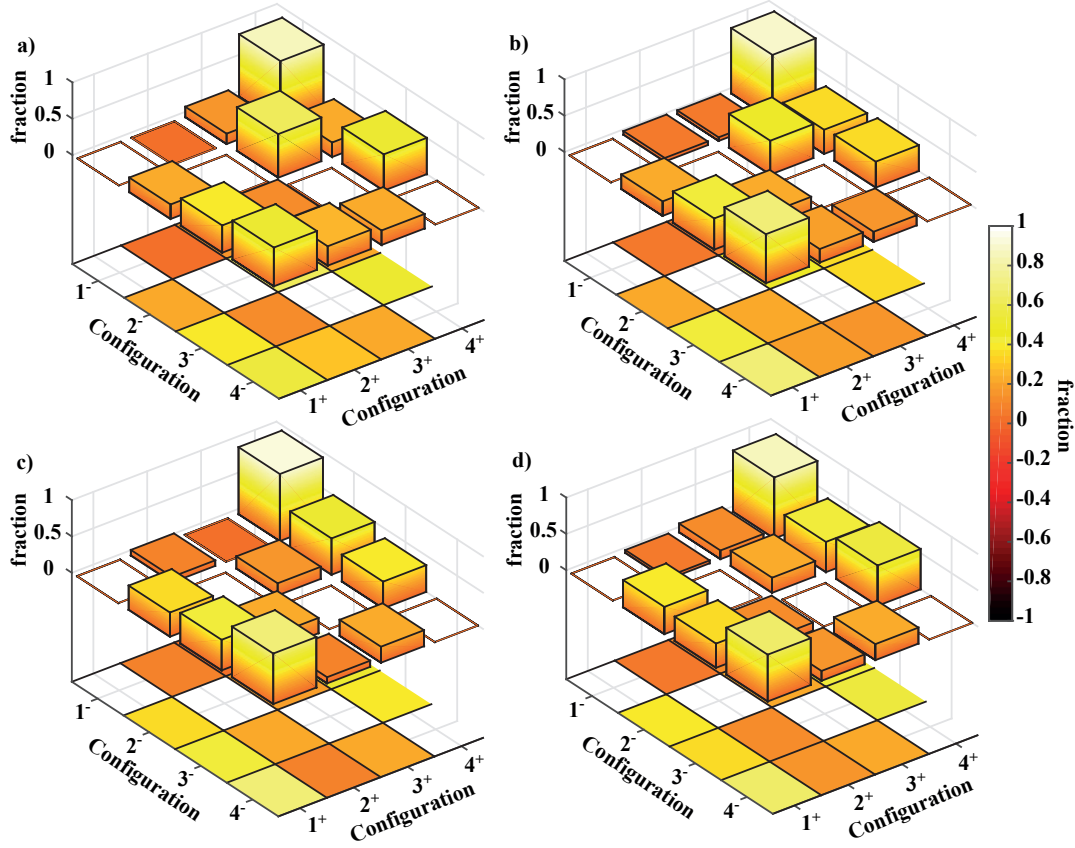
Figure 3:29 Probabilities of transitions between different emission configurations for 10 µW (a), 15 µW (b), 20 µW (c) and 30 µW (d). 1^-, 2^-, 3^- and 4^- correspond to initial configuration and 1^+, 2^+, 3^+ and 4^+ corresponding to final configuration of the transition.

(a-d) shows schematic diagrams of transitions obtained at four excitation powers using data presented in Figure 3:26 and Figure 3:29, where the width of the arrows corresponds to the transition probability and the radius of corresponding circle represents the transition time of the emission configuration. All the three transition channels are possible for emission states '2', '3' and '4' that is in controversy with a model based on the linear charge trapping. Thus, our system is either driven by two charge centers or by a single defect with 4 charge states both having nonlinear charge trapping dynamics.
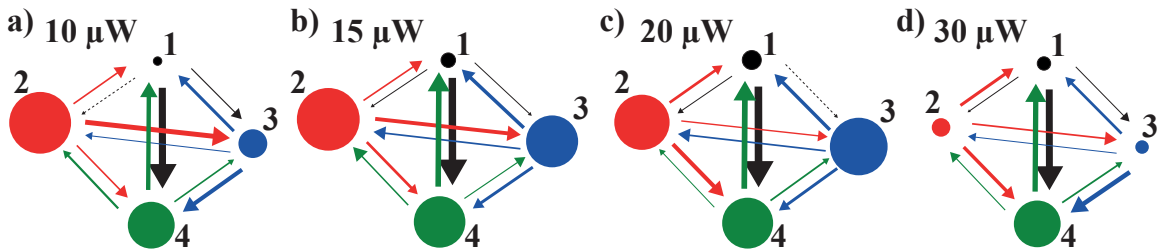
Figure 3:30 Probability diagrams showing schematically the transitions between the 4 configurations, for 10 µW (a), 15 µW (b), 20 µW (c) and 30 µW (d) excitation powers. Radii of the circles

correspond to the ratio between lifetime of corresponding configuration and lifetime of configuration 4.

In conclusion, using the charge state mapping of the defect(s) in the QD vicinity by the QD excitonic emission energy we successfully studied the charge trapping processes in the QD environment. In particular, we found an intriguing probability distribution of transitions between different charge states revealing nonlinear trapping of the charges by the defect(s).

3.5.4 Accessing exciton static dipole using the spectral diffusion process with jumps over multiple discrete emission states

Among 15 samples with slow dynamics behaviour examined, we found several structures with spectral jumps among several tens of energy states that are introduced by a certain number of charges trapped in the vicinity of QDs. These structures allow for probing of the excitonic energy and QD electronic structure responses to the increasing electrical field. Figure 3:31(a) shows an image of slow dynamics measured at $60\,\mu W$ excitation power of sample VII revealing discrete jumps of emission lines across several energy levels. Figure 3:31(b) shows 3 sets of spectra measured at the moments of transitions between different emission configurations. If several discrete transitions happen faster than the used integration time (1 s), then the spectrum consists of several peaks corresponding to the same excitonic complex shifted due to QCSE (Figure 3:31(b)).

Figure 3:31(c) shows statistics of the excitonic line energies extracted from spectral measurements collected during 13 min with time difference $t_{tot} = 2\,s$ between two consecutive measurements. Several peaks in these data reveal the most frequent emission states of the measured QD. Figure 3:31(d) shows 20 out of the 46 identified emission configurations. These emission configurations were arranged according to the energy of the most intense lines, the common interstate transitions and the visibility of the ground state excitonic complexes X^- and X_0, as will be discussed in the following. We also divided these emission configurations into 3 groups by similarities in shapes of different emission states. The most frequent interstate transitions were the transitions between group 1 (2) and group 2 (3) confirming our arrangement of different emission configurations. Transitions between group 1 and group 3 were rarely observed.
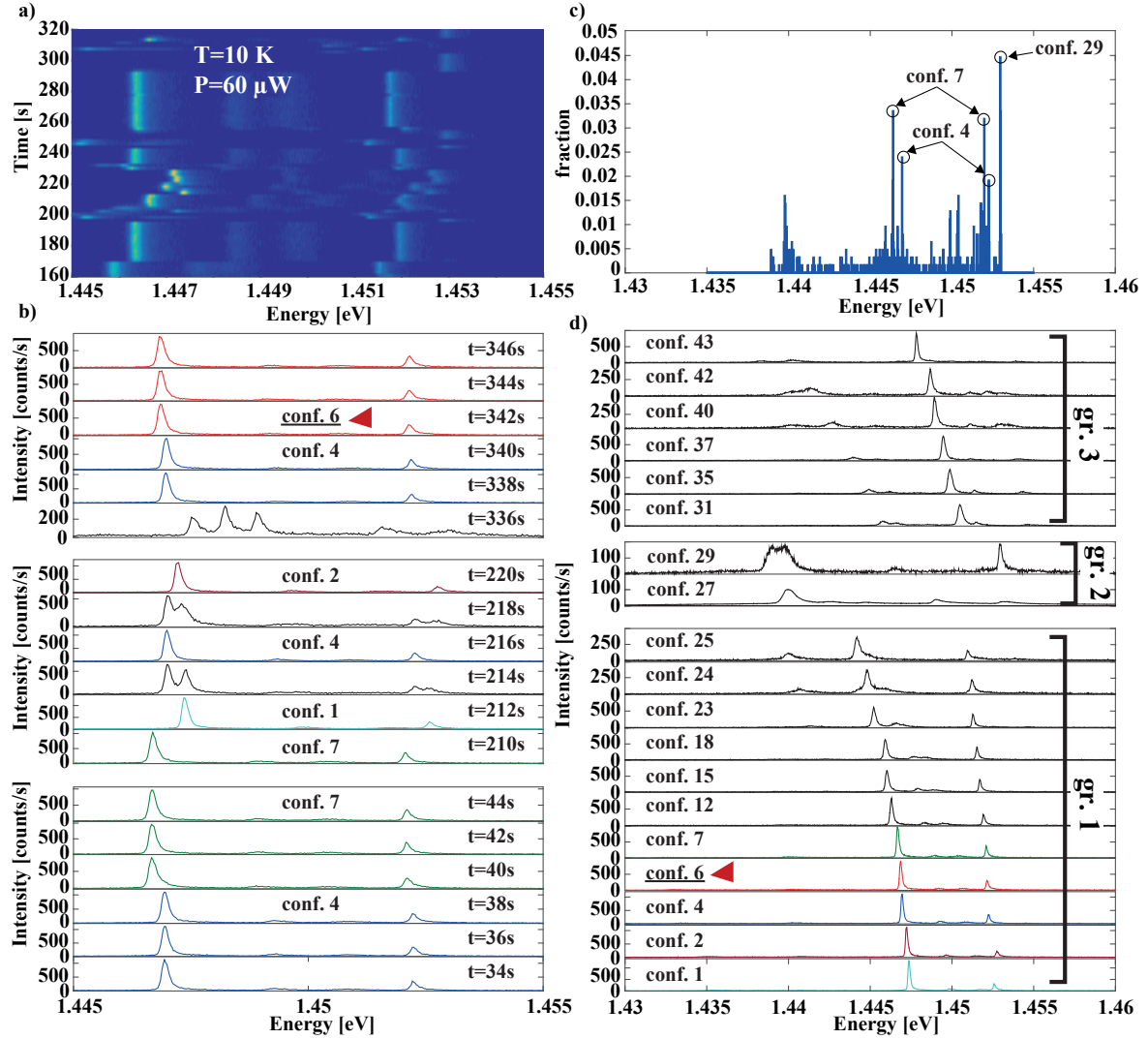
Figure 3:31 Jumps of spectral lines between many emission configurations (sample VII, see Table 3:1). In a) the image of spectral dynamics shows line shifts between discrete energy states. In b) spectra show 3 transition events between different emission configurations. In c) statistics of emission lines show clear peaks corresponding to the most frequently occupied emission configurations. In d) 20 emission configurations are shown.

In Figure 3:31(d) the brightest transitions for group 1 of the emission spectra are the excited state lines, although the excitation power is below the saturation level of the ground state excitonic complexes. Ground state excitonic transitions are visible only in a log scale due to the strong intensity suppression of these complexes by the intrinsic electric field. Figure 3:32(a) shows the most frequently appearing spectra in this time resolved set of spectra. For states 4 and 9 the neutral and charged excitons are visible on top of a background emission that is ~10 meV wide. Similar background appears in several structures with intrinsic electric field fluctuations, while in the absence of electric field fluctuations this background disappears. In Figure 3:32(a), each spectrum was obtained through an averaging of all measured spectra corresponding to the same emission state. For all states shown in Figure 3:32(a) at least 10 spectra were observed, thus we significantly increased

the signal to noise ratio. Figure 3:32(b) shows the corresponding RTS plotted as time traces of each emission state occupation.
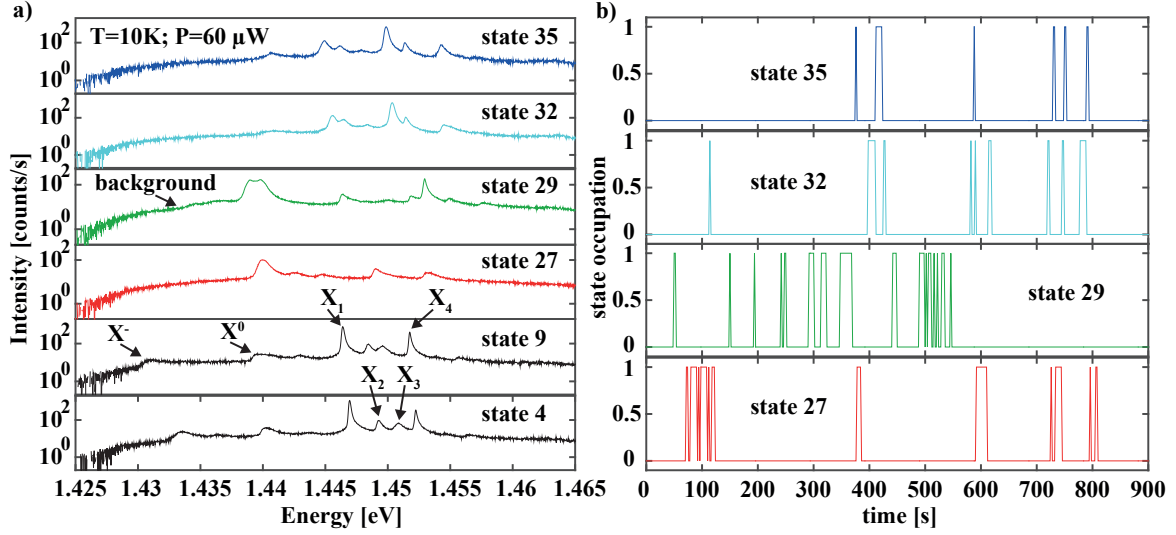
Figure 3:32 Spectra (a) and population signals (b) of the most frequently appearing emission states of Figure 3:31.

Figure 3:33(a) shows emission states plotted in a false-3D figure where each spectrum is normalized by the some factor optimizing the visibility of the main spectral lines. The used normalization factor is different for the lower and higher energy part of the figure for emission states 1 to 25. For the part of Figure 3:33 (a) below 1.444 meV, the normalization factor is 6 times smaller making the ground state excitonic lines X^-, X^0 and X^+ visible for the first 20 emission configurations. For the emission states from 1 to 26 ('group 1'), excitonic lines shift to lower energy nearly linearly as a function of the state number. At higher emission state numbers 24-26, excited state lines X_{1-3} almost converge to a single line. We did not observe afurther energy shift of these lines. Instead, spectral configurations with very broad low intensity emission lines appeared as an extension of the X^+ transition as also visible in Figure 3:31(d) and Figure 3:32(a).

We attribute these spectra to the emission states corresponding to the further evolution of 'group 1' spectra at higher internal electric field values. This arrangement is due to the preferential transitions from 'group 1' emission states to these spectral configurations. Figure 3:33(b) shows the image of slow dynamics revealing transition pathways between different groups of emission spectra. For better representation of the lower energy emission lines, we again chose different normalization constants for the parts of the spectra below and above 1.445 meV. From the emission configurations 27-30 ('group 2') the system can transit to the emission configurations 1-25 ('group 1') or to the emission configurations 31-45 ('group 3') as can be well seen in the histogram shown in Figure 3:33(c). Interestingly, the number of observed direct and reverse transitions, that is, $x \rightarrow y$ and $y \rightarrow x$ is nearly equal, which could be a sign of established equilibrium in the system with realized detailed balance.
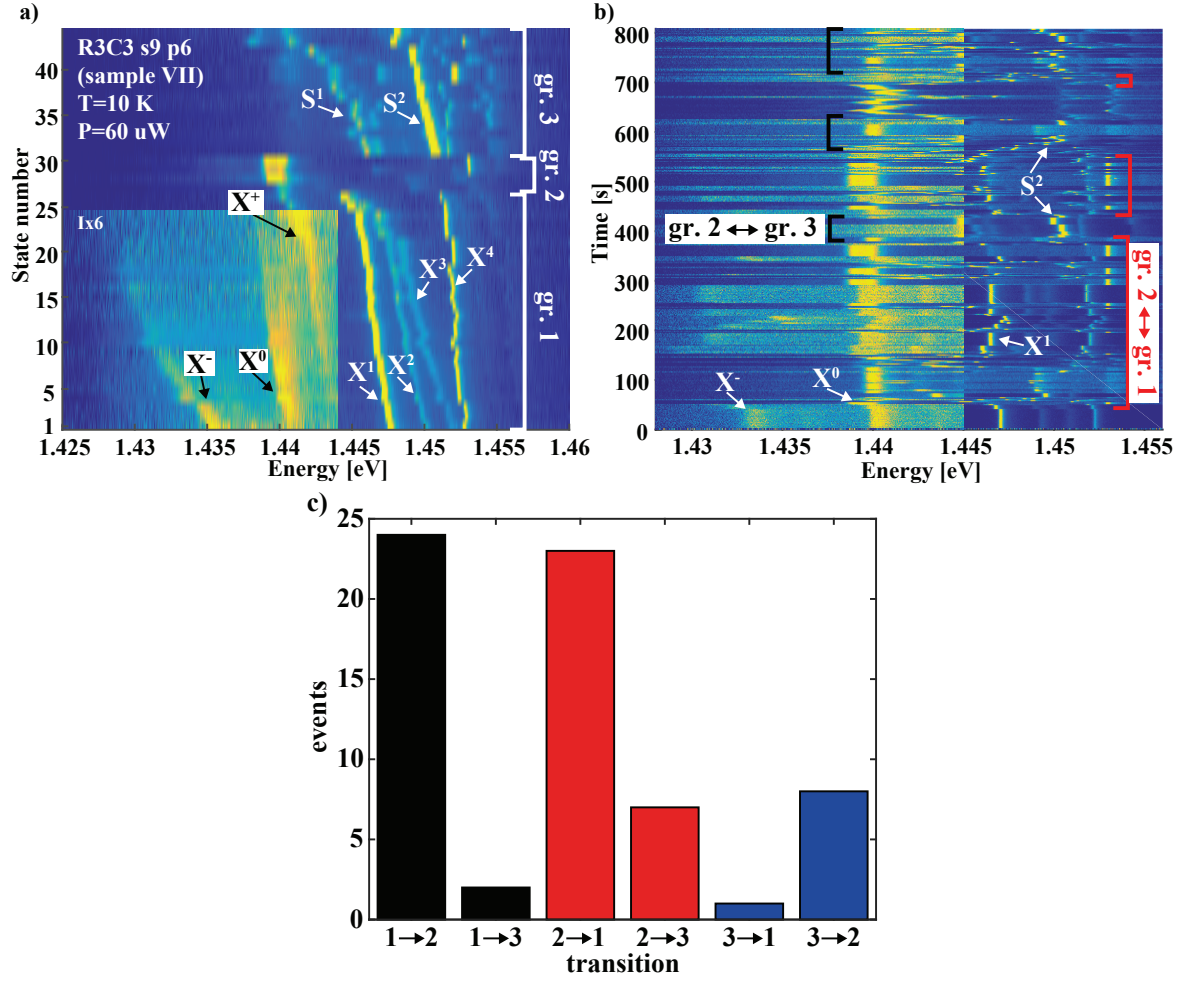
Figure 3:33 QD emission states (a), slow spectral dynamics shown as a false 3D figure (b) and intergroup transitions observed (c) (sample VII, see Table 3:1).

Figure 3:34 shows the energy and peak intensity of the main emission lines for 'group 1' emission states. We observed linear dependence of the emission state energy on the state number as can be seen in Figure 3:34(a). The line intensity of the neutral exciton did not vary significantly (Figure 3:34(c)) while X^+ (X^-) transition intensity increases (decreases) with the state number, which can be due to the QD predominant charging by positive carriers at the higher intrinsic electrical field values. While jumping to 'group 2' emission configurations a radical change of the QD emission spectrum is observed. This spectrum modification can be due to charging of the QD with several excess carriers, or due to some effects caused by a strong inhomogeneous electric field created by charge centers very close to the QD that remain unclear at this point.

Corresponding to higher local electric field values, 'group 3' spectral configurations do not have lower energy features that could be attributed to the QD s-shell. We assume that this is due to the complete suppression of the excitonic ground state with the strong internal electric field. Similar effect was observed in other structures, in particular, 'sample II' discussed in Section 3.5.5 has very

low intensity of the ground state transition while excited state lines are ~2 orders of magnitude more intense.
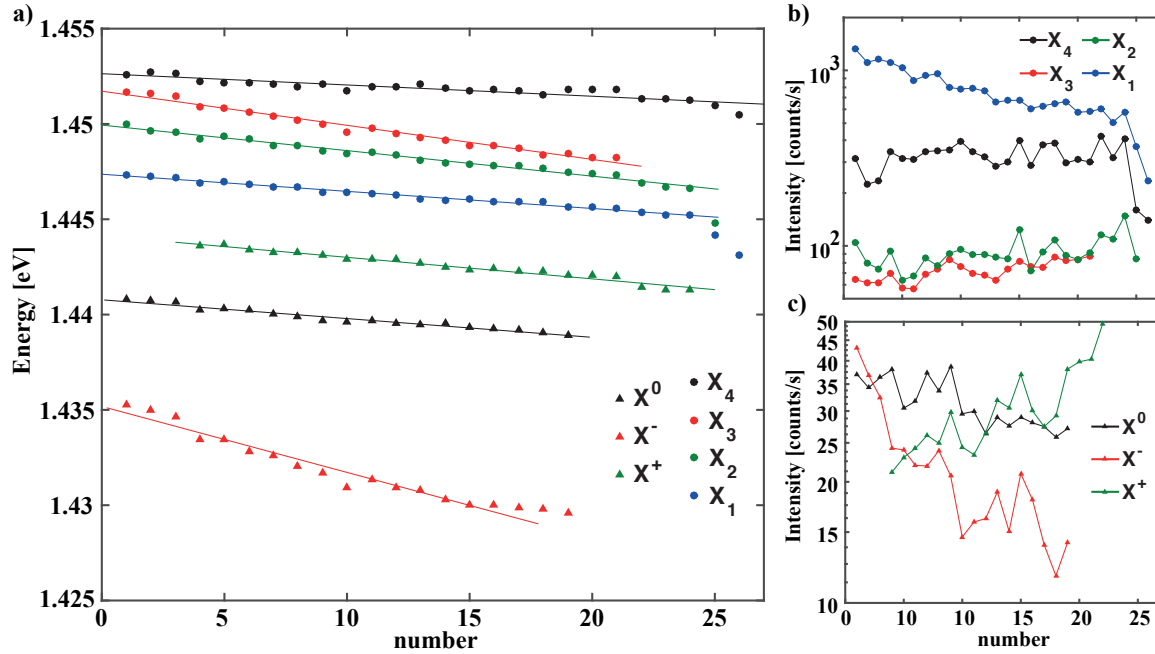
Figure 3:34 Emission energy (a) and intensity dependence of the excited (b) and ground (c) state lines versus the emission configuration number (sample VII, see Table 3:1).

Analysing the energy of the different excitonic species as a function of the emission state number, we estimated the ratio between electronic dipoles of the different excitonic complexes. We found a nearly linear dependence of the different line energies on the emission state number (see Figure 3:34(a)). Following a similar procedure to the one reported in [149], the ratio between the dipole moments $\mu_{1,2}$ of the two excitonic complexes is the ratio between the corresponding energy slopes $\alpha_{1,2}$: $r_{ij} = \frac{\mu_j}{\mu_i} = \frac{\alpha_j}{\alpha_i}$. Table 3:2 shows the ratio between the dipole moment of the excitonic complex corresponding to the column label to the dipole moment of an excitonic complex corresponding to the row label for all 7 excitonic transitions observed. The charged exciton has ~3 times larger permanent dipole than the neutral exciton, which is consistent with results obtained for the structure revealing jumps across 4 emission states (section 3.5).

	X^-	X^0	X^+	X_1	X_2	X_3	X_4
X^-		0.28 ±0.06	0.33 ±0.07	0.26 ±0.04	0.39 ±0.07	0.52 ±0.10	0.17 ±0.06
X^0	3.51 ±0.79		1.15 ±0.21	0.91 ±0.14	1.36 ±0.22	1.82 ±0.31	0.60 ±0.19
X^+	3.06 ±0.63	0.87 ±0.16		0.80 ±0.11	1.18 ±0.17	1.58 ±0.24	0.52 ±0.15
X_1	3.85 ±0.66	1.10 ±0.17	1.26 ±0.17		1.49±0.16	1.99±0.23	0.66 ±0.17
X_2	2.58 ±0.45	0.74 ±0.12	0.84 ±0.12	0.67 ±0.07		1.34 ±0.16	0.44 ±0.12

X₃	1.93 ±0.36	0.55 ±0.09	0.63 ±0.09	0.50 ±0.06	0.75 ±0.09		0.33 ±0.09
X₄	5.9 ±1.9	1.67 ±0.51	1.91 ±0.55	1.52 ±0.39	2.27 ±0.59	3.03 ±0.82	

Table 3:2 Ratio between permanent dipole moments of the brightest excitonic complexes observed in the emission configurations 1 to 26. Each cell value corresponds to the ratio of the dipole of the excitonic complexes in the column to the dipole of the excitonic complex in the row.

3.5.5 Influence of the intrinsic field fluctuations on the binding energy of different excitonic transitions.

Electrical field oriented along different QD axes can lead to an opposite energy shift of different excitonic complexes. We observed both blue and red energy shifts of different emission lines during the spectral diffusion processes. Energy shifts opposite in sign have been reported previously for negatively charged exciton and neutral exciton (biexciton) transitions in CdTe QDs[157]. Although these observations are in controversy with a simple Stark shift induced by tilting of the confinement potential, opposite energy shifts of different excitonic complexes were observed experimentally under 'lateral' electrical field[155] and were explained by the competition between the band-tilting and the decreased Coulomb attraction energy[155], [156]. The blue shifts of s- and p- excitonic shells are also reported in [138].

In our structures opposite energy shifts were observed between different excitonic complexes including neutral exciton and biexciton and excited state transitions. Figure 3:35(a) shows a set of spectra of the structure with the neutral exciton and biexciton transitions shifting towards opposite energy sides. This effect is a spectral diffusion counterpart of a vanishing exciton-biexciton binding energy in the QCSE experiments with the 'lateral' electric field[158]–[160]. Exciton-biexciton binding energy fluctuations happened on the energy scale ~1 meV, superimposed on the bigger scale shifts visible in peak energy traces shown in Figure 3:35(b) obtained from the spectra where neutral and biexcitonic lines could be identified. These fluctuations of the neutral exciton and biexciton emission energies led to fluctuations of their energy separation by ~1 meV, as shown in the histogram in Figure 3:35(c).
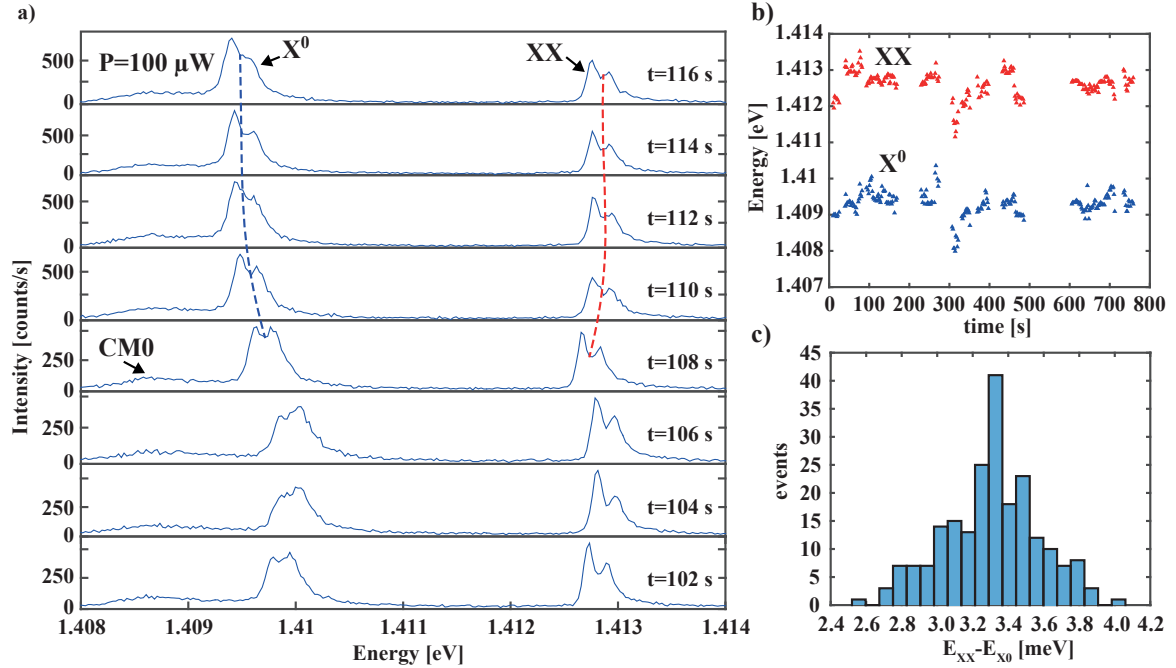
Figure 3:35 Evolution of the neutral exciton and biexciton energy positions. In a) spectra show opposite energy shifts of the neutral exciton and biexciton lines. In b) peak energy positions of neutral exciton and biexciton are shown as a function of time. In c) a histogram shows statistics of energy difference between the neutral exciton and biexciton obtained from the spectral measurements.

The blue shift of excitonic transitions significantly depends on the QD size as for bigger QDs more effective spatial separation of carriers is possible[156]. Figure 3:36 (a) shows an image of slow dynamics of the sample II that revealed several meV blue shifts of emission lines. The QD emission consists of a single ground state excitonic transition X_0 and the excited state transitions. The spectral diffusion of the higher energy lines is accompanied by the energy shift of the ground state line X_0 confirming that it is not a CM line. This low intensity emission line is very well visible in the spectra extracted from the temporal measurement of this sample (Figure 3:36(b)). As can be seen in this figure the excited state consists of several peaks almost 2 orders of magnitude more intense than the ground state transition. It is so although the excitation power is not much higher than the saturation power of the QD neutral excitonic transition. We attribute this effect to the emission suppression due to decreased transition dipole moment due to decreased electron-hole overlap at high internal electrical field.

The temporal evolution of this structure could be divided in three parts. During the first 28 s the QD emission lines jumped across several discrete energy levels. Then in between 28 and 44 s the QD emission energy varied in a smooth manner and finally stabilized after 44 s. After stabilization the spectral diffusion processes could not be recovered without sample heating up to the room temperature and cooling down in the darkness. Remarkably, during continuous variation of the emission energy that is between 28 and 42 s the ground state excitonic line X_0 and excited state line X_5 shifted towards higher energy side while excited state lines X_{1-4} were synchronously red shifted.
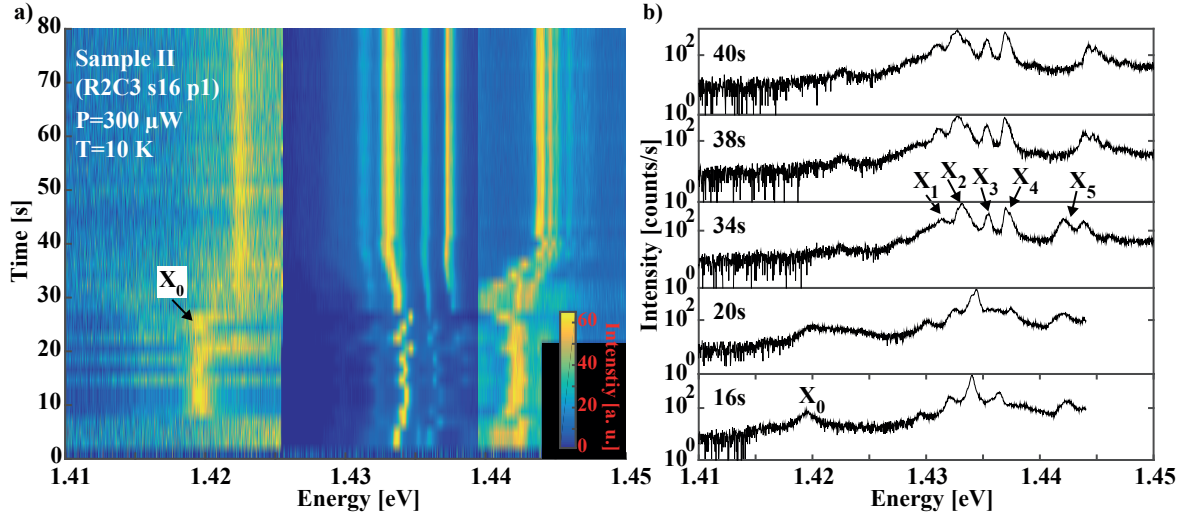
Figure 3:36 Image of spectral dynamics (a) and spectra (b) revealing opposite energy shift of different spectral features of the same QD (sample II).

Blue shift of the emission line X_5 is well visible in Figure 3:37(a) showing peak energies of the excited state lines X_{1-5}. Emission line X_5 shifted towards higher energies by ~4 meV while lower energy states are shifted to the lower energy side only by ~0.85 meV. Thus, the effect of the band tilting due to the electrical field created by some charge centres in the proximity of the QD is much smaller than the reduction of the Coulomb attraction energy. Figure 3:37(b) shows temporal evolution of the energy separation between X_4 and X_5 lines that increased nearly linearly from 2.6 meV to 7 meV. We did not find any experimental report of comparable energy shifts appearing in the spectral diffusion process or in the usual QCSE of a QD in the vertical or lateral electric fields. The value of the blue shift of excitonic transitions significantly increases for bigger QDs as reported in [156] therefore anomalously big blue shifts observed in our QDs could be explained by bigger pyramidal QD size in comparison with a size of typically used self-assembled QDs.
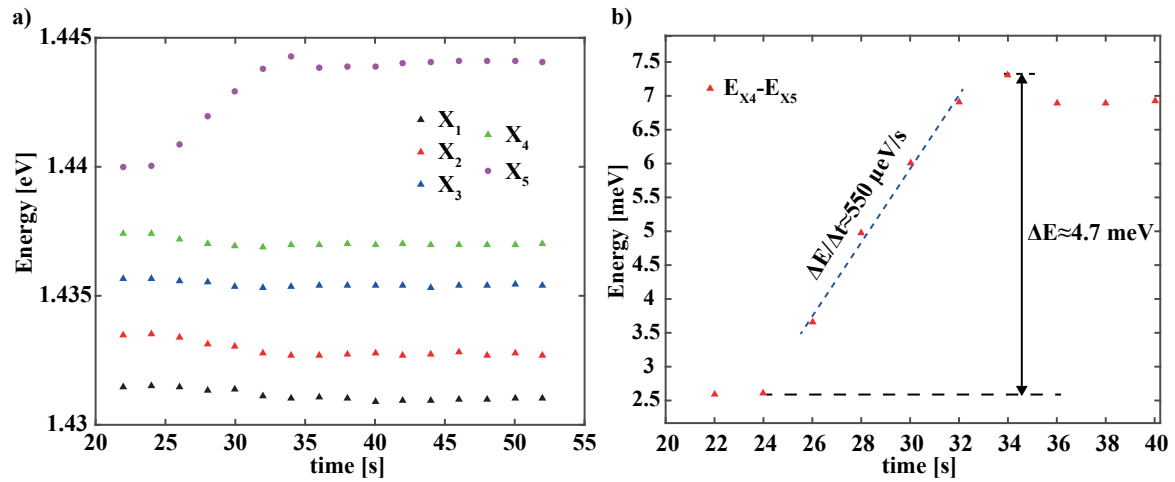
Figure 3:37 Peak energy of emission lines of sample II (a) and change in energy separation between X_4 and X_{exc} lines (b).

It should be noticed that in this structure the QD is nominally shifted by 180 nm from the L3 PhC cavity center. Design size of PhC holes is the smallest used for devices implemented on this chip. Thus, the distance between the QD and PhC hole surfaces is one of the biggest among all devices. However, this structure revealed very pronounced spectral diffusion. Thus, we discard PhC hole surface field induced spectral diffusion as the possible explanation of observed phenomena.

3.6   Coupling of a spectrally diffusing QD exciton and an optical cavity mode

An excitonic transition can be brought into resonance with a CM using temperature variation of the exciton-CM detuning, varying the CM energy by a gas condensation in the PhC holes, or by using the QCSE[161], [162]. Taking into advantage the built-in electric field leading to the spectral diffusion of the QD exciton complexes, we are able to scan a CM by an exciton transition. For this purpose we identified two structures that have a long living spectral diffusion of the exciton transitions in the vicinity of the CM. Figure 3:38(a, b) shows images of slow dynamics revealing the spectral diffusion of excitonic transitions in the vicinity of an L3 PhC cavity mode. These images were obtained from consecutive spectral measurements in two different devices containing QDs shifted by 180 nm (a) and 120 nm (b) from the center of an L3 PhC cavity.
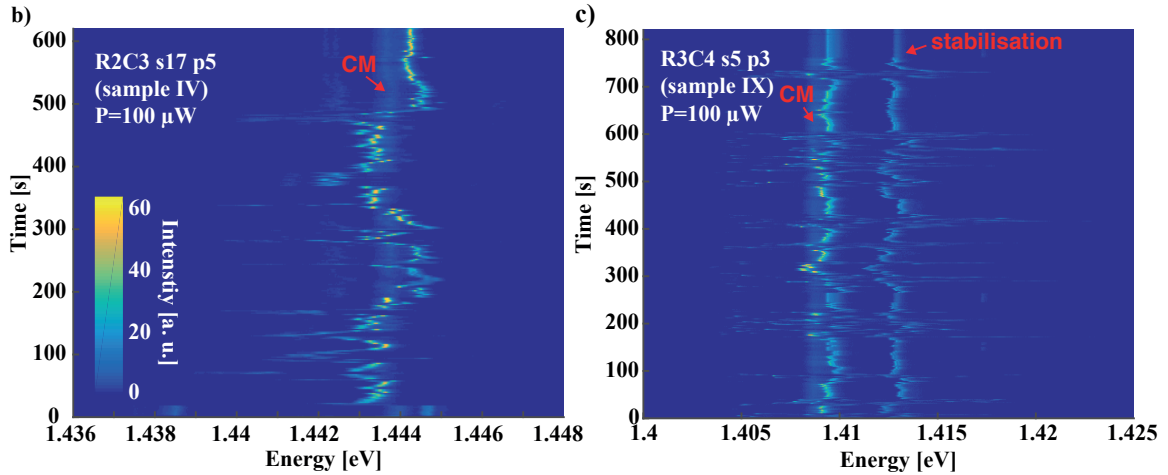
Figure 3:38 Images of spectral diffusion measured in structures having a neutral excitonic transition coupled with an optical cavity mode.

In both structures we identified a QD transition in the vicinity of the CM as a neutral exciton due to well resolved FSS splitting, as can be seen in a set of spectra shown in Figure 3:39. In Figure 3:39(a) the most intense line is the neutral exciton while in Figure 3:39(b) both neutral exciton and biexciton transitions have comparable intensities. In both structures detuning between the CM and the neutral exciton transition varied by ~1 meV. Thus, we were able to probe the exciton-CM coupling without changing semiconductor lattice temperature, gas condensation or an implementation of complicated heterostructures for the QCSE. We identified cavity mode observed in samples IV (Figure 3:39(a)) as the first excited CM, that is CM1, while in another sample excitonic transition was coupled with the ground state CM0 (Figure 3:39(b)). FWHM of CM0 and CM1 were ~0.95 meV and ~0.75 meV correspondingly.
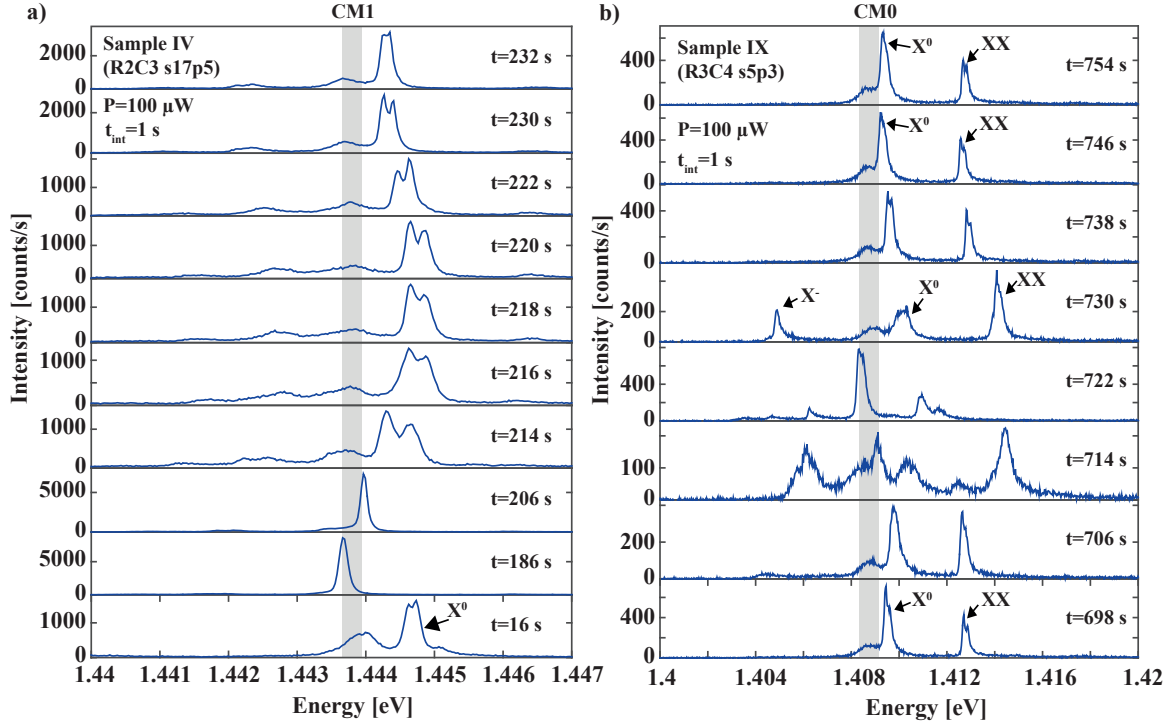
Figure 3:39 Spectra of 2 structures showing energy variation of neutral exciton (a) and both neutral exciton and biexciton (b). In both cases neutral excitonic line crosses different CMs of an L3 PhC cavity.

In order to probe exciton-CM coupling we chose spectra that show neutral excitonic lines with FWHM lower than 250 µeV. Then intensity traces of neutral exciton and biexciton transitions were obtained integrating emission of these lines in a 500 µeV spectral window centered at the corresponding line peak position. We also used normalization factor $\alpha = (500\ \mu eV)/(27\ \mu eV)$ equal to the ratio between spectral window and an energy interval corresponding to a single pixel of our CCD detector. Bottom panels of Figure 3:40(a, b) show integrated intensity obtained for the main transitions visible in Figure 3:39. These integrated intensity traces clearly show neutral exciton intensity enhancement appearing when its energy is in resonance with the CM. It should be noticed that the integrated intensity of the biexciton decreases when the neutral exciton is tuned in resonance with the CM in Figure 3:40(b).

Intensity enhancement is a consequence of light redirection in the objective through CM and interplay between excitation and emission rates. Emission of the neutral exciton detuned from a CM is close to saturation at excitation power used in this experiment (P=100 µW), that is, exciton pumping rate is of the order of off-resonant excitonic emission rate. While tuned in resonance neutral exciton emission rate increases by several times due to Purcell enhancement. Thus, the exciton is not saturated anymore and its measured intensity increases. Due to the same effect biexcitonic emission slightly decreased when neutral exciton shifts in resonant with the CM (Figure 3:40(b)). That is due to lower probability of forming biexcitons in the QD at higher neutral exciton emission rates.
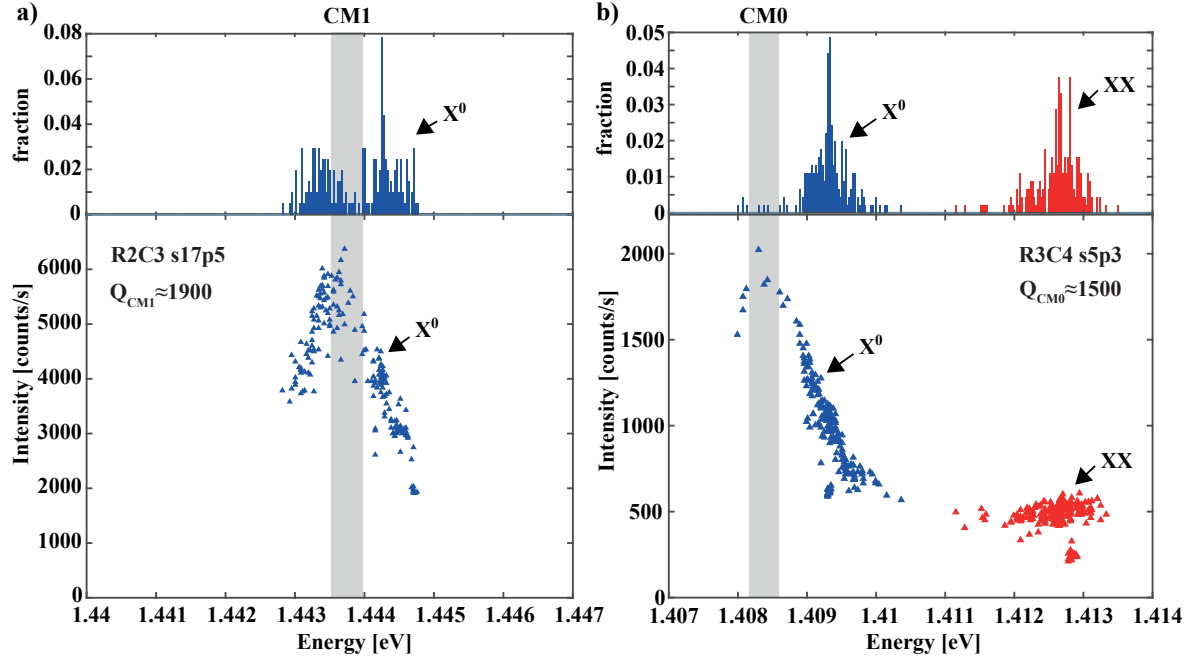
Figure 3:40 The exciton coupling with CM1 (a) and CM0 (b) scanned by spectrally fluctuating QD excitonic line for 2 different structures. Intensity points (bottom) are obtained through integration of excitonic line in a 500 μeV energy window. Center of integration region is the line peak energy. Corresponding emission energy statistics is shown in the top part.

Histograms shown in top panels of Figure 3:40 show statistics of appearance of the main emission lines in consecutively measured emission spectra. In a) and b) excitonic transition appear in resonance less frequently leading to just a few points in these histograms. In Figure 3:40(a) a clear antibunching of the neutral exciton and the cavity mode emission energies is observed. At first sight, neutral exciton energy fluctuations should not be connected with an influence of the CM. However, this antibunching can appear due to an influence of the CM on an average QD occupation with an electron-hole pair. Several groups recently reported an observation of two different types of QD environment charging during investigation of colloidal QD blinking[154], [163]. In colloidal QDs the first type of blinking happened due to charging/discharging of the QD core while the second type appeared due to surface charge fluctuations. In analogy, charge traps in the QD environment can be populated either by the carriers excited in the bulk GaAs or by the carriers captured in the QD[100]. In the case of population with QD captured carriers, efficiency of this process significantly depends on the average time of the QD occupation with an electron-hole pair that depends on the emission rate of the QD.

When the neutral exciton overlaps with the CM its emission rate is significantly enhanced due to Purcell effect, reducing the average QD occupation with the electron-hole pair. Thus, an average occupation of the QD significantly depends on the exciton-CM detuning conditions. If this mechanism takes place then excitonic emission energy evolves as following. The neutral exciton energy drops to the values specific to the lower excitation power each time when the neutral exciton overlaps with the CM. If by accident charging of the trap is enough to overpass CM, then fluctuations

will continue at the other energy side of the CM till the moment when the neutral exciton will again overlap with the CM.
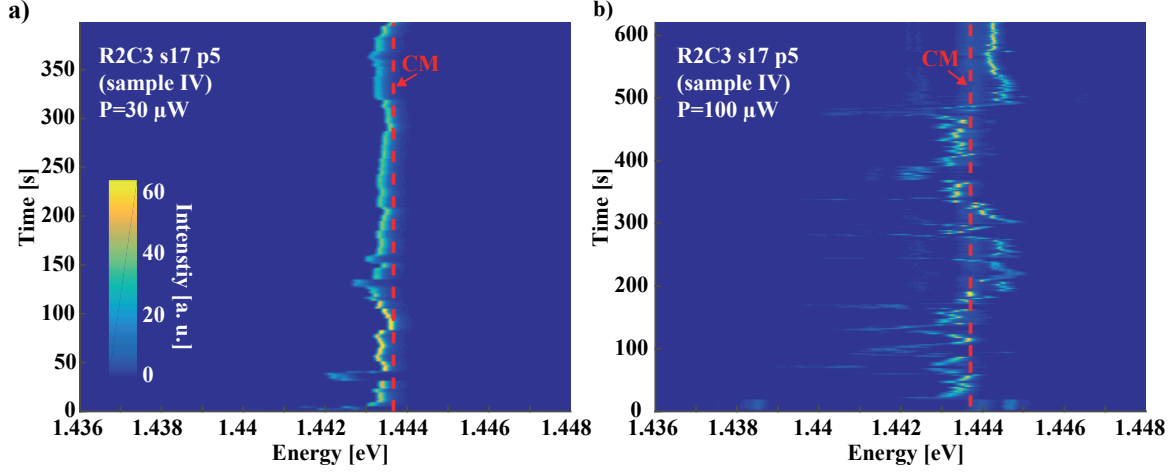
Figure 3:41 Images of neutral exciton spectral diffusion in the vicinity of the CM measured at two excitation powers, that is, 30 µW in a) and 100 µW in b). CM position is shown by red dashed line broken at the positions where neutral exciton time-energy traces overlap with it.

Indeed, spectral diffusion of the neutral exciton behaves according to the model described above. Figure 3:41(a, b) shows spectral diffusion of the neutral exciton measured at two different excitation powers. In a) excitation power is ~3 times lower than the saturation level of the QD exciton while in b) excitation power P=100 µW corresponds to the saturation level of a typical QD in this sample. Already at this point it should be noticed that increase in amplitude of the energy fluctuations correlates with the excitation power corresponding to a nearly unity occupation of the QD with an electron-hole pair. In Figure 3:41(b) at each time point where neutral exciton overlaps with the CM the neutral exciton energy drops to the average energy values typical for the lower excitation power, that is, to the neutral exciton energies shown in Figure 3:41(a). Energy fluctuations in vicinity of this position form the red side bunch in the histogram shown in Figure 3:40(a). Blue side bunch visible in this histogram is formed in case if an amount of charge trapped in the QD environment is enough to shift neutral exciton to the blue side of the CM, in other words, for overpassing CM by neutral exciton. In this case the emission rate of the neutral exciton is sufficiently low for sustaining high average QD population and therefore QD environment is efficiently charged. If the neutral exciton is shifted in resonance with the CM then the emission rate increases again and the neutral exciton energy drops again to the red energy side of the CM. Thus, antibunching of the spectrally diffusing neutral exciton and the CM can be fully explained by the charge traps in the QD environment predominantly populated by the electron-hole pairs captured in the QD.

3.7   Emission intermittency of site-controlled pyramidal QD

Besides spectral diffusion we also observed emission intermittency in pyramidal QD emission. This effect was also accompanied by the excitonic spectral diffusion. In this structure we also observed the biggest absolute shift of a single excitonic transition (Figure 3:42). In a) and b) two stages of QD ground state emission are shown. During the dark stage that happened during the first ~40 s no

QD excitonic lines are observed except a single event as can be seen in the spectrum measured at t=8 s in Figure 3:42(a). A very wide background continuing from 1.435 eV to higher energies is visible with QWR emission line at the 1.478 eV.
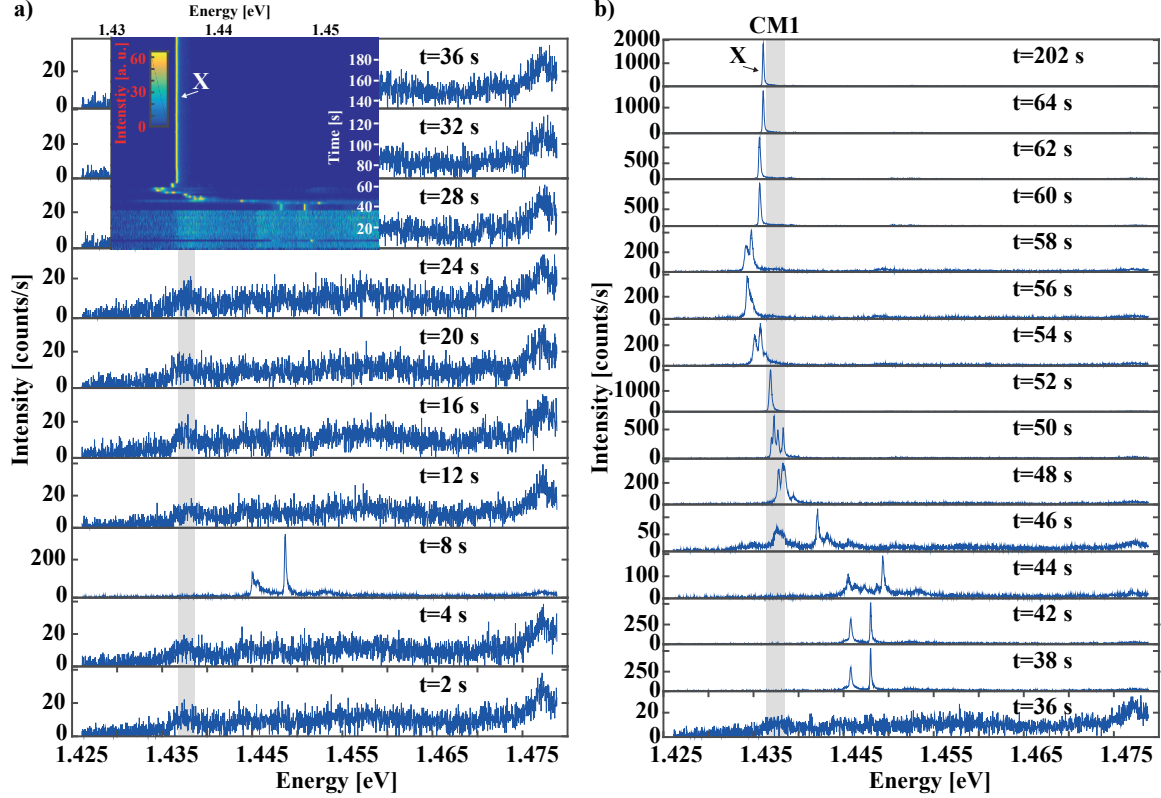
Figure 3:42 Time-delayed ignition of QD luminescence. In a) and b) spectra are taken during dark and bright emission regimes correspondingly. Image of spectral dynamics for this structure is shown in an insert in a). Measurements were provided at 10 K.

At the bright stage, narrow lines accidentally appear in the emission spectra (Figure 3:42(b)). Between $t = 38\ s$ and $t = 42\ s$ time points QD emission remained unchanged but then started to shift to the lower energy side. These energy shifts were discrete as can be concluded from emission spectra taken at $t = 44 - 50\ s$. In these spectra several narrow lines are visible, probably due to the accumulation of several line jumps during the spectrometer integration time $t_{int} = 1\ s$. Jumps of the emission line between discrete energy levels are also confirmed by the narrow linewidth observed in the spectra during the energy shifts of emission lines. Continuous spectral diffusion would lead to smearing of the emission lines to a width of ~1 meV, as the energy shift was ~1 meV per 1 s ($\Delta E/\Delta t \approx 1$ meV/s) and integration time was 1 s. During the spectral diffusion process, the emission line is shifted by ~15 meV to the lower energy side and then stabilises after ~2 meV shift backwards to higher energies. Remarkably, spectral diffusion is stops after $t = 64\ s$ with no emission line spectral diffusion observed afterwards. This spectrum stabilization is irreversible at the low temperature but can be recovered through sample heating up to room temperature and cooling down to the temperatures appropriate for PL measurements.
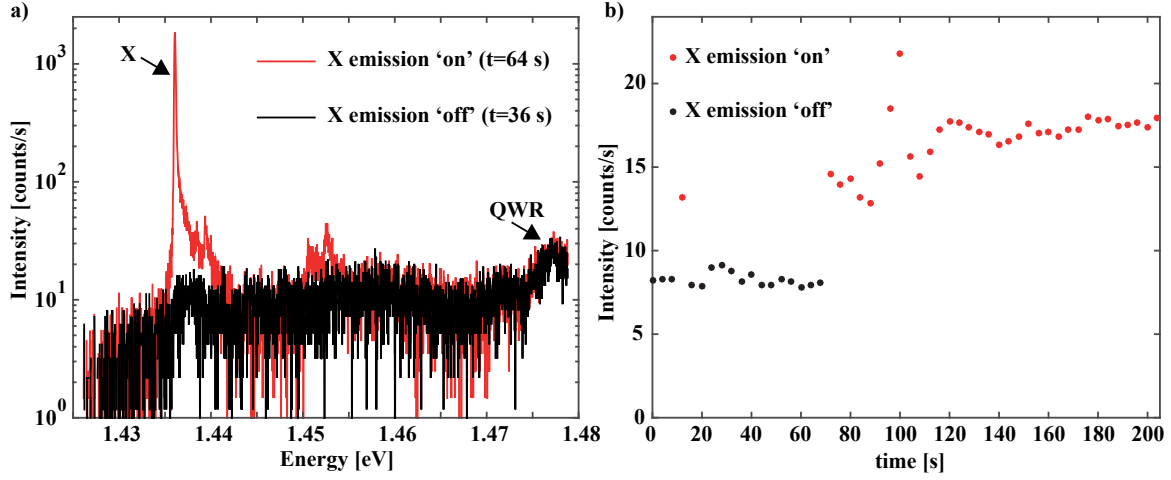
Figure 3:43 Spectra showing 'off' and 'on' QD emission regimes (a) and integrated intensity over the *whole* measured spectral region as a function of time (b). The background is mainly defined by the CCD dark noise since only a constant noise corresponding to the intensity at 1.425 eV was extracted.

Figure 3:43(a) shows two emission spectra corresponding to the dark and bright emission stages. Background and QWR emission nicely overlapped in both spectra. Therefore the processes leading to the QD blinking and spectral diffusion do not affect QWR emission. The independence of the QD spectral diffusion processes from the background and QWR emission is also confirmed by the total emission intensity. Figure 3:43(b) shows intensity integrated over the *whole* measured spectral region $\Delta E = 52.6$ meV with $\alpha = (\Delta E \, [\mu eV])/(27 \, [\mu eV])$ normalization factor. We observed a significant increase of integrated intensity in the bright region even though the QD emission line has a very narrow peak with FWHM $= 160 \, \mu eV$ that is negligible in comparison with the integration window. Thus, this background emission appears due to mechanisms different from the fast spectral diffusion of the QD emission line.

Blinking observed in this device can be explained by suppression of the QD trapping of electrons or holes. Thus, during the dark period, carriers can escape from the QD only through nonradiative decay channels. An explanation of the following exciton redshift is not yet clear for us. If we assume that charges in the environment were compensated by photo-excited impurities leading to the reduction of the electrical field at the QD position, then the red shift of excitonic transitions during the bright period can be hardly understood.

Although the red shift can be due to reversed blue shift with increasing field due to competing band-tilting and the Coulomb attraction energy, its value is limited to a few meV for a reasonable QD size ~20 nm[156]. Increasing electrical field with time would explain the red shift of the QD excitonic emission but then mechanisms of the QD emission suppression are not clear as in this picture the dark stage of the QD emission corresponds to the lowest electrical field values.

As a conclusion it is worth to notice that if this structure was exposed to any light during cooling or alignment processes then no blinking or spectral diffusion could be observed. Therefore we can predict a strong variation of the fraction of the QDs with slow dynamics processes depending on the

level of the scattered light inside the cryostat. This cannot be completely avoided, as the position of the sample in respect with collecting objective should be at least once controlled with optical camera.

3.8   Conclusion

In this chapter, we described the optical properties of the QD isolated with an L3 PhC cavity. We first presented a novel technique for QD spectral isolation using unique energy control of the QDs grown in the pyramidal recesses of different sizes. We then considered the possible effect of an internal electrical field on the inhomogeneous broadening of a QD ensemble emission as well as on the individual QD excitonic linewidth. We next presented evidence for strong electric field fluctuations in the QD environment, due to fabrication imperfections, leading to spectral diffusion and emission intermittency. These processes, observed in QD-PhC structures, revealed non-trivial transition dynamics between several charged states. Remarkably, we were able to show that the charge centers causing slow dynamics processes should either be a single charge center with a possibility of multicharging, or several interacting charge centers. Additionally, we highlighted the importance of the experiment preparation procedure for the investigation of the slow dynamics processes: in particular, the influence of light exposure on the QD spectral diffusion and emission intermittency.

Chapter 4   Coupling of single site-controlled quantum dot to a photonic crystal cavity

4.1   Introduction

Proportional to the exciton-CM overlap, the coupling strength significantly varies with the QD position in the PhC cavity due to the spatial inhomogeneity of the CM electric field pattern. In particular, the intensity of the central lobe of the lowest energy L3 PhC CM has FWHM ~100 nm. Thus, the QD positioning precision should be around a few tens of nanometers for QD overlap with at least 80 % of the CM electrical field maximum. Different groups succeeded in achieving such a precision with self-assembled QD using post growth positioning methods that allowed achieving strong coupling light-matter interaction regime [6], single photon source[164], [165], entangled photon source[38] and macroscopic photon polarization rotation [166].

Scalable QD-based systems need QDs with both site- and energy-control, which is achievable with our pyramidal QDs. It was shown that site-control of our QDs allows alignment precision down to ~15 nm ensuring excellent CM-exciton coupling strength [72] together with high spectral reproducibility [25]. Those studies permitted the observation of deterministic weak coupling of single QDs with PhC CMs, manifested by co-polarization and intensity enhancement effects on the QD emission [167].

Taking into account the limitations and advantages of our system, we found that it is extremely useful for probing the CM electric field spatial distribution. The site-controlled QD serves as a point-like dipole probe similar to a scanning near-field microscopy (SNOM) tip that allows directly probing the near-field pattern of the optical mode of a single PhC cavity [168] or the hybridized mode of two coupled PhC cavities [169]. For probing the CM electric field distribution, a first experiment one could think about is probing of the maxima and minima of the CM electric field. This could be achieved by comparison of the exciton-CM interaction in the system with a single QD placed in the maxima of the CM electric field or its nodes. The QD positioning with zero CM overlap is in fact more ambitious to achieve than positioning at the CM maxima because of the small extension of the CM node and the finite size of the QD. At the same time, probing the position of the CM node is of high interest for separating effects induced by the CM and surrounding photonic environment, as well as for comparing experimental and theoretical CM field patterns.

Here we demonstrate how the CM field antinodes as well as the CM zero field point could be probed using the site- and energy-control of our pyramidal QD system. Using polarization-resolved measurements of devices with differently positioned QDs we were able to observe significant variations in the co-polarization effect of our QD excitonic emission, which reflects variations in the exciton-CM coupling strength. Interestingly, we observed Fano resonance effects in the emission of the QD in PhC cavities that can be completely suppressed by shifting the QD into the CM node.

4.2   Integration of QD - PhC L3 cavity structure

4.2.1   Structure design and implementation

Our design for probing exciton-mode coupling consists of a single QD deterministically positioned inside an L3 PhC cavity. We chose specific 5 QD positions that correspond to different overlaps between the QD and an electric field pattern of the ground state CM0. This optical mode has the highest overlap with the QD positioned at the center of the L3 PhC cavity (Figure 4:1(a)). As can be seen in the same figure, other high QD-CM0 coupling points are the side CM antinodes that are shifted by ~180 nm from the center of the PhC cavity. Overlap between CM0 and QD shifted by Δ~90 nm with respect to the center is nearly zero (Figure 4:1(b)). Thus, devices with Δ=0 nm and Δ=180 nm shifted QDs are suited for probing the main maxima of the CM0 electrical field while devices with Δ=90 nm shifted QD serve for probing the CM0 node. We also implemented QDs shifted by Δ=60 nm and Δ=120 nm for probing intermediate QD-CM0 overlaps (Figure 4:1(b)).

L3 PhC CM electrical field pattern shown in Figure 4:1 was calculated using the finite-difference method [170] by Clement Jarlov. The electromagnetic field is calculated only for the symmetry plane of the PhC slab, that is, at the half of the membrane height. Calculations were limited only to a 2D plane. Finite thickness of the slab was taken into account using an effective dielectric constant $\epsilon_{eff}(r)$ at the symmetry plane, which is approximated by calculating the effective index of TE modes guided by 1D slab with the same thickness as the PhC slab[171].

The same structures can be used for probing QD-CM1 overlaps. The first excited CM1 has nearly zero overlap with QD positioned at the center of the PhC cavity (Figure 4:1(a)) while devices with Δ=60 nm, Δ=90 nm and Δ=180 nm shifted QD show intermediate values of the QD-CM1 overlap (Figure 4:1(a, b)). The QD shifted by Δ=120 nm is still not perfectly positioned at the second CM1 zero field point (Figure 4:1(b)). Thus, small fluctuations of the actual position of such QD and CM1 antinode positions can introduce enough QD-CM1 overlap for being indistinguishable from the intermediate overlap values that are expected for Δ=60 nm shifted QD.
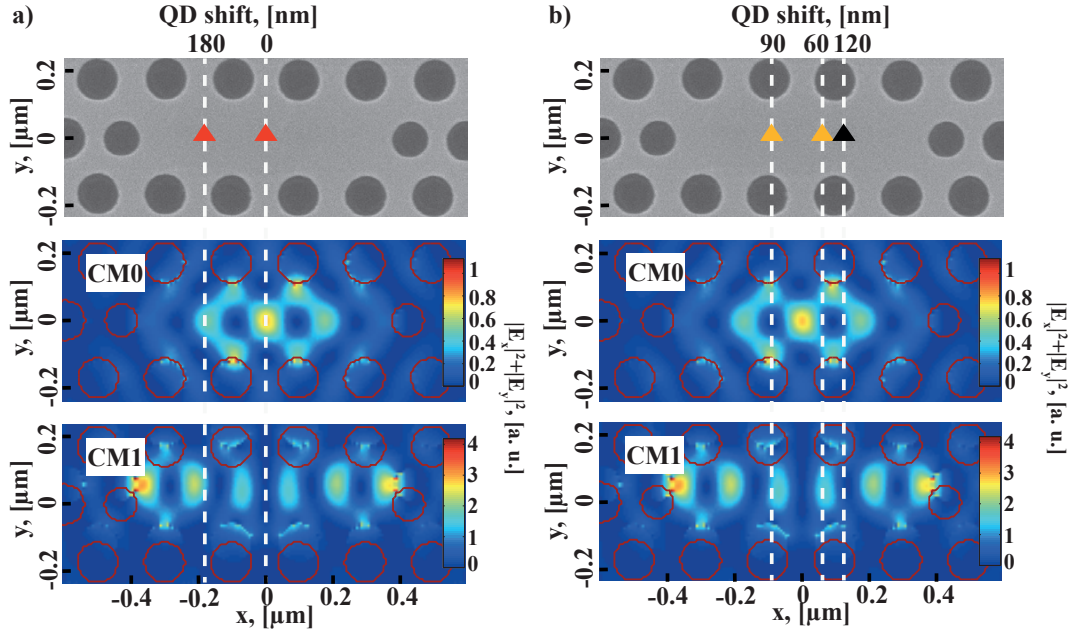
Figure 4:1 QDs with prescribed positions in a modified L3 PhC membrane cavity. SEM image with schematic QD positions (top panels), and calculated intensity patterns of the CM0 (center panel) and CM1 (bottom panel) modes. Different designs allow exploring the best and the worst QD-CM0 overlaps. For details describing calculation method see text.

Figure 4:2 shows the x and y E components of the CM0 and CM1 mode patterns. At the y/a=0 (a=200nm) in Figure 4:2(a, c), that is, the L3 PhC cavity horizontal symmetry axis, both CM0 and CM1 optical modes have zero E_x field component, therefore the electric field is oriented along the y axis Figure 4:2(b, d). Thus, the biggest coupling strength is achieved there between the CM and transitions with the biggest y dipole component (the QD exciton).
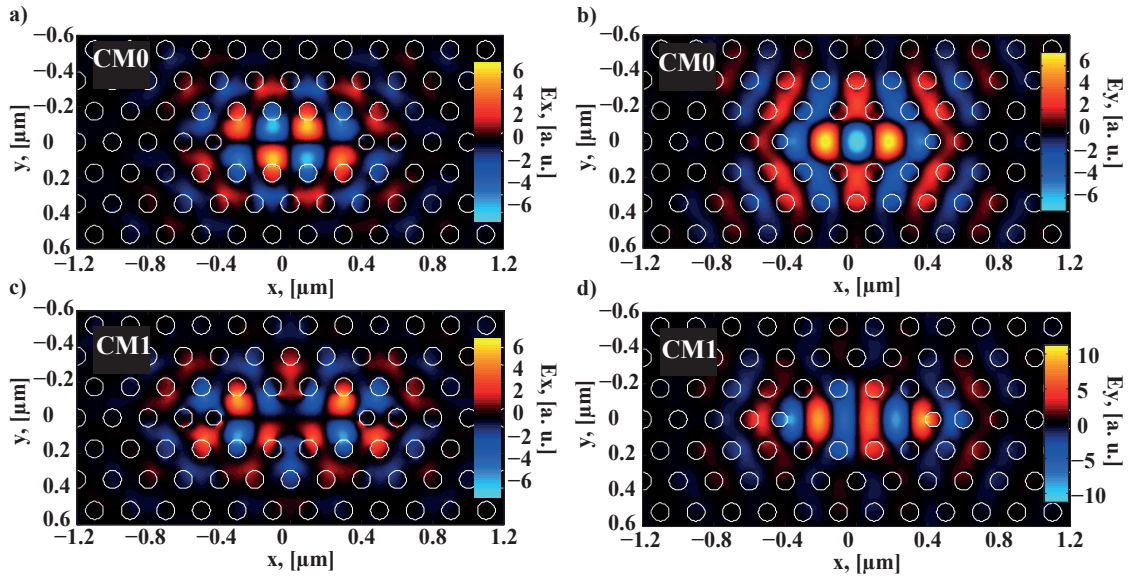
Figure 4:2 Ey and Ez field components distributions of the two lower energy level PhC cavity modes. Other parameters as in Figure 4:1.

4.2.2 Optical mode spectrum

Figure 4:3(a, b) shows the PL spectra of an L3 PhC cavity with a single QD shifted by 120 nm (a) and 60 nm (b). Peaks labeled CM0-3 are L3 PhC cavity peaks while other optical transitions visible in the spectra are excitonic transitions. These devices have different hole sizes thus allowing to couple different CMs with the s-state of the QD emission. The two lowest energy modes are vertically polarized (Figure 4:3(a)) separated by ~20 meV, thus their interaction with excitonic transitions can be considered independently, since exciton-CM coupling by phonon scattering processes extends to a ~3 meV coupling range [72]. The two higher energy modes (labeled CM2 and CM3) are vertically and horizontally polarized (Figure 4:3(b)), respectively. These two modes are separated by 10-15 meV and blue shifted from the CM1 of the device by ~40 meV. CM2 and CM3 modes can overlap spectrally at high energies (see Figure 4:3; the low Q factor of CM3 contributes to this overlap).

The vertically polarized modes show Q- factors of 1000-4000 while CM3 has Q-factor ~100, suggesting it is weakly confined. Exciton coupling to both CM2 and CM3 significantly complicates the interpretation of DOLP data, therefore we focus on modes CM0 and CM1. A more detailed study of the L3 PhC cavity mode structure with a single QD at delta=0 was presented by Milan Calic in his thesis [15].
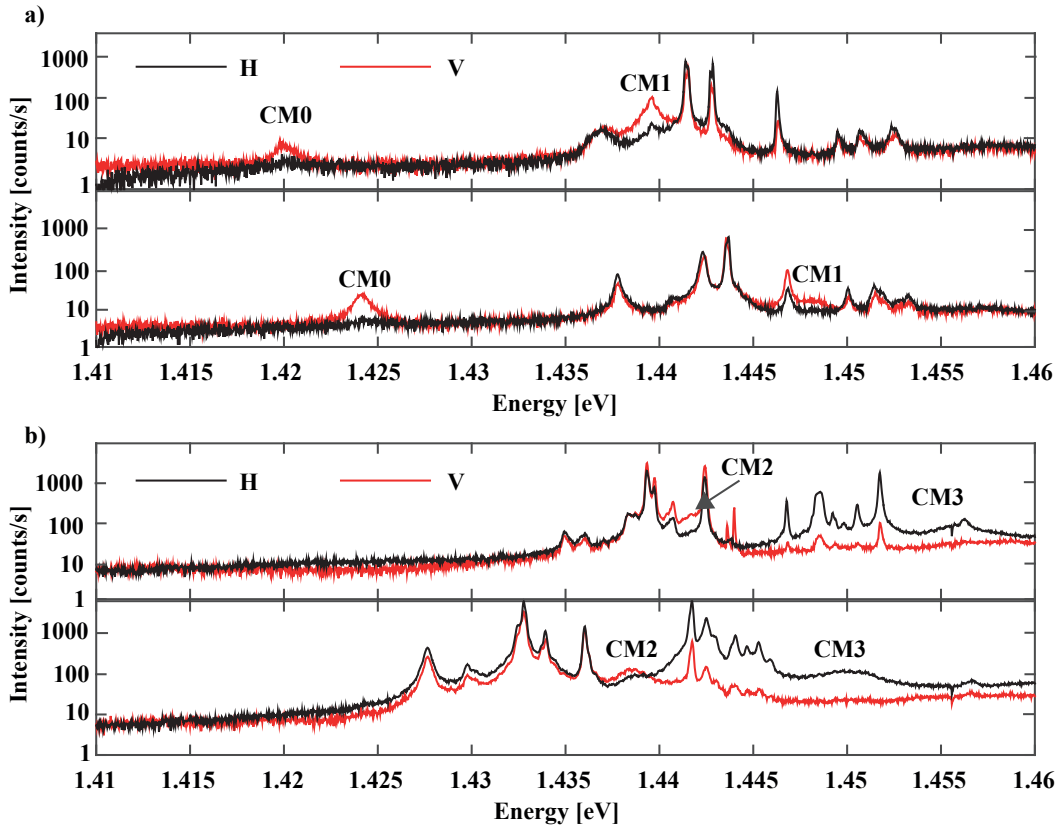
Figure 4:3 Polarization-resolved spectra showing the first 4 excited cavity modes: CM0 and CM1 in a) and CM2 and CM3 in b). Spectra in a) (b)) we obtained in devices with Δ=120 nm (Δ=60 nm) shifted QD and PhC hole radii r≈65 nm (r≈55 nm). T=10 K, 300 μW excitation power. No water deposition was applied.

Figure 4:4 shows the energy of the CM0 and CM1 resonances obtained from data as in Figure 4:3 for several tens of devices, as a function of the nominal PhC hole radius. The gray regions show the zone of QD ground state emission energy where probability of obtaining devices with ground state excitonic transitions coupled with CM0 or CM1 is high. We observed ~10 meV fluctuations in CM position energy corresponding to fluctuations of PhC hole diameter by ~2 nm due to fabrication imperfections.
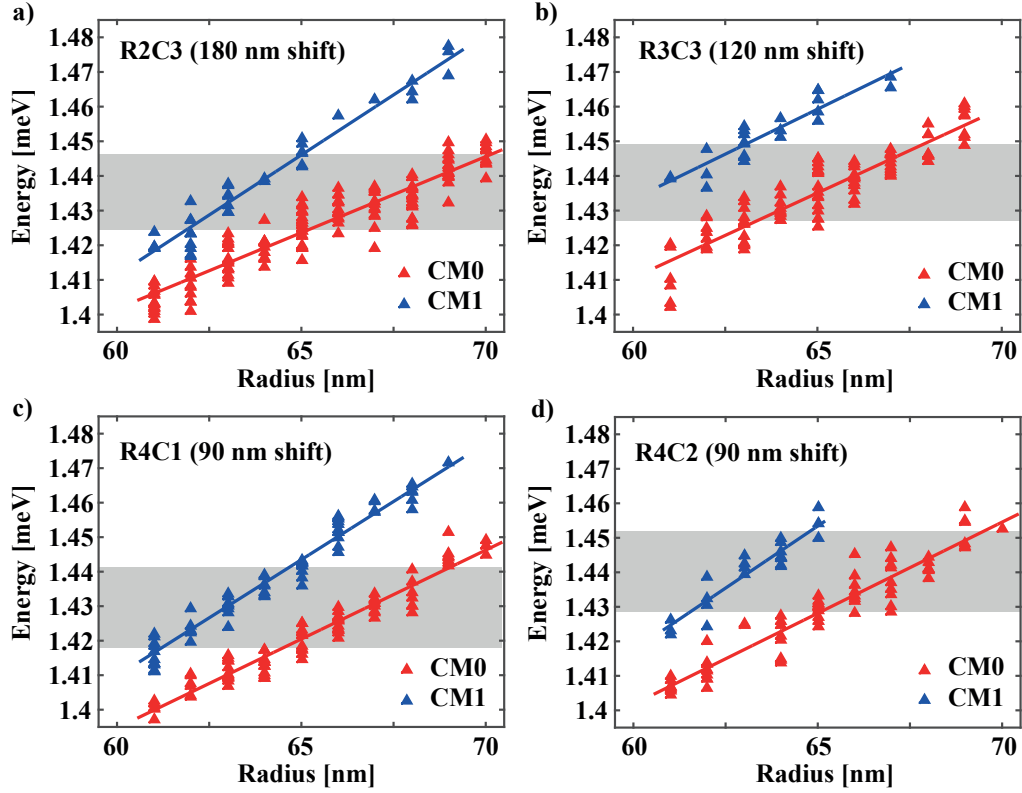
Figure 4:4 Measured energies of the two lowest energy TE cavity modes (CM0 and CM1) of the L3 PhC cavities versus (nominal) PhC hole radii for structures with different QD shifts.

The energy spacing between CM0 and CM1 slightly increases at higher PhC hole size (Figure 4:4). This effect is summarized in Figure 4:5. The lowest energy separation between CM0 and CM1 is ~15 meV, for the smallest hole sizes, still assuring independent coupling of an excitonic transitions to each of these two cavity modes (at least at low temperatures).
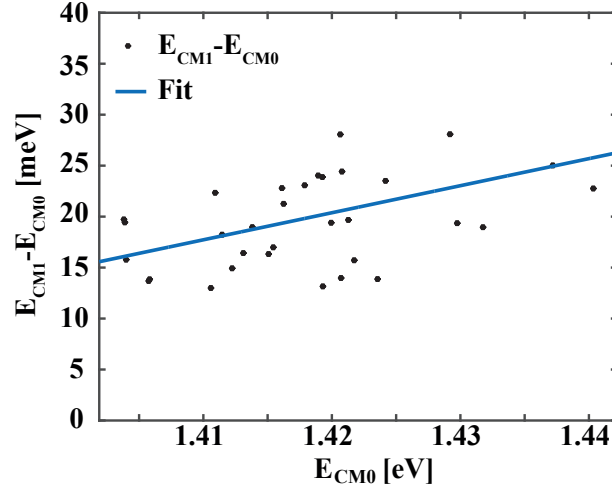
Figure 4:5 Measured energy spacing between the CM0 and CM1 modes, as function of CM0 energy. Data extracted from Figure 4:4(a).

4.3   Radiative coupling of QD-excitons and cavity modes

CM-exciton co-polarization effects observed when a QD excitonic transition is tuned near resonance with a CM are a good indication for CM-exciton weak coupling [72]. This effect appears due to predominant excitonic emission through the linearly polarized CM, because of both suppression of the vacuum optical density of states in the PhC bandgap and the high CM density of states. However, polarization of the excitonic transitions does not necessarily reflect the difference in the photon density of states of different optical modes. Here we discuss the case in which the polarization properties of the excitonic transitions can be used to map the photon density of states.

4.3.1   Charged and neutral QD excitonic transitions in inhomogeneous photonic environment

The main excitons observed in the samples discussed here are the charged exciton X^- with two electrons in the s-shell, the neutral (mainly heavy-hole) exciton X^0 and the biexciton XX (Figure 4:6(a, c); see also the discussion in 1.2.4 and Figure 1:6). We did not observe other transitions as excited charged exciton with one electron on the s-shell and another on the p-shell [172]. The number of different excitonic lines presented in the observed spectra remains low even at excitation powers one order of magnitude higher than the s-shell saturation power level, reflecting no formation of higher charged complexes.
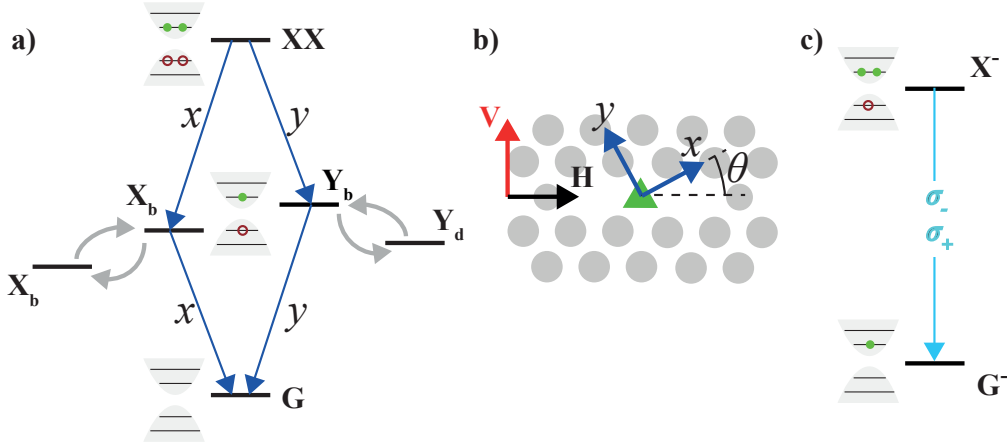
Figure 4:6 Biexction-exciton cascade (a), geometry of the neutral exciton transitions, polarization dipole directions (b) and charged exciton transition (c). Gray arrows in a) show transitions between neutral exciton dark (X_d, Y_d) and bright (X_b, Y_b)) states.

Optical transitions between the bright neutral exciton states $|X_b\rangle = \frac{1}{\sqrt{2}}(|-1\rangle - |-1\rangle)$ and $|Y_b\rangle = \frac{1}{\sqrt{2}}(|-1\rangle + |-1\rangle)$ and the ground state $|G\rangle = |0\rangle$ reveal a fine-structure splitting (FSS) that is ~100 µeV in the discussed samples. These transitions have linearly polarized dipoles $d_{X_b} = \frac{D_{X_b}}{\sqrt{2}}(e_H \cos\theta + e_V \sin\theta)$ and $d_{Y_b} = \frac{D_{Y_b}}{\sqrt{2}}(-e_H \sin\theta + e_V \cos\theta)$ as shown in Figure 4:6(b). Although we introduced different dipole moment amplitudes D_{X_b} and D_{Y_b}, polarization resolved measurements of our QDs reveal nearly equal emission intensities for both dipole orientations, indicating $D_{X_b} \approx D_{Y_b}$. Unity vectors $\{e_H, e_V\}$ are chosen as the two main symmetry axis of the PhC cavity (Figure 4:6(b)). By design e_V also points to the substrate surface misorientation direction. Angle θ is arbitrary in our structures although some devices revealed neutral exciton dipoles oriented exactly along $\{e_H, e_V\}$ axes.

The neutral exciton also has two dark excited states $|X_d\rangle = \frac{1}{\sqrt{2}}(|-2\rangle - |-2\rangle)$ and $|Y_d\rangle = \frac{1}{\sqrt{2}}(|-2\rangle + |-2\rangle)$. These states are shifted by ~500 µeV [16]from the bright exciton doublet, and have a fine structure splitting of ~1 µeV. Energy difference between the dark and bright excited states is smaller than the Boltzman energy $kT > 0.9\ meV$ at our $10 - 70\ K$ experimental temperature range. Therefore, the average occupation probabilities of $|X_d\rangle$, $|X_b\rangle$, $|Y_d\rangle$ and $|Y_b\rangle$ excitons are nearly equal. Transitions between these excitonic states are possible through spin flip processes[16].

Taking into account all four neutral excitons, the most general $|X^0\rangle$ state can be written as a superposition of two bright and two dark states

$$|X^0\rangle = a|X_b\rangle + b|Y_b\rangle + c|X_d\rangle + d|Y_d\rangle$$

with $|a|^2 + |b|^2 + |c|^2 + |d|^2 = 1$. All $|X_b\rangle$, $|Y_b\rangle$, $|X_d\rangle$ and $|Y_d\rangle$ states can decay through nonradiative decay channels while bright states $|X_b\rangle$ and $|Y_b\rangle$ can also do so through optical modes. Spontaneous emission rates Γ_{rx} and Γ_{ry} of the $|X_b\rangle$ and $|Y_b\rangle$ states can be different due to different D_{X_b} and D_{Y_b} dipole amplitudes as well as due to polarization dependent LDOS of the vacuum optical field.

Thus, the decay rate of the superposition state $|X^0\rangle$ can be estimated as $\Gamma_{nr} + |a|^2\Gamma_{rx} + |b|^2\Gamma_{ry}$. Here we assumed the same nonradiative decay rate Γ_{nr} for all four states [87]. Therefore, decay rate of the neutral excitonic transition can significantly depend on the absolute values of c and d phases. Here we also considered negligible effect of the spin flip processes on the emission rate of the $|X^0\rangle$ state.

Different Γ_{rx} and Γ_{ry} decay rates can significantly affect polarization of the neutral exciton emission and could be visible in the polarization-resolved PL measurements. We estimated this effect using the following rate equation:

$$\frac{\partial N_X}{\partial t} = -\left(\Gamma_{nr} + \Gamma_{rx}\cos^2\vartheta + \Gamma_{ry}\sin^2\vartheta\right)N_X + P(1 - N_X)$$

where N_X is the occupation number of the neutral exciton excited state and P is the pumping rate. The angle ϑ allows accounting for all different phases a and b. Solving this rate equation in the steady state regime we get the occupation number of the exciton excited state $N_X = \frac{P}{P + \Gamma_{nr} + \Gamma_{rx}\cos^2\vartheta + \Gamma_{ry}\sin^2\vartheta}$. Then the intensity of the emission through x and y polarized modes can be estimated as $I_x(\vartheta) = \frac{P\Gamma_{rx}\cos^2\vartheta}{P + \Gamma_{nr} + \Gamma_{rx}\cos^2\vartheta + \Gamma_{ry}\sin^2\vartheta}$ and $I_y(\vartheta) = \frac{P\Gamma_{ry}\sin^2\vartheta}{P + \Gamma_{nr} + \Gamma_{rx}\cos^2\vartheta + \Gamma_{ry}\sin^2\vartheta}$.

Intensities I_x and I_y are equal if the decay rate does not depend on the mode polarization. However, this changes in case of an inhomogeneous photonic environment leading to different decay rates $\Gamma_{rx} \neq \Gamma_{ry}$. Averaging over all possible angles we get $I_x = \frac{P\Gamma_{rx}}{\Gamma_{ry} - \Gamma_{rx}}\left(\sqrt{\frac{P + \Gamma_{nr} + \Gamma_{ry}}{P + \Gamma_{nr} + \Gamma_{rx}}} - 1\right)$ and $I_y = \frac{P\Gamma_{ry}}{\Gamma_{ry} - \Gamma_{rx}}\left(1 - \sqrt{\frac{P + \Gamma_{nr} + \Gamma_{rx}}{P + \Gamma_{nr} + \Gamma_{ry}}}\right)$. Then the degree of linear polarization $DOLP = \frac{I_y - I_x}{I_y + I_x}$ strongly depends on the excitation power:

$$DOLP = \frac{\Gamma_{ry} + \Gamma_{rx} - \Gamma_{ry}\sqrt{\frac{P + \Gamma_{nr} + \Gamma_{rx}}{P + \Gamma_{nr} + \Gamma_{ry}}} - \Gamma_{rx}\sqrt{\frac{P + \Gamma_{nr} + \Gamma_{ry}}{P + \Gamma_{nr} + \Gamma_{rx}}}}{\Gamma_{ry} - \Gamma_{rx} - \Gamma_{ry}\sqrt{\frac{P + \Gamma_{nr} + \Gamma_{rx}}{P + \Gamma_{nr} + \Gamma_{ry}}} + \Gamma_{rx}\sqrt{\frac{P + \Gamma_{nr} + \Gamma_{ry}}{P + \Gamma_{nr} + \Gamma_{rx}}}}$$

At very low excitation power we get $DOLP_{min} \approx 0$ while at the high pumping rate limit $P \gg \Gamma_{rx}, \Gamma_{ry}, \Gamma_{nr}$ we get the highest (and power-independent) linear polarization with $DOLP_{max} = \frac{\Gamma_{rx} - \Gamma_{ry}}{\Gamma_{rx} + \Gamma_{ry}}$. Indeed, with increasing excitation power the states with lower decay rate will be saturated while emission intensity of the states with higher decay rate will continue to increase leading to growing linear polarization of neutral exciton emission.

It should be noted that the presence of the biexcitonic complex changes the polarization of the neutral excitation since it could decay with different probabilities to the different exciton FSS complexes in the inhomogeneous photonic environment. However, this model provides good qualitative description of the neutral exciton polarization at different pumping rates. Thus, we get qualitative measure of the local density of states using neutral exciton polarization at high pumping rate limit if dipole amplitudes D_{X_b} and D_{Y_b} are equal.

In contrast to the neutral exciton, the charged excitonic transition has two-fold degenerate excited states $\left|\pm\frac{3}{2}\right\rangle$ and ground states $\left|\pm\frac{1}{2}\right\rangle$. Only transitions $\left|\frac{3}{2}\right\rangle \rightarrow \left|\frac{1}{2}\right\rangle$ and $\left|-\frac{3}{2}\right\rangle \rightarrow \left|-\frac{1}{2}\right\rangle$ are possible due to optical selection rules. These transitions have dipoles $d_L = \frac{D_{X^-}}{\sqrt{2}}(e_H \cos\theta - ie_V \sin\theta)$ and $d_R = \frac{D_{X^-}}{\sqrt{2}}(e_H \cos\theta + ie_V \sin\theta)$ with nonvanishing complex phase resulting in the emission of left and right circularly polarized photons in the homogeneous photonic environment. The charged exciton excited state can be written as $|e\rangle = a\left|\frac{3}{2}\right\rangle + b\left|-\frac{3}{2}\right\rangle$ where $|a|^2 + |b|^2 = 1$. Decay rate from this state to the ground state is $\Gamma_{nr} + \frac{|a|^2 + |b|^2}{2}\Gamma_{rx} + \frac{|a|^2 + |b|^2}{2}\Gamma_{ry} = \Gamma_{nr} + \frac{1}{2}(\Gamma_{rx} + \Gamma_{ry})$ where Γ_{nr} is non-radiative decay rate of the charged exciton, Γ_{rx} and Γ_{ry} are emission rates through the two optical modes polarized along arbitrary left oriented pair of unity vectors $\{e_x, e_y\}$.

Thus, the charged exciton has the single decay rate independent on the excited state prepared in the QD. This decouples polarization of the charged excitonic emission from the QD excitation rate since the saturation power of the charged excitonic transitions does not depend on the particular state $a\left|\frac{3}{2}\right\rangle + b\left|-\frac{3}{2}\right\rangle$. Using the rate equation model described above we get $I_x = \frac{P\Gamma_{rx}}{P + \Gamma_{nr} + \Gamma_{rx} + \Gamma_{ry}}$ and $I_y = \frac{P\Gamma_{ry}}{P + \Gamma_{nr} + \Gamma_{rx} + \Gamma_{ry}}$ providing $DOLP = \frac{\Gamma_{ry} - \Gamma_{rx}}{\Gamma_{ry} + \Gamma_{rx}}$. Since the charged exciton transitions have the single dipole amplitude D_{X^-}, its polarization directly reflects the LDOS of the optical modes. We should also note that in the real experiment the collection efficiency of emission through different modes can vary providing $DOLP = \frac{\alpha\Gamma_{ry} - \Gamma_{rx}}{\alpha\Gamma_{ry} + \Gamma_{rx}}$ with rate α between y and x polarized mode collection efficiencies. However, this rate is usually close to one ($\alpha \approx 1$).

4.3.2 CM interaction with charged and neutral excitons

We considered in the section 4.3.1 the decay through optical modes with spectrally broad density of states. However, in cavities the LDOS is strongly frequency-dependent near resonance. In this case, one should consider the CM optical field as a quantum state, and the exciton-CM interaction can be described using the Jaynes-Cumming model. This model conserves the number of excitations in the system, that is, only transitions between the states $|m\rangle_X |n-1\rangle_{ph}$ and $|m-1\rangle_X |n\rangle_{ph}$ are possible. Here m and n are Fock states of the exciton and photon modes. For example, charged (neutral) exciton and charged (neutral) biexciton correspond to the $|1\rangle$ and $|2\rangle$ number states. We can limit the considered exciton modes to $|0\rangle$ and $|1\rangle$ states if the biexciton and other multiparticle complexes are far detuned in energy from the exciton and CM transitions thus providing negligible coupling with the CM. This condition is always satisfied for charged exciton while it is often broken for neutral exciton because the neutral exciton to neutral biexciton energy separation is ~0.1-2 meV in our QDs [173], that is, much less than the exciton-CM phonon coupling strength and quite often of the order of the CM linewidth.

In order to clarify the influence of the biexcitonic transition we can use the low pumping excitation regime, that is, the average occupation of the CM and exciton is $\ll 1$. This corresponds to pumping rate $P \ll \kappa, \gamma$ where κ is the CM dissipation rate and γ is the lowest decay rate of the excitonic state $|X^0\rangle$. Taking into account much faster CM dissipation rate $\kappa \gg \gamma$ we limit the pumping rate by the

decay rate of the dark exciton state defined by the nonradiative dissipation rate γ_{nr}. For our QDs, the nonradiative decay rate is estimated as $\gamma_{nr} \approx 0.3~\mu eV$ for the temperature range ~10-40 K.

We start the analysis of the exciton-CM interaction with the charged exciton complex. This transition is well isolated from all other QD complexes including the neutral exciton. The exciton-CM coupling strength can be written as $g = \sqrt{\frac{\hbar\omega_{CM}}{2\epsilon_0 V}}\Phi_k(\vec{r})\vec{d}\cdot\vec{\xi}(\vec{r})$[15] where $\Phi_k(\vec{r})$ is the cavity field wavefunction, $\vec{d}$ the exciton dipole moment, $\vec{\xi}(\vec{r})$ a unit vector along the polarization of the CM field at the position of the dipole, and V is the effective mode volume. The orientation $\vec{\xi}(\vec{r})$ of the CM electric field can vary significantly depending on the position $\vec{r}$ of $\vec{d} = D\vec{\varepsilon}_d$ in the PhC cavity. Figure 4:7 shows $\vec{\xi}(\vec{r})$ for the plane position $\vec{r}$ at the middle of the membrane slab in the PhC cavity, arbitrarily positioned inside the L3 PhC cavity. Irrespective of the dipole position, the photon emitted through the CM will always have the same polarization properties in the far field region. We assume in the following vertical CM polarization in the far field region, i.e., $\vec{\varepsilon}_{CM} = \vec{e}_V$ (Figure 4:7), since we focus in our experiments on the CM0 and CM1 that have such nearly perfect linear polarization in the vertical direction.

Misorientation between $\vec{\xi}(\vec{r})$ and $\vec{\varepsilon}_{CM}$ can introduce a phase shift between the photons emitted through the CM and the spontaneous emission decay channels in the far field region. Indeed, the photon emitted through the CM always has the same polarization properties in the far field emission region while the spontaneously emitted photon will keep the phase of the dipole. Let us suppose that the CM electric field forms an angle θ with the e_V axes, that is, $\vec{\xi}(\vec{r}) = \vec{e}_y$ (Figure 4:7) while the transition dipole polarization $\vec{\varepsilon}_d = \frac{1}{\sqrt{2}}(\vec{e}_y \pm i\vec{e}_x)$, which corresponds to the left and right circular polarization in a homogeneous photonic environment (as expected for the X- transition).
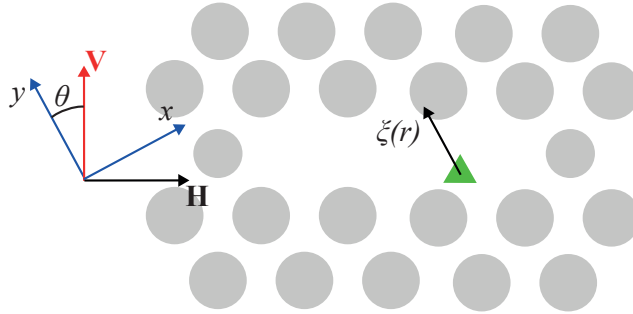
Figure 4:7 The QD (a dipole source) positioned at an arbitrary point inside the PhC L3 cavity. The arrow indicates the orientation of the CM0 electric field $\vec{\xi}(\vec{r})$ at the plane position at the middle of the membrane slab (see text). V and H denote the cavity axes of symmetry, while x and y are the coordinate system of the CM electric field at the QD position, assumed to be oriented in the y direction.

In this case, the photon emitted through the spontaneous emission channel will have polarization $\vec{\varepsilon}_{sp} = \frac{1}{\sqrt{2}}(\vec{e}_y \pm i\vec{e}_x)$ yielding $\vec{\varepsilon}_{sp} = \frac{1}{\sqrt{2}}e^{\pm i\theta}(\vec{e}_V \pm i\vec{e}_H)$ in the $\{\vec{e}_H, \vec{e}_V\}$ basis. The photon emitted through the cavity decay channel has linear polarization $\vec{\varepsilon}_{CM} = e^{i\varphi}\vec{e}_V$ in the far field region. Here

we assume some constant phase shift φ between the spontaneous and the CM emissions that will be discussed in the following. The total phase difference reads $\varphi \mp \theta$ depending on the initial transition dipole orientation $\vec{\varepsilon}_d = \frac{1}{\sqrt{2}}(\vec{e}_y \pm i\vec{e}_x)$. Thus, the phase between the spontaneously emitted photon and the CM photon is set by the angle θ between the field orientation at the particular position of the point dipole $\vec{\xi}(\vec{r})$ and the CM polarization in the far field region, that is, $\vec{e}_V$. However, in our devices the QD is ideally positioned on the horizontal symmetry axes of the PhC cavity. This provides the orientation of the electric field at the position of the QD exactly along vertical axes $\vec{\xi}(\vec{r}) \approx \vec{e}_V$ (Figure 4:2). As a result, the phase difference between photons emitted through the CM and the spontaneous emission decay channel is equal to φ irrespective of the charged exciton dipole orientation.

Considering $\vec{\varepsilon}_d = \frac{D_{X-}}{\sqrt{2}}(\vec{e}_V \pm i\vec{e}_H)$ for the $\left|\pm\frac{3}{2}\right\rangle \rightarrow \left|\pm\frac{1}{2}\right\rangle$ transitions of X-, the CM-exciton coupling strength is $g = \frac{D_{X-}}{2}\sqrt{\frac{\hbar\omega_{CM}}{\epsilon_0 V}}\Phi_k(\vec{r})$ for any excited state $|e\rangle = \cos\vartheta \left|\frac{3}{2}\right\rangle + \sin\vartheta \left|-\frac{3}{2}\right\rangle$. Indeed, the excited state $|e\rangle$ can decay either to $\left|\frac{1}{2}\right\rangle$ or to $\left|-\frac{1}{2}\right\rangle$ through an interaction with the CM, yielding

$$g = \frac{D_{X-}}{2}\sqrt{\frac{\hbar\omega_{CM}}{\epsilon_0 V}}\Phi_k(\vec{r})(|a|^2 + |b|^2) = \frac{D_{X-}}{2}\sqrt{\frac{\hbar\omega_{CM}}{\epsilon_0 V}}\Phi_k(\vec{r})$$

Thus, CM-exciton interaction does not lift the two-fold degeneracy of the charged exciton energy level with respect to the projection of the angular moment on the quantization axes. This degeneracy is transferred to the polariton states, that is, the eigenstates of the Jaynes-Cumming Hamiltonian formed by hybridization of the exciton and photon wavefunctions. Therefore, the charged exciton can be considered as a single two-level system with excited state $|e\rangle$ and ground state $|g\rangle$ since the CM-exciton interaction does not depend on the exciton angular momentum projection. The corresponding Hamiltonian reads:

$$\mathcal{H} = \hbar\omega_{X-}\sigma^+\sigma + \hbar\omega_{CM}a^+a + g(a^+\sigma + \sigma^+a)$$

Here $\sigma^+(\sigma)$ and $a^+(a)$ are creation (annihilation) operators of the charged exciton and CM photon respectively. This Hamiltonian is diagonalized with the following polariton wavefunctions:

$$|-, n_{ph}\rangle = \cos\beta \, |e\rangle|n_{ph} - 1\rangle - \sin\beta \, |g\rangle|n_{ph}\rangle$$

$$|+, n_{ph}\rangle = \sin\beta \, |e\rangle|n_{ph} - 1\rangle + \cos\beta \, |g\rangle|n_{ph}\rangle$$

where $|n_{ph}\rangle$ is a CM photon Fock state, the phase $\beta = \tan^{-1}\frac{2g}{\Delta + \sqrt{4g^2 + \Delta^2}}$, where the exciton-CM detuning $\Delta = \omega_{CM} - \omega$. These states correspond to energy levels:

$$E_{\pm, n_{ph}} = \hbar\left(\omega_{CM}n_{ph} - \frac{\Delta}{2} \pm R_{n_{ph}}\right), R_{n_{ph}} = \sqrt{n_{ph}g^2 + \frac{\Delta^2}{4}}$$

Transitions are only possible between polaritons with number of excitations different by a single excitation, that is, $|\pm, n_{ph}\rangle \rightarrow |\pm, n_{ph} - 1\rangle$ and $|\pm, n_{ph}\rangle \rightarrow |\mp, n_{ph} - 1\rangle$ providing emission at $\hbar\omega_{CM} \pm (R_{n_{ph}} - R_{n_{ph}-1}) \approx \hbar\omega_{CM}$ and $\hbar\omega_{CM} \pm (R_{n_{ph}} + R_{n_{ph}-1})$ energies. If $n_{ph} = 1$ then $|-,1\rangle \rightarrow |g\rangle|0\rangle$ and $|+,1\rangle \rightarrow |g\rangle|0\rangle$ are the only possible transitions. These transitions lead to the doublet emission structure with $\hbar(\omega_{CM} - \frac{\Delta}{2} \pm \sqrt{n_{ph}g^2 + \frac{\Delta^2}{4}})$ peak energies for both vertical and horizontal polarizations.

The neutral exciton-CM system is described in a very similar way although some differences can be observed. Interaction between the neutral exciton with nonzero FSS energy and the CM can be described using the following Hamiltonian:

$$\mathcal{H} = \hbar(\omega - \frac{\delta}{2})\sigma_{X_b}^+\sigma_{X_b} + \hbar(\omega + \frac{\delta}{2})\sigma_{Y_b}^+\sigma_{Y_b}) + \hbar\omega_{CM}a^+a$$
$$+ g[a^+(\sigma_{X_b}\sin\theta + \sigma_{Y_b}\cos\theta) + (\sigma_{X_b}^+\sin\theta + \sigma_{Y_b}^+\cos\theta)a]$$

where $\sigma_{X_b(Y_b)}^+$ ($\sigma_{X_b(Y_b)}$) and $a^+(a)$ are creation (annihilation) operators of the bright exciton state $|X_b\rangle$ ($|Y_b\rangle$) and the CM photon, respectively. $|X_b\rangle$ and $|Y_b\rangle$ transitions have $g_{X_b} = g\sin\theta$ and $g_{Y_b} = g\cos\theta$ interaction strengths with the CM defined by the angle θ (Figure 4:6(b)). The interaction of a FSS exciton with the CM can be retrieved from the two extreme cases. The first case corresponds to the higher energy state $|Y_b\rangle$ dipole parallel to the CM electric field at the QD position, that is, for $\theta = 0$. Then the Hamiltonian takes the following form:

$$\mathcal{H} = \hbar(\omega - \delta)\sigma_{X_b}^+\sigma_{X_b} + \hbar\omega\sigma_{Y_b}^+\sigma_{Y_b} + \hbar\omega_{CM}a^+a + g[a^+\sigma_{Y_b} + \sigma_{Y_b}^+a]$$

where ω is the frequency of the $|Y_b\rangle$ state. This Hamiltonian can be diagonalized using the following polariton wavefunctions:

$$|D, n_{ph}\rangle = |X_b\rangle|n_{ph} - 1\rangle$$

$$|-, n_{ph}\rangle = \cos\beta\,|Y_b\rangle|n_{ph} - 1\rangle - \sin\beta\,|G\rangle|n_{ph}\rangle$$

$$|+, n_{ph}\rangle = \sin\beta\,|Y_b\rangle|n_{ph} - 1\rangle + \cos\beta\,|G\rangle|n_{ph}\rangle$$

where CM-exciton detuning $\Delta = \omega_{CM} - \omega$ and $\beta = \frac{1}{2}\tan^{-1}\frac{2g}{\Delta}$. These polariton states correspond to the eigen energies $\hbar(\omega_{CM}n_{ph} - \Delta - \delta)$, $\hbar(\omega_{CM}n_{ph} - \frac{\Delta}{2} - R_{n_{ph}})$ and $\hbar(\omega_{CM}n_{ph} - \frac{\Delta}{2} + R_{n_{ph}})$ with $R_{n_{ph}} = \sqrt{n_{ph}g^2 + \frac{\Delta^2}{4}}$. The possible transitions are $|D, n_{ph}\rangle \rightarrow |D, n_{ph} - 1\rangle$, $|\pm, n_{ph}\rangle \rightarrow |\pm, n_{ph} - 1\rangle$ and $|\pm, n_{ph}\rangle \rightarrow |\mp, n_{ph} - 1\rangle$ providing emission at $\hbar\omega_{CM}$, $\hbar\omega_{CM} \pm (R_{n_{ph}} - R_{n_{ph}-1}) \approx \hbar\omega_{CM}$ and $\hbar\omega_{CM} \pm (R_{n_{ph}} + R_{n_{ph}-1})$ energies. If $n_{ph} = 1$ then the only possible transitions are $|D, 1\rangle \rightarrow |G\rangle|0\rangle$ and $|\pm, 1\rangle \rightarrow |G\rangle|0\rangle$. These transitions lead to the horizontally polarized singlet at $\hbar(\omega_{CM} - \Delta - \delta)$ energy and vertically polarized doublet at $\hbar(\omega_{CM} - \frac{\Delta}{2} \pm \sqrt{g^2 + \frac{\Delta^2}{4}})$ peak energies. Thus, in the case of neutral exciton with one FSS component dipole-aligned along the CM field at the dipole

position, the exciton-CM system forms three polariton states in contrast to the charged exciton. The horizontally polarized emission is defined by the spontaneous emission from the dark exciton state $|D, 1\rangle$ yielding the singlet in the emission spectrum. The vertically polarized emission has the doublet structure identical to the charged exciton case.

The polariton structure significantly changes if the two neutral exciton dipoles are not aligned with the CM field at the position of the emitter. Although the general solution with arbitrary θ has complicated form, a simple analytical solution can be obtained in case of $\theta = \frac{\pi}{4}$ and detuning corresponding to the CM exactly between the neutral exciton FSS components. Then the Hamiltonian has the following form

$$\mathcal{H} = \hbar(\omega - \frac{\delta}{2})\sigma^+_{X_b}\sigma_{X_b} + \hbar(\omega + \frac{\delta}{2})\sigma^+_{Y_b}\sigma_{Y_b} + \hbar\omega_{CM}a^+a + \frac{g}{\sqrt{2}}\left[a^+\left(\sigma_{X_b} + \sigma_{Y_b}\right) + (\sigma^+_{X_b} + \sigma^+_{Y_b})a\right]$$

The eigenvectors of this Hamiltonian are two lower and higher energy polariton states having eigenfrequencies $\omega_{CM} \pm \sqrt{g^2 + \frac{\delta^2}{4}}$:

$$|-, n_{ph}\rangle = \left(\cos^2\frac{\alpha}{2}|X_b\rangle + \sin^2\frac{\alpha}{2}|Y_b\rangle\right)|n_{ph} - 1\rangle - \frac{1}{\sqrt{2}}\sin\alpha\,|G\rangle|n_{ph}\rangle$$

$$|+, n_{ph}\rangle = \left(\sin^2\frac{\alpha}{2}|X_b\rangle + \cos^2\frac{\alpha}{2}|Y_b\rangle\right)|n_{ph} - 1\rangle + \frac{1}{\sqrt{2}}\sin\alpha\,|G\rangle|n_{ph}\rangle$$

and the polariton corresponding to the eigenfrequency ω_{CM}:

$$|D, n_{ph}\rangle = \frac{1}{\sqrt{2}}\sin\alpha\,(|X_b\rangle - |Y_b\rangle)|n_{ph} - 1\rangle + \frac{1}{\sqrt{2}}\sin\alpha\,|G\rangle|n_{ph}\rangle$$

where $\sin\alpha = \frac{2g\sqrt{n_{ph}}}{\sqrt{4g^2 n_{ph} + \delta^2}}$. All three polariton states can emit photons through the CM emission channel in contrast to the case of $\theta = 0$ due to nonzero fraction of the $|G\rangle|n_{ph}\rangle$ state in each polariton state. Thus, the triplet structure is expected in both horizontal and vertical emission spectra. Assuming $n_{ph} = 1$, the dark polariton $|D, 1\rangle$ emission rate through the CM can be estimated as $\Gamma^{CM}_D = \frac{1}{4\frac{g^2}{\delta^2}+1}\kappa$ while emission rate of the bright polaritons $|\pm, n_{ph}\rangle$ is $\Gamma^{CM}_B = \frac{4\frac{g^2}{\delta^2}}{4\frac{g^2}{\delta^2}+1}\kappa$ yielding $\frac{\Gamma^{CM}_D}{\Gamma^{CM}_B} = \frac{\delta^2}{4g^2}$. Thus, $\frac{\Gamma^{CM}_D}{\Gamma^{CM}_B} = 1$ if the coupling strength g is half of the fine-structure splitting δ. This gives rise to the triplet structure in the vertically polarized emission. Interestingly, in our QD system FSS splitting is very close to the exciton-CM coupling as retrieved from the polarization-resolved measurements. Unfortunately, the neutral exciton dipole orientation with $\theta = \frac{\pi}{4}$ discussed here is very rare; therefore we were not able to identify a structure with such appropriate parameters.

Thus, among the different excitonic transitions, the charged exciton is the most suitable for probing CM-exciton interaction. This transition provides a decay channel through the CM that is independent of the particular preparation conditions of the charged exciton state. We also expect very similar

interaction of the charged excitons in different devices. In contrast, the neutral exciton-CM interaction significantly depends on the particular neutral exciton FSS dipole orientation yielding complex polarization dependence on excitation power. Additionally, we show that it is very important to ensure positioning of the QD on the main axis of the liner PhC cavity for probing exciton-CM interaction with co-polarization effect. Emission properties of the charged exciton-CM system

4.3.3   Power dependence of the excitonic transitions

Devices with a QDs incorporated in the center of L3 PhC cavity ($\Delta=0$) provide the strongest interaction between the L3 PhC CM0 and the QD excitons. Figure 4:8(a, b) shows polarization-resolved and DOLP spectra obtained at several excitation powers for two different structures, labeled 'A' and 'B'. Both structures have charged excitonic transitions detuned by less than 1 meV from CM0. The charged excitonic transitions in both structures revealed strong co-polarization with the CM0 attaining DOLP≈90%. Higher energy excitonic and biexcitonic transitions showed opposite behavior. As can be seen in DOLP spectra in Figure 4:8(a), excitonic and biexcitonic transitions reveal clear "anti-polarization" with respect to CM0. This behavior is typically observed in our devices for excitonic transitions detuned at higher energies with respect to CM0 by 2-5 meV. We call this behavior 's-shape' due to its profile in DOLP spectra [15]. Structure B shows unpolarized emission of the higher energy transitions at the observed detuning points. We assume that it is due to more than 6 meV energy detuning between CM0 and higher energy transitions. As will be shown in the following, almost 100 % of all measured structures reveal such s-shape behavior although the detuning parameters at which the horizontal polarization is the most pronounced slightly varied between different structures.
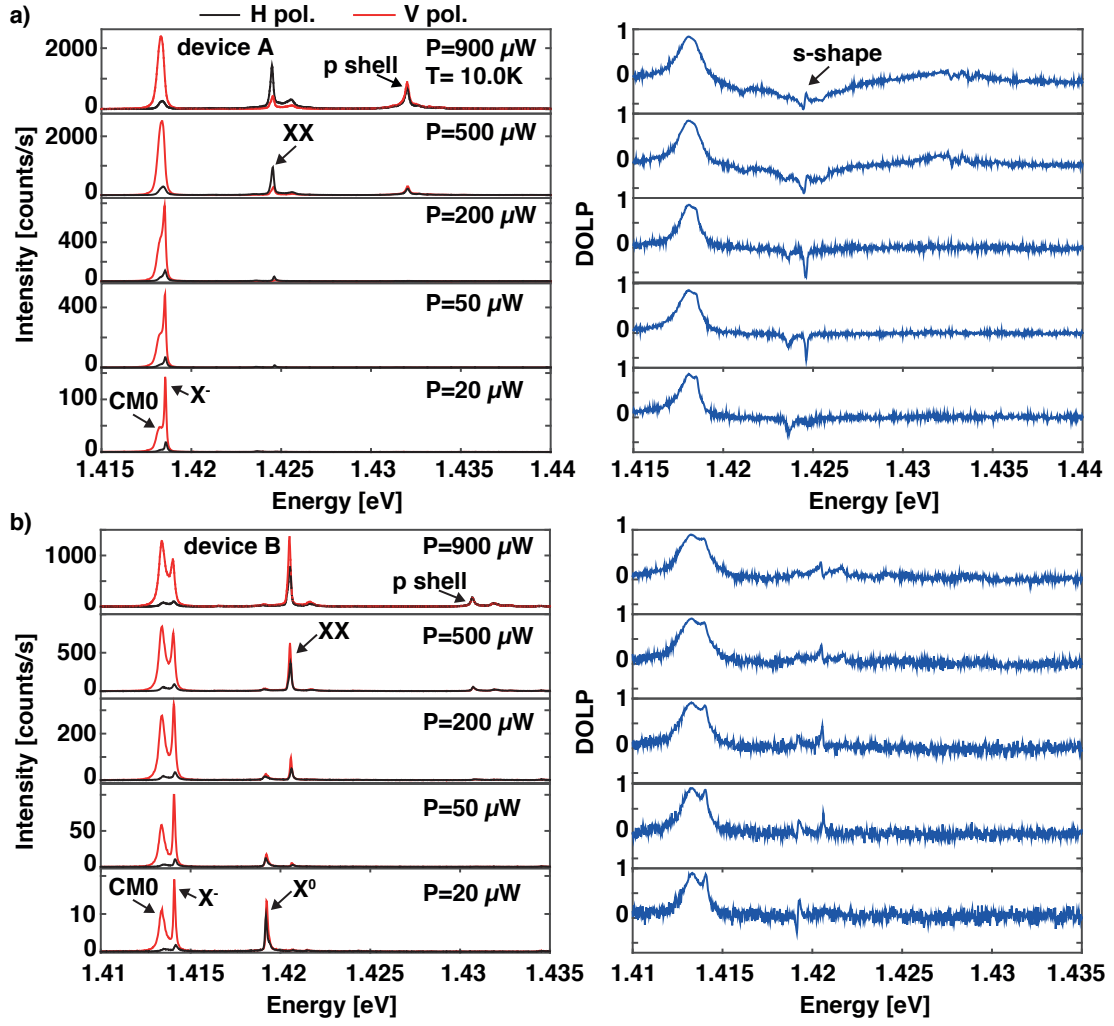
Figure 4:8 Polarization-resolved and DOLP spectra of a single QD in the center (Δ=0 nm position) of an L3 PhC cavity for a set of excitation powers; for device A (a) and device B (b).

We fitted the polarization-resolved PL spectra using several Lorentzians. Figure 4:9(a, b) shows horizontally and vertically polarized exciton-CM0 emission fitted with two Lorentzians. Although a slight discrepancy is visible for the tails of these spectra, this method gives a good approximation of the integrated intensity as well as of the full width at half maximum (FWHM) of the observed lines. The latter serves as a measure of dissipation processes in the QD-cavity system.
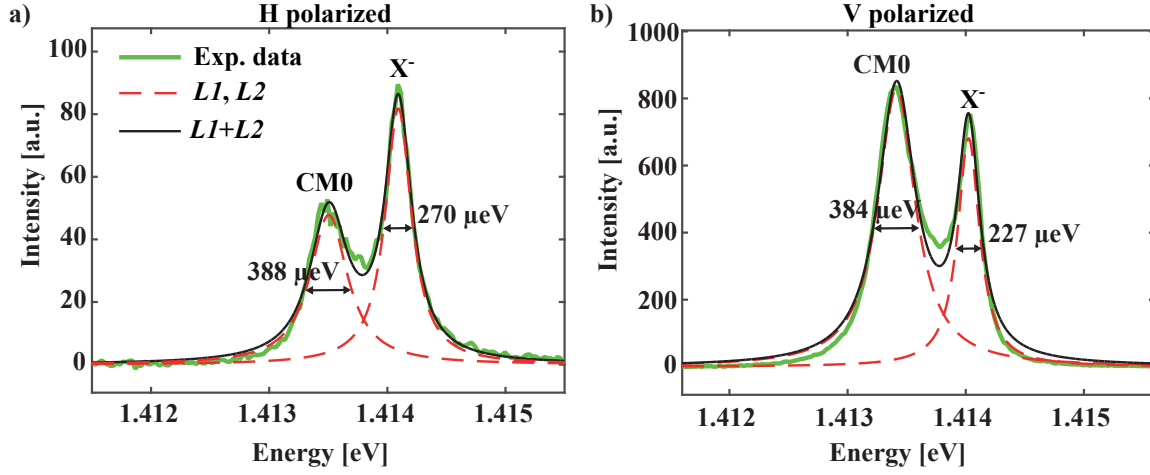
Figure 4:9 Horizontally (a) and vertically (b) polarized components of the charged exciton-CM0 spectra of structure 'B' at excitation power P=500 µW (same spectra of Figure 4:8(b), 2nd panel from top). CM0 and charged exciton lines were fitted with Lorentzians '*L1*' and '*L2*'.

Fitting the main optical transitions with Lorentzian line shapes, we analyzed the power dependence of the s-shell transitions, that is, charged and neutral excitons and biexcitons, and the electron p-shell transitions that are detuned by ~10 meV to higher energies (Figure 4:8 (a, b). As discussed previously, the DOLP of the charged exciton, or of the CM0 line, do not depend on the excitation power (Figure 4:10(a)). Polarization of the charged exciton and the CM0 were robust against a power-induced variation of the exciton - CM0 energy detuning. Figure 4:10 (b) shows the charged exciton - CM0 energy difference and the biexcitonic shift to lower energies at higher powers as ex-plained by increasing effective sample temperature at higher excitation powers. Power dependences of both charged exciton - CM0 detuning and relative energy shift (black solid line in Figure 4:10 (b)) almost perfectly overlap since at low temperature (T=10 K) the CM0 energy is less sensitive to temperature variations than the excitonic transition.
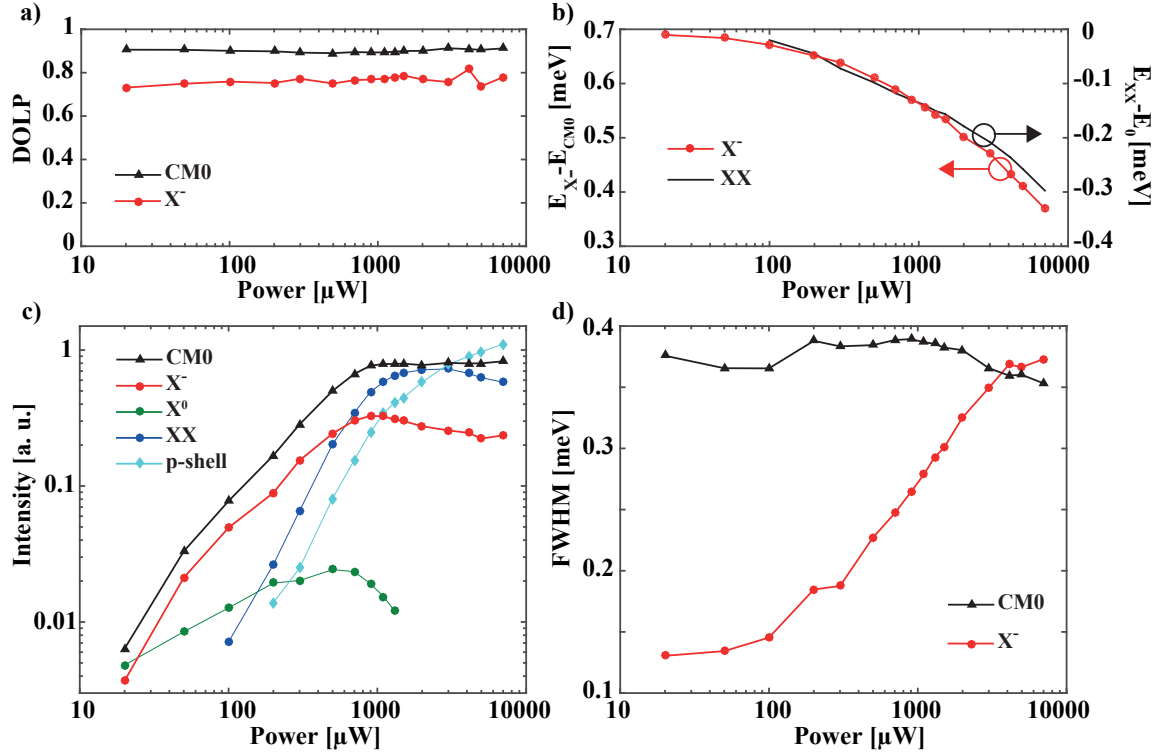
Figure 4:10 Dependence of the characteristics of CM-exciton coupling on excitation level: CM0 and charged exciton (X$^-$) DOLP (a), X$^-$ - CM0 and XX - CM0 detuning (b), intensity of the main optical transitions (c) and FWHM of CM0 and of X$^-$ (d), all plotted as a function of excitation power. All data obtained for structure 'B' (Figure 4:8(b)). In (b) we shifted the excitonic energy E_{X-} by the biexcitonic energy E_0 obtained at the excitation power $P = 10\ \mu W$.

Figure 4:10(c) shows the power dependence of the main excitonic transitions and the CM0 line. We did not find correlations between the power dependence of higher energy transitions and CM0, thus a direct exciton-CM coupling and phonon-mediated coupling are the main pumping mechanisms of the CM. The same observations were obtained in other devices based on site-controlled pyramidal QDs [15], [72]. At higher excitation power we observed significant broadening of the charged excitonic transition. While FWHM of the charged exciton is around 120 µeV at low excitation power, it increases up to the 380 µeV (Figure 4:10(d)) at excitation powers ~10 times higher than its saturation limit. Excitonic energy red shift at higher excitation power corresponds to increase in temperature of just a few kelvin that is not enough for such a linewidth broadening [15]. Therefore, we attribute this power broadening to the increasing fluctuations of the QD charge environment.

4.3.4 Co-polarization and interference effects in the X$^-$-CM0 system

In the following we present a study of the CM-exciton coupling in structure 'A'. Figure 4:11 (a, b) shows temperature tuning of the charged exciton line of structure 'A' into resonance with CM0. The DOLP of the charged exciton increased from ~70% at ~1 meV detuning up to ~94% in the resonance with the CM0. This effect is expected due to CM-induced Purcell enhancement of the

charged exciton emission rate. Right at resonance we estimate DOLP $\approx \dfrac{1 - \frac{\Gamma_{sp}}{2\alpha\Gamma_{CM}}}{1 + \frac{\Gamma_{sp}}{2\alpha\Gamma_{CM}}}$, where Γ_{sp} is the

spontaneous emission rate of the charged exciton in the PhC band gap and Γ_{CM} is the emission rate through the CM. The ratio between coupling efficiencies of the direct and indirect emission to the detector is $\alpha \approx 1.34$ [167]. Thus, the modification of the charged exciton emission rate due to interaction with CM0 (Purcell factor) is around 12, that is, $\Gamma_{CM} \approx 12\,\Gamma_{sp}$.
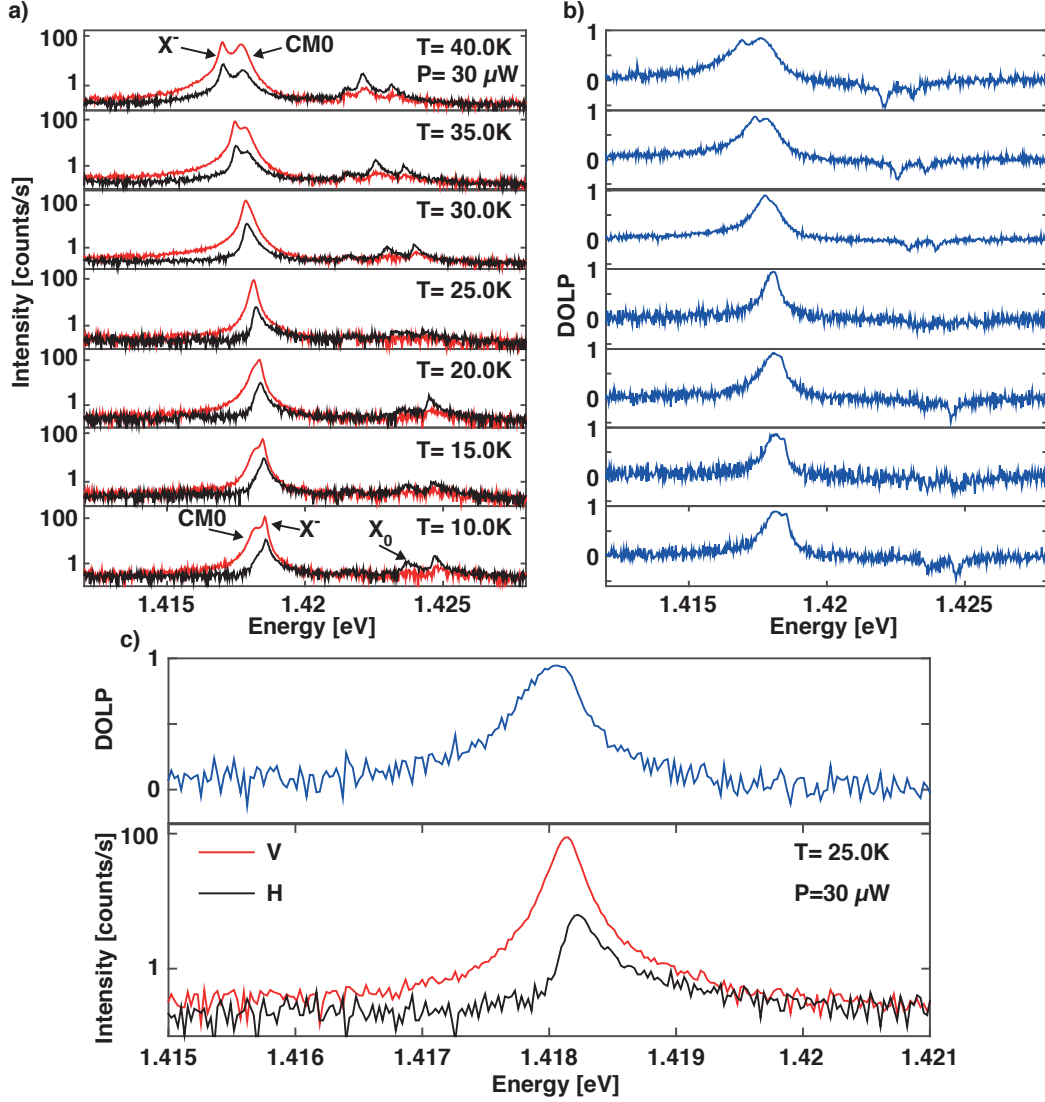
Figure 4:11 Temperature scanning of a CM0 through the charged exciton line of a single QD positioned at the center of an L3 PhC cavity corresponding to the Δ=0 nm (structure 'A' in Figure 4:8). Polarization-resolved and corresponding DOLP spectra obtained at a set of temperatures are shown in a) and b). In c) an X-axis zoom of the polarization-resolved PL spectra with corresponding DOLP on top are obtained right at resonance showing different line shapes for horizontally and vertically polarized exciton-CM emission.

The DOLP spectrum at resonance has slightly asymmetric shape (top panel Figure 4:11(c)). This is due to the different line shapes of the charged exciton emission for horizontally and vertically polarized spectral components. At resonance the vertically polarized emission is predominantly formed

by emission through the CM while horizontally polarized emission is formed by spontaneous emission into free space. Thus, the vertically polarized charged exciton spectrum reproduces the CM lineshape while the horizontally polarized component has asymmetrical lineshape that is typical for the charged exciton emission in our structures. This asymmetric lineshape is also visible in the charged exciton emission spectra of spectrally isolated QDs at low excitation power (section 3.3).

Detuning between the charged exciton and the CM0 lines was controlled using both temperature tuning and water vapor condensation. The amount of condensed water was controlled by the pressure in the cryostat before cooling down. Using this procedure, we obtained ~1 meV variations of exciton-CM detuning. After pumping the cryostat to the target pressure at room temperature, we started the cooling process, which led to residual water vapor condensation at 273 K inside the PhC holes. After cooling down to 10K we varied the temperature for fine-tuning of the exciton-CM0 energy difference.

Figure 4:12 shows polarization-resolved spectra (a, c) and corresponding DOLP spectra (b, d) at a set of temperatures. These measurements were obtained with device 'A'. Using different initial pressures for two different cooling processes, we obtained exciton-CM resonance at T=28 K (a) and T=36 K (c) for the same structure. At resonance DOLP spectra revealed ~90 % charged exciton co-polarization with the CM0, while the DOLP was negative for the neutral exciton and biexciton transitions visible at higher energy (yellow and blue traces in Figure 4:12 (b, d), respectively). These lines were identified using power dependence measurements as in Figure 4:10(a).
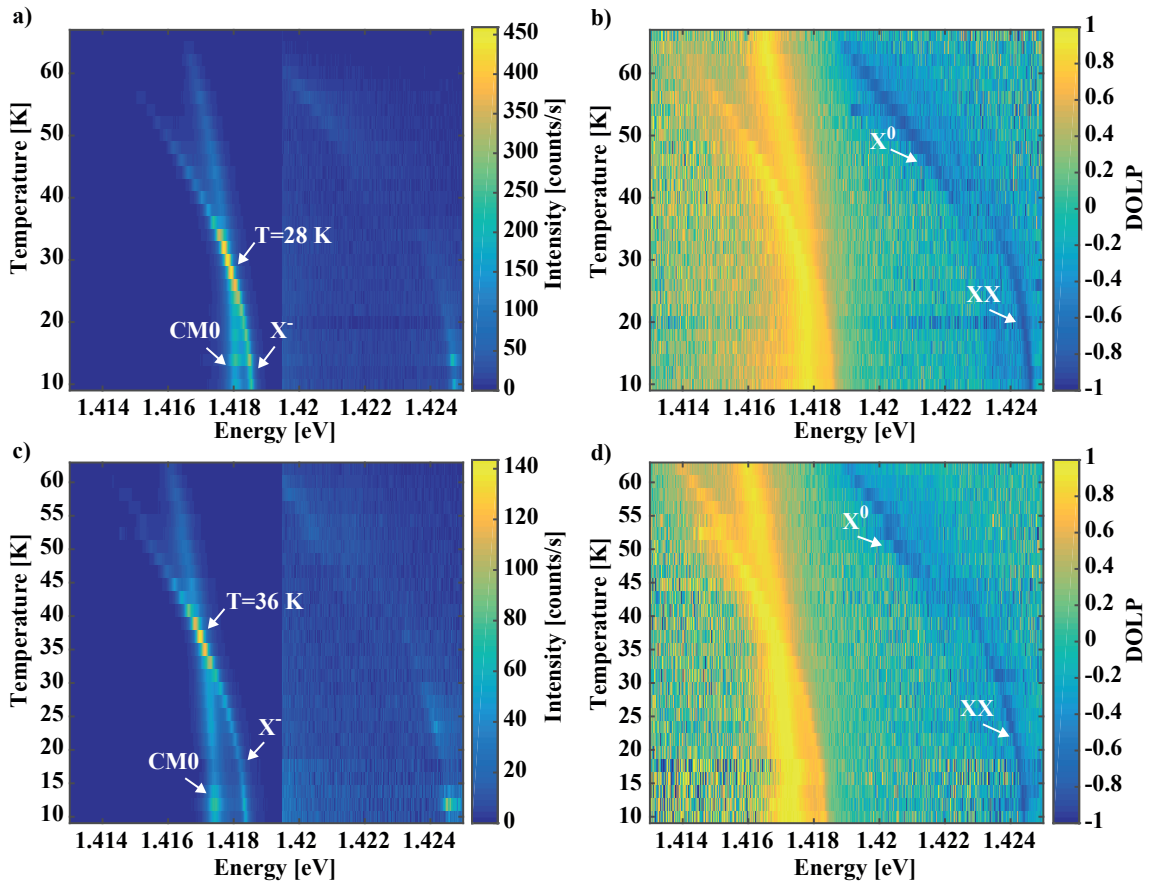
Figure 4:12 Vertically polarized intensity (a, c) and corresponding DOLP (b, d) color maps showing temperature scanning of a CM0 line with a QD charged exciton line (structure 'A'). Polarization-resolved data were obtained with no water vapor condensation (a, b) and small water condensation (c, d) providing CM red shift by ~0.5 meV.

Using the fitting procedure of the charged exciton-CM0 system with two Lorentzians we obtained the temperature dependence of their intensities and FWHM. At resonance the total emission intensity of the charged exciton-CM0 significantly increased due to Purcell enhancement of the emission rate. At temperatures higher than 50 K, the charged exciton line shifts out of resonance thus decreasing its radiative decay rate while its nonradiative decay rate significantly increases leading to significant intensity reduction. Such temperature-activated non radiative losses can be attributed to hot-exciton thermal escape through the higher energy states of electron and holes [174], [175]. In our QD structures, these energy levels can be QD excited states and electron-hole states of the QWR-like heterostructures grown in the wedges of the pyramidal recesses.
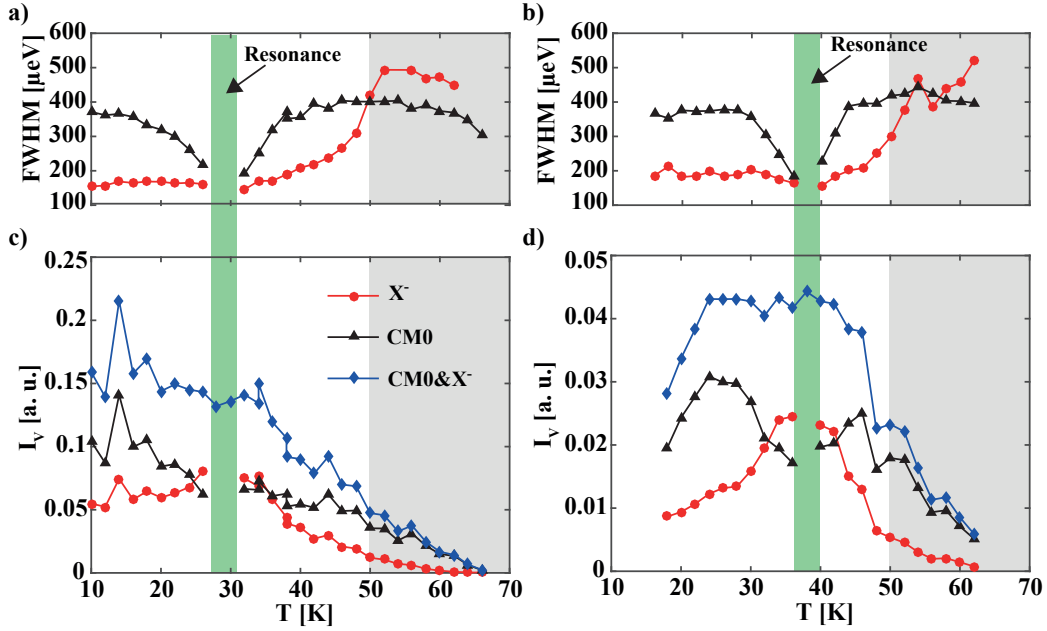
Figure 4:13 FWHM (a, b) and intensity (c, d) of charged exciton, CM and charged exciton-CM system obtained at different temperatures with no water vapor condensation (a, c) and small condensation providing CM red shift by ~0.5 meV (c, d). Grey regions correspond to the temperatures at which nonradiative processes dominant over light emission, leading to the significant intensity as well as lifetime reduction as discussed below.

Additionally to the intensity reduction, we observed significant broadening of the excitonic linewidth (top panels of the Figure 4:13(a, b)) at temperatures T>40 K. Similar temperature broadening is widely observed in self-assembled QD structures and usually explained by exciton-phonon interactions [144], [176]–[179]. Such linewidth broadening of excitonic transitions can influence the CM-exciton emission characteristics, therefore we focus on the temperature region T<50 K. Interestingly, we observed the CM narrowing in the resonance with the excitonic transition. The

same effect was previously reported for PhC cavities [15] and µ-pillar based structures [180] explained by the CM interaction with the phonon sideband of the excitonic line [171], [180].

Fitting both the vertically and horizontally polarized PL spectra we obtained DOLP as a function of the charged exciton-CM0 detuning for both condensation conditions (Figure 4:14(a, b)). In this figure, charged exciton-CM0 detuning was defined as $\Delta = E_{X-} - E_{CM0}$ thus the temperature increases from positive to negative detuning values. The DOLP of the QD increases from ~0.4 at Δ ~2 meV to ~0.85 at resonance due to dominant emission through the cavity decay channel. The DOLP spectrum is asymmetric about zero detuning due to the s-shape behavior of the charged exciton polarization[15] leading to the dominant horizontally polarized emission at positive detuning, as can also be seen for the neutral exciton and biexciton in Figure 4:12(b, d). Additionally to the CM0 and charged exciton DOLP values, we plotted the total DOLP of the charged exciton-CM0 system defined as $\frac{IV-IH}{IV+IH}$ where $IV = IV_{X^-} + IV_{CM0}$ and $IH = IH_{X^-} + IH_{CM0}$ are integrated intensities of the vertically and horizontally polarized exciton-CM system emission. As expected, these DOLP values lay between DOLP values of the charged exciton and CM0. Fitting with two Lorentzians is not accurate at detuning values smaller than the FWHM of charged exciton, therefore we refer to total DOLP in this case.

Surprisingly, the maximum of charged exciton DOLP is observed not in the direct resonance but at ~±0.5 meV detuning while the DOLP of the CM0 depends on the detuning conditions. This effect is directly seen in the polarization-resolved spectra normalized by the maximum of the charged excitonic line (Figure 4:14(c)). At negative detuning the CM0 intensity is more pronounced in the normalized vertically polarized spectra (T=10K and T=16K in Figure 4:14(c)) while at positive detuning relative intensity of the CM0 is bigger in the horizontally polarized spectra (T=38K and T=40K in Figure 4:14(c)). The corresponding DOLP spectra are shown in Figure 4:14(d), again confirming this observation.
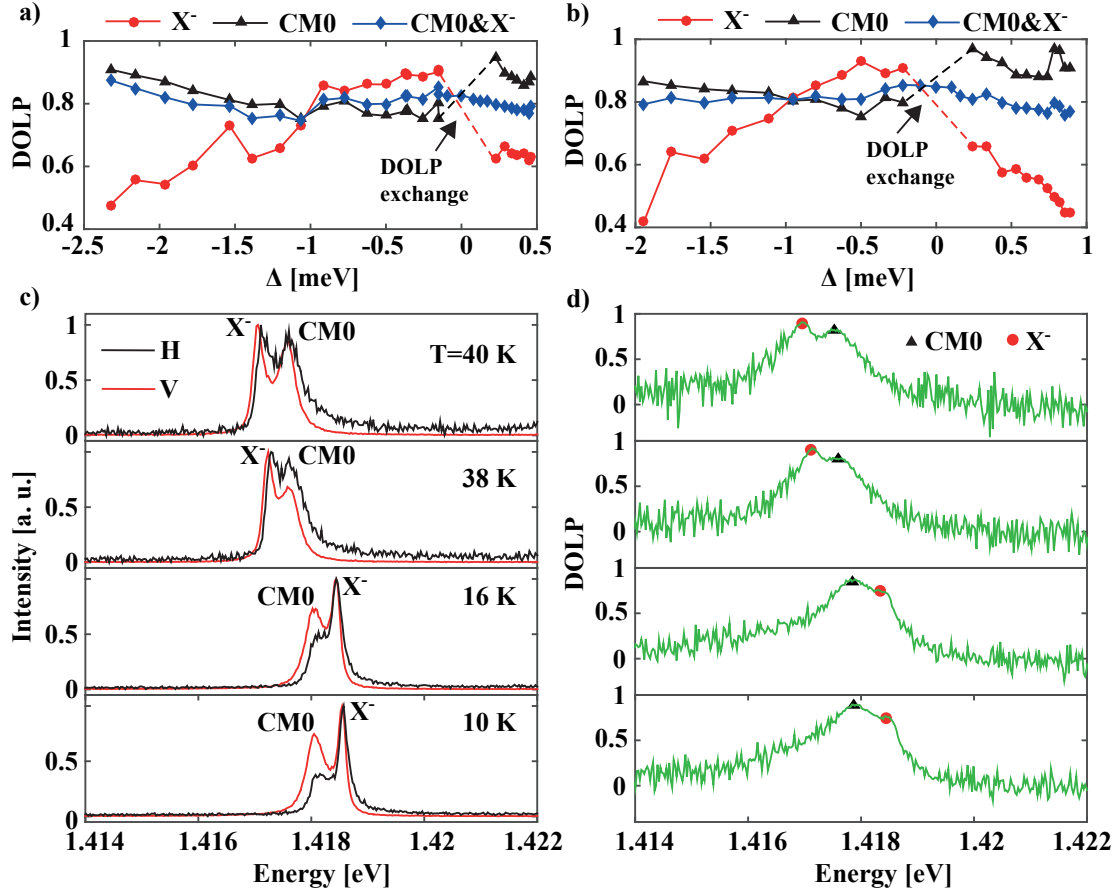
Figure 4:14 DOLP of charged exciton and CM0 lines as a function of detuning (a, b), polarization-resolved spectra at positive and negative detuning normalized by charged exciton peak intensity (c) and corresponding DOLP spectra (d). DOLP points in a) and b) correspond to fits of polarization resolved data obtained with no and small condensation conditions providing resonances at T=28 K and T=38 K, respectively. Polarization-resolved and DOLP spectra in c) and d) were obtained with no condensation corresponding to data shown in Figure 4:12(a, b). Polarization-resolved spectra were normalized by the peak intensity of the charged excitonic transition X⁻ and correspond to data shown in Figure 4:12(a, b).

This result is remarkable, as in the weak coupling regime CM polarization is usually assumed to be internally defined by the properties of the PhC cavity and does not depend on the exciton-CM0 detuning. In the strong coupling regime emission at both polariton branches is contributed by exciton decay through direct (spontaneous emission) and indirect (emission through the CM) decay channels. Destructive interference between direct and indirect decay channels can introduce dependence of the CM polarization on the detuning. Indeed, at positive detuning CM emission is attributed to the lower energy polariton $|-,1\rangle$ while for the negative detuning CM emission is attributed to the higher energy polariton $|+,1\rangle$. $|-,1\rangle$ and $|+,1\rangle$ polaritons have different phase between the exciton-like and CM-like components $|e\rangle|0\rangle$ and $|g\rangle|1\rangle$:

$$|-,1\rangle = \cos\beta \left(|e\rangle|0\rangle - \tan\beta \, |g\rangle|1\rangle \right)$$

$$|+,1\rangle = \cos\beta \, (\tan\beta \, |e\rangle|0\rangle + |g\rangle|1\rangle)$$

where $\tan\beta = \frac{2g}{\sqrt{4g^2+\Delta^2}-\Delta} > 0$ for any detuning $\Delta = E_{X^-} - E_{CM0}$ and positively defined coupling strength g. Thus, the phase between direct and indirect emission at the wavelength of the CM changes by π when the detuning changes its sign. Depending on the phases and pattern overlap between exciton and CM field radiation this could lead to the change from constructive to destructive interfering regime or vice versa (see Chapter 1). This effect is well visible in Figure 4:12(b, d)) for exciton and biexciton transitions that are detuned at higher energies with respect to the CM.

These interference effects can be extracted from the analysis of the detuning dependence of the emission rates of the polariton branches. Without taking into account pure dephasing and interaction with phonons, these emission rates read $\Gamma_\pm^V = \frac{\kappa+\gamma_V}{2} \pm \left[\frac{\kappa-\gamma_V}{2}\cos 2\beta + \chi\sqrt{\gamma_V\kappa}\cos\varphi\sin 2\beta\right]$ as was shown in Chapter 1. This yields $\Gamma_\pm^V(\Delta=0) = \frac{\kappa+\gamma_V}{2} \pm \chi\sqrt{\gamma_V\kappa}\cos\varphi$ at zero detuning. Emission at the wavelength of the CM is contributed by one of the polaritons depending on the detuning sign; in particular, if the system is prepared in the $|+,1\rangle$ ($|-,1\rangle$) state for $\Delta < 0$ ($\Delta > 0$), then the QD-exciton system emits at the energy of the CM.

We could consider an experiment in which the CM-exciton system is prepared in $|+,1\rangle$ and $|-,1\rangle$ polariton states for $\Delta < 0$ and $\Delta > 0$, respectively, that is, in the CM-like state. Such a state has emission rate $\Gamma_{CM} = \Gamma_{CM}^V + \Gamma_{CM}^H$ where Γ_{CM}^V and Γ_{CM}^H are emission rates through vertically and horizontally polarized modes. The emission rate through the vertically polarized modes changes for different detuning sign since $\Gamma_{CM}^V(-|\Delta|) - \Gamma_{CM}^V(|\Delta|) = \Gamma_+^V(-|\Delta|) - \Gamma_-^V(|\Delta|)$ yielding $2\chi\sqrt{\gamma_V\kappa}\cos\varphi\,\sin 2\beta$. In the limit $|\Delta| \to 0$ one gets $\pm 2\chi\sqrt{\gamma_V\kappa}$ difference depending on the phase φ.

In a similar way we get the emission rate of the CM-like state from the polariton emission rate through the horizontally polarized modes. Assuming negligible interference between horizontally and vertically polarized free space modes, to which polaritons couple through the direct and indirect decay channels, we get that polariton emission rate through horizontally polarized modes reads $\Gamma_\pm^H = \frac{\gamma_H}{2}(1 \pm \sin 2\delta\beta)$. Here, we defined $\delta\beta = \beta - \frac{\pi}{4}$ for convenience since $\delta\beta = 0$ corresponds to the zero detuning point ($\Delta = 0$). Polariton emission rate through the horizontally polarized modes does not depend on the detuning sign but only on its absolute value: $\Gamma_+^H(-|\Delta|) = \frac{\gamma_H}{2}(1 - \sin 2|\delta\beta(\Delta)|) = \Gamma_-^H(|\Delta|)$; in other words, it is described by the symmetric function with respect to $\Delta \to -\Delta$ transformation.

Therefore, the emission rate through the vertically polarized modes changes by $2\chi\sqrt{\gamma_V\kappa}\cos\varphi\,\sin 2\beta$ while the emission rate through the horizontally polarized modes does not change between detuning points $\Delta = \pm|\Delta|$. Corresponding polarization properties of the exciton-CM system are convenient to describe in terms of the degree of linear polarization DOLP. We get $DOLP_\pm = \frac{\Gamma_\pm^V - \Gamma_\pm^H}{\Gamma_\pm^V + \Gamma_\pm^H}$ since polaritons are eigen functions of Hamiltonian while back action of the free space modes on the population of the polaritons can be assumed negligible for our range of parameters. Excitonic DOLP is defined as $\frac{\Gamma_+^V - \Gamma_+^H}{\Gamma_+^V + \Gamma_+^H}$ for $\Delta > 0$ and $\frac{\Gamma_-^V - \Gamma_-^H}{\Gamma_-^V + \Gamma_-^H}$ for $\Delta < 0$ while cavity mode DOLP

reads $\frac{\Gamma_+^V - \Gamma_+^H}{\Gamma_+^V + \Gamma_+^H}$ for $\Delta < 0$ and $\frac{\Gamma_-^V - \Gamma_-^H}{\Gamma_-^V + \Gamma_-^H}$ for $\Delta > 0$. Figure 4:15 shows the calculated DOLP as a function of detuning. Although in these calculations we do not take into account interaction with phonons as well as the pure dephasing, the obtained curves qualitatively reflect the observed effects. Cavity mode 'DOLP exchange' appears while detuning changes sign (CM crosses exciton), in good correspondence with the experimental results (Figure 4:14(a, b)). At the detuning $\Delta_{ext} = \frac{g}{\chi \cos \varphi} \left(\sqrt{\frac{\gamma}{\kappa}} - \sqrt{\frac{\kappa}{\gamma}} \right)$ the DOLP attains its minimum due to the destructive interference between emission through the CM and the free space modes (see Chapter 1) well corresponding to the observed s-shape in our PhC cavity based devices.
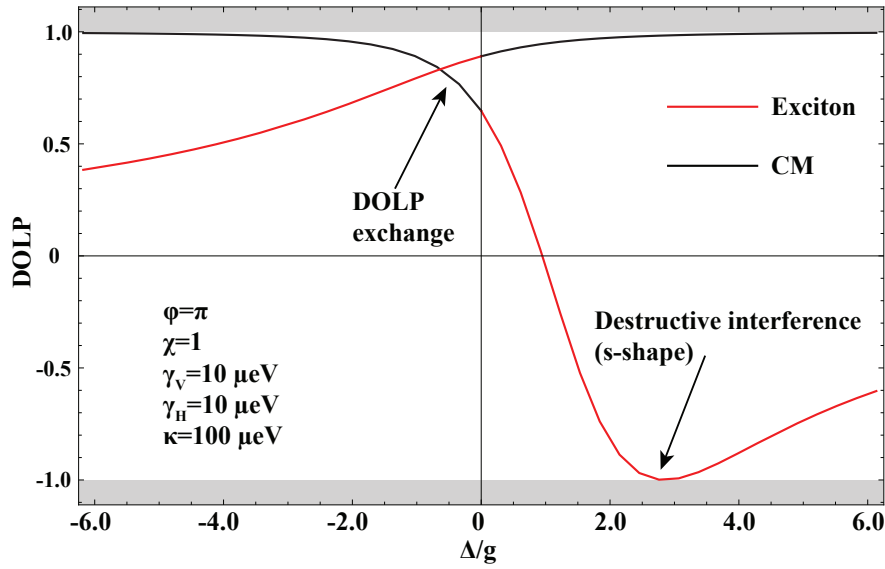
Figure 4:15 DOLP of exciton and CM calculated from the polaritonic emission rates.

Summarizing, we observed clear CM-exciton interference effects in polarization resolved PL measurements. These interference effects are explained by the hybridization of exciton and photon states providing competing exciton-CM decay channels into the same vertically polarized free space mode reservoir as well as the emission of horizontally polarized photons at the CM energy. For negative detuning this provides 'DOLP exchange' between the exciton and CM spectral lines near the zero detuning point. This effect is expected to be very sensitive to the exciton-CM coupling regime, disappearing in the weak coupling regime. We did not observe the Rabi splitting at zero detuning in our system, due to high CM and QD damping rates relative to the coupling strength, thus our system does not achieve the coherent coupling regime. However, the observed dependence of the cavity mode DOLP on the detuning can be a sign that our system operates in an intermediate coupling regime at which the exciton-photon hybridization starts to drive the system behavior. Additionally, QD vertically polarized emission is strongly suppressed for positive detuning due to the destructive interference as discussed in the Chapter 1. This effect holds independently of the coupling regime in the system and depends mainly on the geometrical overlap between free space mode patterns as

well as on the particular phase difference between the CM and exciton emission. In the following we will show how this effect depends on the particular QD position inside the L7 PhC cavity.

4.3.5 Purcell enhancement of X⁻ radiative decay rate

We further investigated the charged exciton-CM0 coupling using time-resolved PL measurements of the PL spectra of structure 'A'. Figure 4:16 shows the scheme of the time-resolved PL setup used. This setup is a modification of the setup used for polarization-resolved measurements described in the Figure 2:12. The Ti:Saphire laser was operated in the mode-locked mode providing 3 ps laser pulses with 80 MHz repetition rate. A part of the excitation beam was sent to a fast photodiode, serving as reference for the timing measurements. As a single-photon detector we used a PicoQuant τ-SPAD-FAST APD with 150-200 ps temporal resolution, positioned at the monochromator's output. For each spectrally filtered photon Arriving at the APD, the time delay from the reference (pump laser pulse) is counted by a fast pulse time counting unit (Time Harp 260 TCSPC board, with a 25 ps time bin width).
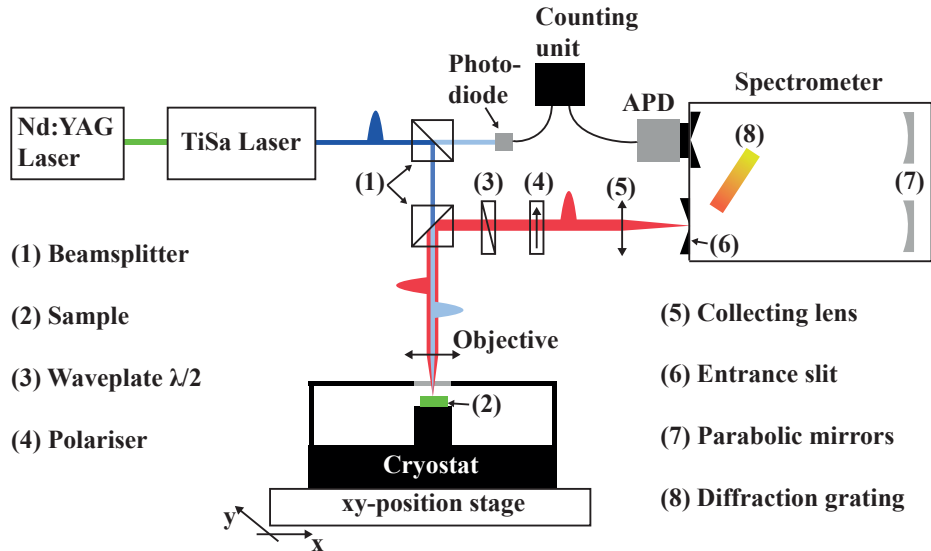
Figure 4:16 Scheme of the time-resolved PL setup.

Figure 4:17 shows time-resolved traces of the charged exciton recombination measured at T=28 K (a) and T=38 K (b) corresponding to the polarization-resolved data shown in Figure 4:12(a). At T=28 K the charged exciton was in resonance with CM0 while at 38 K the exciton-CM detuning was ~450 μeV. These traces reveal biexponential shape that is typical for neutral exciton, while charged exciton usually has single exponential decay[181], [182]. This difference is usually explained by the conversion of neutral exciton dark states into the bright states. This process is not possible for charged excitons since they do not have dark states. However, biexponential decay of the charged exciton can be observed if there are several QD feeding sources [183]. Electron-hole pairs excited in the GaAs membrane typically serve as the main source of the QD feeding while the additional source can be impurities incorporated in the vicinity of the QD.
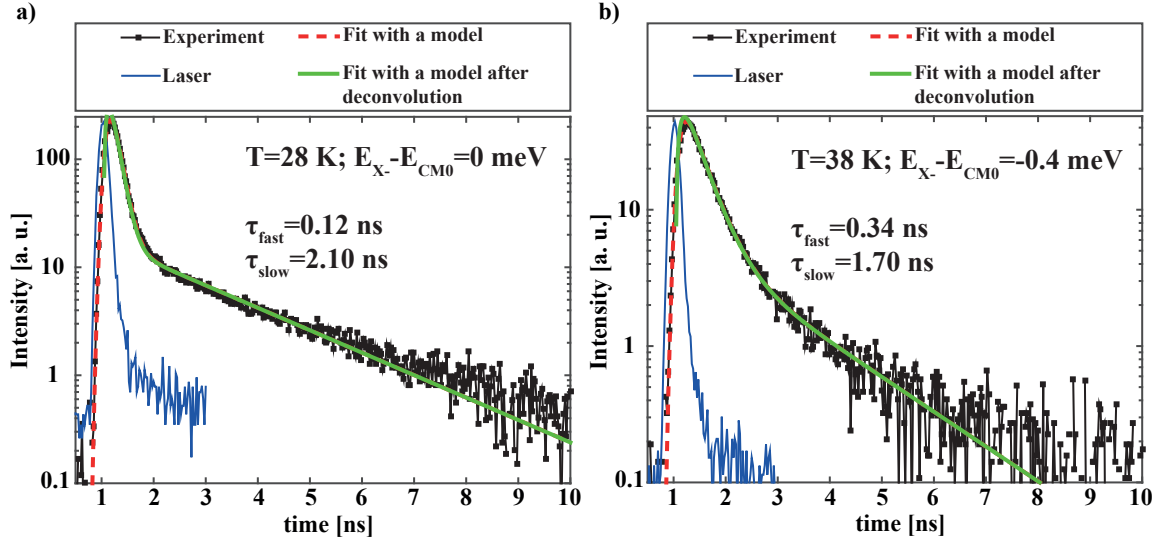
Figure 4:17 Time-resolved traces of the decay of the charged exciton state at T=28 K (a) and T=38 K (b) fitted with a biexponential decay model. At T=28 K (a) the charged exciton is in direct resonance with CM0 as can be seen in the corresponding polarization-resolved and DOLP maps (Figure 4:12(a, b)). These time-resolved measurements were obtained for structure 'A'.

This impurity-feeding source can populate the QD with both electrons and holes, leading to QD feeding with excitons. The slow decay time component of the charged excitonic transitions (3 ns at 10 K, see Figure 4:19) is very close to the one measured for the slow component of the carbon impurity (in GaAs) emission (3.4 ns at 10 K, see Figure 4:19). Similar slow decay times were revealed for the neutral exciton as discussed in the Chapter 5. The fast component of the time-resolved trace in Figure 4:18 reflects the response function of the detector.
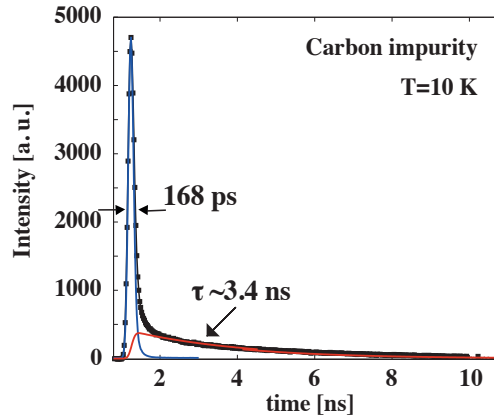
Figure 4:18 The decay time of the carbon impurity state measured at 829 nm (1.4956 eV). The fast decay follows the shape of the APD detector's response, while the slow part shows a decay time τ≈3.4 ns.

Therefore, we fitted the time-resolved traces using the model based on two different exciton-feeding sources. The first source is the electron-hole pairs excited in the bulk GaAs at much higher energies

than the QD excitonic transitions. These pairs cool down to the QD ground state through interactions with phonons during several tens of ps, thus populating the QD on a much shorter time scale than the typical decay time of the excitonic transitions. The second exciton-feeding source is nearby (mostly carbon) impurities that release carriers with relatively long characteristic time, leading to the slow decay component of the QD excitons time traces. This model is described by the following rate equations

$$\frac{\partial P_E(t)}{\partial t} = -\gamma_E P_E(t), \frac{\partial P_C(t)}{\partial t} = -\gamma_C P_C(t), \frac{\partial P_X(t)}{\partial t} = -\gamma_X P_X(t) + \gamma_E P_E(t) + \gamma_C P_C(t)$$

where $P_E(t)$, $P_C(t)$ and $P_X(t)$ are the populations of the QD excited state, an impurity state in the vicinity of the QD and the excitonic complex with corresponding emission rates are γ_E, γ_C and γ_X. Assuming $P_E(0) = A$, $P_C(0) = B$ and $P_X(0) = 0$ we get the following decay of the exciton population

$$P_X(t) = \frac{A\gamma_E}{\gamma_E - \gamma_X}\left(1 - e^{-(\gamma_E - \gamma_X)t}\right)e^{-\gamma_X t} + \frac{B\gamma_C}{\gamma_X - \gamma_C}\left(1 - e^{-(\gamma_X - \gamma_C)t}\right)e^{-\gamma_C t}$$

Fitting with this biexponential model we obtained Purcell-enhanced charged exciton radiation decay time $\tau_X = \frac{1}{\gamma_X}$ as low as 120 ps (Figure 4:17(a)), that is ~10-15 times smaller than the typical decay time of our charged excitonic transitions of the QDs in the bulk GaAs. The CM decay has the same biexponential behavior as the charged excitonic transition, confirming that excitonic transitions detuned by ~5 meV have negligible coupling with the CM0. Figure 4:19(a, b) shows the slow and fast decay components of the charged exciton and the CM0 at different exciton-CM0 detuning obtained from the time-resolved measurements of the same structure. Initial detuning between charged exciton and CM0 was set using different water vapor condensation, and then temperature tuning was applied as described above. Thus, we obtained direct resonance of the charged exciton with the CM0 at two different temperatures, namely, 28 K in a) and 38 K in b) corresponding to no and small water condensation. Figure 4:19(a, b) shows a clear reduction of the charged exciton lifetime at temperatures higher than 50K. We explain this effect by thermally activated nonraditative decay of the charged exciton, since this lifetime reduction was accompanied by a significant decrease of the emission signal intensity (bottom panels of Figure 4:13(a, b)). The charged exciton lifetime $\tau_X = \frac{1}{\gamma_X}$ was significantly reduced at resonance with the CM, showing very similar values for measured resonance temperatures (120 ps for T=28 K and 140 ps for T=36 K, see also Figure 4:20).
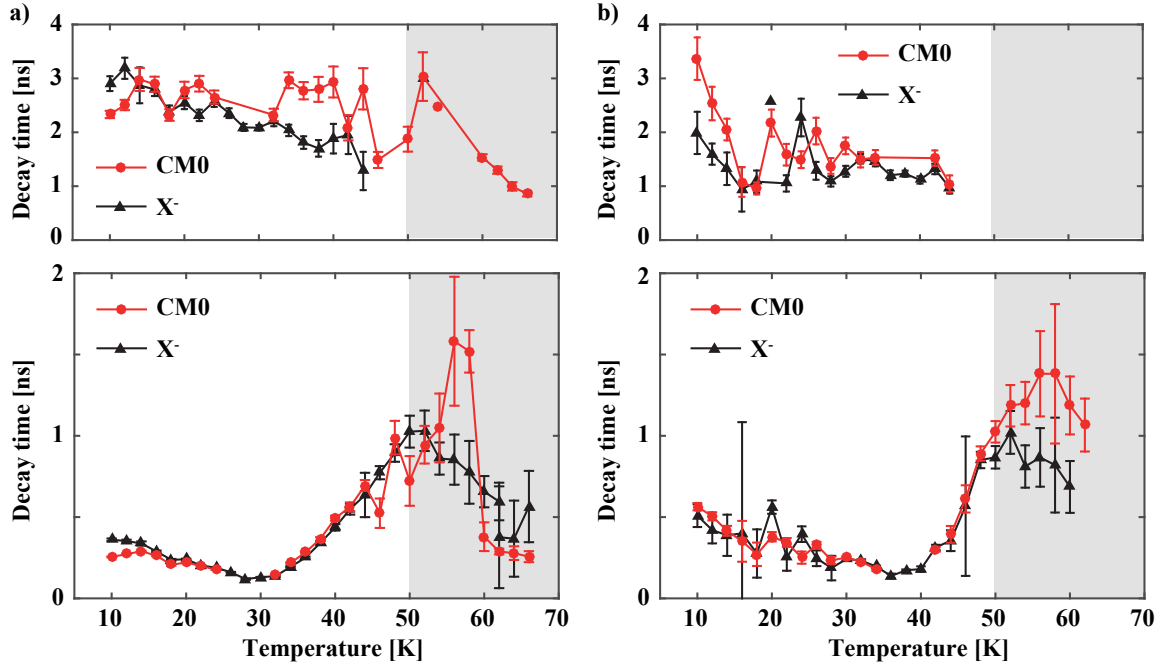
Figure 4:19 Slow (upper panel) and fast (lower panel) decay times of the charged exciton at different temperatures. Time-resolved data in a) and b) were obtained without and with small condensation respectively. Corresponding polarization resolved data are shown in Figure 4:12(a, b). The shadowed regions for T>50 K correspond to the temperature regions for which nonradiative excitonic decay rate dominates decay through optical modes.

We did not find any correlation between the slow decay time $\tau_C = \frac{1}{\gamma_C}$ and the CM-exciton detuning conditions (upper panels of Figure 4:19(a, b)), supporting the assumption of the external QD feeding source. The slow decay time constantly decreased with temperature, as can be attributed to the nonradiative losses of the carriers trapped by impurities. We observed a clear asymmetry between the negative and positive exciton-CM0 detuning as shown in Figure 4:20(a, b). This effect can be explained by the phonon assisted exciton-CM interactions [167], [184] providing higher emission rate through CM at the negative detuning and leading to the asymmetric lifetime reduction. In Figure 4:20(b) the exciton lifetime is around twice smaller at -1 meV detuning then at 1 meV even though the charged exciton has higher nonradiative decay rate at positive detuning.
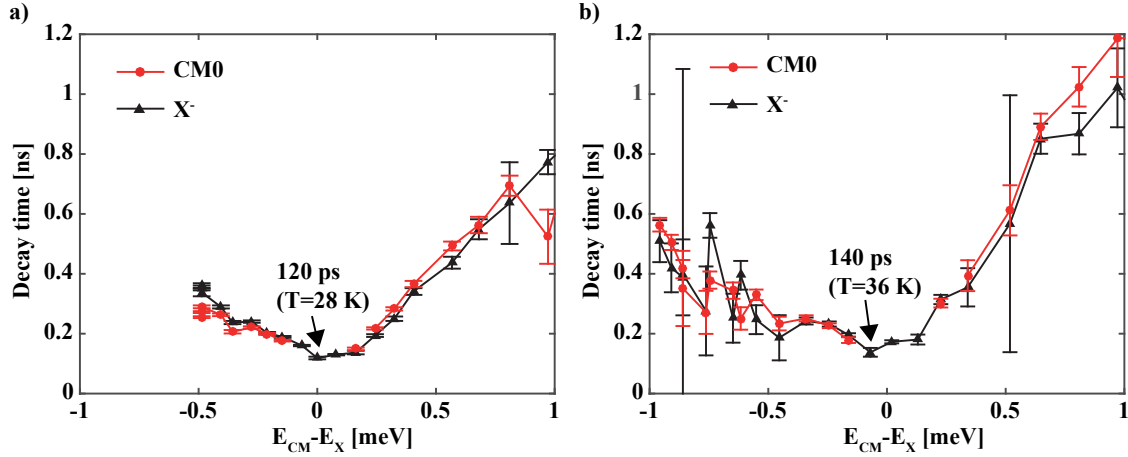
Figure 4:20 Decay time of the charged exciton as a function of detuning. Time-resolved data in a) and b) correspond to the polarization resolved data shown in Figure 4:12(a, b).

4.4 Probing a CM near field with a single QD

Here we show how the exciton-CM spatial overlap can be probed using a single site-controlled QD integrated with the L3 PhC cavity. In this study we mainly focused on the probing of the first and the second CM0 antinodes as well as the CM0 node, that is, the PhC cavity points that represent the main features of the CM electric field distribution. Shifting the QD to the CM0 node we were able to significantly reduce the exciton-CM0 coupling strength. The exciton-CM overlap was recovered for the QD shifted to the second CM0 field antinode. Applied also for CM1, this approach allowed comparing the CM0 and CM1 electric field distributions with modeled ones.

4.4.1 Probing the spatial distribution of CM0

As described previously, exciton-CM coupling is manifested by the charged exciton co-polarization with a CM. We expect the same behavior for the biexcitonic transition since it has a single excited state decaying through both CM and spontaneous decay channels. Using excitation power 3 times higher than the average saturation limit of the QD excitonic transition in the bulk GaAs, we brought the DOLP of the neutral excitonic transition to similar values as the DOLP of charged exciton. Thus, we expect that all QD excitonic transitions will reflect the coupling with the CM in the same way.

As shown previously, the QD positioned at the center of the PhC cavity reveals a temporal Purcell factor of ~10. Another QD position for which we expect a local maximum in exciton-CM coupling is Δ~180 nm (Figure 4:1(a)). Indeed, we obtained very strong exciton-CM co-polarization for almost all such measured devices. Figure 4:21(a, b) shows typical polarization-resolved and DOLP spectra measured in 13 devices with Δ=180 nm nominal QD shift from the center of the L3 PhC cavity. Here we introduced detuning as the difference between emission energy and CM energy, that is, $E - E_{CM}$. All devices had the same (nominal) PhC hole diameter $r_{PhC} \approx 66\,nm$ that provides the best CM spectral matching conditions with the QD excitonic transitions. We show here only spectra of devices, which do not have defective PhC cavities or spectral diffusion that deteriorate the spectrally resolved measurements (13 good devices out of a series of 20). These devices

137

reveal very efficient exciton-CM interaction, as can be concluded from strong co-polarization effect at zero detuning in Figure 4:21(a, b).

Figure 4:21 Polarization-resolved and DOLP spectra of 13 devices with single QD shifted by 180 nm from the L3 PhC cavity center. Spectra were taken from a scan of 20 structures with the same nominal PhC hole diameter $r_{PhC} \approx 66\ nm$. Here, detuning corresponds to the difference between emission and CM0 energy $E - E_{CM0}$. Spectra were acquired at 10 K under 300 µW excitation power.

Figure 4:22(a, b) shows polarization-resolved and DOLP spectra obtained in another set of 16 PhC devices with hole diameter $r_{PhC} \approx 64\ nm$ providing CM shifted to the lower energy side with respect to the exciton transitions. These devices also contain Δ=180 nm shifted single QDs. The CM0 line remains well visible even at > 20 meV detuning, highlighting efficient coupling to the excitonic emission. Our QD structures do not have wetting layers, thus off-resonant CM feeding is not possible through a hybridization of a QD exciton with 2D wetting layer states[50]. Off-resonant feeding observed in our devices could be attributed to the QWR-like structures formed in the wedges of the pyramidal recesses. However, we doubt this process is important since we observe clear correlation between off-resonant CM emission and the QD position in the L3 PhC cavity as will be shown in the following. We consider the fast spectral diffusion processes of the QD excitonic transitions as the possible explanation of this off-resonant CM emission[185].
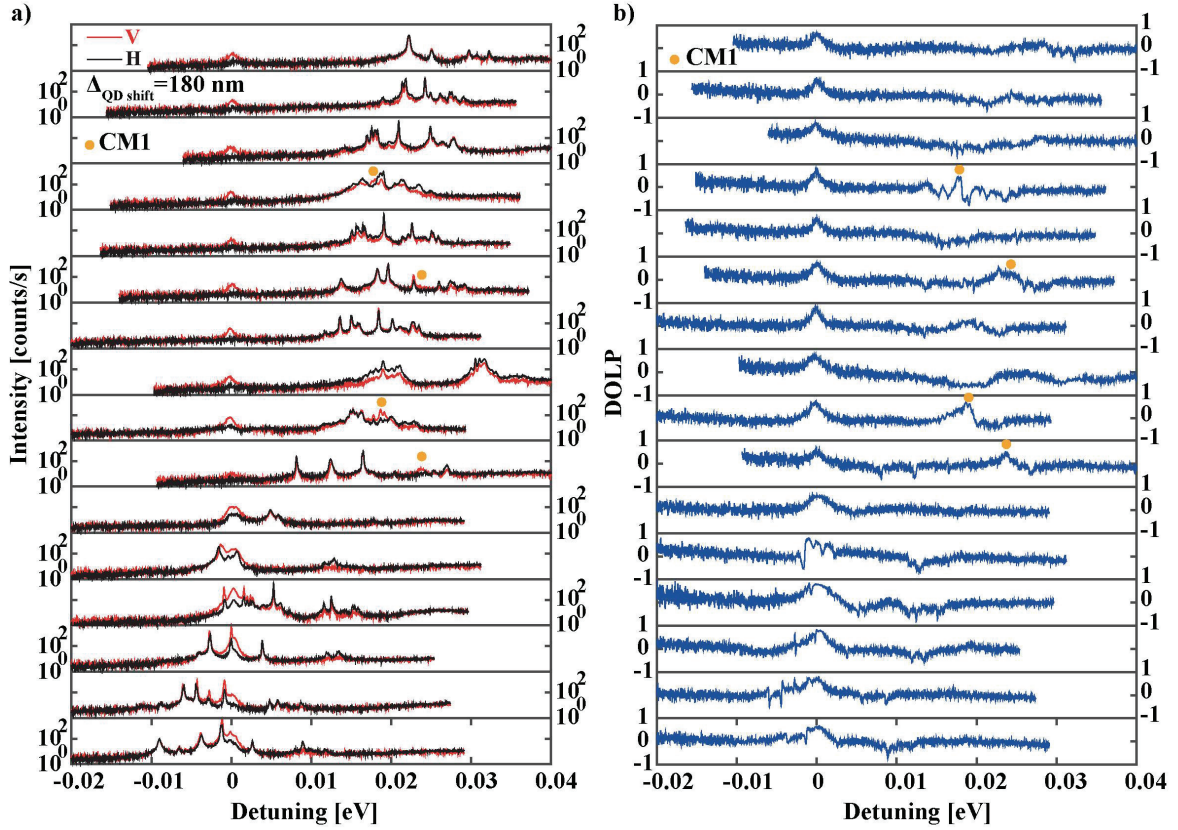
Figure 4:22 Polarization-resolved (a) and DOLP (b) spectra of 16 devices with single QD shifted by 180 nm from PhC cavity center with strong off-resonant emission of CM0. Spectra were taken from a scan of 16 good devices out of a series of 20 structures with the same nominal PhC hole diameter $r_{PhC} \approx 64\ nm$. Here detuning corresponds to the difference between peak and CM0 energy $E - E_{CM0}$. Spectra were obtained at 10 K temperature under 300 µW excitation conditions.

The picture significantly changes for QDs shifted by ~90 nm from the L3 PhC cavity center to the L3 CM node. Figure 4:23 shows all devices with Δ=90 nm QD shift, out of ~150 measured, for which CM0 could be identified. In the other devices CM0 emission was lower than the noise level. Remarkably, excitonic transitions reveal here much lower co-polarization with the CM0 at resonance while CM0 off-resonant emission is almost invisible for exciton-CM0 detuning exceeding several meV. The QD transitions show very small co-polarization with the CM0 in resonance oppositely to the devices with Δ=0 nm and Δ=180 nm. This low DOLP, as well as the weak off-resonance CM emission, is a manifestation of nearly zero exciton-QD overlap.
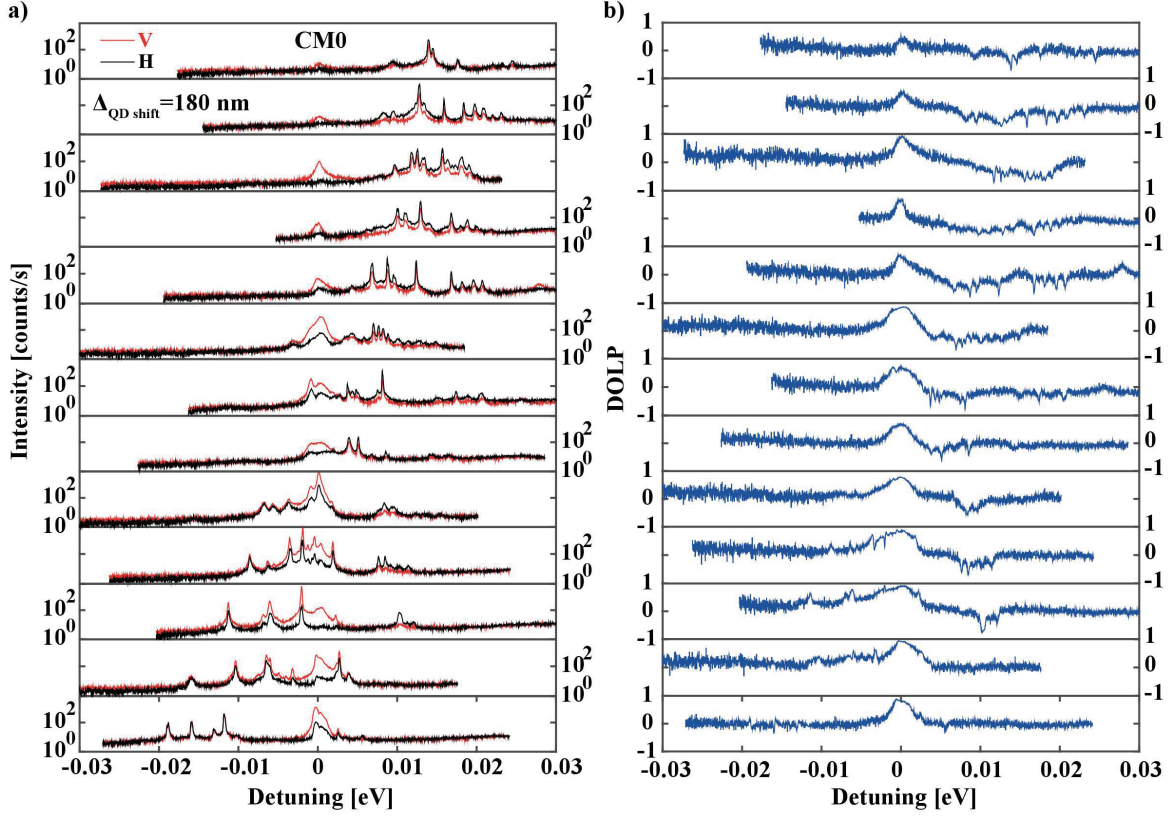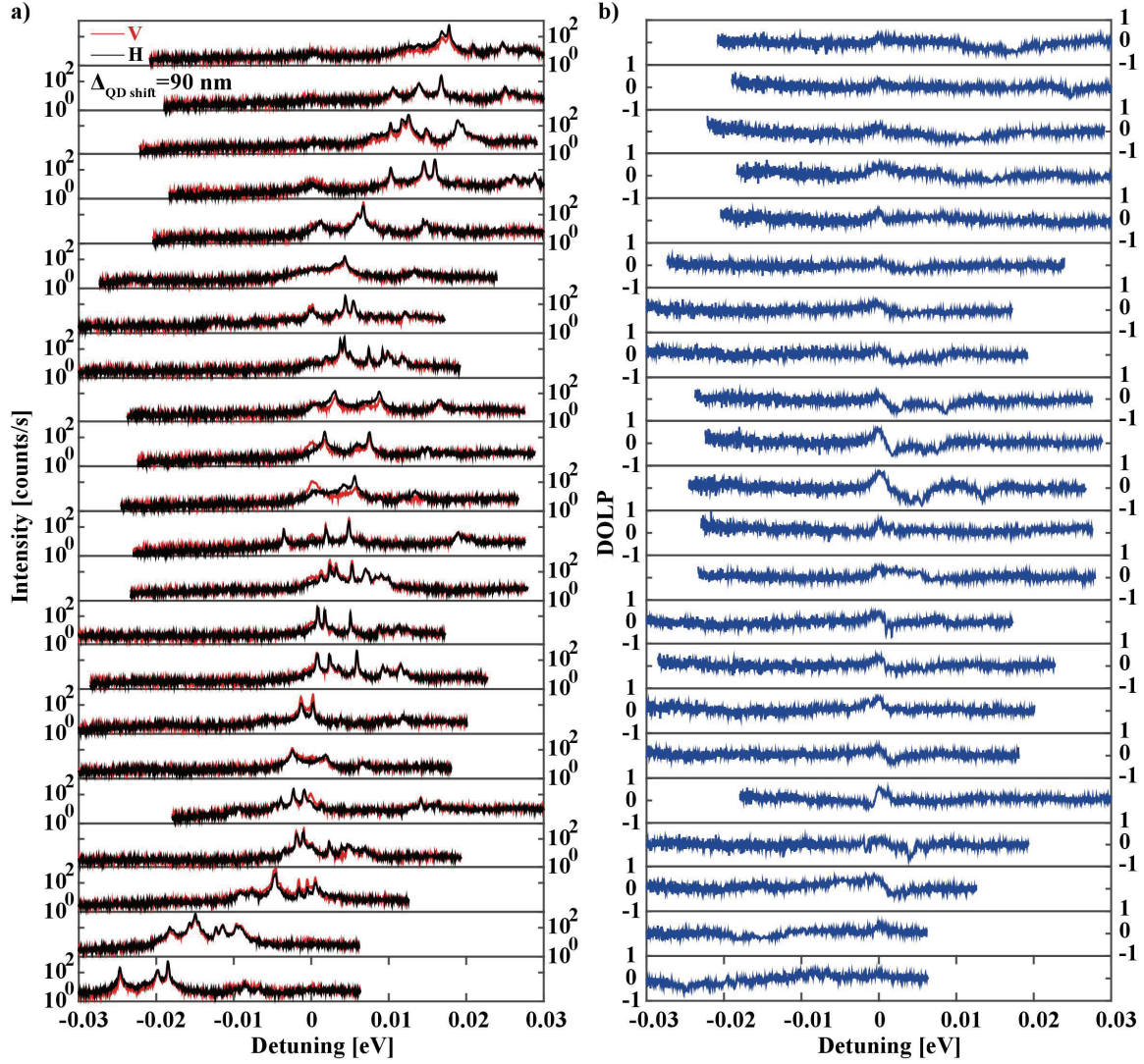
Figure 4:23 Polarization-resolved and DOLP spectra of structures with single QD shifted by Δ=90 nm from the PhC cavity center. Only spectra with the most pronounced cavity mode emission are shown here. Spectra were obtained at 10 K temperature under 300 μW excitation power.

Since for each designed Δ we implemented a thousand devices on the chip with nearly identical optical properties, we were able to run statistical study of the exciton-CM coupling as a function of the QD position inside the L3 PhC cavity. For this purpose, we analyzed polarization-resolved data measured at identical conditions (T=10 K, P=300 μW, excitation spot focused on the position of the QD), obtaining polarization-resolved integrated intensity of the main excitonic lines. Due to the large number of spectra to be analyzed, we adopted a simplified method to obtain the integrated intensity of each peak: for each excitonic line identified in the spectrum, we integrated the intensity in a 500 μeV energy window centered at the excitonic line peak energy. Identification of excitonic lines was automatized allowing to process the big sets of data measured. We filtered all peaks with prominence ($\frac{I_{min}-I_{max}}{I_{min}}$) less than 0.1 taking into account only the well-pronounced excitonic lines. Since the energy separation between the excitonic transitions is usually >1 meV, this procedure

gives very close results to the fitting with Lorentzian line shape, as we demonstrate here by comparing the two methods. The bottom panel of Figure 4:24 shows the integrated intensity of the charged exciton transition of structure 'A' obtained both through fitting with Lorentzian line shapes and by spectral integration. The fitted intensity previously shown in Figure 4:13(b) very well overlaps with the integrated intensity (bottom panel Figure 4:24). We also repeated the same procedure for the horizontally polarized emission, obtaining DOLP of charged excitonic transition (top panel of the Figure 4:24). These curves overlap with precision that is more than enough for our study.
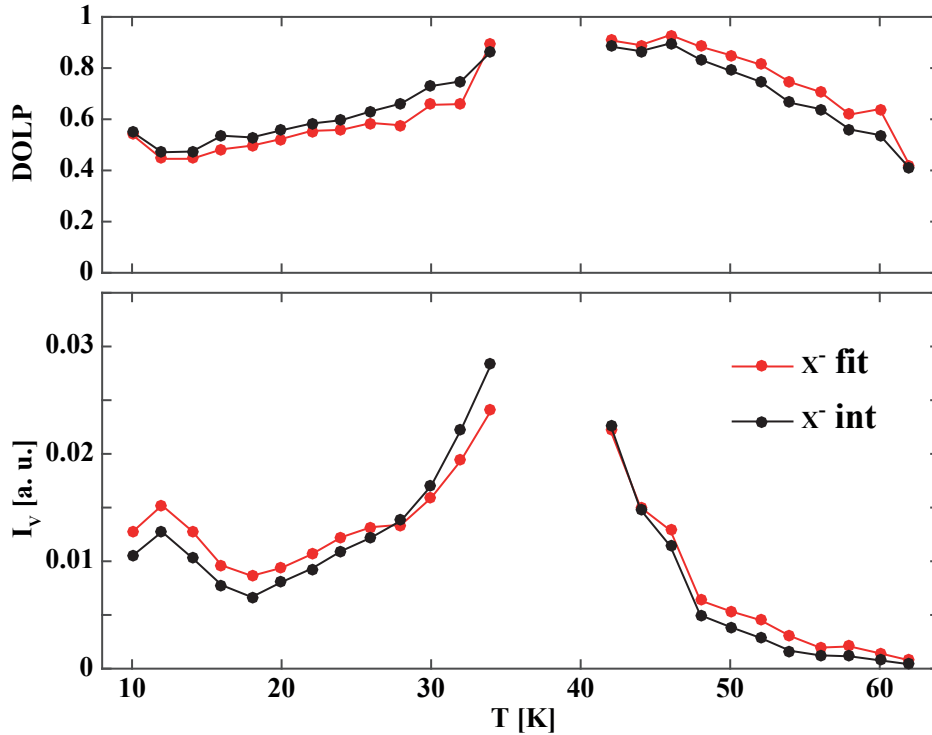
Figure 4:24 Intensity of vertically polarized emission of the X$^-$ (bottom panel) and corresponding DOLP (top panel) obtained using two different procedures. Black data points ("int") correspond to the integration in a 500 µeV energy window centered at the charged exciton energy. Red data points ("fit") were obtained through fitting of both the CM0 and the charged exciton with Lorentzian line shapes.

Figure 4:25(a, b) is a statistical summary of two QD shifts Δ=90 nm and Δ=180 nm showing polarization-resolved intensity values and corresponding DOLP of excitonic transitions as a function of exciton-CM detuning. These data points were obtained from the spectra shown in Figure 4:21, Figure 4:22 and Figure 4:23. The CM energy was manually identified for each device considering the expected energy position for the PhC hole size. With this procedure we were able to display the effect of exciton-CM coupling for the particular design, averaging over all uncertainties such as errors in the alignment of QD positioning, PhC matrix disorder that can induce fluctuations in the CM antinode position, fluctuations of the exciton dipole amplitude among different QDs, etc.

In correspondence with the polarization-resolved data shown in Figure 4:23, the statistically obtained DOLP distributions reveal smaller exciton-CM interaction for the Δ=90 nm QD shift design (Figure 4:25(b)), in agreement with the calculated CM0 field pattern; the average DOLP at resonance was less than 50%. This value corresponds to the less than 2.3-fold emission rate enhancement in the direct resonance with respect to the emission rate in the PhC bandgap. The emission rate in the PhC matrix is already suppressed in comparison with the free space case, thus the Purcell enhancement is close to unity; that is, there is almost no emission enhancement as compared to emission into free space. This is also well visible in the bottom panel of the (Figure 4:25(b)) since the intensity data points are randomly scattered showing no enhancement of the vertically polarized emission component. In opposite, devices with Δ=180 nm QD shift provide much higher exciton-CM0 co-polarization in the direct resonance with very pronounced intensity enhancement (decrease) of the vertically (horizontally) polarized emission. Vertically polarized emission intensity was enhanced by more then the order of magnitude while horizontally polarized emission intensity was suppressed by ~3 times for $\Delta = 180$ nm relative to $\Delta = 90$ nm QD shifts.

We also observed higher fluctuations in DOLP values for devices with Δ=90 nm, which can be explained as following. For the small deviations Δx, near the CM field node, the field is linear in Δx, that is, $E_{CM}(x + \Delta x) - E_{CM}(x) \approx 2\pi \frac{\Delta x}{\lambda} E$ since the electrical field of the mode can be estimated as $E_{CM}(x) = E \sin 2\pi \frac{x}{\lambda}$. At the CM antinode the electrical field is quadratic in Δx providing $E_{CM}(x + \Delta x) - E_{CM}(x) \approx -2E(\pi \frac{\Delta x}{\lambda})^2$. Since the exciton-CM coupling $g \propto E_{CM}$, for randomly distributed Δx we expect the largest coupling strength variations near the CM node. Therefore, we expect bigger DOLP fluctuations for the devices with Δ=90 nm shifted QD due to the PhC matrix disorder as well as the QD position fluctuations

It should be also noticed that our QD size is around 20 nm. Therefore, it is never at the exact zero CM field point due to its finite size. Assuming that the amplitude of the electrical field depends only on the distance from the CM node located at the position $\vec{r}_0$ we can estimate an electrical field value at the position $\vec{r}$ in the close proximity of the CM node as $E_{CM}(r) \approx 2\pi \frac{|\Delta\vec{r}|}{\lambda} E$ where $\Delta\vec{r} = \vec{r} - \vec{r}_0$. Considering QD as a disk with a diameter D and a height small enough for neglecting electrical field amplitude variations over vertical direction we get an average electrical filed over the QD as $\bar{E}_{CM} \approx \frac{2\pi D}{3\lambda} E$. Therefore, the minimum coupling strength is $g_{min} \approx \frac{2\pi D}{3\lambda} g_{max}$. For the QD size $D \approx 20$ nm and wavelength $\lambda \approx 340$ nm we obtain $g_{min} \approx 0.1 * g_{max}$ that provides $g_{min} \approx 5$ μeV for our coupling strength values[167]. However, these calculations do not include the exciton's electrical density distribution over the QD that could decrease the minimum coupling strength due to electron density bunching in the center of the QD.
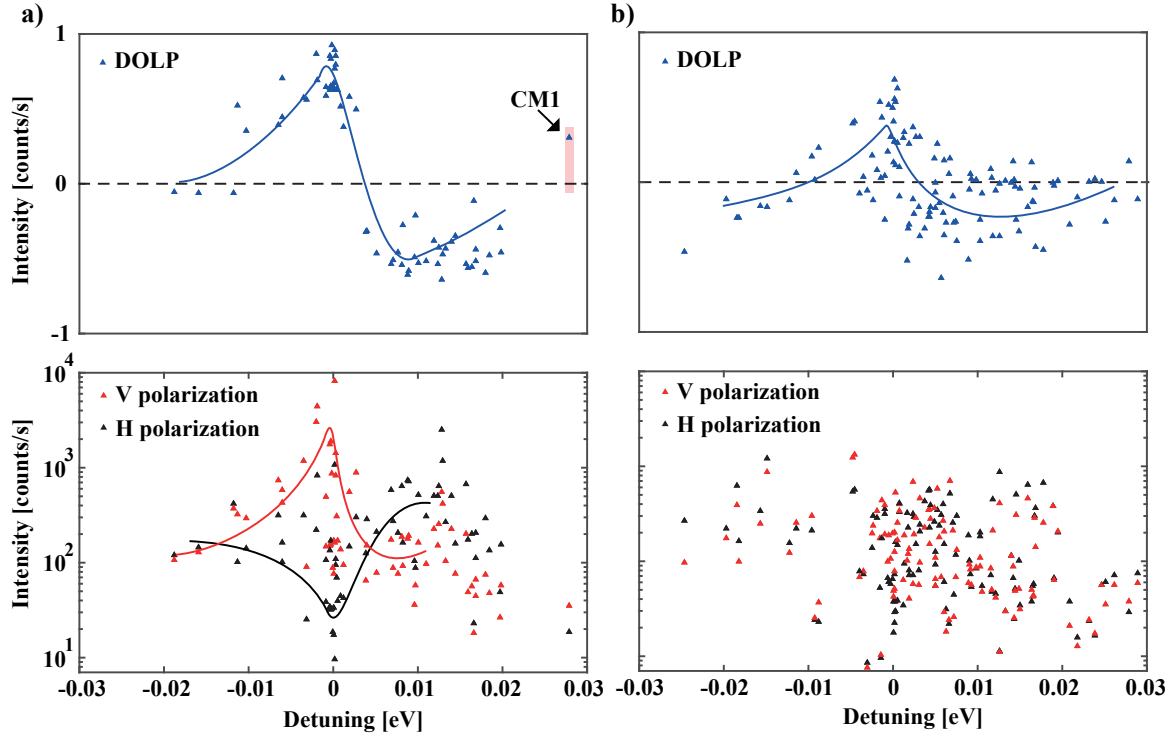
Figure 4:25 Polarization-resolved DOLP (top) and intensity (bottom) obtained for two groups of devices with Δ=180 nm (a) and Δ=90 nm (b) (extracted from spectra shown in Figure 4:21 and Figure 4:23). All data were obtained at 10 K temperature under 300 µW excitation power. Black and red points in b) are integrated intensities of horizontally and vertically polarized excitonic emission components.

Applying this procedure to the devices with Δ=0, Δ=90, Δ=120 and Δ=180 nm QD shifts, we clearly observe the difference in exciton-CM0 coupling in both the integrated polarization-resolved intensity as well as the corresponding DOLP spectra (Figure 4:26(a, b)). Devices with the QD at Δ=0 and Δ=180 nm CM0 antinodes reveal very pronounced exciton-CM0 co-polarization at resonance. Devices with QD at the node (Δ=90 nm shift) and at the half maximum of the CM0 antinode (Δ=120 nm shift) reveal correspondingly very low or moderate co-polarization with CM0. This result is in good correspondence with the calculated CM0 field distribution (Figure 4:1).
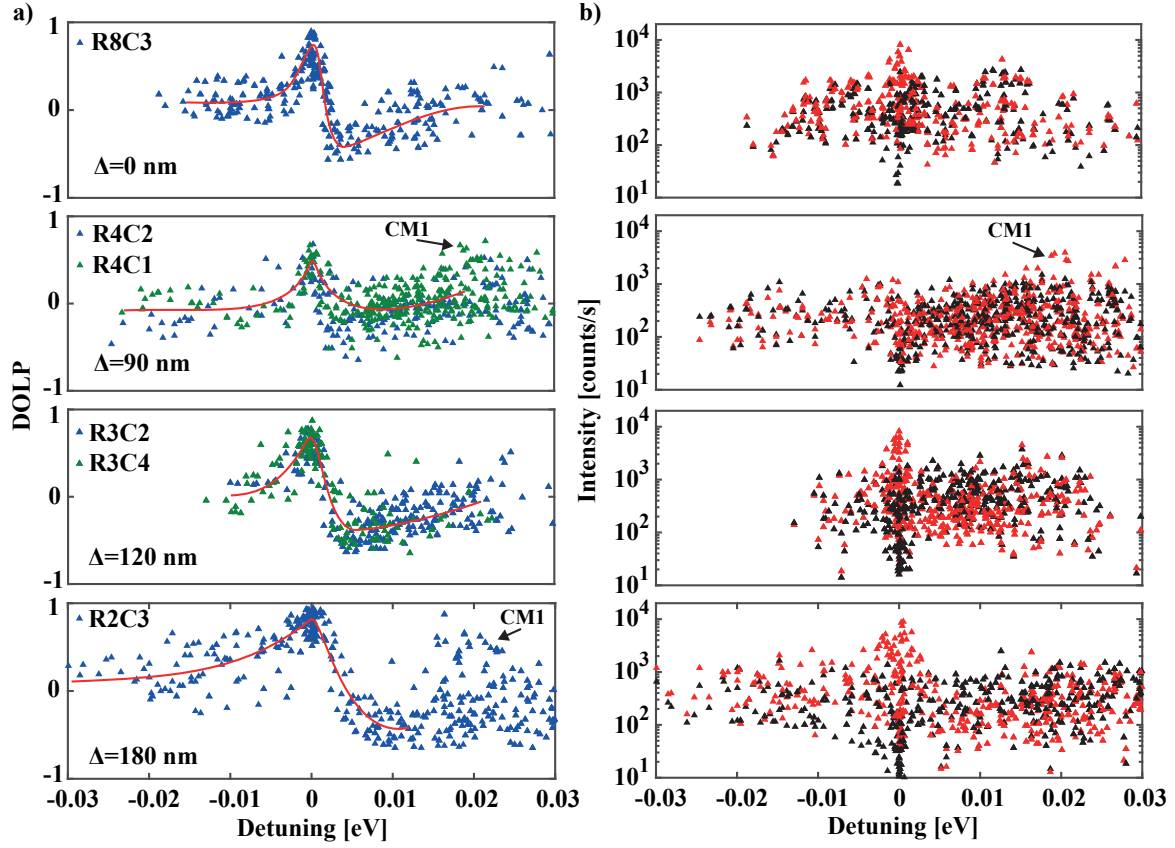
Figure 4:26 DOLP (a) and polarization-resolved intensity (b) of excitonic lines for 0 nm, 90 nm, 120 nm and 180 nm QD positions in an L3 PhC cavity versus detuning from resonance $E - E_{CM0}$ obtained in several hundred of different devices for each QD position design. The red curves in the DOLP spectra serve as the guides for the eye. Corresponding spectra were obtained at 10 K temperature under 300 μW excitation power. Black and red points in b) are integrated intensities of horizontally and vertically polarized excitonic emission components.

We were not able to see the impact of the difference in the exciton-CM0 overlap between the structures with Δ=0 and Δ=180 nm shifts. This is due to at least ten-fold enhancement of the emission rate through the CM0 (Γ_{CM}) in comparison with the emission rate through the spontaneous decay channel (Γ_{PhC}). Thus, we assume the ratio between these decay channels as $k = \frac{\Gamma_{PhC}}{\alpha \Gamma_{CM}} \ll 1$ where α is a rate between y and x polarized mode collection efficiencies.. Then, the degree of linear polarization can be estimated as $DOLP \approx 1 - 2k$. Thus, the DOLP variance is proportional to the variance of the rate k, that is, $\Delta DOLP \approx -2\Delta k$. If we compare two very small ratios k_1 and k_2 where $k_1 < k_2 \ll 1$ then $|\Delta DOLP| < 2k_2 \ll 1$. Due to the high scattering of the DOLP data points it is hard to distinguish between DOLP values that are different by less than 0.2. However, we succeeded in the probing of the CM zero field point, which is already a very challenging task. This achievement is possible due to the site- and spectral-control of our pyramidal QDs.

At positive detuning, the intensity and DOLP data points show clear dominant horizontal polarization for all QD shifts Δ except Δ=90 nm. This s-shape behavior explained above was observed pre-

viously in a single QD-PhC cavity system with Δ=0 nm[15]. Remarkably, this effect is quenched if the CM0-QD coupling strength is zero as clearly observed in DOLP of devices with Δ=90 nm shifted QD (Figure 4:26(a)). Increasing the QD-CM0 overlap at the second CM0 antinode recovers the predominant horizontal excitonic polarization at the positive detuning, as can be seen in the emission of devices with Δ=120 nm and Δ=180 nm shifted QDs. As was noted before, this observation can be explained by the interference between spontaneous emission and emission through the CM. It could be assumed that reducing the QD-CM overlap would suppress exciton decay through the CM eliminating the interference effect between spontaneous and CM channels. However, the CM can still regain a photon emitted into free space by the exciton and vice versa. The result of such free space modes back action is complete suppression of the QD emission at the zero detuning point if the exciton-CM coupling strength is nearly zero. Therefore, the s-shaped suppression observed for Δ=90 nm could be due to phase $\varphi = {}^{\pi}/_{2}$ or reduced spatial overlap χ for a QD shifted the CM node.

4.4.2 Probing the spatial profile of the first excited CM1 mode

We applied the procedure described above for probing the exciton-CM1 coupling efficiency. The first excited cavity mode CM1 has a different field pattern than the CM0 one (Figure 4:1). QDs shifted by Δ=0 and Δ=120 nm fall into the zero CM1 field points while Δ=90 nm and Δ=180 nm shifted QDs match the first and the second CM1 antinodes at their FWHM. Thus, we expect very low co-polarization for Δ=0 and Δ=120 nm QD shifts while Δ=90 and Δ=180 nm should provide much higher co-polarization with this mode. Figure 4:27 shows polarization-resolved and DOLP spectra obtained for Δ=180 nm QD shift. All these devices form a complete set of structures with the same PhC hole radii for square R2C3 providing the lowest exciton-CM1 detuning. For all of these devices the excitonic transitions are strongly co-polarized at resonance while their emission intensity is enhanced by ~1 order of magnitude. The CM0 peak is also visible at the lower energies revealing ~20 meV splitting between CM0 and CM1 (Figure 4:27(a)).
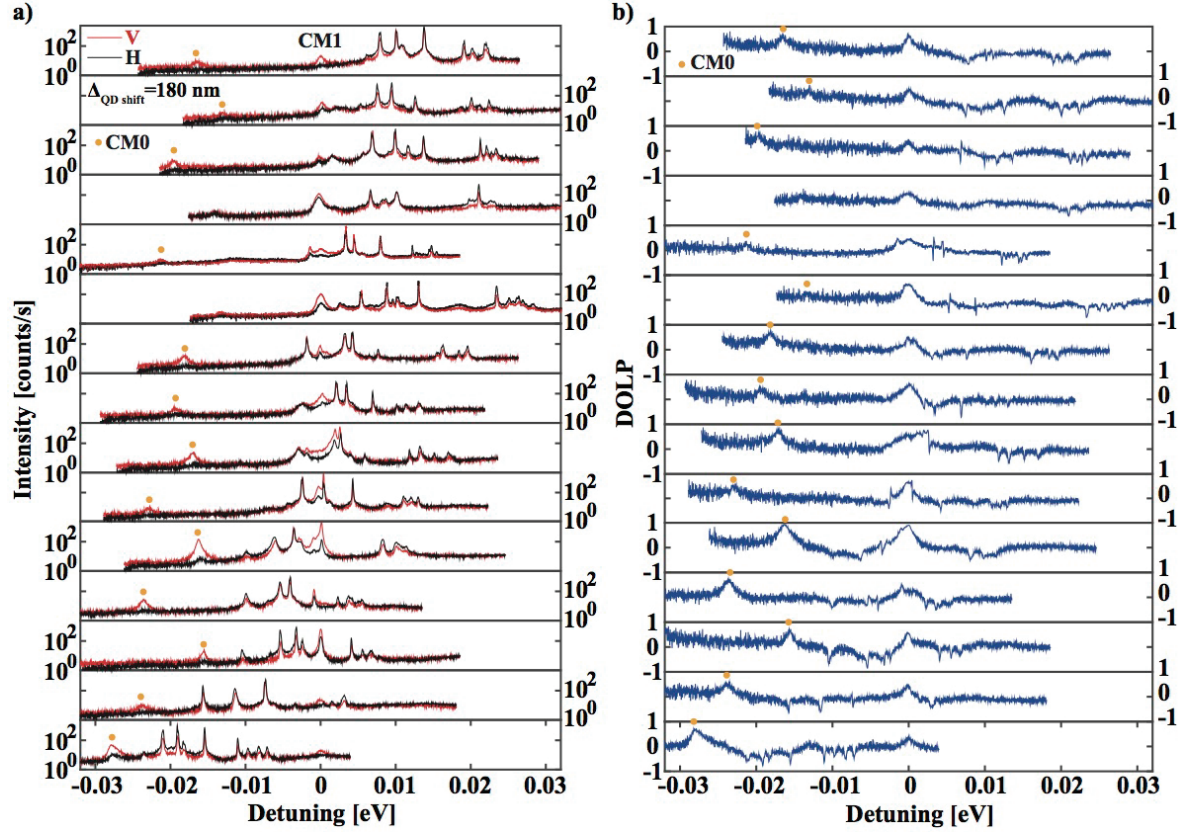
Figure 4:27 Polarization-resolved (a) and DOLP (b) spectra of structures with a single QD shifted by 180 nm from the PhC cavity center showing spectral scanning of the CM1 by single QD transitions. Here detuning corresponds to $E - E_{CM1}$. Spectra were obtained at 10 K under 300 μW excitation power.

For the structures with the Δ=90 nm, CM1 was much less visible than for Δ=180 nm shifted QD (Figure 4:28). It should be noticed that contrary to the devices with Δ=180 nm, we did not observe off-resonance CM0 emission for Δ=90 nm. Taking into account the nonzero QWR-CM spatial overlap for all QD shifts, suppression of off-resonant cavity mode emission directly confirms that only the QD transitions pump the cavity modes spectrally detuned by ~50 meV from QWR emission energy.
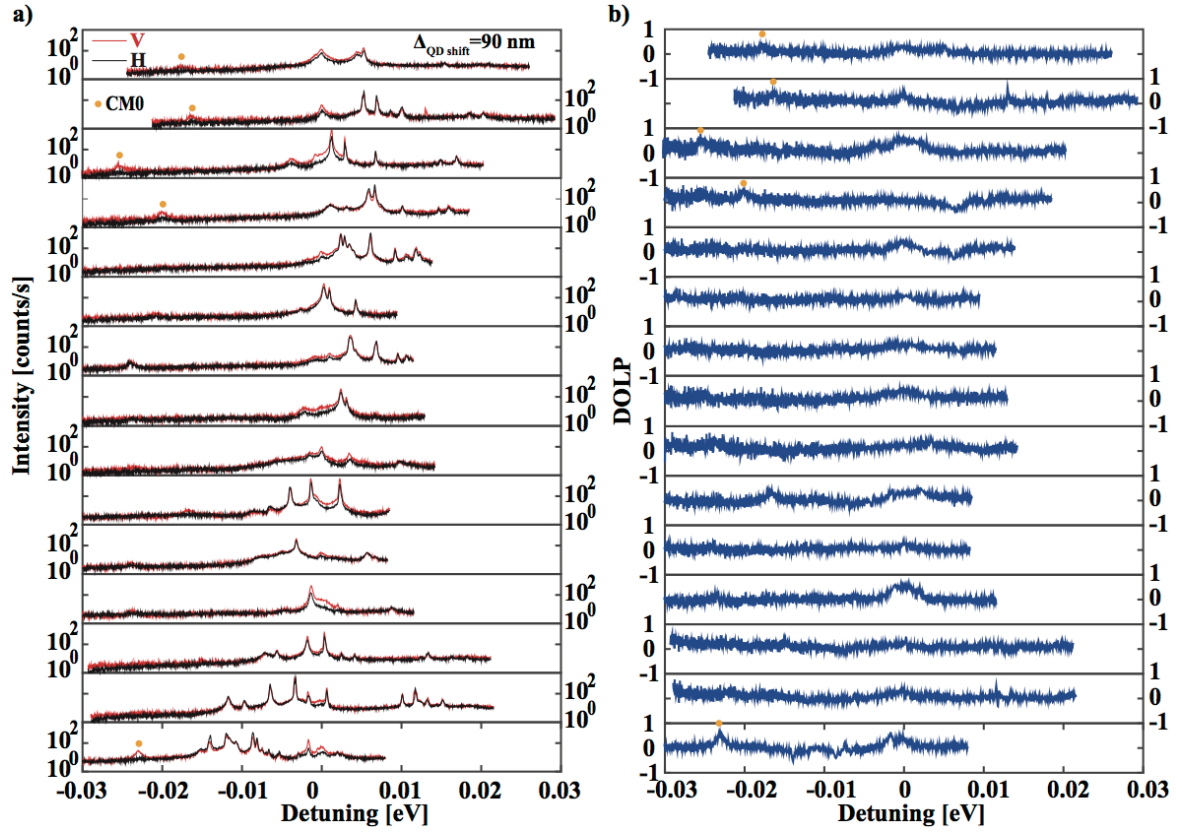
Figure 4:28 Polarization-resolved and DOLP spectra of structures with single QD shifted by 90 nm from the PhC cavity center. Only spectra with the most pronounced cavity mode emission were chosen. Here detuning corresponds to y $E - E_{CM1}$. Spectra were obtained at 10 K under 300 μW excitation power.

Figure 4:29(a, b) shows the integrated intensity for the two polarizations and corresponding DOLP, summarizing the effect of QD shift on the QD-CM1 coupling efficiency. We were able to identify only a few structures with Δ=0 shifted QD with CM1 spectral fingerprints, therefore just a few data points are available for structures with Δ=0 nm. Exciton-CM1 co-polarization was very low for this design as can be seen in the top panel of the Figure 4:29. Structures with Δ=90 nm and Δ=120 nm revealed very similar exciton-CM1 co-polarization with DOLP around 0.5, although in these structures CM1 modeling predicts different QD-CM1 overlaps (Figure 4:1). We assume that the high scattering of the data points hid the DOLP difference for these structure designs. Since the Δ=90 and Δ=120 nm shifts put the QD between the CM1 node and antinode, these positions provide smaller difference in the QD-CM1 overlap in comparison with the structures having QD at the CM node and antinode (Δ=0 nm and Δ=90 nm (Δ=180 nm) in the case of the CM0). Thus, the scattering of DOLP points due to the PhC matrix disorder as well as the QD position fluctuations could overcome the difference of the DOLP values of these devices. Devices with Δ=180 nm reveal the strongest co-polarization of the excitonic transitions with respect to CM1. This is expected, since the CM1 pattern is bunched at the edges of the PhC cavity, providing higher field amplitude for the second CM1 antinode as can be seen in Figure 4:1b).
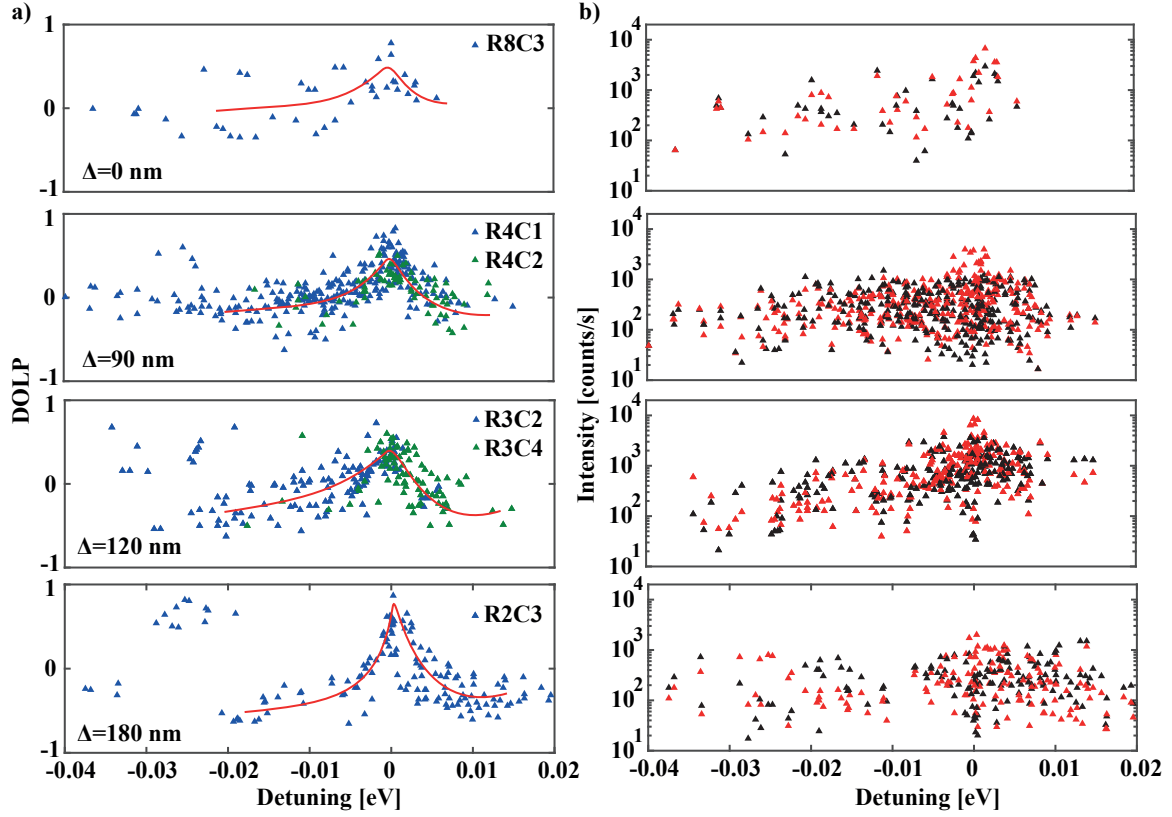
Figure 4:29 DOLP (a) and polarization-resolved intensity (b) spectra of individual excitonic lines for Δ=0 nm, 90 nm, 120 nm and 180 nm QD positions in an L3 PhC cavity. Here detuning corresponds to $E - E_{CM1}$. The red curves in the DOLP spectra serve as guides for the eye. Corresponding spectra were obtained at 10 K under 300 µW excitation power. Black and red points in b) are integrated intensities of horizontally and vertically polarized excitonic emission components. Off-resonant CM0 peaks lead to the vertically polarized points in a) at around -25 meV detuning.

4.5 Tuning the predominant horizontal polarization at positive exciton-CM detuning

As was mentioned previously, QD transitions with sufficient QD-CM overlap show predominantly horizontally polarized emission at 2-5 meV positive detuning, thus revealing the s-shape like behavior in the DOLP spectra as explained by the interference in the exciton direct and indirect decay channels. Paying attention to this interference process, we studied the effect of the QD position inside an L3 PhC cavity on this s-shape behavior. Interestingly, we observed s-shapes with nearly vanishing visibility for the QD shifted to the CM0 node. We proposed several mechanisms that could lead to this effect. This effect is remarkable since it further highlights the role of the CM in the appearance of the s-shape behavior.

Figure 4:30(a, b) shows polarization-resolved and DOLP spectra obtained for structures with Δ=90 nm. We chose here devices with QD excitons in between CM0 and CM1 assuring the positive detuning of the excitons with respect to CM0. We did not observe s-shape behavior in these devices.

Instead, all excitonic transitions are almost perfectly unpolarized as can be seen in both the polarization-resolved and the DOLP spectra in Figure 4:30(a, b). Thus, we show unambiguously that the s-shape is eliminated for structures with nearly zero CM-exciton coupling strength.
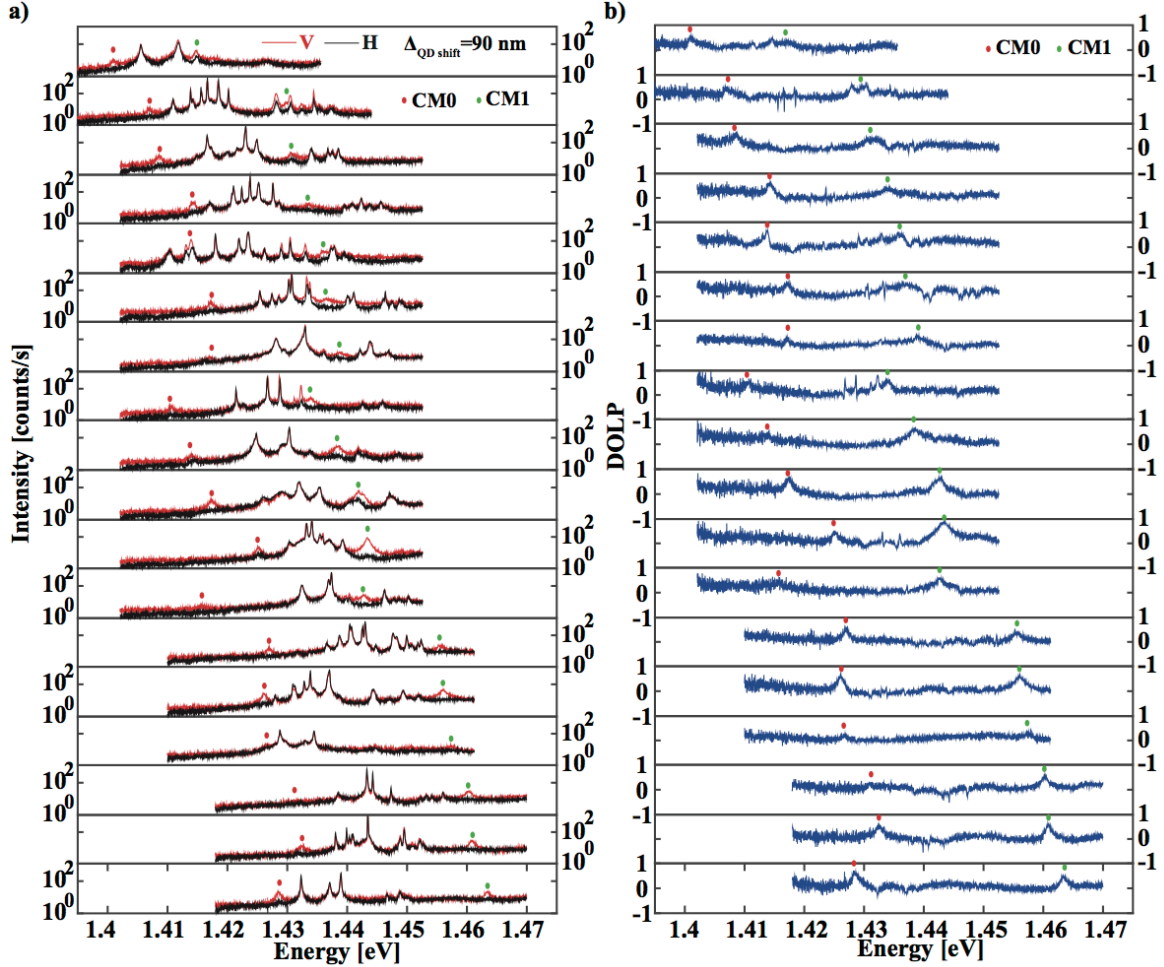
Figure 4:30 Polarization-resolved (a) and DOLP (b) spectra of QDs placed at the first antinodes of CM0 (Δ=90nm). Spectra were obtained at 10 K under 300 µW excitation power.

We obtained statistics of this effect from measurements of several tens of devices that have QD excitonic transitions between CM0 and CM1, that is, for the positive detuning from the CM0 (see Figure 4:31). Remarkably, we prove statistically that devices with important exciton-CM0 overlap (Δ=0nm) have a clear horizontal polarized emission at positive detuning while structures with very small excition-CM0 overlap (Δ=90 nm) reveal nearly zero vertical polarization of the excitonic transitions. This finding is robust against averaging over different devices that could potentially have nonzero fluctuations of the exciton-CM coupling strength. These fluctuations remain negligible due to high site-control precision of our QD structures as well as the control over the PhC hole size.
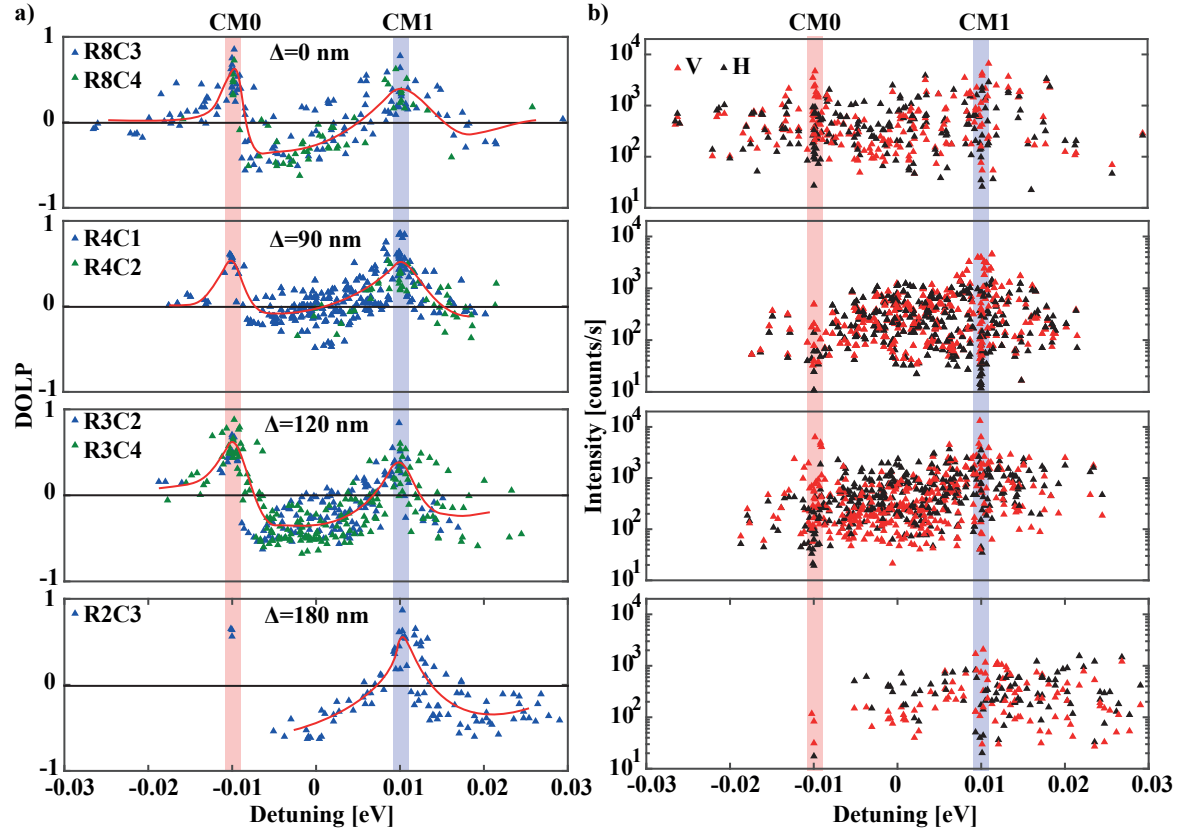
Figure 4:31 DOLP (a) and polarization-resolved intensity (b) for different QD shifts. Here detuning corresponds to the normalized detuning $\frac{0.02\ eV}{E_{CM1}-E_{CM0}}(E-\frac{E_{CM0}+E_{CM1}}{2})$ between emission peaks and the center energy of CM0-CM1 doublet $\frac{E_{CM0}+E_{CM1}}{2}$. The red curves in the DOLP spectra (a) serve as guides for the eye. Corresponding spectra were obtained at 10 K under 300 µW excitation power. Black and red points in b) are integrated intensities of horizontally and vertically polarized excitonic emission components.

Interestingly, the interference effect at the origin of the s-shape does not disappear if the exciton-CM coupling strength nearly vanishes. Instead, the interference appears exactly in the resonance therefore the excitonic emission becomes predominantly horizontally polarized at zero detuning. Figure 4:32(a, b) show modeling of the exciton emission rates through vertically polarized free space modes and DOLP for a set of exciton-CM coupling strength values. This modeling is obtained using the Wigner approximation as was discussed in the section 1.4.2.2. As the exciton-CM coupling strength approaches zero, the minimum of the exciton emission rate shifts to the zero detuning point following the relationship $\frac{g}{\chi\cos\varphi}\left(\sqrt{\frac{\gamma_V}{\kappa}}-\sqrt{\frac{\kappa}{\gamma_V}}\right)$ as can be seen in Figure 4:32(a). For nearly zero coupling strength the excitonic transition is everywhere unpolarized except the small spectral region near zero detuning (Figure 4:32(b)). Therefore, even for vanishing exciton-CM coupling the s-shape is conserved in the form of a DOLP dip at zero detuning (Figure 4:32(b)).
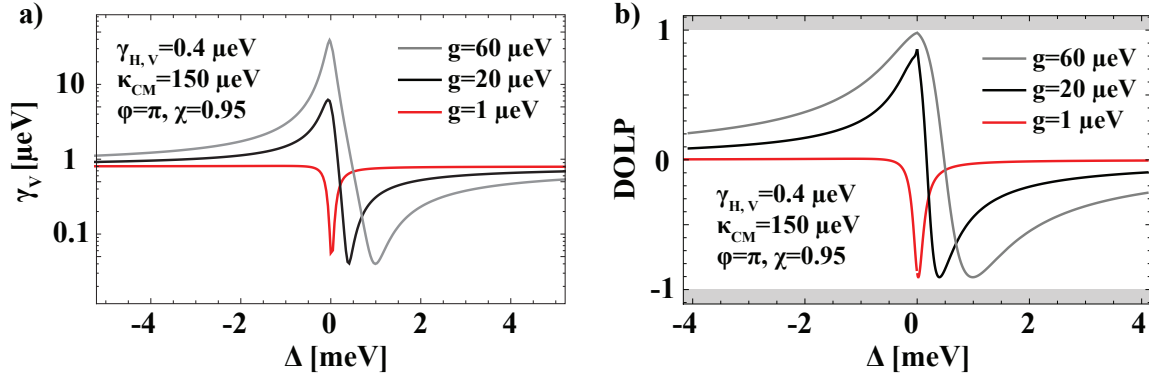
Figure 4:32 Calculated exciton decay rate (a) and DOLP (b) for a set of exciton-CM coupling strengths.

However, in our experiments the s-shape almost completely vanished for the structures with nearly zero coupling strength (Figure 4:31). This discrepancy with the modeling can be explained by either changes in the phase φ between direct and indirect decay channels or lowering of the spatial overlap χ due to QD shifts. Another reason can be pure dephasing that can potentially reduce the visibility of the interference picture below resolution of our system. However, we cannot estimate the effect of pure dephasing as it is not accounted for by our model. It should be noted that in the section 5.5.2 we will demonstrate the predominant horizontal emission of the QDs integrated with an L7 PhC cavity having excitons at (spectral) resonance with a CM they do not couple with. These excitonic transitions have identical optical characteristics including the pure dephasing as in the samples discussed in the present chapter. Since the possible explanation of this effect is the interference between direct and indirect exciton decay channel, we doubt that the vanishing of the s-shape for the 90 nm QD shift appears due to pure dephasing processes.

4.6 Conclusions

In this Chapter we first discussed the expected difference between the polarization properties of charged and neutral excitons as well as the biexciton, which is crucial for mapping exciton coupling strength with an optical field. Using both time-resolved and polarization-resolved measurements, we investigated the Purcell enhancement of the QD emission positioned exactly at the first CM0 antinode. We investigated the effect of the QD position inside the L3 PhC cavity on the exciton-CM coupling strength using the co-polarization effect. Relying on the high position and energy control of our QDs, we eliminated Purcell enhancement by positioning the QD exactly at the zero field point, and then recovered a high Purcell factor by shifting the QD further to the second CM0 antinode as was revealed by polarization-resolved measurements. In a similar manner we showed difference in coupling between the first excited CM1 and the excitonic transitions of differently shifted QDs. These observations were robust against statistical averaging over several hundreds of structures. We observed interference effects in the decay of the exciton-CM system leading to the pronounced detuning dependence of the CM polarization (DOLP exchange) as well as to the vanishing of vertically polarized emission component of QD optical transitions (s-shape). These effects are successfully explained by the interference in the direct and indirect exciton decay channels, as suggested by [43] and [186]. Varying the QD position, we suppressed the s-shape of the DOLP spectra; this effect is not yet fully understood.

Chapter 5   Coupling of site-controlled quantum dots systems to photonic crystal cavities

5.1   Introduction

Although some progress in deterministic integration of systems of semiconductor quantum dots (QDs) with photonic-confinement elements has been achieved using coupling of self-assembled QDs with different types of photonic cavities[36], [64], [66], [187], [188] control over position, energy and polarization of the QD systems is essential for the scaling up of this technology. Here, we demonstrate the deterministic radiative coupling of a system of four site-controlled pyramidal QDs[28] to prescribed modes of a photonic crystal (PhC) membrane cavity. The radiative coupling is observed in the co-polarization of the exciton and cavity lines, as well as in the Purcell enhancement of the exciton decay time.

5.2   Integration of QD- PhC L7 cavity structure

5.2.1   Structure design and implementation

Our designs for integrating multiple QDs with an L7 PhC cavity consists of two and four QDs deterministically positioned inside an L7 PhC cavity. We positioned two QDs at ±200 nm (along the x axis) from the L7 PhC cavity center ('central' position), targeting the best overlap between the fundamental mode CM0 and the QDs, as shown in Figure 5:1(a). Calculations of CM fields provided by Clement Jarlov (2D finite difference time domain, FDTD, method [171]) also predicted nonzero, nominally identical overlap between these 2 QDs and CM1 (and weak coupling to CM2). The structures with 4 QDs are shifted by ±200 nm ('central' position) and ±600 nm ('side' position) from the L7 PhC cavity center, respectively. These QDs exhibit different, but deterministic, spatial overlaps with the lobes of the three lowest order CMs, represented by their calculated near field patterns in Figure 5:1(b). Calculations predicted nearly equal overlap between all 4 QDs and CM1 antinodes, while CM0 has much stronger coupling with the central QDs and CM2 has much stronger overlap with the side QDs.
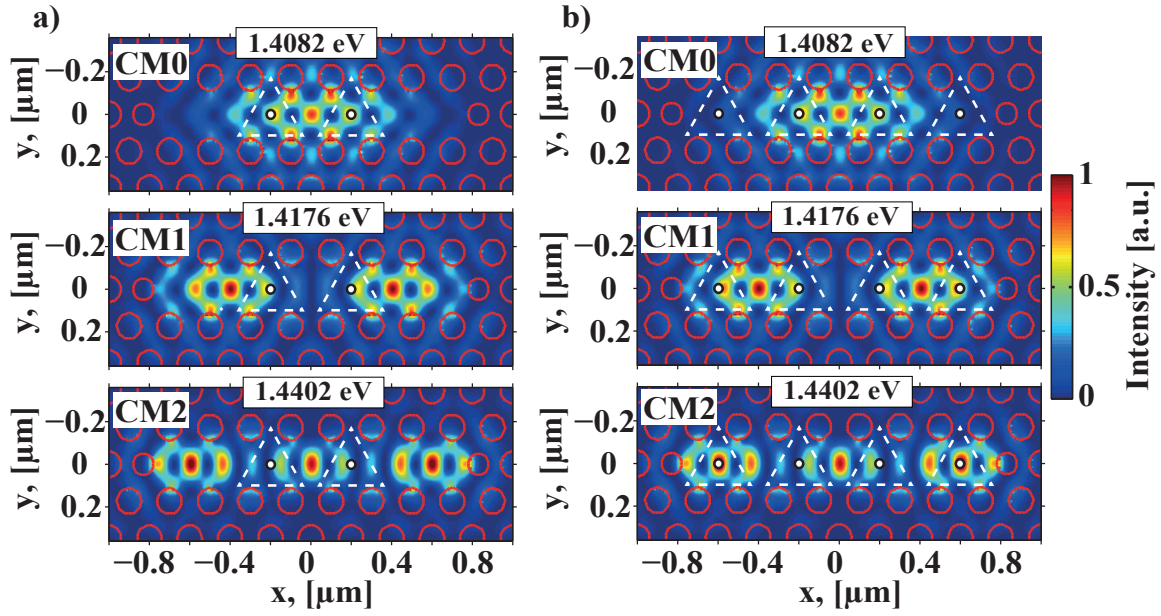
Figure 5:1 2D-FDTD calculated intensity patterns of the three lowest energy modes of an L3 PhC cavity (energies indicated). a) A device with 2 QDs. b) A device with 4 QDs. CM modelling is provided for PhC structures with hole radii r=60 nm and pitch a=200 nm [171].

5.2.2 Optical mode spectrum

Figure 5:2 shows the measured PL spectra for two L7 PhC cavities containing four QDs each. The polarization-resolved spectra were obtained for devices with PhC nominal hole radii r≈62 nm and r≈64 nm. Although we expected only 3 CMs that can spectrally overlap with QD excitonic transitions, as inferred from Figure 5:2 (a), typical spectra show up to 4 CMs (Figure 5:2(b)) with Q-factors of around 1000-3000, as obtained from their off-resonant emission. The peaks labeled CM0-3 are L7 PhC cavity resonances while other lines visible in the spectra represent excitonic transitions of the QDs. These first 4 modes are vertically polarized (Figure 5:2(a, b)). The lowest energy modes CM0 and CM1 are separated at least by ~10 meV while CM2 and CM3 are separated by ~25 meV, thus their interaction with excitonic transitions can be considered independently, since the exciton-CM coupling range is limited by phonon scattering processes to ~3 meV [72]. Energy separation between CM2 and CM3 significantly fluctuated as will be discussed in the following.
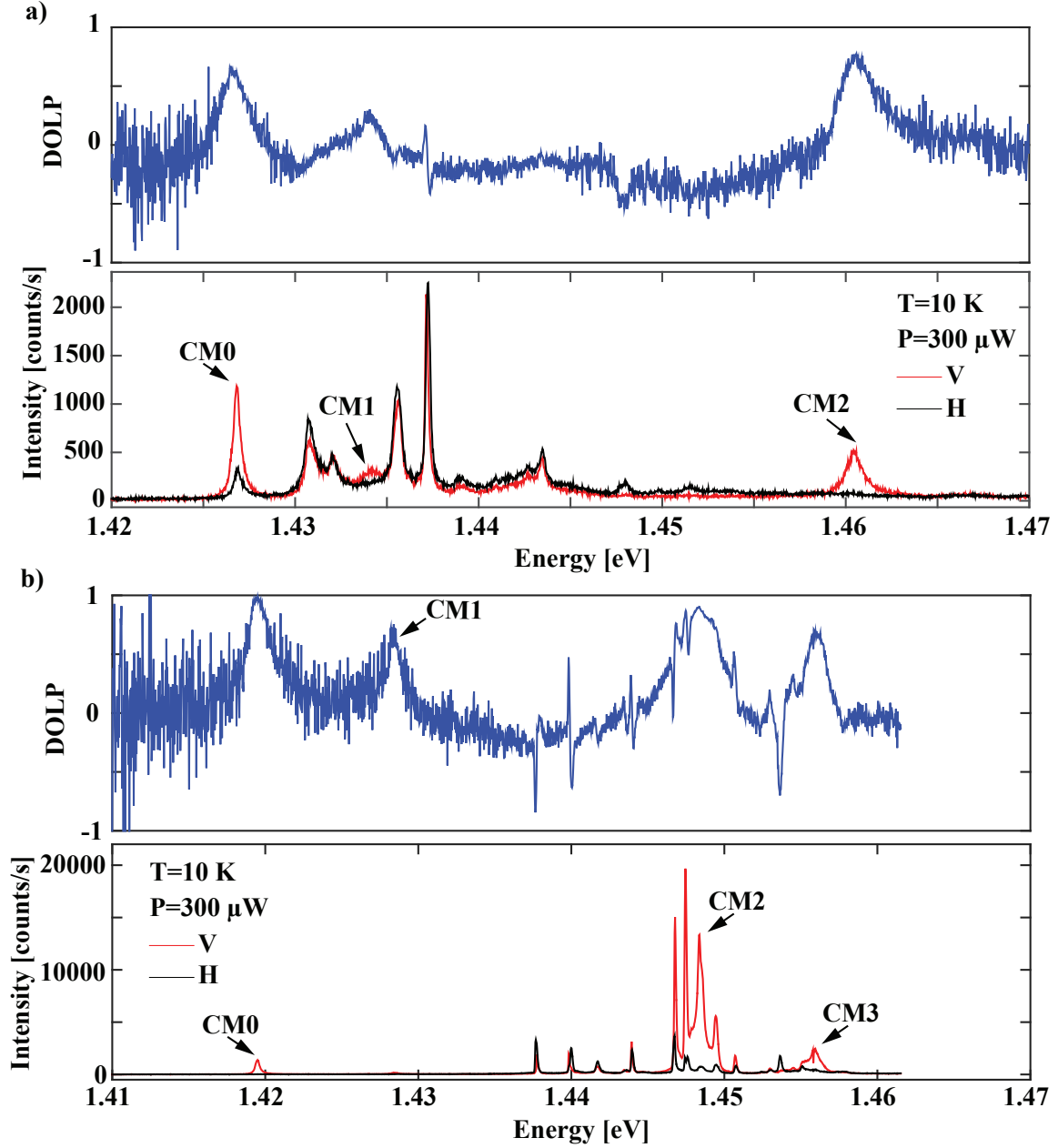
Figure 5:2 Polarization-resolved PL intensity and DOLP spectra showing the first four cavity modes CM0 – CM3. Spectra in a) and b) were obtained in devices with 4 QDs in the L7 PhC cavity with PhC hole radii r≈64 nm and r≈62 nm, respectively. T=10 K, 300 µW excitation power. No water vapor deposition was applied in this case.

Figure 5:3 (a) shows the energy positions of the CM0-CM3 modes as a function of PhC hole size, acquired from ~100 devices with 4 QDs in the L7 PhC cavity. Depending on the device position with respect to the center of the QD array (see Figure 2:15), the central energy of the QD ensemble emission varied between 1.41 eV and 1.44 eV while the inhomogeneous broadening remained below 10 meV. Thus, we were able to identify devices with ground state excitonic transitions in the

spectral vicinity of all first three CMs. We observed ~10 meV fluctuations of CM0 and CM1 reso-nance energy, corresponding to fluctuations of PhC hole radius by ±1 nm. We attribute this imper-fection to the precision of our fabrication procedure. While CM2-CM3 energy separation is ~10 meV for the structures with the lowest hole radii (the lowest CM emission energy), CM2 and CM3 converge to a single CM at higher energies as can be seen in Figure 5:3(a). Luckily, CM2 is in resonance with QD transitions in devices with the smallest PhC hole radii providing at least 10 meV separation with respect to the other CMs. Therefore, all devices with CM2 coupled with the ground state excitonic transitions can be considered independently of the other CMs.
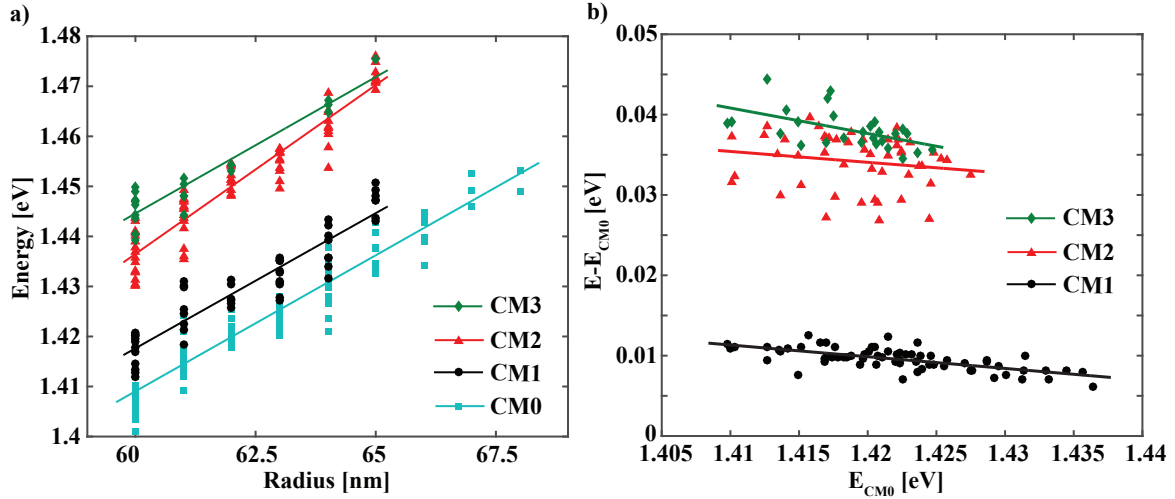
Figure 5:3 Measured energies of the first four TE cavity modes (CM0-CM3) of the L7 PhC cavities versus PhC hole radius (a); and the energy separations of the CM1-CM3 modes with respect to the CM0 one versus the CM0.

Figure 5:3(b) shows the energy of modes CM1-CM3 relative to the emission energy of CM0 as a function of the emission energy of CM0. The energy separation between CM0 and CM1-CM3 slightly decreased for structures with higher energy of CM0, that is, for structures with larger PhC hole radii (Figure 5:3(b)). The CM0-CM1 energy separation fluctuates by a few meV while CM0-CM2 and CM0-CM3 energy separations are much more dispersed as expected for higher energy confined levels. Although we did not find higher CMs in the energy region below 1.48 eV using this statistical study, additional CMs were observed at higher energies with respect to the CM3 by variations of the DOLP value of the QD excitonic transitions while they are tuned in and off reso-nance with these modes (see section 5.5). These modes showed lower interaction with the QDs as well as lower quality factor, which leads to CM-exciton 'bad cavity' coupling regime, explaining their absence in the off-resonant emission of the QWR transitions (1.47-1.48 meV) and QD excited state (1.45-1.46 meV).

5.3   Probing CM near fields with sets of QDs

5.3.1   Probing the spatial distribution of CM0

Devices with the two and four symmetrically positioned QDs provide a perfect playground for probing QD-CM spatial overlaps. Symmetrically positioned QDs provide twice as rich spectral structure in comparison with a single QD integrated with the L7 PhC cavity, increasing the possibil-

ity of spectral overlap between excitonic transitions and prescribed CMs. In the following we demonstrate how designs presented in Figure 5:1(a, b) could be used for probing an overlap of L7 PhC cavity modes with point dipoles at deterministic positions.

Figure 5:4(a, b) shows typical polarization-resolved PL and DOLP spectra measured for devices with two QDs (±200 nm shifts, "central" QD position) integrated with the L7 PhC cavity. Panels in Figure 5:4(a) show polarization-resolved spectra obtained in devices with increasing PhC hole radii from 60 to 64 nm. We used very high excitation power in order to saturate the QD excitonic transitions and provide sufficient pumping of all CMs, to increase the signal to noise ratio of our CMs strongly highlighting their positions.

Mainly CM0 and CM2 are visible in these spectra while the intensity of the CM1 and CM3 modes are negligible, providing qualitative measure of the CM0-CM3 coupling with 'central' QDs. While the apparent 'central' QD coupling with CM0 is in good correspondence with the calculations of the near field pattern (Figure 5:1), higher order modes show unexpected behavior. According to the calculated CM1 pattern, it should be well coupled with both 'central' and 'side' QDs (Figure 5:1). However, QD excitons in resonance with the CM1 showed very weak co-polarization effect. Moreover, this mode is much weaker in resonance than the off-resonance emission of the CM0 as can be seen in several spectra in Figure 5:4(a). Thus, we conclude that direct coupling of excitonic emission to the free-space modes is much stronger than the coupling to the CM1.

According to the calculations of the near field pattern of CM2 'central' QDs slightly overlap with weak CM2 antinodes at ±200 nm (Figure 5:1(a)). However, this mode is well visible in the polarization-resolved and DOLP spectra in Figure 5:4(a, b)). Additional mode CM3 is very weak in all spectra thus we also conclude that this mode has very small coupling with 'central' QDs that is a sign of the small CM3 electrical field amplitude at ±200 nm of the L7 PhC cavity. Interestingly, this observation correspond to the modeling of the second excited mode ('CM2') as can be seen Figure 5:1(a).

Figure 5:4 Polarization-resolved PL (left) and DOLP (right) spectra of L7 PhC cavities containing 2 QDs shifted by ±200 nm from the cavity center. Nominal PhC hole radii increase, from top to bottom, from 60 to 64 nm with 1 nm step, providing systematic CMs shift to the higher emission energies by ~6 meV steps.

We probe 'side' QD coupling with the L7 PhC CM0-CM3 using 4 QD in L7 PhC cavity devises (Figure 5:1). These structures with 4 QDs positioned at ±200 nm and ±600 nm from the L7 PhC cavity center provided much better pumping of the CM1 and CM3 then 2 QD in L7 PhC cavity structures as concluded from polarization-resolved measurements. Figure 5:5(a, b) shows polarization-resolved and DOLP spectra of 4 QD in L7 PhC cavity structures with well visible CM0-CM3 peaks. These spectra were obtained in 5 devices with nominal PhC hole radii varying between 60 nm and 64 nm from top to bottom panel. Higher intensity of the CM1 and CM3 in polarization-resolved spectra of structures with 4 QDs (Figure 5:5(a)) than with 2 QDs (Figure 5:4(a)) in L7 PhC cavity highlights better coupling of these modes to the 'side' than with 'central' QDs. It can be seen that CM2 and CM3 converge to the same energy position as was already shown in Figure 5:3(b). This effect was not observed in calculations since only a single mode was observed at the CM2-CM3 energy region. We assume that it can be attributed to fabrication disorder.
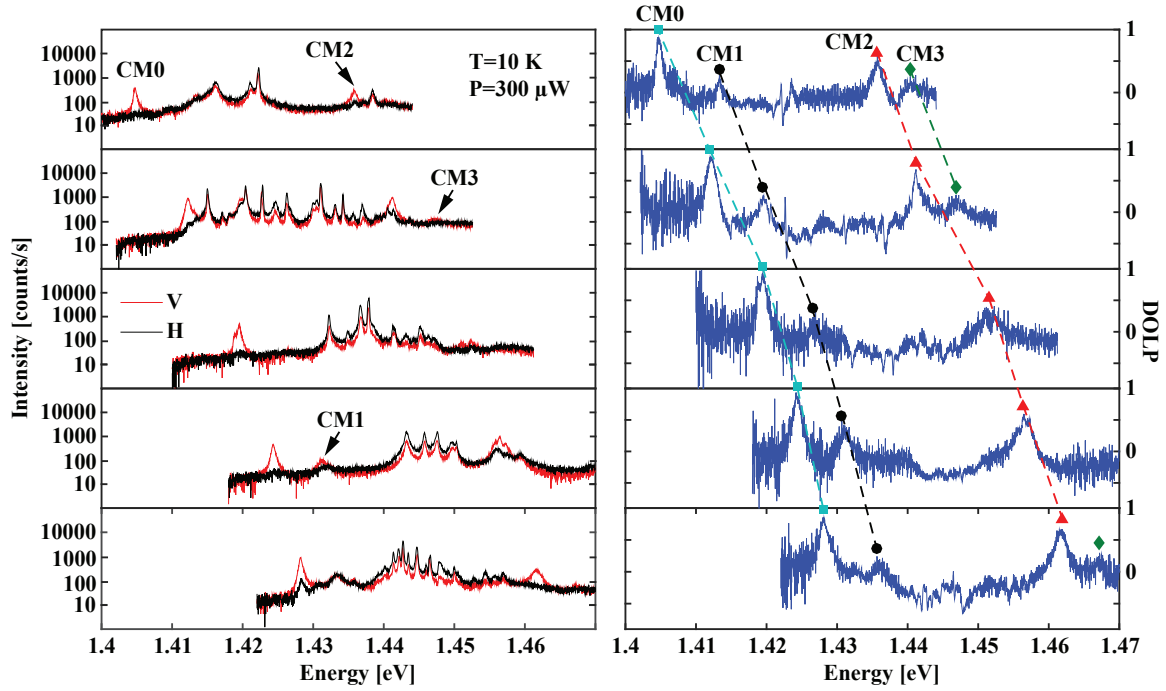
157
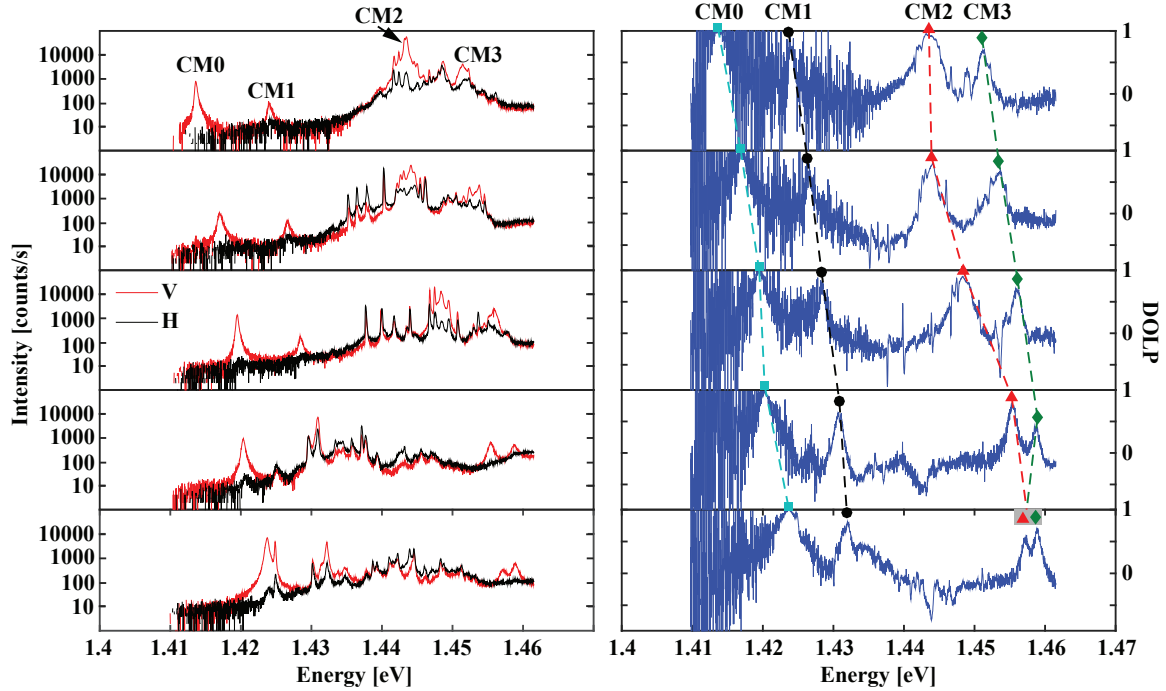
Figure 5:5 Polarization-resolved PL (left) and DOLP (right) spectra of L7 PhC cavities containing 4 QDs shifted by ±200 nm ('central' position) and ±600 nm ('side' position) from the cavity center. Nominal PhC hole radii increase, from top to bottom, from 60 to 64 nm with 1 nm step providing CMs shift to the higher emission energies by ~6 meV steps.

All devices revealed predominantly horizontal polarization in-between modes as can be seen in DOLP spectra in Figure 5:5. We assume that this effect is caused by the same interference process as in case of the single QD coupled to the CM (section 4.5). In case of 4 QDs it is hard to predict the phase between the QD excitonic emission through spontaneous decay channel and through different CMs. Therefore, we expect predominant horizontal polarization appearing at different detuning sign for different QD positions as well as for different CMs.

Using the same type of statistical study previously applied for a single QD in L3 PhC cavity (Chapter 4) we proved the difference in CM pumping between 2 and 4 QDs in the L7 PhC cavity. Figure 5:6 shows the DOLP and polarization-resolved intensity of different emission lines as a function of spectral position with respect to the average of CM0 and CM2 (a, b), and to the average of CM0 and CM1 (c, d). For this purpose, we integrated the intensity of each excitonic transition in a 500 μeV window as described before (section 4.4). We normalized the energy axis for each analyzed spectra in such a way that a chosen pair of CMs always falls at the same energy positions. For example, in Figure 5:6(a, b) we extracted the mean energy of all CM0 and CM2: $\frac{E_{CM0}+E_{CM2}}{2}$ from the energy of excitonic transitions. Thus, the zero point in Figure 5:6(a, b) corresponds to the energy position of the CM0 and CM2 doublet center. Then we multiplied the energy of all excitonic transitions by the scaling factor $\Delta_{02} = \frac{\langle E_{CM2}-E_{CM0}\rangle}{E_{CM2}-E_{CM0}}$ providing an efficient detuning defined as $\frac{\langle E_{CM2}-E_{CM0}\rangle}{E_{CM2}-E_{CM0}}(E - \frac{E_{CM0}+E_{CM2}}{2})$. Thus, CM0 and CM2 always fall at the same energy points, reducing

scattering of polarization-resolved intensity and DOLP data due to uncertainty in CM0-CM2 separation energy. The same procedure was applied for the CM0 and CM1 in Figure 5:6(c, d) providing Detuning $= \frac{\langle E_{CM1} - E_{CM0}\rangle}{E_{CM1} - E_{CM0}}(E - \frac{E_{CM0} + E_{CM1}}{2})$. This normalization did not significantly change detuning of excitonic transitions in real energy units since deviation of the energy difference between CM0 and CM1 as well as CM0 and CM2 was much smaller then the mean value of energy difference between these modes themselves.

DOLP in resonance with CM0 and CM2 was as high as 90% revealing predominant excitonic emission through these cavity modes. In Figure 5:6(b) vertically polarized intensity points are significantly enhanced in the resonance with the CM0 and CM2 while horizontally polarized intensity points are suppressed due to predominant excitonic emission through the CM0 and CM2. At the same time CM1 was almost uncoupled with QD excitonic transitions. DOLP value in resonance with CM1 was lower then 50 %. Therefore, we conclude that the emission through the CM1 was lower then the spontaneous emission rate suppressed by the PhC environment. This can be also seen in the spectra formed by polarization-resolved intensity points (Figure 5:6(b)). Both horizontal and vertical emission components of the excitonic emission have similar value. Just a few structures revealed CM3 peak in the polarization resolved spectra revealing its low coupling efficiency with 'central' QDs.

Figure 5:6 Polarization-resolved intensity (b, d) and DOLP (a, c) of individual lines extracted from polarization-resolved spectra measured in ~100 L7 PhC cavities containing 2 QDs (±200 nm, 'central' position). Energy scale is normalized to the CM0-CM2 difference in a, b and to the CM0-CM1 transition in c, d (see text). These spectra were obtained at 10 K under 300 µW excitation power (all QDs were excited).

Clear s-shape behavior as discussed in Chapter 4 is visible for QD transitions in spectral vicinity with CM0. QD transitions at energies lower than CM0 are unpolarized (Figure 5:6(a, c)) while DOLP of transitions at energies higher than CM0 dropped very fast to the ~-0.5 value (Figure 5:6(a, c)). Emission of the excitonic transitions in-between CMs revealed predominant horizontal polarization as can be seen in Figure 5:6(a, c). That can be explained by the superposition of the different s-shapes induced by CM0-CM3.

Figure 5:7 shows DOLP and polarization-resolved intensity of different emission lines as a function of spectral position with respect to CM0-CM1 (a, b), CM0-CM2 (c, d) and CM1-CM2 (e, f) doublets, in structures with 4 QDs in the L7 PhC cavity. Here, we applied similar normalization procedure as described above. These structures revealed much stronger co-polarization effect between CM1 and excitonic transition (Figure 5:7(a, b)) than in Figure 5:6, revealing better coupling of the 'side' QDs with CM1 then the 'central' QDs. This difference in coupling leads to the very big scattering of the DOLP points as can be seen in Figure 5:7(a). In the resonance DOLP of excitonic emission varied from almost zero to the nearly 80 % as expected taking into account that these structures contain QDs positioned at both 'bad' and 'good' coupling positions at ±200 nm and ±600 nm from the L7 PhC cavity center.

The strongest co-polarization was observed for excitonic transitions in resonance with CM0 and CM2 as can be seen in Figure 5:7(c, e) while polarization resolved intensity points in Figure 5:7(d, f) show strong absolute intensity enhancement in the resonance with these modes. That is due to the high (300 µW) power level used in this experiment, above the saturation limit of QDs grown in bulk GaAs. Simultaneous suppression of horizontal emission and enhancement of vertical emission highlights the predominant excitonic decay through vertically polarized emission modes.

Interestingly, we observed two minima in DOLP points between CM1 and CM2 as can be seen in Figure 5:7(e). These minima can be either a result of the s-shape induced by multiple CM structure or a fingerprint of an additional (low-Q) mode in-between CM1 and CM2. Just a few structures have QD excitons in resonance with CM3, revealing very big scattering of the data points since the CM3 was detuned to the higher energies with respect to the excitonic emission energy. Therefore, we investigated CM3 coupling with 'side' and 'central' QDs using water vapor condensation technique as will be discussed in the following.
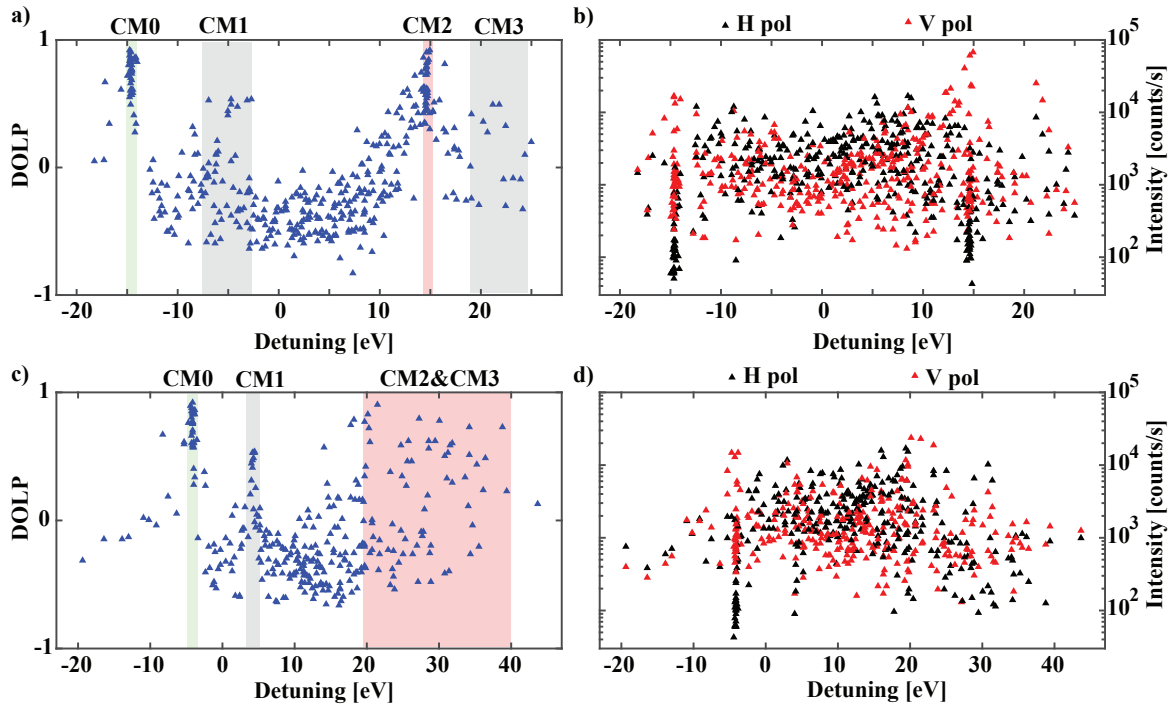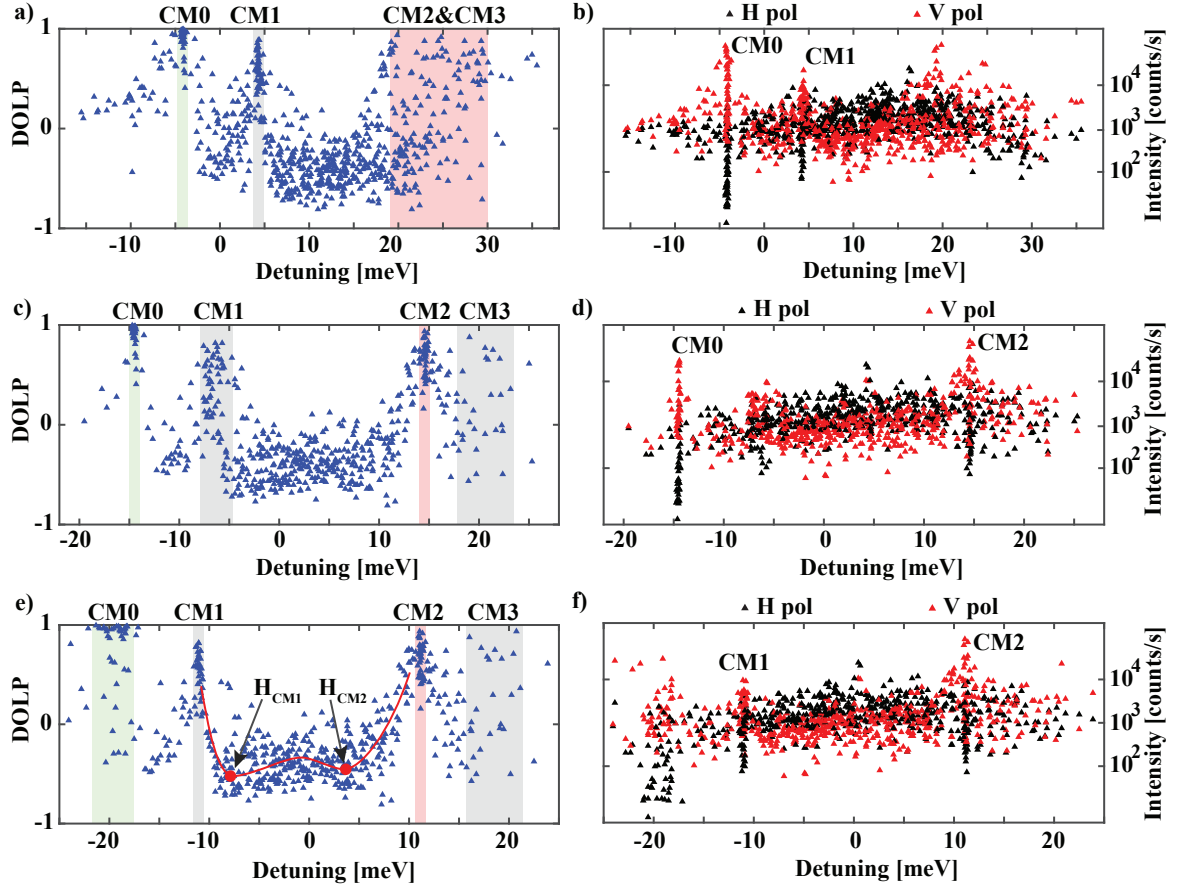
Figure 5:7 Polarization-resolved intensity (b, d, f) and DOLP (a, c, e) of individual lines extracted from polarization-resolved spectra measured in ~100 L7 PhC cavities containing 4 QDs (±200 nm and ±600 nm, 'central' and 'side' positions). Energy scale is normalized to the CM0-CM1 difference in a, b; to the CM0-CM2 transition in c, d and to the CM1-CM2 transition in e, f (see text). The red line in e) is a guide to the eye. These spectra were obtained at 10 K under 300 µW excitation power (all QDs were excited).

In conclusion, we qualitatively probed CM0-CM3 mode overlap with QDs at two well-defined positions (±200 nm and ±600 nm from PhC center) using the deterministic positioning of site-controlled pyramidal QDs. We identified the best CMs of an L7 PhC cavity for coupling excitonic transitions of these 4 QDs. We observed a clear discrepancy between experimental and calculated CM structure of the L7 PhC cavity not only in the spectral domain but also for the CM near field pattern using site-controlled QDs as the point dipole probes. In particular, CM1 was expected to provide efficient coupling with all 4 QDs positioned at around ±200 nm and ±600 nm from the L7 PhC cavity center, being in close proximity to its antinodes. However, 'center' QDs (±200 nm) show stronger coupling to the free space modes than to the CM1, while 'side' QDs (±600 nm) show moderate coupling with this mode. At the same time, CM2 coupled with all 4 QDs while theoretical modeling predicted coupling with only 'side' QDs. In the following we will focus on the study of the coupling between 4 QDs and CM0-CM3 for selected structures.

5.4   Four QD-excitons coupled to the same PhC cavity mode

5.4.1   Identification of individual QDs in spectra using spatial scanning technique

Among all devices we could identify several structures with the CM2 coupled to the 4 QD excitonic transitions. Figure 5:8(a, b) shows two such devices with 4 QDs in L7 PhC cavity having all 4 QD excitons coupled with the CM2. The QDs are positioned as shown in Figure 5:1(b). These structures have very similar exciton emission energies (~5 meV spread of different QD excitonic transitions) and the same (nominal) PhC hole radii r≈61 nm. Both structures had strong excitonic co-polarization with the CM2 on both sides of the CM resonance without revealing any s-shape behavior. This fact is remarkable since it reveals that the interference between spontaneous decay channel and decay channel through the CM2 (see section 1.4.2.2) is negligible. This can be a result of the phase between spontaneous emission and emission through the CM2 being close to $\pi/2$. In this case, π phase flip does not change constructive to destructive interference conditions when CM2-exciton detuning changes sign [43].
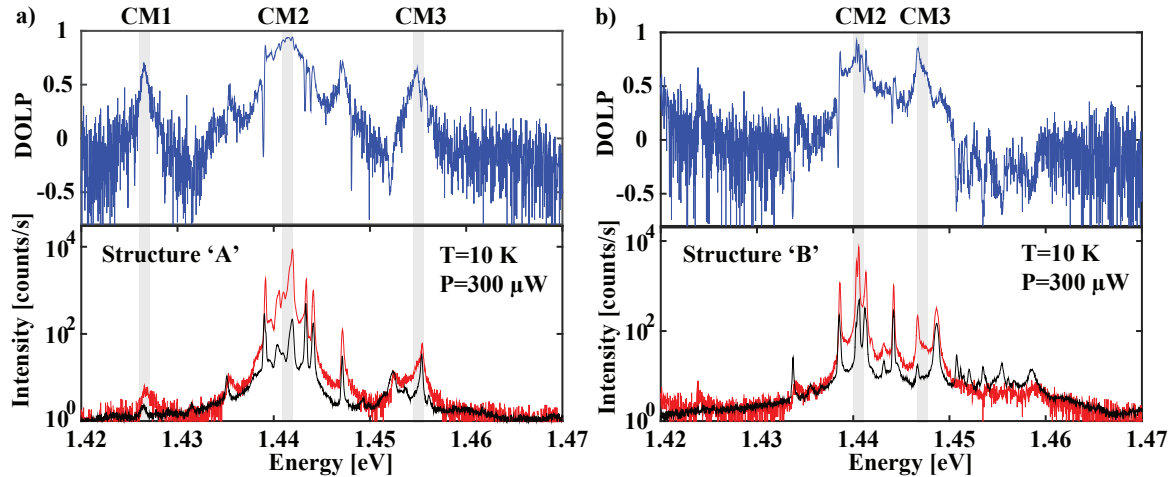
Figure 5:8 Polarization-resolved and DOLP spectra of two structures containing 4 QDs in the L7 PhC cavity having all excitonic transitions coupled with the same CM2. Structures 'A' (a) and 'B' (b) are adjacent structures on the sample, corresponding to the same nominal PhC hole radius r≈61 nm.

We chose structure 'A' for studying CM2 coupling with excitonic transitions of 4 different QD excitons since this structure shows more than 10 meV CM2-CM3 separations, thus coupling of the QD excitons with CM2 can be considered independently from the coupling with CM3. Quantitative probing of different QD coupling with the same CM needs assigning of each excitonic transition observed in polarization-resolved spectra to its corresponding QD. The low-temperature photolumi-nescence (PL) spectra of the different QDs in the system were identified by scanning the ~1µm-wide excitation laser spot across the sample, which was mounted on a high-precision (50 nm) mo-torized XY stage. Figure 5:9 shows an example of such polarization-resolved and DOLP spectra ac-quired with excitation at four different spot positions along the PhC cavity (labelled by X_{spot}). The intensity variations in each spectrum observed with varying excitation position allow identification

of the different QDs in the system. The maximum (V-polarized) DOLP value allows us to estimate spectral position of CM2.
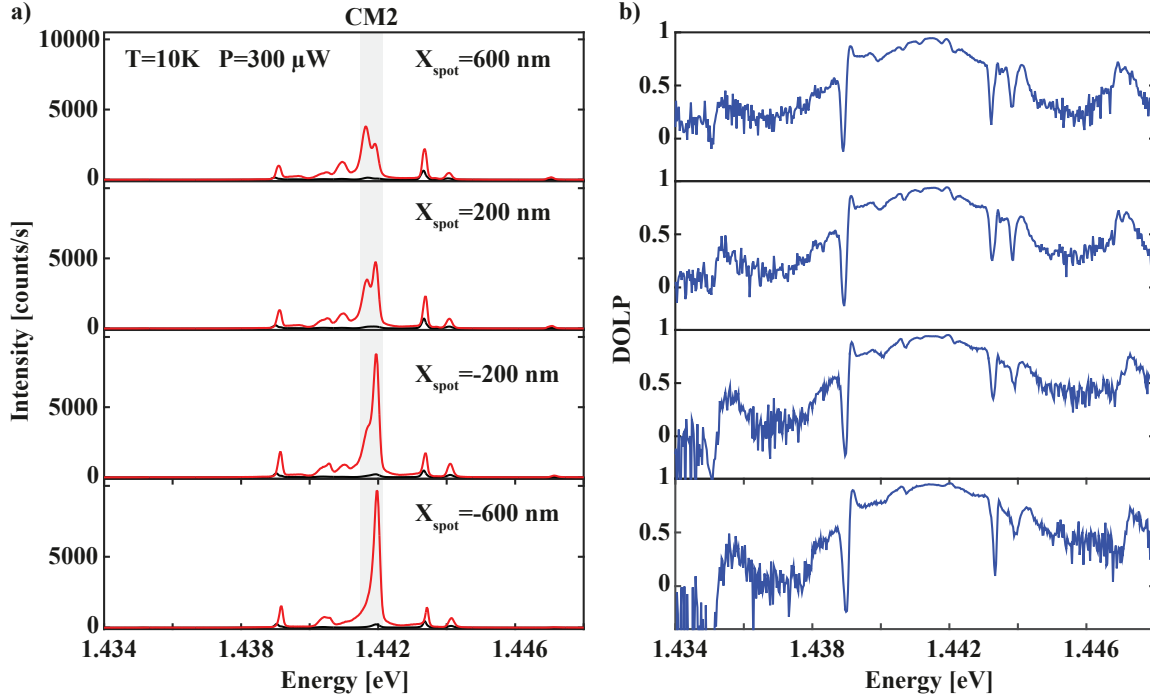
Figure 5:9 Polarization-resolved and DOLP spectra at different excitation spot positions of structure A of Figure 5:8. The spectral position of CM2 is marked in a). X_{spot} corresponds to the x coordinate of the point on the line $y = 0$ in Figure 5:1.

The scanning-PL spectra are summarized in Figure 5:10, which shows the integrated intensity of each PL peak, displayed on a brightness scale, as a function of energy and excitation position. Each of the four QDs is thus identified in the PL spectra. In addition to the excitonic transitions, biexcitonic transition 'QD2 XX' of QD2 is also visible as was identified by its power dependence as well as the opposite FSS splitting of this transition with respect to its excitonic counterpart 'QD2 X1'.
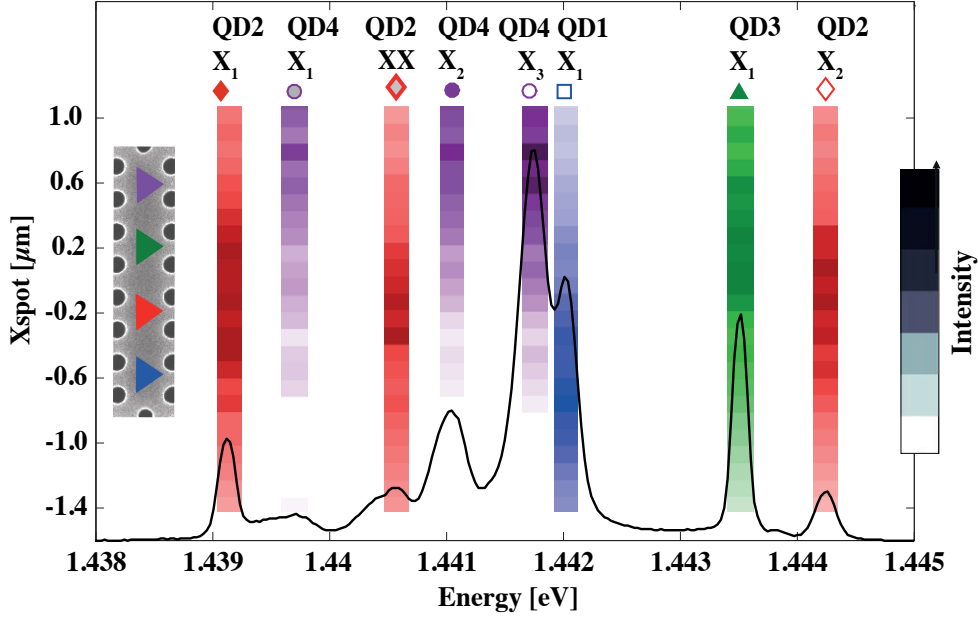
Figure 5:10 Spatial and spectral scanning map of the 4 QD emission of structure 'A' (intensity on the graded color saturation scale; each color is separately normalized to its peak value). The spectrum at the bottom is taken at the cavity center, with linear intensity Y scale. The same QD labelling is used in all figures below. CM2 is in direct resonance with QD4 X_3 and QD1 X_1 emission lines (Figure 5:9(a)).

CM2 is identified based on the energy position expected for the PhC hole radii r≈61 nm as shown in Figure 5:3(a) as well as by its energy variations with water vapour condensation and temperature variation. Figure 5:11(a) shows the polarization-resolved spectra obtained at intermediate water vapour condensation conditions at T=10 K and excitation power P=300 µW. This condensation shifted CM2 to lower energies by ~5 meV, while the QD optical transitions remain at the same energy positions. CM3 is also visible at higher energies as indicated in both polarization-resolved and DOLP spectra in Figure 5:11(a, b). Thus, CM redshifts induced by condensation allows us to clearly identify the CM2 and CM3 peaks. The most intense excitonic transition is the one that is coupled to CM2 as can be seen by comparing the polarization-resolved spectra shown in Figure 5:9(a) and those in Figure 5:11(a). This is expected since the P=300 µW excitation power is above saturation limit of the QD positioned in bulk GaAs.
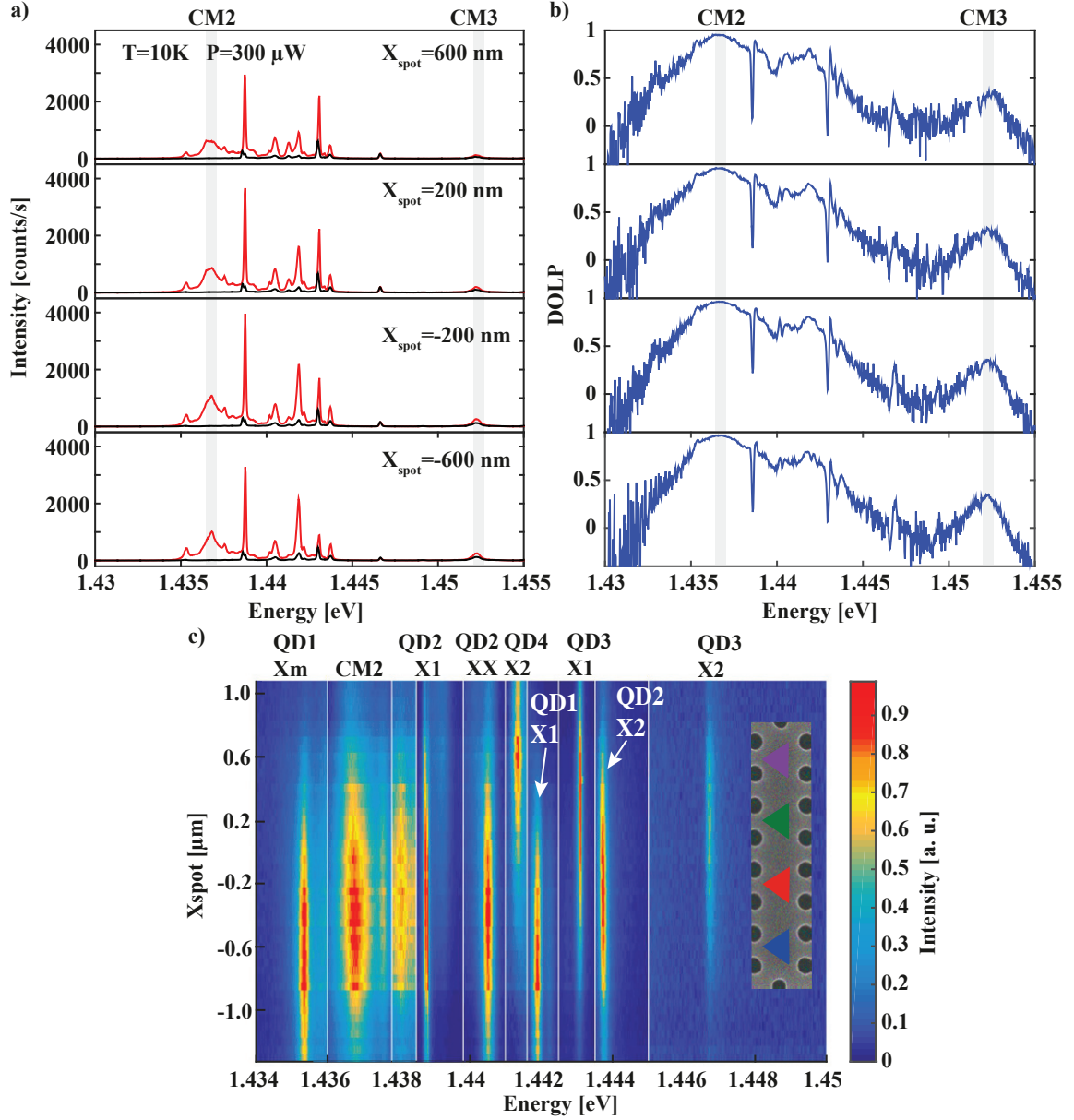
Figure 5:11 Polarization-resolved (a) and DOLP (b) spectra at different excitation spot positions as well as the spatial-spectral scanning map in c). All measurements were obtained at T=10 K, P=300 µW and intermediate water vapour condensation leading to ~5 meV CM2 red shift.

Figure 5:11(c) shows the spatial-spectral map acquired after the water vapor deposition step described above. Additional peaks enhanced by the presence of CM2 are now visible at lower energies with respect to the main excitonic transitions. We attribute these transitions to charged exciton complexes of QD1 and QD2. Taking into account only the most pronounced QD transitions, the resulting decomposed individual QD spectra are displayed in Figure 5:12. All transitions fall within a 5 meV wide range, allowing their coupling with CM2 through the phonon-mediated coupling mechanism[72]. These individual QD spectral lines were extracted from PL spectra acquired without water condensation.
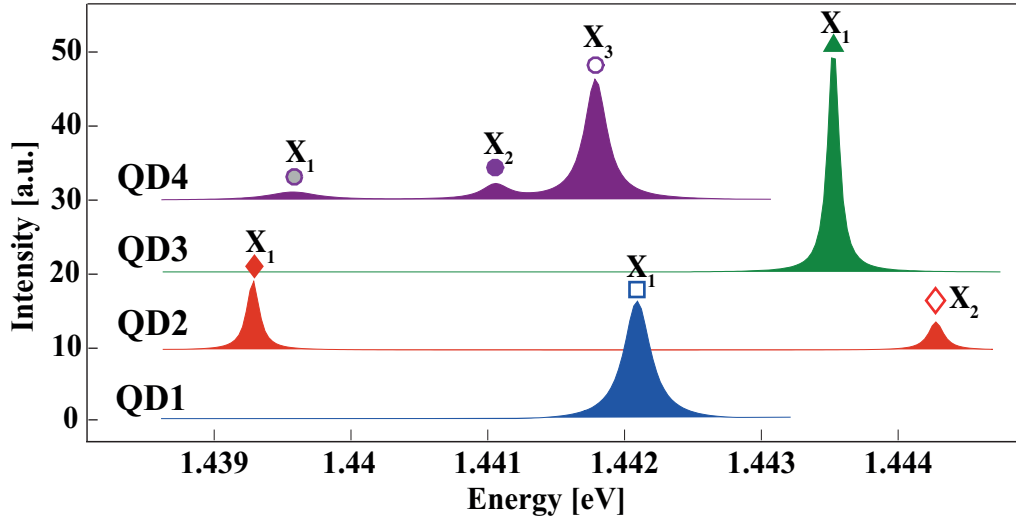
Figure 5:12 Individual excitonic transitions of each QD of structure 'A'. The same QD labelling is used in all figures below. The decomposition of the excitonic lines corresponds to the spectrum shown as the black solid line in Figure 5:10 using spatial scanning data shown in Figure 5:10 and Figure 5:11.

5.4.2 Identification of the QDs corresponding to the different optical transitions using spectral diffusion

As was discussed before, our QDs may suffer from the spectral diffusion, and this effect was also observed in our 4 QDs in the L7 PhC cavity structures. Remarkably, this effect was very rare. During ~400 hours of measurements of this structure this effect was observed 6 times and lasted less then 5 min. We did not observe any correlation with experimental parameters as temperature, excitation conditions or cooling procedure. Thus, we assume that this spectral diffusion processes could be caused by a metastable state of the charge centers in the vicinity of the 4 QD ensemble of the structure 'A'.

Although spectral diffusion is an unwanted process that can affect polarization-resolved measurements, it can be useful in identification of lines corresponding to the same QD. Thus, we supported our spatial scanning technique by searching for spectral diffusion of different QDs. In structure A, only a single QD revealed spectral diffusion during a measurement session and therefore we could easily correlate excitonic transitions corresponding to the different QDs. Figure 5:13 shows a set of spectra obtained sequentially with integration time $t_{int} = 1\,s$ and spectrometer dead time $t_{dead} = 1\,s$. In these spectra, excitonic transitions of QD1 revealed clear spectral diffusion while the positions of excitonic transitions of QD2, QD3 and QD4 remained unchanged. QD3X3 transition is in resonance with the CM2, thus we labeled this peak as 'CM$_2$'.
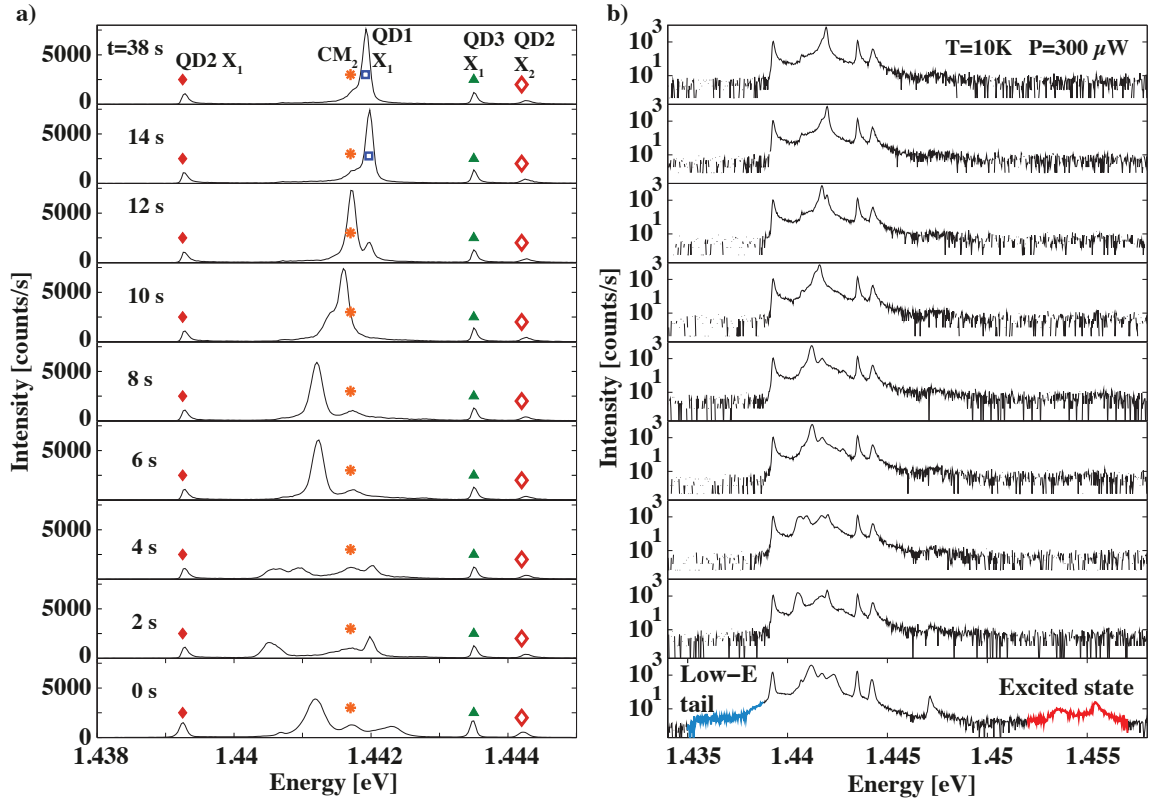
Figure 5:13 Time-resolved spectra showing spectral diffusion of QD1 plotted using linear (a) and logarithmic (b) intensity scales. In the logarithmic scale (b) additional spectral features as a low-energy tail (low-E tail) and excited state transitions appear at the first seconds of the spectral diffusion process.

Interestingly, QD1 spectrum revealed bistability. At the beginning of the experiment, that is, before spectral diffusion started, spectrum of QD1 consisted of 2 intense transitions, 'QD1 Met.' and 'QD1 X_1' as shown in the bottom panel of Figure 5:14. After stabilization of spectral diffusion process shown in Figure 5:13 the 'QD1 Met.' vanished while 'QD1 X_1' slightly shifted in energy (Figure 5:14). Spectra in Figure 5:14 were obtained with excitation spot position at QD1 and at excitation power much below the saturation limit of these QDs, thus we assign optical transitions visible in these spectra to excitonic transitions of these 4 QDs. The metastable line 'QD1 Met.' appeared in the spectrum from time to time, with no correlation to the sample cooling-down procedure.
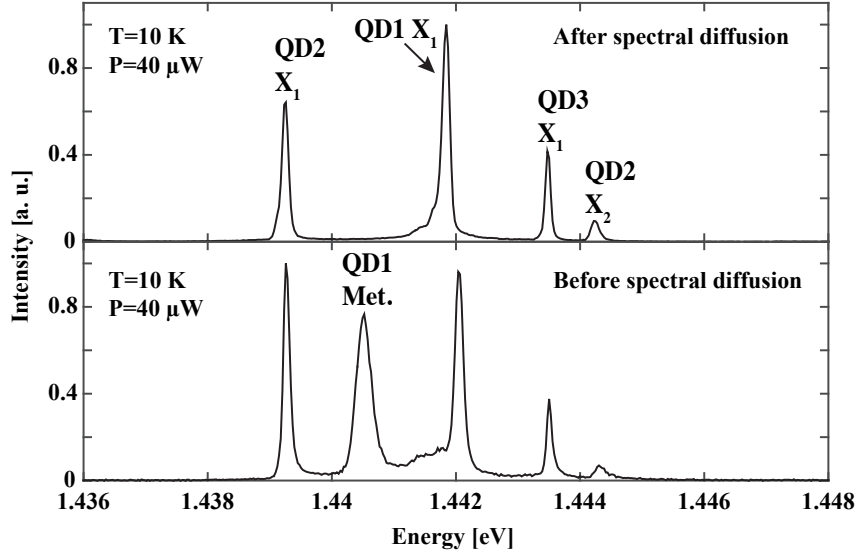
Figure 5:14 PL spectra before (bottom) and after (top) spectral diffusion of QD1 lines shown in Figure 5:13.

During another spectral diffusion event we observed fluctuations of the energy position of the QD2 optical transition 'QD2 X_1'. 'QD2 X_1' was identified as a neutral excitonic transition using its power dependence as well as the clear FSS splitting. After we started to observe fluctuation of the 'QD2 X_1' line, we immediately cut off the excitation laser. After that we simultaneously unblocked the excitation laser beam and started recording the spectral diffusion process with integration time $t_{int} = 2\ s$ and spectrometer dead time $t_{dead} = 1\ s$. Excitonic transition 'QD2 X_1' fluctuated during ~1 min and then stabilized and never revealed spectral diffusion again during subsequent measurements. The emission energy of QD1, QD3 and QD4 once again remained unchanged, confirming the correct QD-exciton assigning.
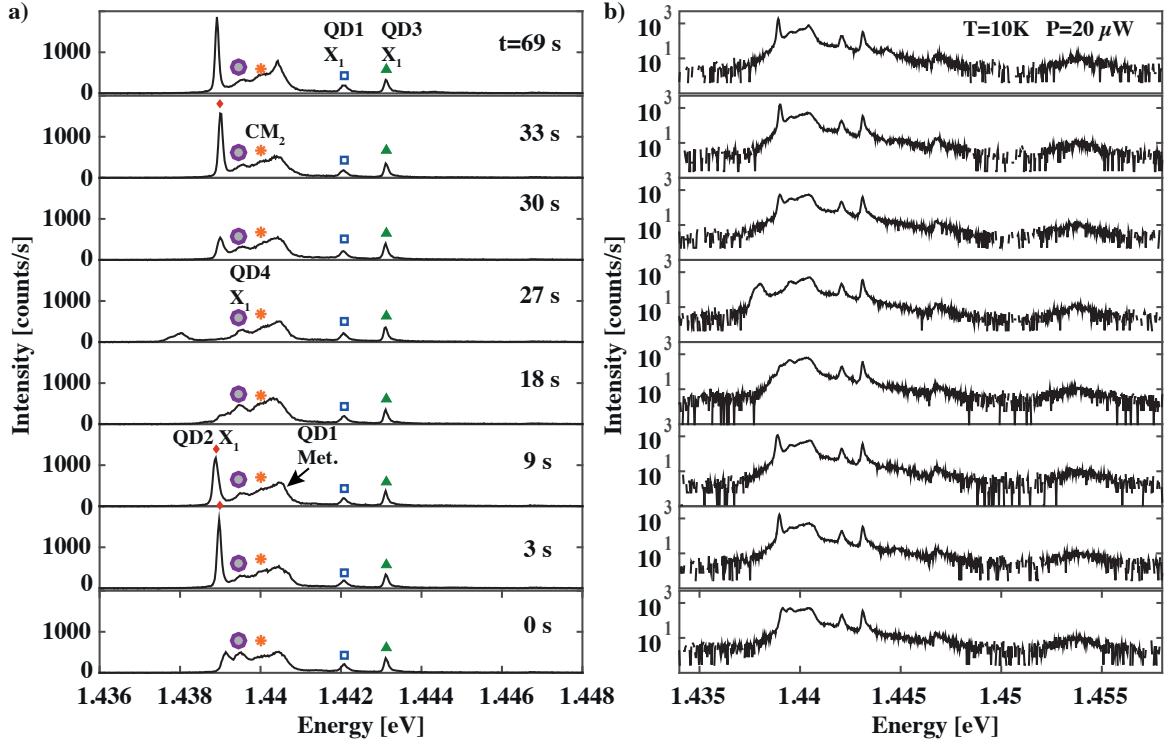
Figure 5:15 Time-resolved spectra showing spectral diffusion of QD2, plotted using linear (a) and logarithmic (b) intensity scales.

Thus, we observed spectral diffusion processes that allowed confirming the correctness of QD-exciton assigning obtained with the spatial scanning technique. Additionally, this demonstrates the local nature of the charging processes revealed by the spectral diffusion of only a single QD out of four QD separated by 400 nm from each other.

5.4.3   Identification of excitonic transitions using power dependence

In order to identify the type of excitonic transitions coupled with CM2 we studied power dependence of optical transitions observed in ±5 meV detuning range from CM2 (in structure A). Figure 5:16 shows polarization-resolved and DOLP spectra of the 4 QD optical transitions coupled with CM2, obtained at several excitation powers. Excitonic transitions of QD2 and QD3 show clear FSS splitting typical for the neutral excitonic transitions. Interestingly, excitons of QD2 and QD3 have transitions nearly perfectly aligned along 'H' and 'V' polarization axes, respectively. Thus, the ~100-150 μeV FSS-marked excitons produced clear fingerprints in the DOLP spectra in Figure 5:16.
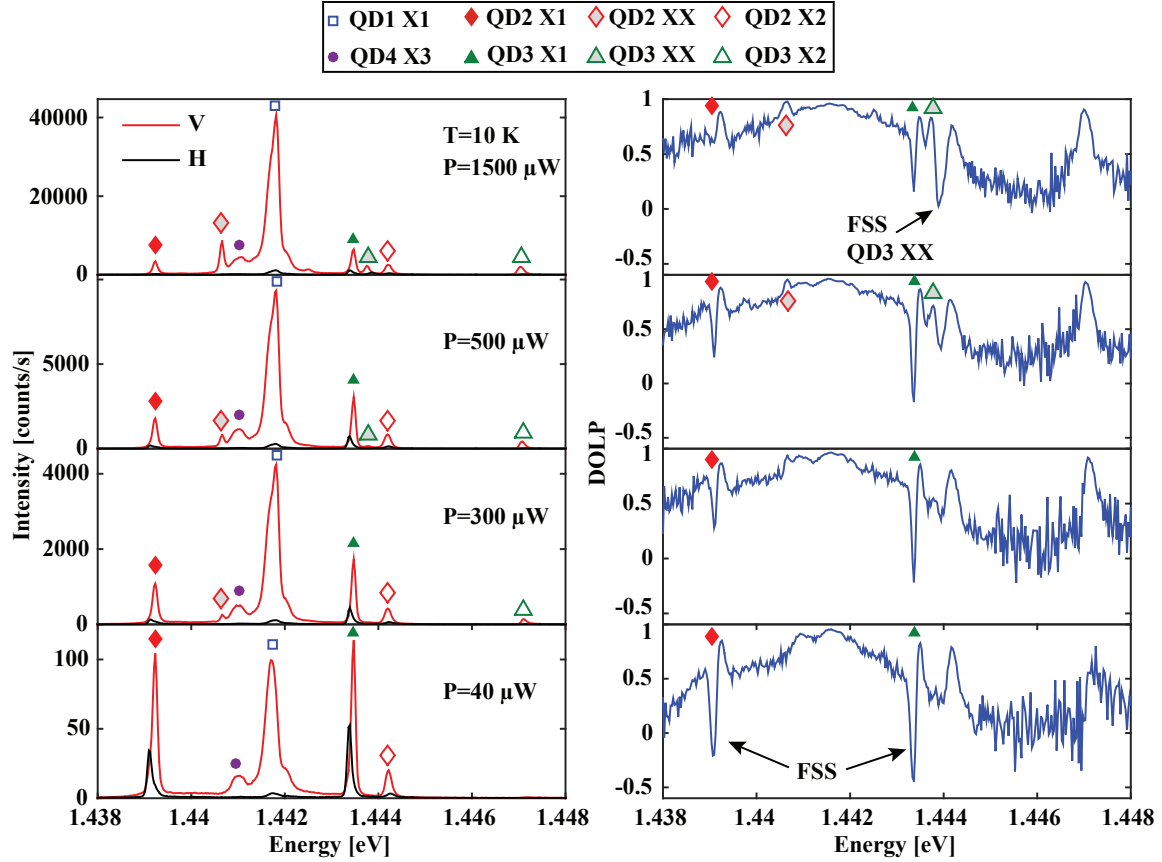
Figure 5:16 Polarization-resolved (left) and DOLP (right) spectra at several excitation powers (structure A). No water vapor condensation was applied.

At low excitation power, all excitonic transitions independently of the detuning conditions, have the same emission intensity as can be seen in the bottom polarization-resolved spectra of Figure 5:16 (P=40 μW). However, transitions detuned from the CM are saturated faster with increasing excitation power then optical transitions at resonance with the CM. Thus, at higher excitation power, emission intensity of the optical transitions at resonance is significantly higher than the intensity of the detuned transitions. In particular, neutral excitonic transitions 'QD2 X_1' and 'QD3 X_1' are around one order weaker than the intensity of 'QD1 X_1' and 'QD4 X_3' that are in direct resonance with the CM2.

Saturation of the neutral excitonic transitions 'QD2 X_1' and 'QD3 X_1' leads to the formation of the biexcitonic complexes 'QD2 XX' and 'QD3 XX'. These transitions have opposite sign of the FSS splitting as can be seen in bottom panel of the DOLP spectra in Figure 5:16 for neutral exciton 'QD3 X_1' and biexciton 'QD3 XX'. The FSS structure of the QD2 biexciton is not visible in these spectra due to the proximity of the 'QD4 X_3' transition enhanced by CM2. However, the FSS structure of both neutral exciton 'QD3 X_1' and biexciton 'QD3 XX' is well visible in the DOLP spectra shown in Figure 5:17. This figure shows polarization-resolved as well as the DOLP spectra obtained at several excitation powers in the same structure A but with water vapor condensed inside the PhC holes. This condensation led to ~5 meV shift towards positive detuning from CM2 of all main transitions. Remarkably, no s-shape profile was observed in the DOLP spectra, leading to co-polarization of the QD excitons detuned less than 5 meV from the CM2 independently of the detuning sign. This is contrary to the results obtained with the single QD in L3 PhC cavity (section 4.3.4)

or with CM0 coupled with the 'central' QDs (QDs shifted by ±200 nm from the L7 PhC cavity center) as can be seen in Figure 5:7(a) in statistical manner for several hundreds of structures and in

Figure 5:29(a) below for a single structure.
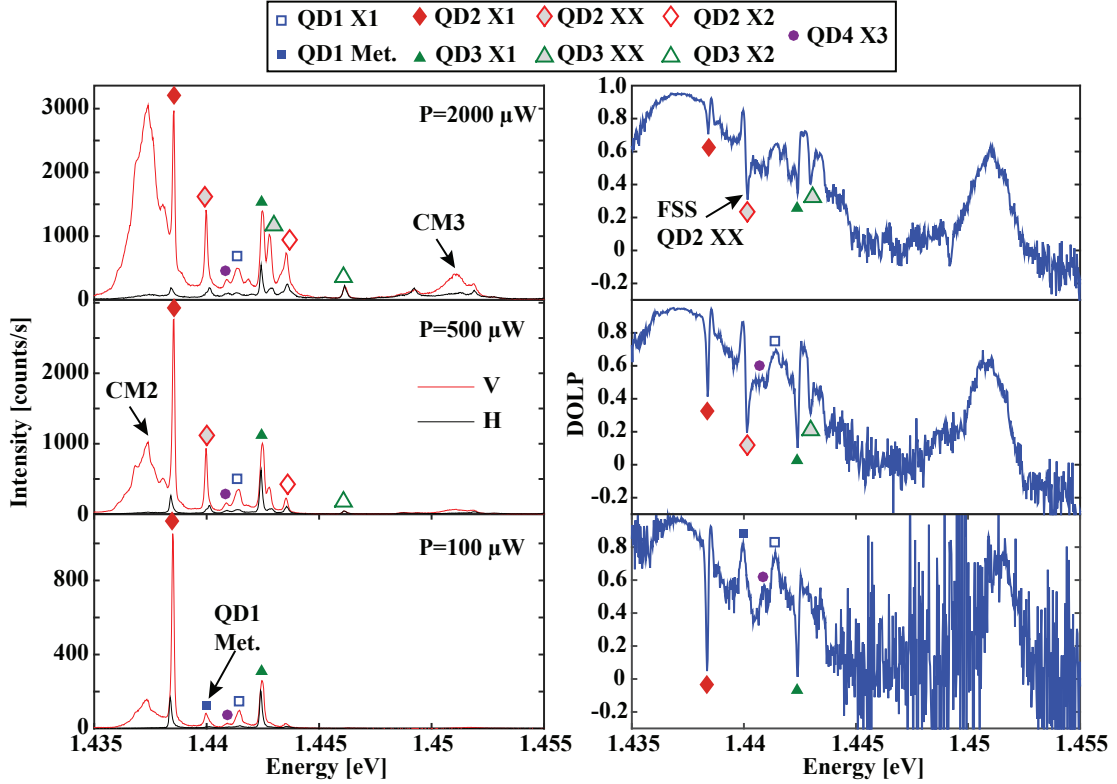
Figure 5:17 Polarization-resolved and DOLP spectra of structure A at several excitation powers, T=10 K. Intermediate water vapor condensation was applied.

The power dependence of the spectral features of structure A with water vapor deposition (as for Figure 5:17) is summarized in Figure 5:18 (a-d). Excitonic transitions of 'side' QDs 'QD1 X_1', 'QD4 X_3' and 'central' QDs 'QD2 X_1', 'QD3 X_1', shown in Figure 5:18(a, b), revealed slightly superliner power dependence with power-law exponents ~1.4 and 1.1, respectively, under above barrier excitation. Line CM2 had two exponents, with a quadratic power dependence at low power, since it is coupled to both lower energy transitions visible as additional peaks superimposed with the CM2 peak in the polarization-resolved spectra of Figure 5:17. After saturation of these peaks, CM2 is mainly populated by the excitonic transition 'QD2 X_1', returning of an exponent of 1.2. Biexcitonic transitions reveal nearly quadratic power dependence as shown for 'QD3 XX' in Figure 5:18(d).
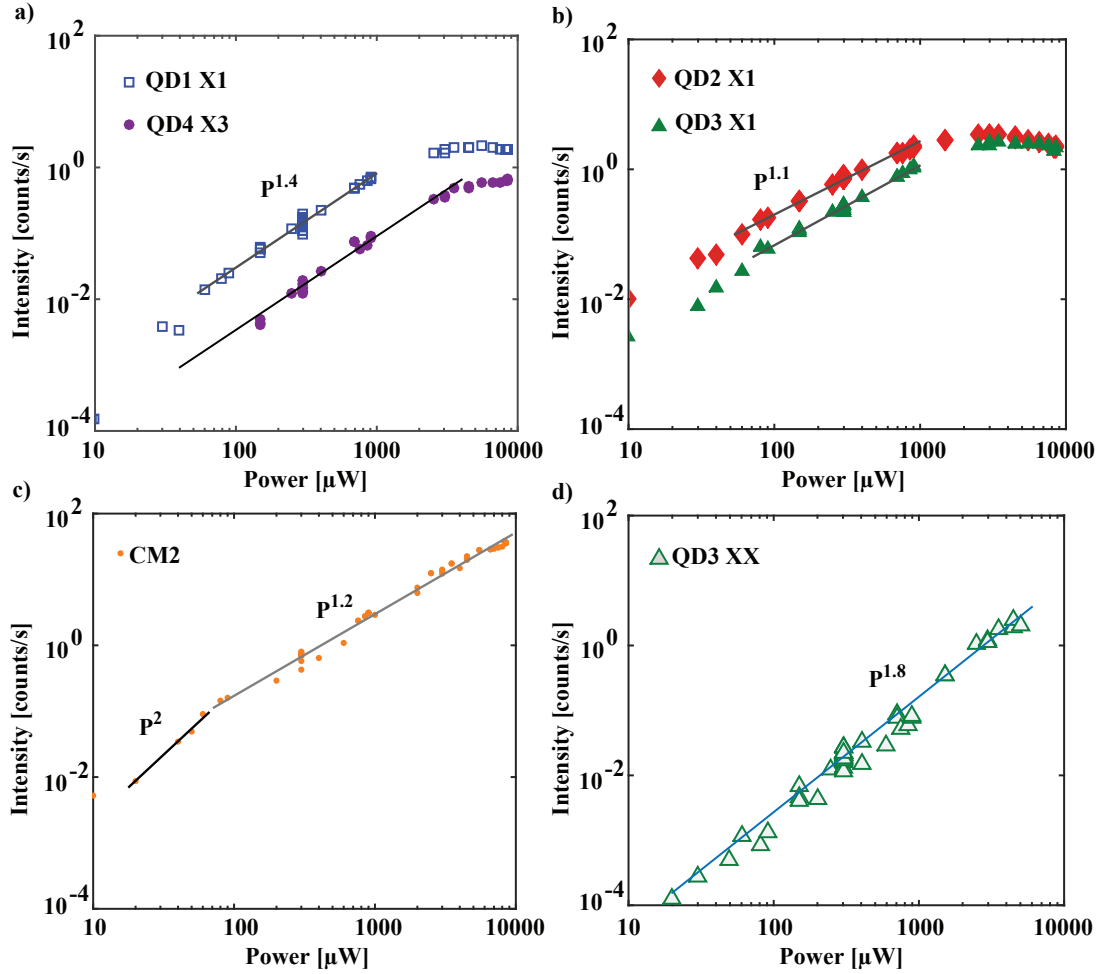
Figure 5:18 Power dependence (log-log plot) of the intensity of the vertically polarized emission of several optical transitions visible in the polarization-resolved spectra in Figure 5:17.

Thus, we distinguished between single and bi-excitonic transitions using their power dependence, confirming that excitonic transitions of the QD1-4 are dispersed by less then 5 meV. Such a small scattering of the excitonic energy allowed coupling of all 4 QD excitons with the same CM through phonon mediation.

5.4.4 Evidence for 4 QD excitons coupling with the same optical mode revealed by co-polarization

Figure 5:19(a) shows the temperature dependence of the V-polarized emission spectra. Increasing sample temperature we sequentially coupled excitonic transitions of all 4 QDs. Although we used the same excitation power level, relative intensity of the uncoupled excitonic transitions significantly decreased with increasing T. We attribute this effect to the temperature induced population of the higher QD energy levels that are shifted by ~10 meV from the excitonic states (see Figure 5:17). Higher energy excitonic transitions have around one order of magnitude faster emission rate, so they dominate at higher sample temperatures. Taking into account the emission rate enhancement due to the Purcell effect, this transition temperature is expected to be higher for the excitonic transitions coupled with CM2. Thus, coupling with CM2 postpones the temperature induced excitonic

emission losses. However, these processes do not affect DOLP (Figure 5:19(b)) as was shown previously, allowing us to use this parameter for CM-exciton coupling characterization.
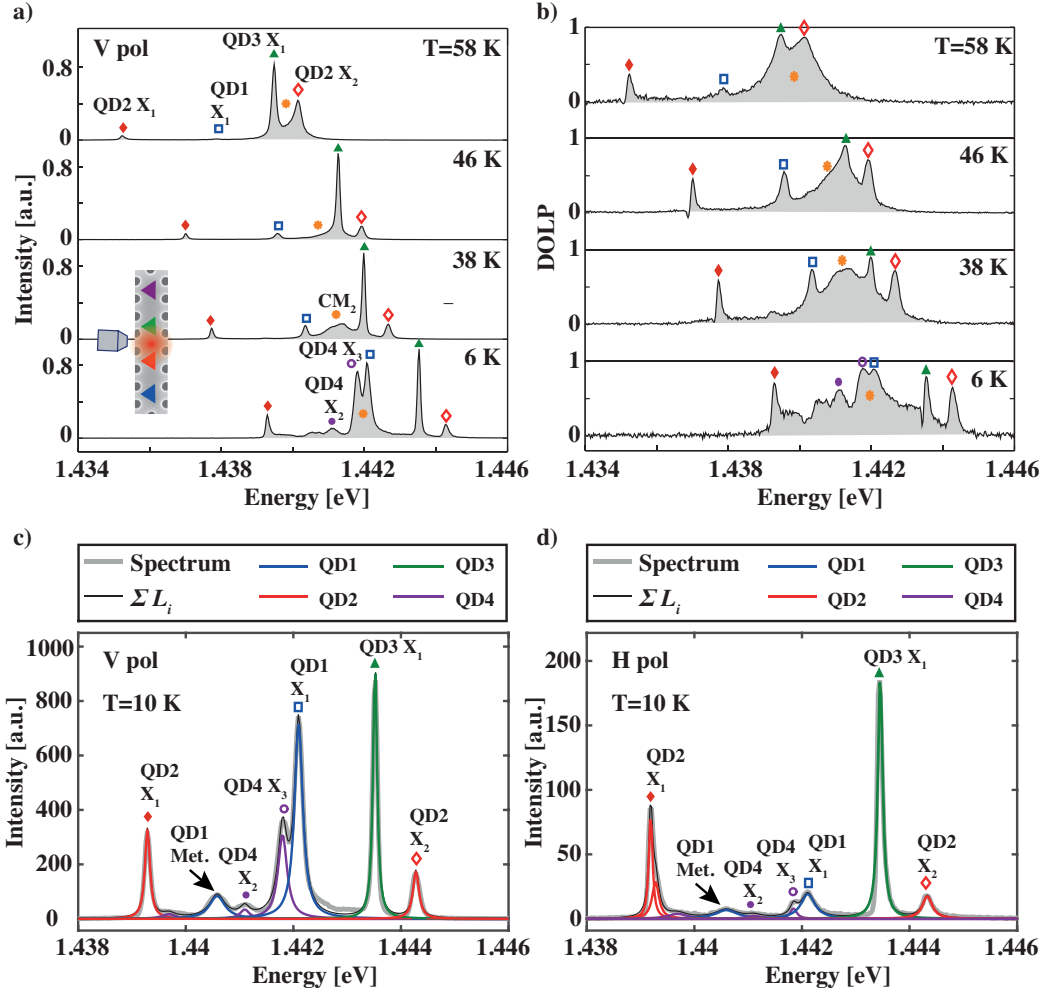
Figure 5:19 Co-polarization of QD emission with the CM at different temperatures: (a) spectra of V polarized emission spectra (H component is much weaker). (b) Corresponding degree of linear polarization (DOLP) spectra. Main excitonic transitions of the QDs are indicated by the same symbols as in Figure 5:10. An example of fitting of polarization-resolved resolved spectra: (c) V polarization, (d) H polarization. Narrow lines correspond to the theoretical model discussed in the text while grey broad lines are experimental spectra.

The excitonic transitions observed in the polarization-resolved spectra (Figure 5:19(a)) were fitted using Lorentzian line shapes as shown in Figure 5:19(c, d). Different FSS components of neutral excitonic transitions 'QD2 X1' and 'QD3 X1' were fitted with different Lorentzian lines. The linewidth of the different excitonic transitions are summarized in Table 5:1. Interestingly, we repeatedly observed broader excitonic transitions of the 'side' QDs while excitonic transitions of the 'central' QDs have nearly resolution limited linewidth, that is, ~80 µeV.

	QD1		QD2			QD3		QD4	
	X1	Met.	X1		X2	X1		X2	X1
			FSS_V	FSS_H		FSS_V	FSS_H		
FWHM [µeV]	185	345	115	150	135	90	105	210	200

Table 5:1 Excitonic linewidth extracted from the fitting procedure shown in Figure 5:19 (c, d).

At higher temperatures 'QD1-X_1', 'QD2 X_1', 'QD4 X_1' and 'QD4 X_2' tune away from the CM and their DOLP decreases, while other transitions (QD2-X_2 and QD3-X_1) tune into resonance, also displaying increasing DOLP up to 0.98. At 38K, we can distinguish clearly the peak corresponding to CM2, showing a quality factor Q≈2500. Thus, the DOLP serves as a measure of the exciton-CM coupling. This is summarized in Figure 5:20, where we plot the DOLP for all observed excitonic transitions (at several temperatures) as function of the energy detuning from CM2. The DOLP remains positive for all detuning values shown, as explained by effects of phonon scattering and pure dephasing for the single QD-CM case[72], [167]
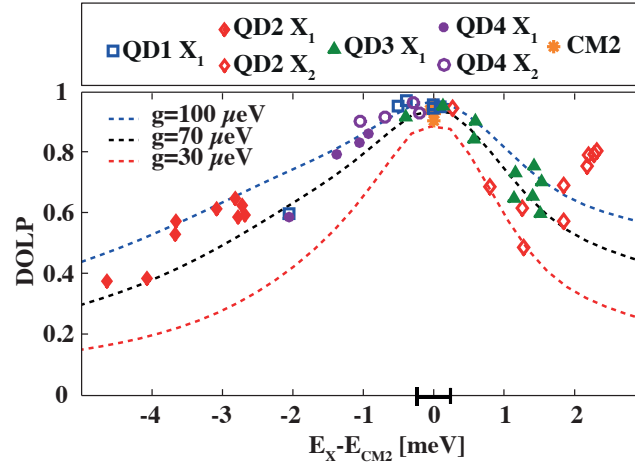
Figure 5:20 Summary of the DOLP values for all observed excitonic transitions at different temperatures, versus detuning energy. Dashed lines correspond to the theoretical model discussed in the text.

The experimental results were interpreted in the framework of a Jaynes-Cummings model including Lindblad terms in the Hamiltonian, accounting for pure dephasing and phonon scattering [167], [189]. Following the procedure found suitable for the case of single QD-CM coupling [167], we calculated the DOLP of the equivalent two-level system as a function of detuning using the same system parameters as for QD2 in Table 1 of reference 14, except for the cavity decay rate, set here to κ=600μeV, and the two-level system pure dephasing rate, set here to γ_d=165μeV. The obtained DOLP values versus detuning are shown by the curves in Figure 5:20 with the exciton-photon coupling parameter g as a parameter. Comparison with experiment suggests coupling values of g~70-100μeV, in agreement with our findings for a similar single QD-CM system [167]. This favourable comparison between experimental and simulated DOLP curves establishes a range of a few meV of detuning in which phonon exchange and pure dephasing allow radiative coupling manifested by CM-X co-polarization. This allows effective coupling of several QD excitons to the same CM, in spite of their dispersion in energy of a few meV.

5.4.5   Enhancement of decay rates of 4 QD excitons coupled with a CM

The effect of CM2 coupling on the dynamics of the 4 QD system was investigated using time-resolved PL spectroscopy. Tuning the CM2 using water vapour condensation, in addition to tuning by temperature variations, extended the range of QD-CM2 detuning. Figure 5:21 shows time-resolved PL traces of the QD4-X_2 transition tuned into resonance with the CM, being almost totally V-polarized, and for the off-resonance (-3meV detuning) QD2-X_1 exciton (T=10K, with condensation). The decay time of the tuned QD exciton is reduced with respect to the detuned one. The detuned transition shows much longer (≈2.2 ns) decay time (possibly limited by non-radiative pro-

cesses) for H-polarized emission, due to smaller coupling of the H-polarized dipole moment with the CM electric field.
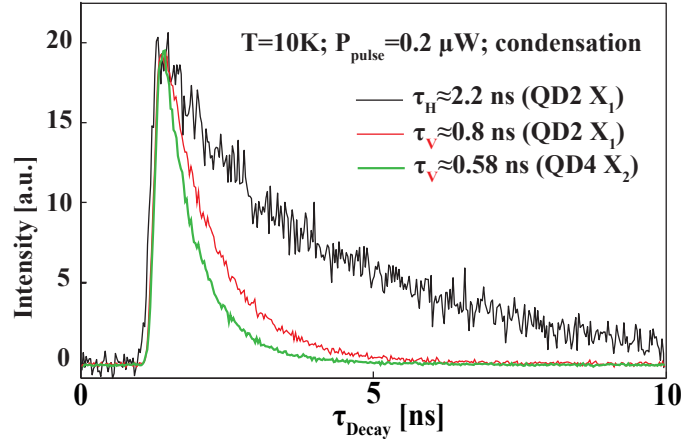
Figure 5:21 Time-resolved PL decay traces for V-polarized transitions (red and green) and H-polarized transition (black) for two spectral lines of the system; QD4X$_2$ transition is in resonance with CM2 (structure A, with condensation).

Figure 5:22 summarizes the measured decay times for the observed excitonic transitions versus CM2 detuning. Minimum decay times of <0.5ns are observed near zero detuning. The measured decay rates of the excitonic transitions versus detuning follow the trend previously observed for a single QD in L3 PhC cavity[190], as modelled by the dashed curves in Figure 5:4(c). In this case we used cavity decay rate κ=600μeV, pure dephasing rate γ_d=165μeV and QD lifetime in the bulk τ_0=1 ns as parameters extracted from PL measurements with an estimated Purcell factor F_P=17. Here, the QD decay rate $g = 1/t_{leak} + 1/t_{nrad}$ is used as the fitting parameter, where τ_{leak} is the QD lifetime in the photonic bandgap and τ_{nrad} is the nonradiative decay rate. Good agreement with experiment is obtained for 0.45<g<1 ns^{-1}, which is close to the corresponding best-fit decay rate of a single QD in the photonic bandgap of an L3 PhC cavity[190]. We thus conclude that all four QDs exhibit a Purcell dynamic effect with respect to the same CM, further supporting the coupling of the entire QD system to the same cavity mode.
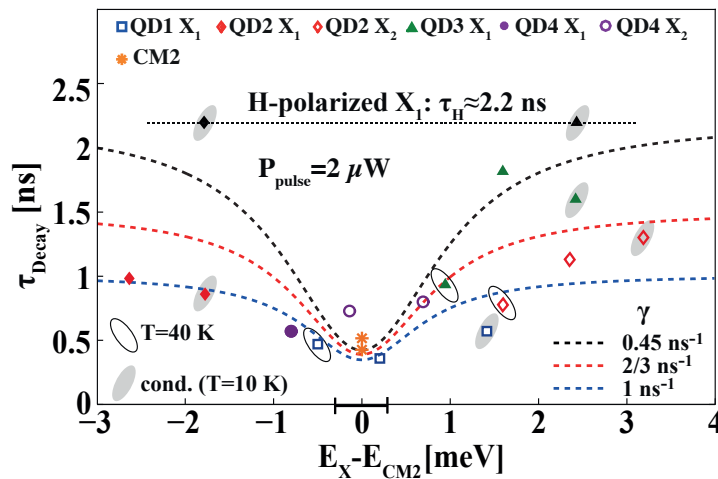
Figure 5:22 Summary of decay times of different QD transitions in structure A as function of the CM2 detuning for V-polarized emission. Data points are marked as follows: no mark: 10K; surrounding ellipse: 40K; grey ellipse: 10K with condensation. For comparison, two values for H-polarized emission are shown at the top.

In conclusion, we demonstrated the simultaneous coupling of a system of four site-controlled QDs with a single optical mode of an L_7 PhC cavity. This (weak) coupling was confirmed by both the co-polarization and the reduced lifetime of the QD excitonic transitions within ±3 meV detuning off the CM energy. Comparison with a two-level system model indicates that this finite detuning range is brought about by both pure dephasing phonon scattering effects.

5.5   Probing coupling of different modes using water vapor condensation

Our site-controlled QDs provide an excellent system for probing near field pattern of a prescribed CM, as was shown in Chapter 4 for a single QD deterministically positioned inside an L3 PhC cavity. Here, we describe probing the CM0-CM3 patterns to the differently positioned QDs. For this purpose we used 4 QD in L7 PhC cavity structures with QDs shifted by ±200 nm and ±600 nm from the cavity center. Using water vapor condensation, we were able to couple different CMs each with the same 4 QD excitonic transitions, probing the CM-exciton overlap for different CMs.

5.5.1   Coupling between 4 QD excitons and CM0-CM2 optical modes

Let us begin with a review of several structures with CM0 and CM1 in the spectral vicinity of the excitonic transitions of the 4 QDs. We identified multiple structures with excitonic transitions coupled with CM0 and CM1 revealing very similar polarization properties. This reflects the reproducibility of the CM near field pattern between different PhC cavity devices since our site-controlled QDs are precisely positioned inside the L7 PhC cavity. Figure 5:23 shows polarization resolved measurements obtained in three structures with CM0 and CM1 in the spectral vicinity of the 4 QD excitonic transitions. Difference in the coupling between the CM0 and CM1 is well visible in the polarization resolved spectra of the structure #1 (Figure 5:23(a)). The intensity of CM0 is of the same order of magnitude as the intensity of CM1 although the CM0 is detuned by at least 5 meV while CM1 is in direct resonance with the excitonic transitions. In Figure 5:23(b, c) the emission of CM0 dominates in the spectra although both CM0 and CM1 overlap with the excitonic transitions. This is in good agreement with results obtained previously (Figure 5:7) with the statistical analysis of the polarization-resolved emission of 4 QD in L7 PhC cavity.
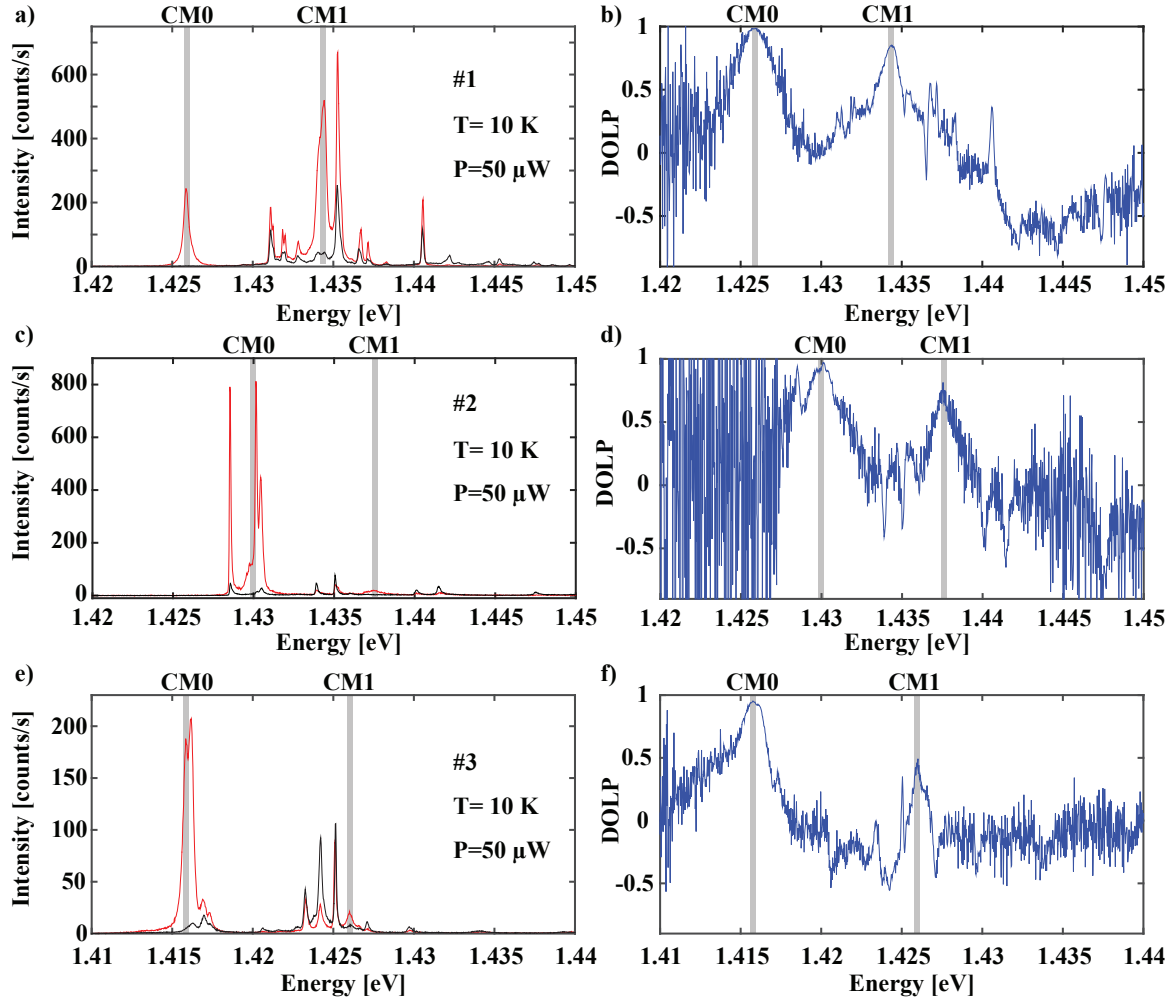
Figure 5:23 Polarization-resolved (a, c, e) and corresponding DOLP (b, d, f) spectra of 3 structures with CM0 and CM1 near the excitonic transitions of the 4 QDs in L7 PhC cavity. Structures #1 and #2 have nominal PhC radii r=64 while structure #3 has PhC hole radii r=61.

Identifying the QDs coupled to the most pronounced excitonic transitions, we found that both 'side' and 'central' QDs have nonzero but weak overlap with CM1. Figure 5:24(a) shows again the polarization-resolved and DOLP spectra of structure #1. The QD sources of the most intense lines were identified using the spatial scanning technique as shown in Figure 5:24(b), revealing that all 4 QDs have excitonic transitions in the spectral vicinity of the CM1. All these transitions showed co-polarization effect, but much weaker than in the case of the CM2 coupled with the 4 QD excitons discussed previously. Already at ~1 meV detuning with respect to CM1, the DOLP of the emission lines decreased below 50 %; thus, for detuning >1 meV the excitons are predominantly coupled to the free space optical modes.

Figure 5:24 Polarization-resolved spectra with DOLP trace on top (a) and spatial-spectral scanning map (b) of structure #1. Spatial scanning was implemented at P=50 µW and T=10 K with collection of the vertically polarized emission. Xh is the higher energy line repeatedly observed in our QD emission spectra.

Figure 5:25(a) shows polarization-resolved and DOLP spectra of structure #2 having QD optical transitions coupled with both CM0 and CM1. The QD sources of the most intense lines were identified using spatial scanning PL as shown in Figure 5:25(b). Only excitonic transitions of the 'central' QDs could be found in the spectral vicinity of CM0. It should be noted that among all measured structures we were not able to find ones with 'side' QD excitonic transitions coupled with the CM0. This can be due to significant enhancement of the 'central' QD excitonic emission intensity as well as strong emission at the wavelength of the CM0 for wide range of detuning (see for example Figure 5:24(a)) that can hide the excitonic peaks of the 'side' QDs for which we expect much smaller

coupling according to the CM0 near field pattern modeling (Figure 5:1(b)). A possible way to counteract this effect is spectral-spatial scanning with collection of only the horizontally polarized emission. However, this needs a significant increase of the integration time (more than 30 s), leading to loss of precision of the spatial scanning due to sample drift.
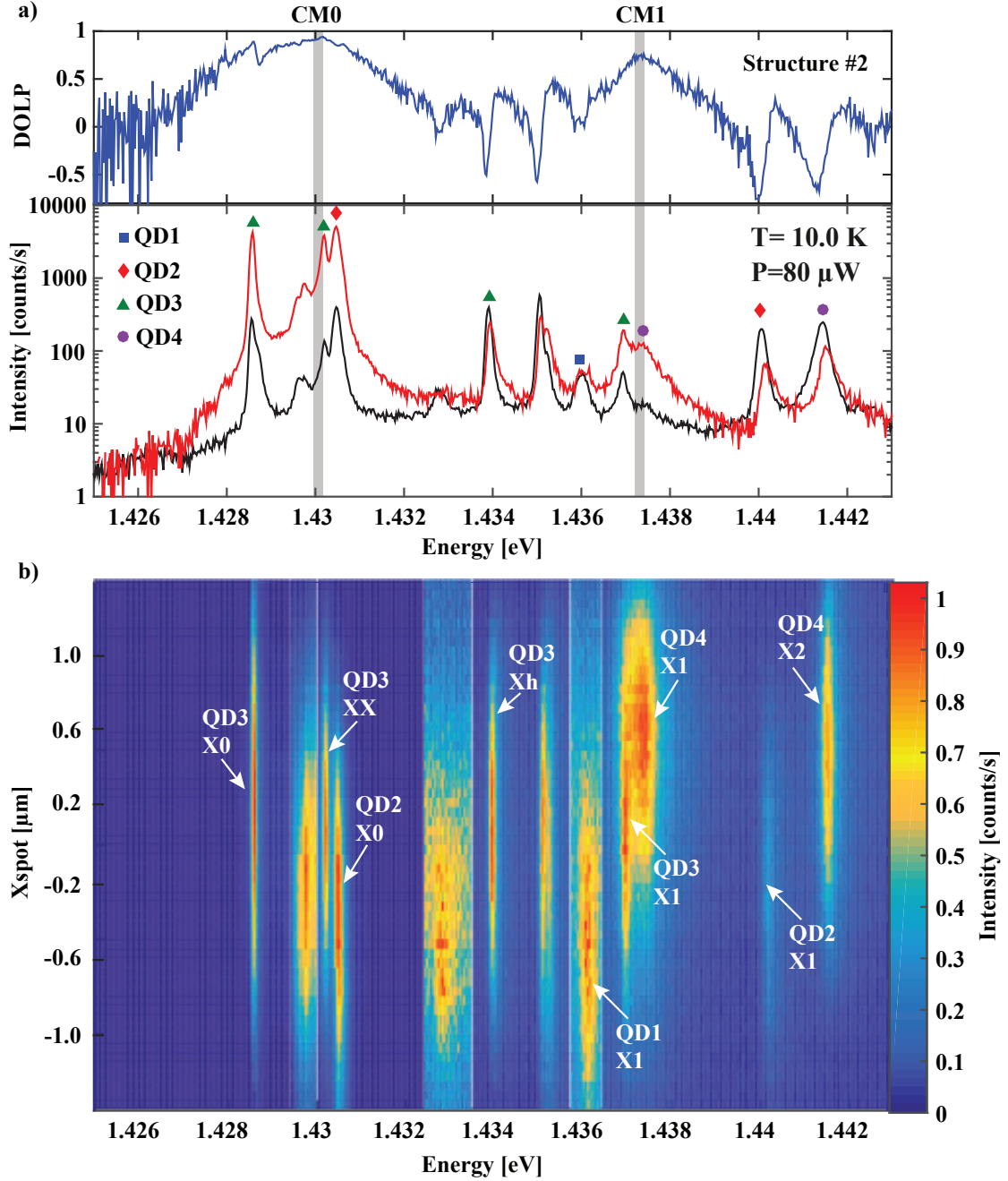
Figure 5:25 Polarization-resolved PL and DOLP spectra (a) and spatial-spectral scanning map (b) of structure #2. Spatial scanning was implemented at P=50 µW and T=10 K with collection of vertically polarized emission.

Excitons of 'side' QDs nearly resonant with CM0 reveal DOLP values as high as 90 %, which corresponds to around 10 times enhanced emission rate through the CM0 in comparison with excitonic emission rate into the PhC bandgap. Excitonic transitions of QD3 and QD4 in resonance with CM1 identified with spatial scanning (Figure 5:25(b)) show <60 % DOLP values, thus the emission rate through the CM1 is almost equal to the emission rate through spontaneous emission decay channels. The emission rate through CM0 is therefore ~10 times bigger than the emission rate through CM1. The emission rate through a CM is proportional to the square of the electric field at the dipole position, therefore the ratio between the electric field amplitude of CM0 at ±200 nm to that of CM1 at ±600 nm position is ~3. This is surprising, since the calculated electric field of CM0 (CM1) has 60 % of their maximum electric field amplitude at ±200 nm (±600 nm) position (see Figure 5:1). Thus, either the antinode position of the CMs does not correspond to the calculations, or the mode volume of CM1 is significantly bigger than that of CM0, leading to ~3 times different CM amplitudes at the maximum of the CM0 and CM1 fields.

Even bigger difference in the coupling of CM0 and CM1 to the 'central' and 'side' QDs was obtained with structure #3. Figure 5:26(a) shows polarization-resolved and DOLP spectra of this structure, having QD1, QD3 and QD4 optical transitions coupled with CM1 while CM0 is slightly detuned to lower energies from the 'central' QD transitions. This device also has 'central' QD excitons well-coupled with CM0, while 'side' QD exciton ('QD4 X1') has DOLP≈0.4, that is, revealing higher emission rate through free space optical modes than through CM1 (Figure 5:26(a)). Excitonic transitions were successfully assigned to their source QDs using spatial scanning, as summarized in Figure 5:26(b).
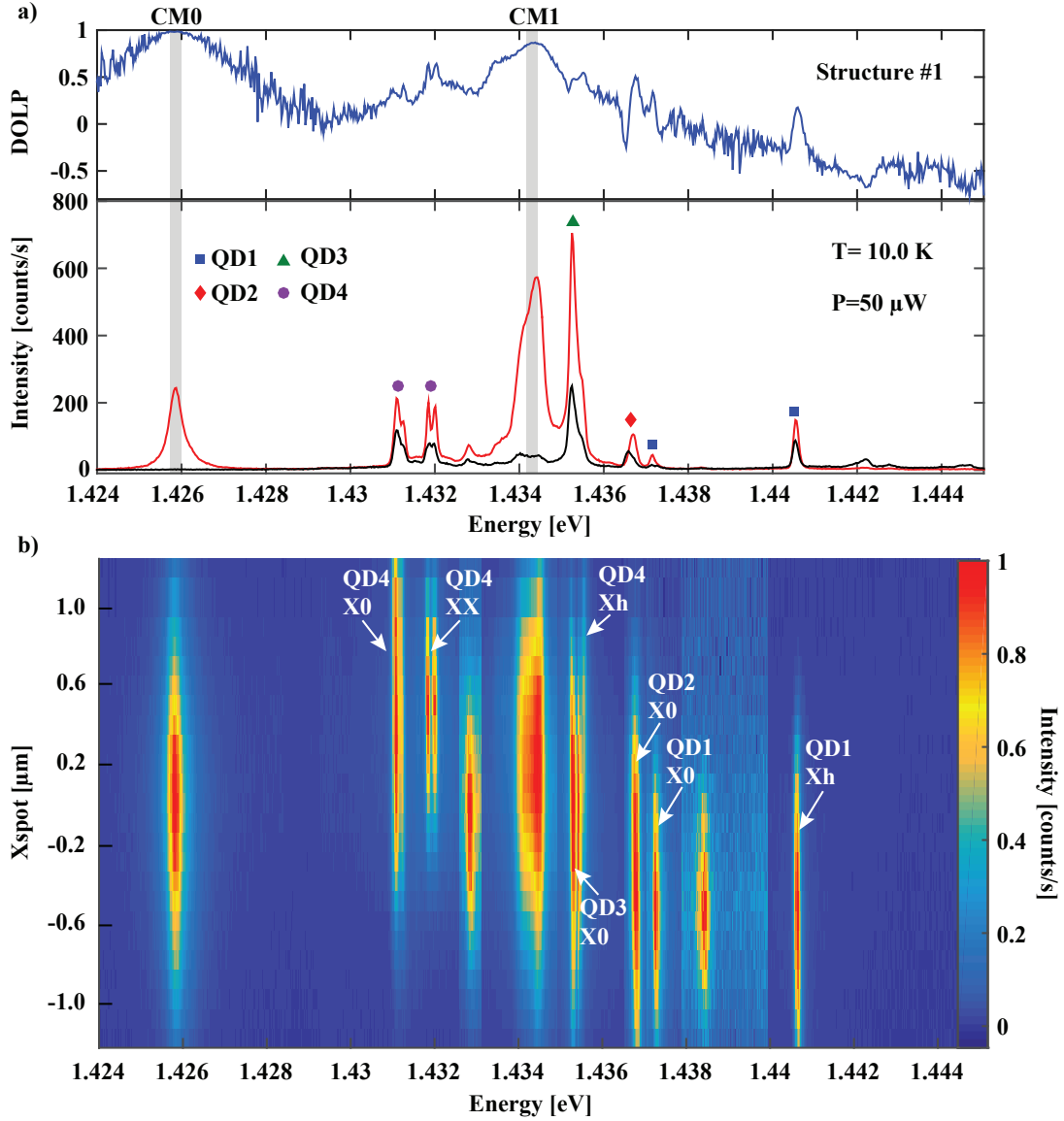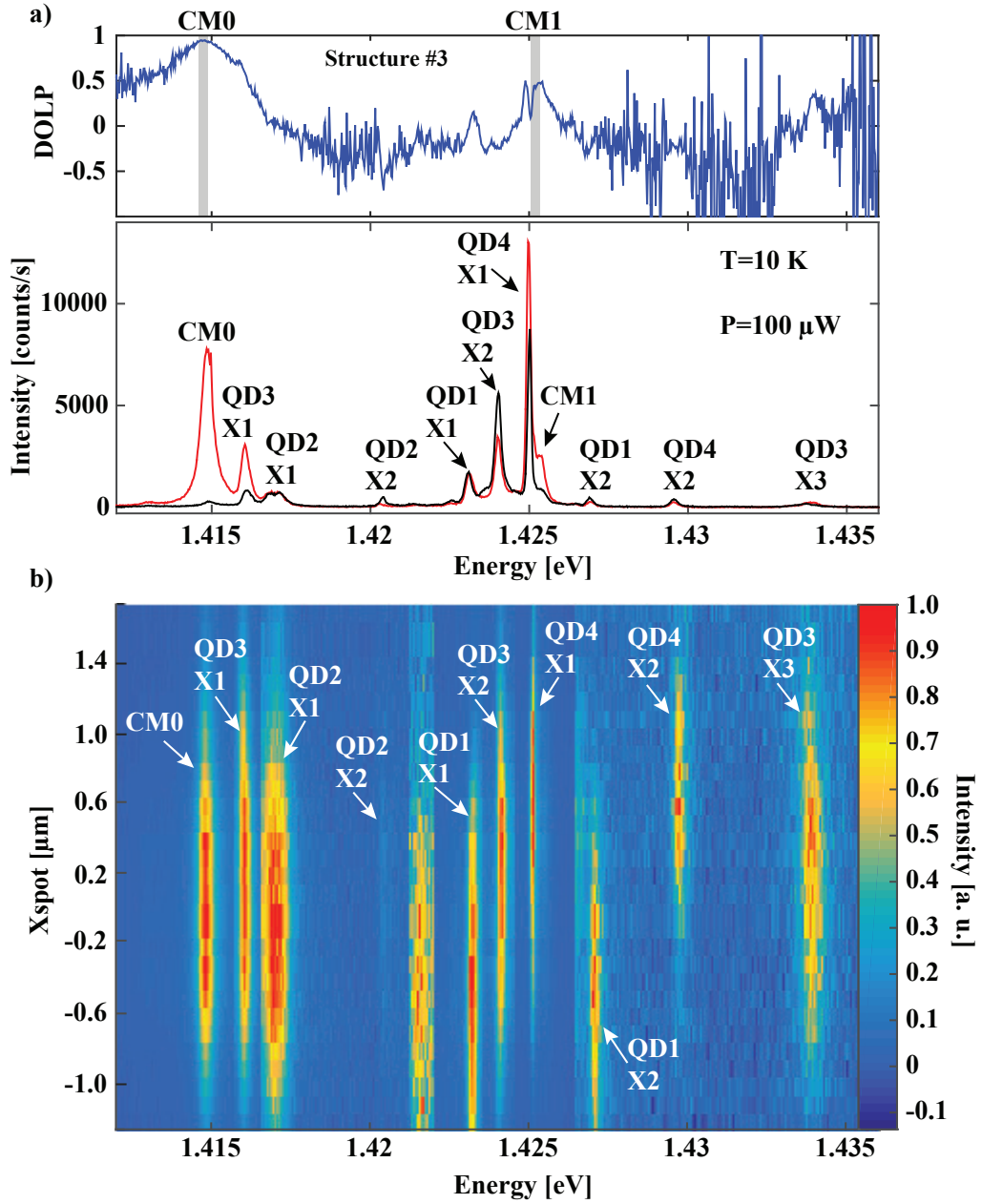
Figure 5:26 Polarization-resolved spectra with DOLP trace on top in a) and spatial-spectral scanning map in b) of structure #3. Spatial scanning was implemented at P=100 µW and T=10 K with collection of only the vertically polarized emission.

Structure #3 has smaller PhC hole radii providing well-separated CM2 and CM3 and smaller CM1-CM2 separation than in structures #1 and #2. Thus, CM2 can be potentially tuned into resonance with the QD excitonic transitions using water vapor deposition, providing the possibility to study coupling with all first 3 CMs using the same structure. For this purpose we spectrally scanned the QD excitons with the CM using temperature and condensation tuning. Figure 5:27(a, b) shows polarization-resolved and DOLP spectra obtained at several water vapor condensation conditions. At the strongest water condensation used in our experiment we tuned CM2 into resonance with the

QD1, QD3 and QD4 excitonic transitions. Their DOLP revealed very high co-polarization effect at resonance with CM2, in exact correspondence with the case of CM2 and 4 QD exciton coupling obtained in the absence of water condensation with structures 'A' and 'B' (Figure 5:8). This confirms that water condensation does not significantly change the CM-exciton overlap and can be used for probing of the different CM near field patterns with the same QD excitonic transitions.
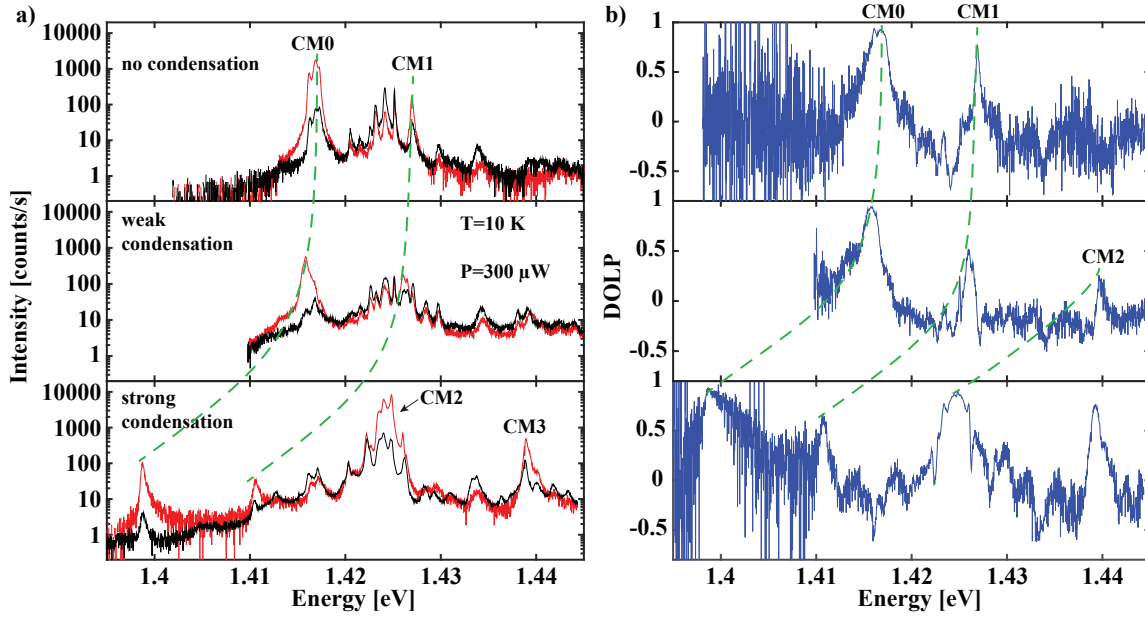
Figure 5:27 Polarization-resolved (a) and DOLP (b) spectra measured at several water vapor condensation conditions of structure #3. All spectra are obtained at T=10 K and P=300 µW. Dashed lines serve as an eye guides, highlighting the position of the first three CMs.

In this structure we obtained ~18 meV CM energy shift to the lower energies at the strongest condensation. Such a strong energy shift of CMs was observed previously [191]–[193]. Interestingly, the CM quality factor slightly increased while water condensed inside the PhC holes as reported in [192]. However, we were not able to change the amount of water condensed in the PhC holes after cooling down the sample, thus we also used the temperature variations for fine tuning of the relative CM-exciton energy position. Figure 5:28(a, b) shows polarization-resolved and corresponding DOLP spectra obtained under weak condensation conditions leading to ~2 meV CM shift. At this condensation conditions CM1 was in resonance with the 'side' QD transition revealing DOLP≈40 %. Transitions of the 'central' QDs coupled with the CM0 revealed fast build up of co-polarization effect while they are being tuned into resonance with CM0.
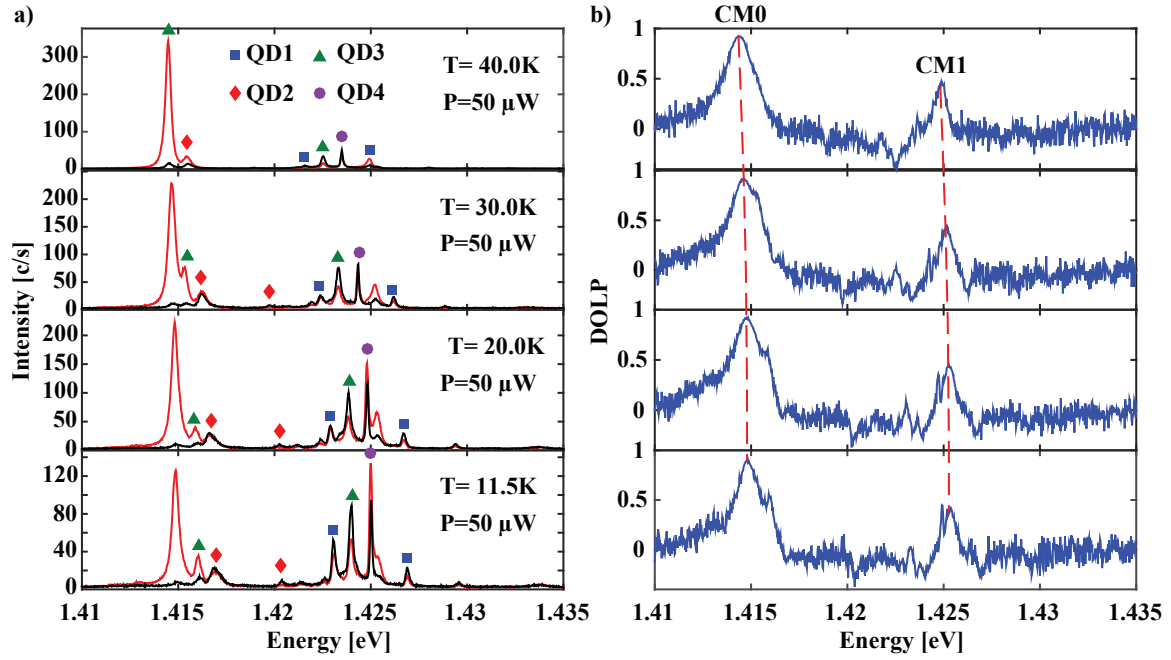
Figure 5:28 Polarization-resolved (a) and corresponding DOLP (b) spectra of structure #3 at a set of temperatures.

In this device we observed typical s-shape behavior (discussed previously for the single QD in L3 PhC cavity, Chapter 4) for the 'central' QD excitons coupled with CM0. Detuned to the higher energy side by several meV, these transitions show DOLP that is very fast reduced to almost negative values. In the vicinity of CM1 the excitonic behavior was different for 'central' and 'side' QDs. Interestingly, 'side' QD excitonic transitions were almost unpolarized at negative energy side of the CM1, which is typical for the s-shape behavior. Simultaneously, the transition of the 'central' QD3 was horizontally polarized at nearly the same detuning conditions.

This effect is well visible in the summary of the DOLP values obtained at weak condensation conditions supplemented by the temperature tuning shown in

Figure 5:29(a). 'Central' ('side') QD excitons reveal the typical s-shape behavior in DOLP spectra in resonance with CM0 (CM1). In the figure, transitions of QD2 and QD3 are green triangles and red diamonds, while transitions of QD1 and QD4 are blue squares and magenta circles. DOLP values of CM0 and CM1 are shown as orange circles. Much stronger CM0 with 'central' QD coupling leading to the pronounced s-shape behavior that dominates over CM1-exciton co-polarization explains this effect.

Figure 5:29(b) shows DOLP spectra of excitonic transitions tuned into resonance with CM2 using water vapor condensation. All excitonic transitions revealed strong co-polarization with CM2 although DOLP values were slightly lower than obtained previously with structure 'A' (Figure 5:20). Leaving aside fluctuations of the DOLP values that can be induced by water condensation as well as fluctuations of the CM characteristics between different devices, we thus confirm the successful

probing of exciton coupling to the first three CMs of the L7 PhC cavity, which favorably compares with the statistically obtained values in Figure 5:7.
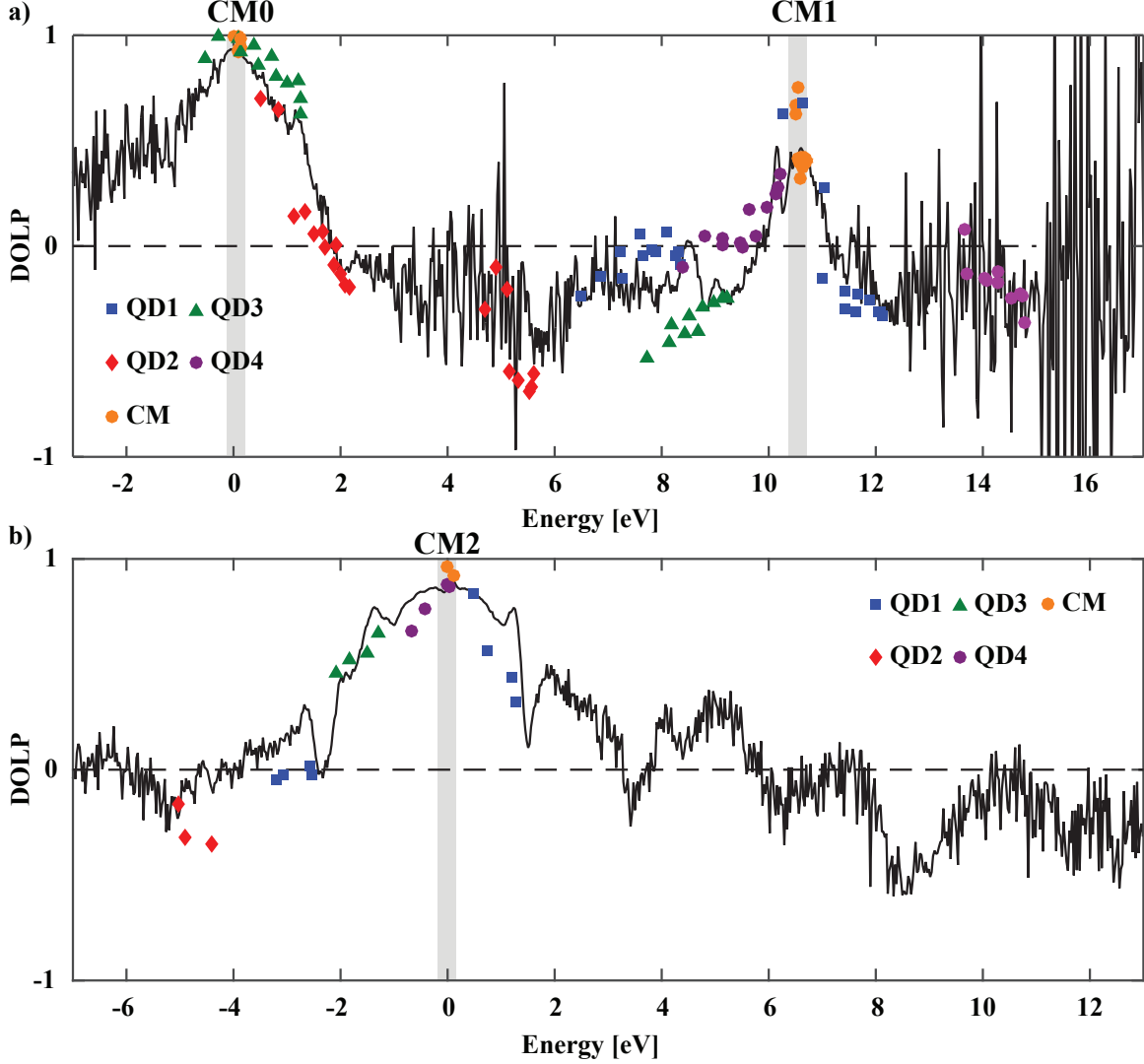
Figure 5:29 DOLP of excitonic lines of structure #3 obtained using condensation and temperature variations near resonance conditions with CM0 and CM1 (a) and CM2 (b). Black curves show DOLP traces of structure #3 obtained at 10 K under P=300 μeV excitation with weak (a) and strong (b) water vapor condensation conditions.

5.5.2   Coupling between 4 QD excitons and CM2-CM3 optical modes

Here, we conclude the study of the coupling of the first four CMs with the excitons at two well-defined positions in the L7 PhC cavity, focusing on the CM2-CM3 doublet. Using structure 'A' that has all 4 QD excitons coupled with CM2 at low temperatures without gas condensation, we investigated coupling between these transitions and CM3. Using water vapor condensation we tuned CM3 into resonance with the same QD transitions. This was possible since the CM2 –CM3 energy difference is around 16 meV in this structure.

Figure 5:30(a) shows polarization resolved spectra obtained at four condensation conditions providing a very wide detuning range between excitonic transitions and the CM2-CM3 doublet. The amount of water vapor condensation increases from top to bottom panels with 'CND' value representing the induced relative energy shift in percentage, with the maximum shift shown in the bottom panel. All spectra were obtained at the same excitation power P=300 µW and low temperature T=10 K. The difference in noise level for the H and V polarized spectra is due to different integration times used to record these spectra since the emission intensity of the excitonic transitions coupled with the CM is around one order of magnitude higher than that of the horizontally polarized component.

CM2 remains well visible in the polarization-resolved spectra even at ~10 meV detuning from the lower energy excitonic transition. Its intensity at these detuning conditions is of similar magnitude as the intensity of the QD excitons. Oppositely, at ~10 meV detuning conditions the weakly coupled CM1 has around one order of magnitude lower intensity once again proving that off-resonant CM emission in our structures strongly depends on the coupling strength that is defined by the CM-exciton overlap. With increasing amount of water condensation, the CM3 approaches the 4 QD excitonic transitions.
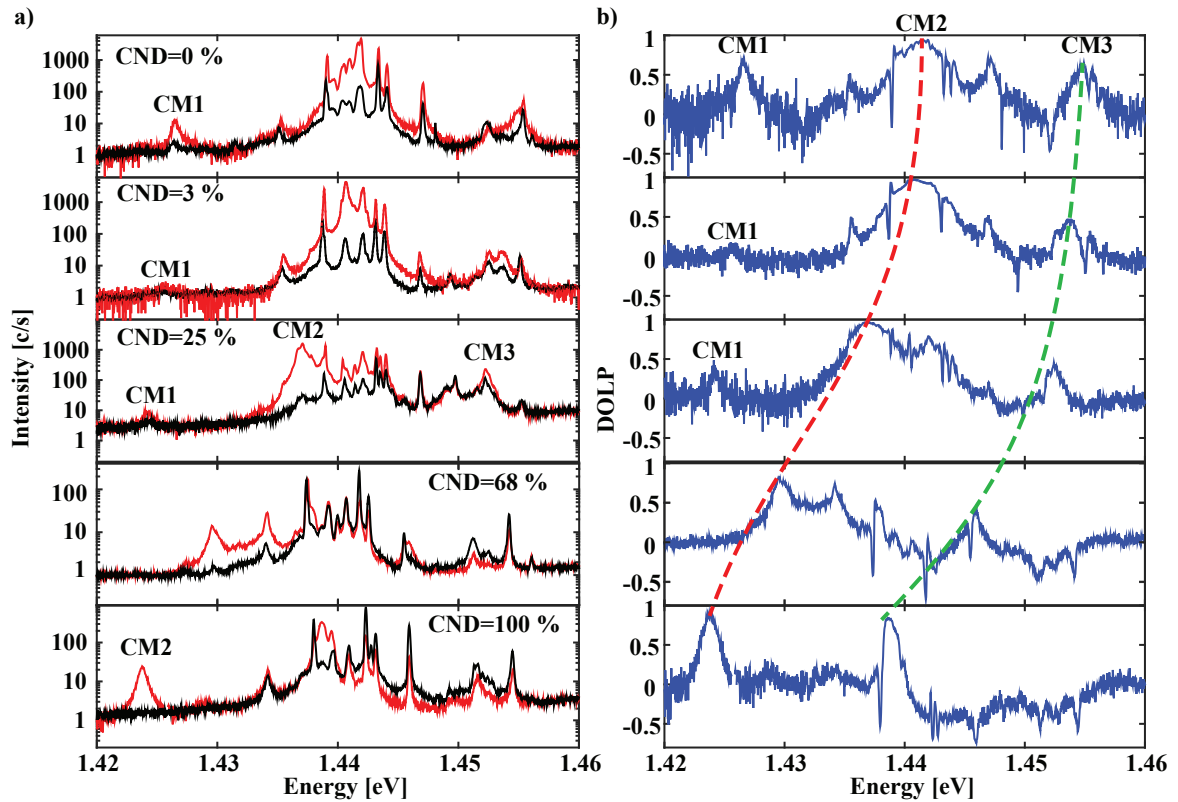
Figure 5:30 Polarization-resolved (a) and corresponding DOLP (b) spectra of 'structure A' at a set of condensation conditions. Dashed lines in the DOLP spectra panels serve as an eye guide for highlighting CM2 and CM3 energy positions. All spectra are obtained at P=300 µW excitation and T=10K.

Figure 5:31(a) shows polarization-resolved spectra obtained at a set of temperatures with CM3 tuned in-between the QD2 and QD3 neutral excitonic transitions 'QD2 X1' and 'QD3 X1'. Remarkably, excitonic transitions of the 'central' QDs show predominant horizontal polarization at both negative and positive detuning. At T=10 K the neutral exciton 'QD2 X1' is detuned by only -0.6 meV towards the lower energies revealing DOLP≈-0.6; thus even at almost direct resonance with CM3, excitonic transitions of the 'central' QDs show perpendicular polarization with respect to CM3. This effect can be explained by either enhancement of the horizontal or suppression of the vertical component of the excitonic emission. The horizontally polarized emission could be enhanced due to coupling of excitonic transitions with the CM of very low quality factor that would be invisible at off-resonant conditions. This effect can be probed by time-resolved measurements as will be discussed in the following. The vertically polarized emission could be suppressed due to interference between direct and indirect decay channels (see Chapter 4).
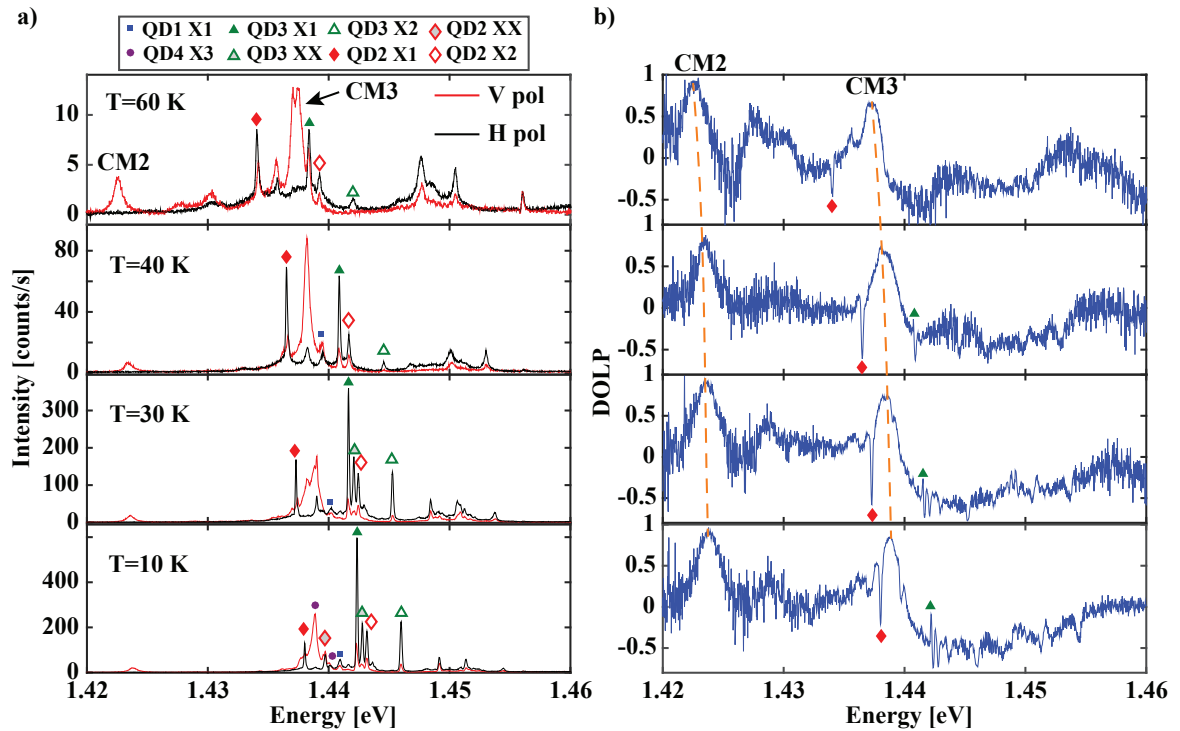
Figure 5:31 Polarization-resolved (a) and corresponding DOLP (b) spectra of structure 'A' at a set of temperatures under strong condensation conditions (panel "CND=100%" of Figure 5:30). Dashed lines in b) serve as an eye guide for highlighting the CM2 and CM3 energy positions.

We summarized the DOLP values of all 4 QD optical transitions as a function of detuning from CM2 in Figure 5:32, showing two panels with DOLP values obtained for the optical transitions of 'central' (a) and 'side' (b) QDs. These data were obtained using the fitting procedure of the main emission lines with Lorentzian lineshape as shown in Figure 5:19(c, d). Interestingly, at 5 meV positive detuning from CM2, excitonic transitions of all QDs show increasing vertical polarization intensity. Such enhancement was also observed for other spectral features in between CM2 and CM3. This effect can be due to a spurious mode in-between CM2 and CM3 that is not visible in the off-resonant emission. Such spurious modes CM_{sp} can appear due to PhC disorder and can be probed

only by direct scanning with the excitonic transitions. However, this mode does not significantly influence the polarization properties of QDs in resonance with CM2 and CM3, therefore we defer the discussion of the CM_{sp}-exciton coupling efficiency.

While Figure 5:32(a, b) shows strong co-polarization effects with CM2 of all 4 QD excitons, the optical transitions of the 'central' and 'side' QDs showed opposite behavior while tuned into resonance with CM3. QD1 and QD4 excitonic emission revealed pronounced co-polarization effect with the CM3 with very clear s-shape behavior (Figure 5:32(b)). Oppositely, QD2 and QD3 excitons were predominantly horizontally polarized (Figure 5:32(a)) as was already noted above. These optical transitions reveal horizontal polarization at almost 5 meV negative detuning from CM3 with the lowest values occurring close to the resonance with CM3.
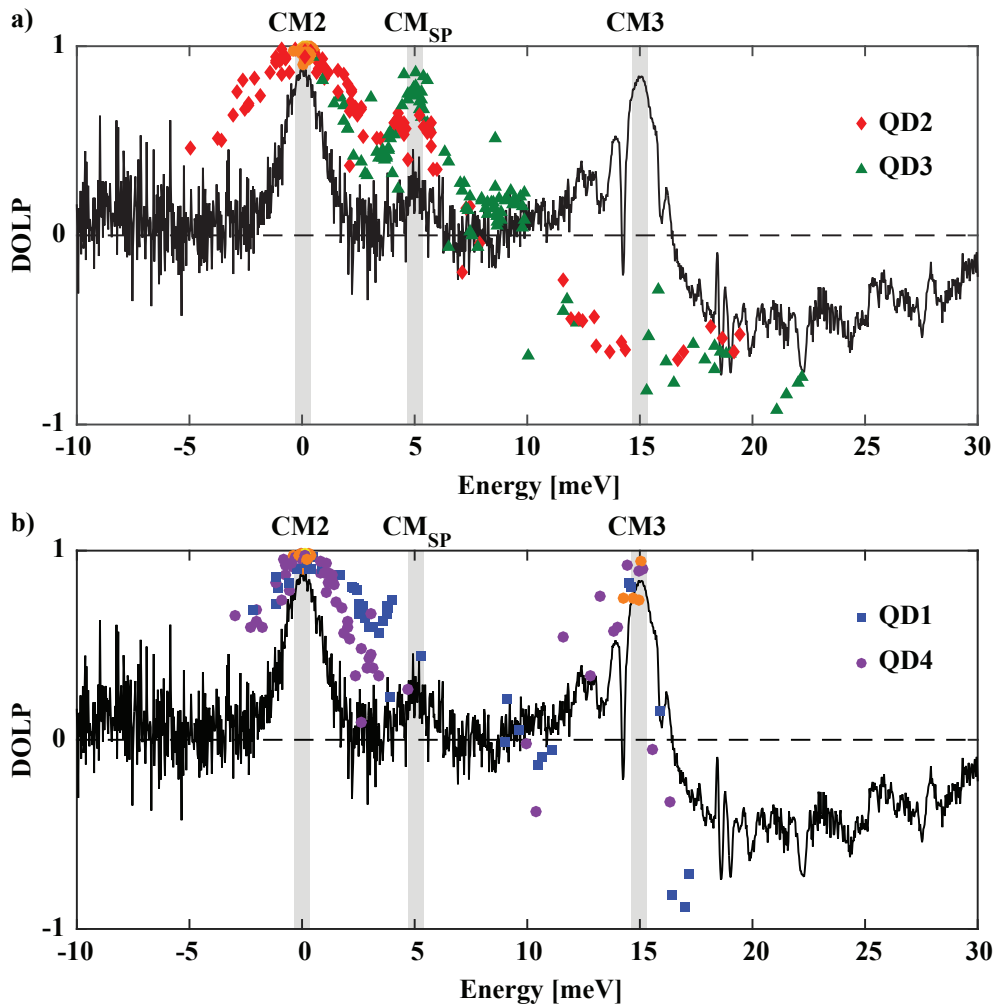
Figure 5:32 DOLP points of 'central' (a) and 'side' (b) QD excitons obtained using condensation and temperature variations. Black curves show DOLP trace of structure 'A' obtained at 10 K under P=300 μeV excitation with strong water vapor condensation conditions that is also shown in the bottom panel of Figure 5:30(b) and Figure 5:31(b).

Figure 5:33 shows decay time of the QD1-QD4 optical transitions tuned in the spectral vicinity of the CM3. In the resonance with the CM3 'side' QD excitons revealed ~0.2 ns decay time with Pur-

cell enhancement factor of ~ 8 assuming excitonic lifetime of 1.5ns in the bulk. This value corresponds well to the DOLP≈0.9 at resonance with CM3 as can be seen in Figure 5:32(b). We were not able to probe the lifetime of the vertically polarized component of the 'QD2 X1' excitonic line since only its horizontally polarized FSS component remains close to the resonance with the CM3 (see Figure 5:31) providing predominantly horizontal emission in the vicinity of the CM3 (Figure 5:32(a)).

Remarkably, the 'QD2 X1' horizontal FSS component showed ~2 ns lifetime, which means that there is no Purcell enhancement of this FSS component caused by the coupling with the horizontally polarized mode located in the vicinity of the CM3. The same result is also valid for the QD3 neutral excitonic transition 'QD3 X1' that has the same lifetime for both the horizontally and the vertically polarized FSS components (Figure 5:33). Therefore, the effect of decreasing DOLP of the 'central' QDs, from the zero DOLP value in-between CM2 and CM3(Figure 5:32) to negative values while approaching the CM3 transition, can not be explained by the presence of the additional horizontally polarized CM.
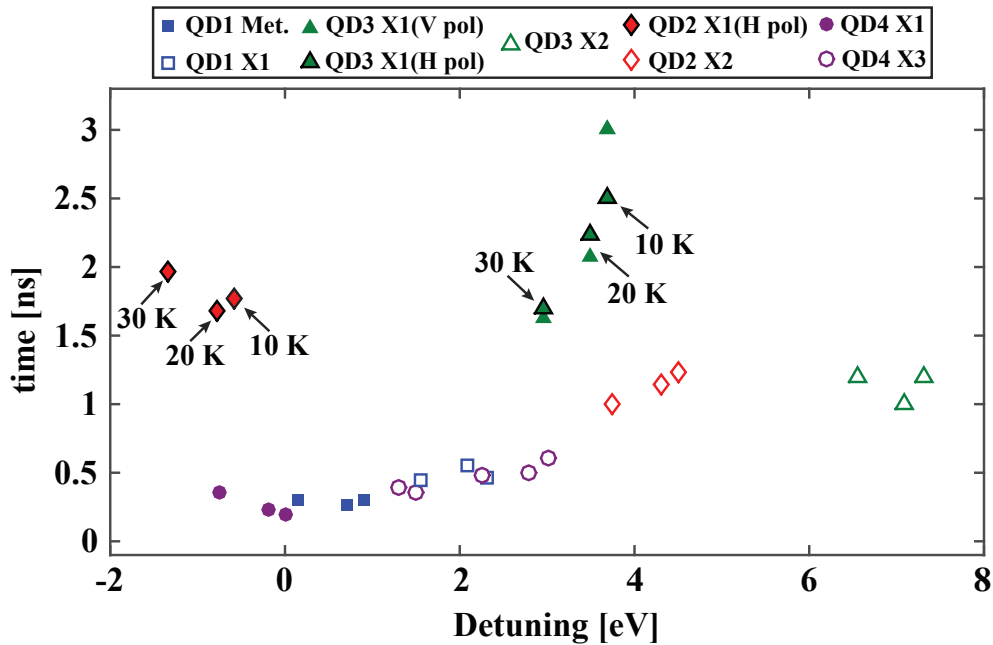
Figure 5:33 Summary of the decay times of the different QD transitions in structure A, obtained via time-resolved PL measurements under different condensation conditions. Detuning is defined as $E - E_{CM3}$.

It should be noted that almost identical decay time of both vertical and horizontal 'QD3 X1' FSS components is in contradiction with the measured negative DOLP values. We expect faster decay of the horizontal FSS component since its emission is several times stronger than the emission of the vertically polarized component. The possible explanation of this discrepancy is the biexponential nature of the neutral excitonic transition dynamics. While coupled with the CM, excitons reveal the biexcitonic decay traces (section 4.3.5) with the fast decay component corresponding to the excitonic decay rate through the CM and the slow decay corresponding to the background QD population

with electron hole pairs. However, in the case of very small coupling with the CM the fast decay component can be defined by either the decay rate through the optical modes or the background population rate depending on their interplay.

The PhC bandgap significantly reduces the density of vacuum optical modes therefore significantly increasing the decay time of QD excitons incorporated in the PhC cavities. As a result, the lifetime of the excitonic transitions in the PhC can be around several tenths of ns [182]. Therefore, the background population rate that has characteristic time ~3 ns as was observed for the charged excitons (section 4.3.5) defines the decay time of 'QD2 X1' and 'QD3 X1' neutral excitonic complexes. We can only estimate the lower limit for the exciton decay time, that is, ~2 ns. Thus, the background QD population hides the suppression of the decay through the vertically polarized modes with respect to the decay through the horizontally polarized modes that provides the dominant horizontal polarization of the 'QD2 X1' and 'QD3 X1' excitons.

This suppression could be due to the interference between direct and indirect decay channels as described in the section 1.4.2.2. Although the coupling strength between the CM3 and the 'central' QD excitons is very small, these optical transitions can interact through the free space modes providing destructive interference in the vertical emission of the 'central' QDs as described in section 1.4.2.2. This interference would lead to the predominantly horizontally polarized emission of the 'central' QDs close to the resonance with the CM3, although we expect narrower spectral region at which it happens (see section 4.5).

5.6   Conclusions

In this Chapter we discussed the integration of 2 and 4 QDs at well-defined positions inside an L7 PhC cavity. Taking advantage of the high reproducibility of our integration method, we studied coupling between the four L7 PhC modes and excitonic transitions with prescribed locations inside the L7 PhC cavity. Statistical study of the polarization properties of structures with 2 and 4 QDs in an L7 PhC cavity allowed identifying the modes suitable for coupling with a system of four QD excitons. Such deterministic integration of semiconductor emitters in a photonic cavity can be scaled up to larger cavities, waveguides, and coupled optical elements, providing an important step towards QD-based integrated quantum photonics.

Chapter 6   Conclusions and outlook

In the course of this thesis we demonstrated advantages of site-controlled pyramidal QDs for integration with photonic cavities. The high position control of these QDs has yielded numerous devices with a single or several QDs incorporated into linear PhC cavities at well-defined spatial positions. The spectral homogeneity of the pyramidal QDs, as well as the high control of the PhC optical mode energy, provides high reproducibility of spectral features observed in the PL spectra of the structures. Thus, we achieved high fabrication yield of nearly identical devices with sufficiently small deviations from the targeted layout, providing an ideal platform for statistical studies of the optical properties of a large variety of photonic structures.

To this end, we addressed the influence of the QD position with respect to the electric field pattern of the CM on the optical properties of the QD excitonic transitions. For this purpose we integrated a single pyramidal QD in an L3 PhC membrane cavity at a set of prescribed positions, among which were positions corresponding to the first and the second CM antinodes as well as a CM node. Time- and polarization-resolved PL measurements showed strong Purcell enhancement of the single-QD exciton positioned exactly at the maximum of the electric field of the ground state CM0. We measured more than tenfold enhancement of the exciton emission rate (excitonic life time reduction from ~1.5 ns to ~120 ps) at direct resonance with the CM0 proving efficient exciton-CM0 coupling. Interestingly, coupling charged excitons with a CM allowed for observing an additional QD population channel with ~3 ns characteristic time that is much longer than the QD absorption time of the free carriers excited in the bulk GaAs. The possible explanation of this population mechanism is QD capturing of carriers trapped by carbon impurities, which has very similar slow decay characteristic time.

One of the most important results of this thesis is a clear demonstration of the impact of the positioning of a single dipole on the CM-induced Purcell enhancement using exciton-CM co-polarization as its probing. Taking advantage of the high reproducibility of devices obtained with our fabrication approach, we aimed at providing statistical evidence of the strong reduction of the excitonic co-polarization with the ground state CM0 while the QD was shifted from the antinode to the node of the CM0 electric field. This effect was demonstrated for several hundreds of devices for each nominal QD position revealing high correspondence between modeled and actual CM electric field patterns. The degree to which the exciton-CM co-polarization is suppressed is limited by the finite size of the QD, that is, around 20 nm. The latter introduces nonzero exciton-CM overlap even if the QD center is exactly at the CM node yielding nonzero exciton-CM coupling strength. However, a QD placed at the zero electrical field of the CM shows an emission rate through the CM that is much lower than the spontaneous exciton emission rate; therefore, the latter dominates providing negligible exciton-CM co-polarization. The high precision of our fabrication approach, allowing misalignment errors as low as ~15 nm, is the core of this experiment. It highlights its importance

for the realization of QD-based photonic circuits that require high alignment precision of multiple QDs with more complex photonic structures. Additionally to the fundamental mode CM0, we investigated the effect of the QD position on the coupling with the first excited mode CM1 getting similar results. Thus we concluded that CM1 also has an actual electric field pattern very similar to its modeled version.

Another major result of this thesis is the explanation of the s-shape behavior found previously in the degree of linear polarization (DOLP) spectra of the single QD exciton in the L3 PhC cavity [15], [72]. Excitonic emission becomes predominantly horizontally polarized (along the cavity axis) for certain positive exciton-CM energy detuning. One of the explanations of this effect proposed earlier [15] was a different excitonic spontaneous emission rate through horizontally and vertically polarized free space optical modes induced by the inhomogeneous LDOS of optical modes in the PhC matrix. Using the position control of our QD system we demonstrated that the s-shape behavior strongly depends on the relative QD position with respect to the CM antinodes. Varying the QD position we clearly showed that the s-shape profile vanishes simultaneously with the exciton-CM coupling when the QD is positioned at the CM node. This, in turn, results in unpolarized excitonic emission, and thus has no relationship with the LDOS inhomogeneity of the optical modes in the PhC matrix [16]. Subsequently, we theoretically explained the s-shape behavior by expanding a model previously developed by Yamaguchi et al. [43] that describes a Fano-like resonance between the direct (spontaneous emission) and indirect (emission through the CM) excitonic decay channels. We showed how this resonance affects excitonic polarization at various exciton-CM energy detunings and the phase difference between the exciton and the CM coupling strengths to the free space modes. Diagonalizing the Janyes-Cumming Hamilton we obtained a simple analytical expression that describes the exciton-CM detuning at which excitons experience the maximum horizontal polarization. This expression can be potentially used for identification of the exciton-CM coupling parameters, such as the phase between the exciton and the CM coupling strengths with the free space modes.

Addressing the question of physical phenomena limiting the optical quality of our pyramidal QDs when embedded in PhC structures we explored spectral diffusion and spectral wandering processes of the QD exciton recombination. We found slow spectral wandering and intermittency of QD excitonic emission that are explained by charge fluctuations in the QD solid-state environment. We observed a strong dependence of the spectral wandering and emission intermittency effects on the sample light exposure history, clearly exhibiting a photon-activated charge trapping in the QD vicinity. We assume that similar charge fluctuations also lead to the pure dephasing observed in the QD excitonic linewidth.

Exploring the charge trapping processes in the QD environment, we developed a correlation technique based on the observation of transitions between different excitonic energy levels induced by the quantum confined Stark effect (QCSE). This technique allowed us to study the nature of charged centers in the vicinity of the QD, leading to spectral jumps between discrete emission energies of the QD excitons. Relating the QD exciton energy to the amplitude of the electric field inducing the QCSE allowed observing unusual spectral response of the QD upon increasing the charge density in its vicinity. Additionally, it allowed probing the ratio between the dipole moments of different excitonic complexes. Scanning spectrally a CM with a single QD exciton tuned by the

fluctuations of the built-in electric field, we observed emission intensity enhancement associated with the CM-induced Purcell effect.

We observed irreversible QCSE-induced exciton spectral shift to the lower energies by more than 10 meV accompanied by the intensity intermittency. Interestingly, decrease in the excitonic energy corresponds to a reduced built-in electric field, which can be a sign of neutralization of charged centers by the excited carriers. We explain the emission intermittency by such high built-in field values that led to QD trapping of only one type of carriers. Such spectral wandering and emission intermittency processes, a novel observation in our QD system, could be used as a measure of further QD optimization.

In the course of this thesis we successfully integrated of up to 4 QDs with an L7 PhC cavity, representing a further development step of pyramidal QD-based PhC cavity integration technology. For several such structures we identified the optical transitions of each QD by means of spatial scanning micro-photoluminescence, accompanied with correlations in spectral wandering traces. Taking advantage of the well identified excitonic transitions, we demonstrated phonon-assisted weak coupling of four different QD excitons with the same CM. Using a combination of temperature- and water condensation- induced exciton-CM tuning allowed probing the coupling of the four QDs to different CMs, thereby probing the modal spatial patterns of the L7 PhC cavity at two well defined positions. Interestingly, we observed orthogonal-polarization of the QD excitons that are tuned into resonance with the L7 PhC optical mode they do not couple with. This effect is explained in a similar way as the s-shape behavior summarized above. Successful demonstration of spatial integration and spectral coupling of the QD and the photonic cavity is an important step towards scalable QD-based technology.

High finessse cavities having an optical mode coupled with multiple high quality QDs could serve as a low-threshold laser systems, whereas two or more QDs integrated with PhC cavities coupled through a PhC waveguide could allow information exchange between stationary excitonic qubits by means of single photons. However, further development in the integration of our QD in PhC cavity systems is necessary for achieving these goals. As was noted previously[15], the Q factor of PhC cavities increases at wavelength higher than 900 nm, mostly due to reduced optical absorption in the membrane material. Therefore, we should target QD-exciton emission and CM resonances in future devices at this spectral range. Since the exciton-CM resonance is spectrally defined by the QD emission wavelength, we should shift the QD emission to wavelengths above 900 nm. This was recently achieved[194] using triethyl galium instead of trimethyl gallium as a MOCVD source. Another outstanding issue is optimization of the QD linewidth. It should include both optimizations of MOCVD growth procedure itself as well as the clean room processing during substrate patterning with inverted pyramids. The latter is probably the main source of defects leading to the spectral diffusion of our QD excitonic lines. Recently, average emission linewith around 50 µeV with minimum values of a few tens of µeV were demonstrated for pyramidal QDs at EPFL [LPN, provate communication]. Combining high finesse QD-PhC cavity systems with resonance photo-excitation instead of above barrier pumping could allow achieving pyramidal QD emission with much reduced spectral diffusion effects.

In conclusion, the results of this thesis demonstrate the advantages of site-controlled pyramidal QDs for photonics and highlight the current drawbacks that should be improved for implementation in various photonic devices relevant to QD-based quantum computation and communication as well as low threshold lasers and single photon sources. Longer wavelength pyramidal QDs could potentially allow integration with higher quality factor photonic cavities that may reach the strong exciton-CM coupling regime, especially if spectral diffusion and wandering is suppressed leading to nearly Fourier-transform limited linewidth of pyramidal QD excitons. Achieving this step is highly important for many quantum optics experiments, in particular, for optical addressing of QD exciton-based stationary qubit. Additionally, our pyramidal QDs could be very suitable for experiments in plasmonics. Exploiting polarization, direction and intensity control of the QD emission by plasmonic devices it should be possible to obtain matrices of highly polarized optical sources[195]. Finally, one could think about not only single-photon but N-photon sources with predefined polarization properties. Such a source could be obtained if one combines N spectrally homogeneous site-controlled pyramidal QDs coupled with a plasmonic antenna. Using the pulsed excitation scheme of QDs in such a device would lead to emission of N-photons on-demand due to the high Purcell enhancement. Such an experiment could also provide a possibility of deterministic study of collective emission of N emitters coupled through a common radiation field. Moreover, using spectrally- isolated QDs (section 3.3), such plasmonic devices could be obtained without additional procedures for QD isolations, which would significantly simplify their fabrication process.

Appendix A

In this appendix we present the precursors fluxes and the partial pressures used during the growth process of our samples. The list of growth runs that yielded the samples mentioned in this thesis is given in Tab. 2.

All samples studied in the course of this thesis were grown by Dr. Alok Rudra using a commercial, low-preassure (20 mbar) Aixtron MOCVD reactor. We used N_2 as carrier gas. The tables presented below list used fluxes, partial pressures and other growth conditions. Fluxes are taken from growth files, while partial pressures of hydrides are calculated by normalizing the total pressure p by the ratio of the precursor flux, $Q_{AsH3} = 233$ sccm, divided by the total flux $Q_{tot} = 7080$ sccm, that is, $P_{AsH3} = \frac{Q_{AsH3}}{Q_{AsH3}} P$. The partial pressure of metalorganics is calculated similarly $P_{MO} = \frac{P_{V,MO}}{P_{bub}} \frac{Q_{MO}}{Q_{tot}} P$ where $P_{V,MO}$ is the metalorganics vapour pressure ~53 mbar for TMGa at -10 ∘C and ~1.13 mbar for TMIn at 17 ∘C while $P_{bub} = 1.2$ bar is the bubbler cylinder pressure. Prefactor $P_{V,MO}/P_{bub}$ accounts for the fact that metalorganics sources are liquid[78]. Tab. 1 shows the vapour pressure for each chemical source and its temperature. Exhaustive lists of metalorganics vapour pressures can be found in [196], [197]. The ratio of the fluxes yields a V/III ratio of 2800.

Precursor/Gas	Flux (sccm)	Thickness (µbar)	Source T(°C)
AsH3	233	660	
TMGa	3.3	0.2325	-10
TMIn	20	0.0532	17

Tab. 1 Fluxes and partial pressures for gasses used during the MOCVD growth.

Tab. 1 shows the list of epitaxial layer sequence used for the QD growth in the main samples utilized for the L3 and L7 PhC integration with a single and multiple QDs. The values are copied from the MOCVD database.

Layer	Material	%	Thickness (nm)	Growth rate (nm/s)	T(°C)	V/III	Source
Buffer	GaAs		4.1	0.007	590	2643	TMGa, AsH3
QD	InGaAs	30	0.268	0.01	590	1714	TMGa, TMIn AsH3
Cap	GaAs		2.5	0.007	590	2643	TMGa, AsH3

Tab. 2 The growth list of the samples Gio15-1B (4877), Gio15-2B (4879), Gio15-4B (4881), Gio15-3A, 3B (4885)

Appendix B

Every EBL[*] system has some inevitable drift of the sample holder relative to the electron beam. The main cause of this drift is changes in holder temperature, which can have two sources: First, the temperature difference between the outside ambient and the inside of the EBL vacuum chamber, causing slow thermalization (and drift) of the holder. Then, heating inside the EBL by the last electron lens, which influences locally the sample temperature, according to the writing pattern. The error introduced by this drift process can be reduced by breaking the EBL design to small parts and realigning to the same AM set before writing each part. In this way, the drift-induced error is reduced to the drift during the writing time of one part, which can be made sufficiently small. This process costs in extra complexity and alignment time, but has the added benefit of providing us with the information on the AM position, which allows us to estimate the errors. In our samples, composed of 45 squares, we chose to realign before writing the PhC pattern in each square, thus limiting the drift time to about 4 min. Figure 1(a) shows the measured coordinates of 3 AMs over time during the whole 193 min. writing time, choosing as zero the coordinates at the last alignment. The coordinates (x_i^j, y_i^j) are measured for the ith alignment mark (i = 1 - 3) before writing of PhC cavities in the jth square, where j = 1, 2,…,45. As the system reports the exact time of alignment, we obtain the time evolution of the coordinates for each alignment mark ($\delta x_i = x_i - x_i^N$, $\delta y_i = y_i - y_i^N$). As we see in Fig. 20(a), we observe almost zero drift of the x coordinates, while the y coordinates change with time by about 0.4 nm/min, or 1.6 nm per square writing period (between alignments). This is due to the structure of the sample holder, where the sample's distance from the center of the holder is small in x, but not in y. Therefore, thermal expansion of the holder has much larger influence on the y coordinate than on x. We also observe that all three AM coordinates follow approximately the same drift trend, which allows for efficient drift compensation by realigning the EBL system at 4 min. intervals.

Comparing coordinates measured at the nearest alignment events ($\delta x_i^j = x_i^j - x_i^{j-1}$, $\delta y_i^j = y_i^j - y_i^{j-1}$), we can estimate the uncertainty in AM recognition. Figure 1(b) shows the coordinate difference as function of time. Due to the very small drift between two alignment events (as we have shown it's equivalent to 1.6 nm), both δx_i and δy_i show pure stochastic time distribution. Plotting histograms of all δx_i and δy_i values (Figure 1(c, d)) we observe the near-Gaussian distribution of the AM positions, with σ_x and σ_y of the order of 8-9nm and a center shift of 0.8 nm in x but 3.2 nm in y (corresponding to the much larger y drift value, as seen in Figure 1(a)). From this analysis we can conclude that the random component in AM position (on the order of s = 8-9 nm) is much more important than the drift component (3 nm), showing that we have indeed reduced the drift effect to an acceptable level. Overall, we estimate our alignment accuracy as ±10 nm (corresponding to >80% of the measurements; we have >95% of the measurements within ±20 nm).

---

[*] Dr. Benjamin Dwir did the electron beam lithography of all samples described in this thesis.
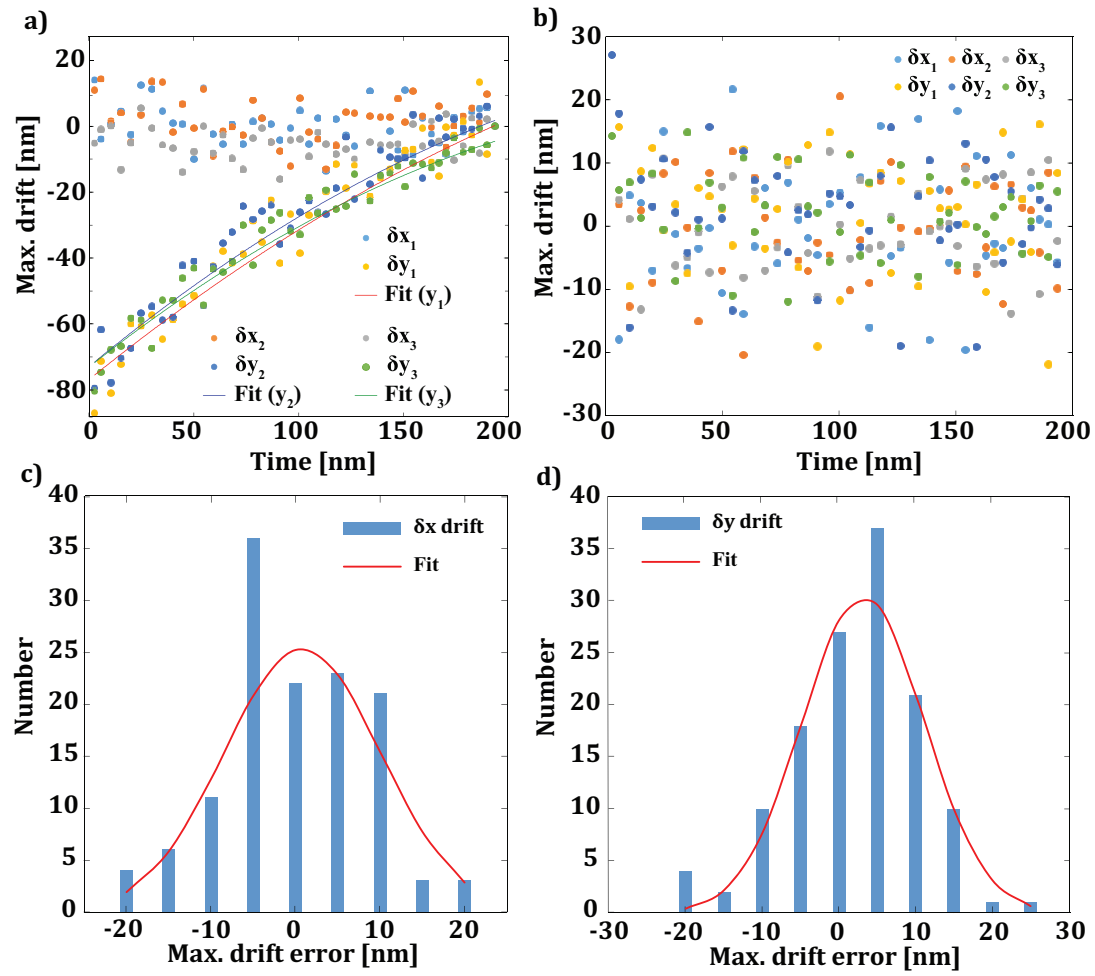
Figure 1 a) Cumulative drift error, as shown by tracing the positions of the three alignment marks used in sample Gio15-2B during the whole writing period (200 min.), plotted relative to the last measurement. b) AM drift error per alignment, as shown by the difference in three alignment mark positions between successive alignments δx_i and δy_i. (c,d) Histograms of δx_i and δy_i from (b), with Gaussian fits (Xcenter = 0.8 nm, Xs = 9.3 nm; Ycenter = 3.2 nm, Ys = 7.9 nm)

Contributions

The author performed all optical measurements presented in this manuscript except the optical characterization of QD ensembles for growth optimization and PhC implementation provided by Clement Jarlov (see flow chart in Figure 2:4; Figure 2:14 and Figure 2:15). The author participated in clean-room fabrication of all samples containing QDs in PhC cavities together with Irina Kulkova, Benjamin Dwir and Alok Rudra. In particular, using clean room tools the author patterned and characterized all samples except the ones presented in Section 3.2 that were patterned together with Irina Kulkova. Benjamin Dwir carried out all electron beam lithography and alignment optimization procedures. Alok Rudra did all MOVPE growth of QDs. Irina Kulkova did patterning and characterization of samples containing spectrally isolated QDs (Section 3.2). The author analyzed all data shown in this manuscript, explained observed effects (Section 4.3.4, 4.3.5) and implemented water vapor condensation tuning of CM energy (Section 5.5). Eli Kapon and Benjamin Dwir designed the structures implemented in these samples while Clement Jarlov modeled PhC cavities using a Mathlab code written by K. F. Karlsson (Linköping University). Dr. Benjamin Dwir and Prof. Eli Kapon supervised the work presented in this thesis.

References

[1]   A. F. Koenderink, A. Alù, and A. Polman, "Nanophotonics: Shrinking light-based technology", *Science* **348**, 516-521 (2015).

[2]   E. Yablonovitch, T. Gmitter, and K. Leung, "Photonic band structure: The face-centered-cubic case employing nonspherical atoms", *Phys. Rev. Lett.* **67**, 2295–2298 (1991).

[3]   A. Chutinan and S. Noda, "Highly confined waveguides and waveguide bends in three-dimensional photonic crystal", *Appl. Phys. Lett.* **75**, 3739 (1999).

[4]   S. Ogawa, M. Imada, S. Yoshimoto, M. Okano, and S. Noda, "Control of Light Emission by 3D Photonic Crystals", *Science* **305**, 227-229 (2004).

[5]   T. Baba, "Slow light in photonic crystals", *Nat. Photonics* **2**, 465–473 (2008).

[6]   K. Hennessy, A. Badolato, M. Winger, D. Gerace, M. Atatüre, S. Gulde, S. Falt, E. L. Hu, and A. Imamoglu, "Quantum nature of a strongly-coupled single quantum dot-cavity system", *Nature* **445**, 896-899 (2007).

[7]   H. Sumikura, E. Kuramochi, H. Taniyama, and M. Notomi, "Ultrafast spontaneous emission of copper-doped silicon enhanced by an optical nanocavity", *Sci. Rep.* **4**, 5040 (2014).

[8]   K. J. Vahala, "Quantum box fabrication tolerance and size limits in semiconductors and their effect on optical gain", *IEEE J. Quantum Electron.* **24**, 523–530 (1988).

[9]   R. J. Coles, N. Prtljaga, B. Royall, I. J. Luxmoore, A. M. Fox, and M. S. Skolnick, "Waveguide-coupled photonic crystal cavity for quantum dot spin readout", *Opt. Express* **22**, 2376 (2014).

[10]   K. Tanaka, E. Plum, J. Y. Ou, T. Uchino, and N. I. Zheludev, "Multifold enhancement of quantum dot luminescence in plasmonic metamaterials", *Phys. Rev. Lett.* **105**, 227403 (2010).

[11]   M. L. Andersen, S. Stobbe, A. S. Sørensen, and P. Lodahl, "Strongly modified plasmon–matter interaction with mesoscopic quantum emitters", *Nat. Phys.* **7**, 215–218 (2011).

[12]   J. Ho, J. Tatebayashi, S. Sergent, C. F. Fong, Y. Ota, S. Iwamoto, and Y. Arakawa, "A Nanowire-Based Plasmonic Quantum Dot Laser", *Nano Lett.* **16**, 2845–2850 (2016).

[13]   Y. Fang and M. Sun, "Nanoplasmonic waveguides: towards applications in integrated nanophotonic circuits", *Light Sci. Appl.* **4**, e294 (2015).

[14]   M. Rohlfing, P. Krüger, and J. Pollmann, "Quasiparticle band-structure calculations for C, Si, Ge, GaAs, and SiC using Gaussian-orbital basis sets", *Phys. Rev. B* **48**, 17791–17805 (1993).

[15]   M. Ćalić, "Cavity Quantum Electrodynamics with Site-Controlled Pyramidal Quantum Dots in Photonic Crystal Cavities", PhD thesis, EPFL (2013).

[16]   P. Lodahl, S. Mahmoodian, and S. Stobbe, "Interfacing single photons and single quantum dots with photonic nanostructures", *Rev. Mod. Phys.* **87**, 347–400 (2015).

[17]   D. Gammon, E. Snow, B. Shanabrook, D. Katzer, and D. Park, "Fine structure splitting in the optical spectra of single GaAs quantum dots", *Phys. Rev. Lett.* **76**, 3005–3008 (1996).

[18] E. Peter, P. Senellart, D. Martrou, A. Lemaître, J. Hours, J. M. Gérard, and J. Bloch, "Exciton-photon strong-coupling regime for a single quantum dot embedded in a microcavity", *Phys. Rev. Lett.* **95**, 67401 (2005).

[19] M. Abbarchi, M. Gurioli, S. Sanguinetti, M. Zamfirescu, A. Vinattieri, and N. Koguchi, "Recombination lifetime of single GaAs/AlGaAs quantum dots", *Phys. Status Solidi* **3**, 3860–3863 (2006).

[20] T. Mano, M. Abbarchi, T. Kuroda, C. A. Mastrandrea, A. Vinattieri, S. Sanguinetti, K. Sakoda, and M. Gurioli, "Ultra-narrow emission from single GaAs self-assembled quantum dots grown by droplet epitaxy", *Nanotechnology* **20**, 395601 (2009).

[21] A. Huggenberger, S. Heckelmann, C. Schneider, S. Höfling, S. Reitzenstein, L. Worschech, M. Kamp, and A. Forchel, "Narrow spectral linewidth from single site-controlled In(Ga)As quantum dots with high uniformity", *Appl. Phys. Lett.* **98**, 131104 (2011).

[22] J. Skiba-Szymanska, A. Jamil, I. Farrer, M. B. Ward, C. A. Nicoll, D. J. P. Ellis, J. P. Griffiths, D. Anderson, G. A. C. Jones, D. A. Ritchie, and A. J. Shields, "Narrow emission linewidths of positioned InAs quantum dots grown on pre-patterned GaAs(100) substrates", *Nanotechnology* **22**, 65302 (2011).

[23] K. Choi, S. Kako, M. J. Holmes, M. Arita, and Y. Arakawa, "Strong exciton confinement in site-controlled GaN quantum dots embedded in nanowires", *Appl. Phys. Lett.* **103**, 171907 (2013).

[24] M. Felici, P. Gallo, A. Mohan, B. Dwir, A. Rudra, and E. Kapon, "Site-controlled InGaAs quantum dots with tunable emission energy", *Small* **5**, 938–943 (2009).

[25] A. Mohan, P. Gallo, M. Felici, B. Dwir, A. Rudra, J. Faist, and E. Kapon, "Record-low inhomogeneous broadening of site-controlled quantum dots for nanophotonics", *Small* **6**, 1268–1272 (2010).

[26] M. Calic, P. Gallo, M. Felici, K. A. Atlasov, B. Dwir, A. Rudra, G. Biasiol, L. Sorba, G. Tarel, V. Savona, and E. Kapon, "Phonon-mediated coupling of InGaAs/GaAs quantum-dot excitons to photonic crystal cavities", *Phys. Rev. Lett.* **106**, 227402 (2011).

[27] P. Gallo, M. Felici, B. Dwir, K. A. Atlasov, K. F. Karlsson, A. Rudra, A. Mohan, G. Biasiol, L. Sorba, and E. Kapon, "Integration of site-controlled pyramidal quantum dots and photonic crystal membrane cavities", *Appl. Phys. Lett.* **92**, 263101 (2008).

[28] A. Lyasota, S. Borghardt, C. Jarlov, B. Dwir, P. Gallo, A. Rudra, and E. Kapon, "Integration of multiple site-controlled pyramidal quantum dot systems with photonic-crystal membrane cavities", *J. Cryst. Growth* **414**, 192–195 (2015).

[29] E. Poem, Y. Kodriano, C. Tradonsky, N. H. Lindner, B. D. Gerardot, P. M. Petroff, and D. Gershoni, "Accessing the dark exciton with light", *Nat. Phys.* **6**, 993–997 (2010).

[30] R. Seguin, A. Schliwa, S. Rodt, K. Potschke, U. W. Pohl, and D. Bimberg, "Size-dependent fine-structure splitting in self-organized InAs/GaAs quantum dots", *Phys. Rev. Lett.* **95**, 257402 (2005).

[31] J. D. Joannopoulos, S. G. Johnson, J. N. Winn, and R. D. Meade, *Photonic Crystals : Molding the Flow of Light (Second Edition)*. Princeton University Press, 2008.

[32] J. P. Reithmaier, G. Sek, A. Löffler, C. Hofmann, S. Kuhn, S. Reitzenstein, L. V Keldysh, V. D. Kulakovskii, T. L. Reinecke, and A. Forchel, "Strong coupling in a single quantum dot-

semiconductor microcavity system", *Nature* **432**, 197–200 (2004).

[33] P. T. Kristensen, C. Van Vlack, and S. Hughes, "Generalized effective mode volume for leaky optical cavities", *Opt. Lett.* **37**, 1649 (2012).

[34] Y. Lai, S. Pirotta, G. Urbinati, D. Gerace, M. Minkov, V. Savona, A. Badolato, and M. Galli, "Genetically designed L3 photonic crystal nanocavities with measured quality factor exceeding one million", *Appl. Phys. Lett.* **104**, 241101 (2014).

[35] C. P. Michael, K. Srinivasan, T. J. Johnson, O. Painter, K. H. Lee, K. Hennessy, H. Kim, and E. Hu, "Wavelength- and material-dependent absorption in GaAs and AlGaAs microcavities", *Appl. Phys. Lett.* **90**, 51108 (2007).

[36] K. Hennessy, A. Badolato, M. Winger, D. Gerace, M. Atatüre, S. Gulde, S. Fält, E. L. Hu, and A. Imamoğlu, "Quantum nature of a strongly coupled single quantum dot–cavity system", *Nature* **445**, 896–899 (2007).

[37] M. D. Birowosuto, H. Sumikura, S. Matsuo, H. Taniyama, P. J. van Veldhoven, R. Nötzel, and M. Notomi, "Fast Purcell-enhanced single photon source in 1,550-nm telecom band from a resonant quantum dot-cavity coupling", *Sci. Rep.* **2**, 321 (2012).

[38] A. Dousse, J. Suffczyński, A. Beveratos, O. Krebs, A. Lemaître, I. Sagnes, J. Bloch, P. Voisin, and P. Senellart, "Ultrabright source of entangled photon pairs", *Nature* **466**, 217–220 (2010).

[39] K. De Greve, L. Yu, P. L. McMahon, J. S. Pelc, C. M. Natarajan, N. Y. Kim, E. Abe, S. Maier, C. Schneider, M. Kamp, S. Höfling, R. H. Hadfield, A. Forchel, M. M. Fejer, and Y. Yamamoto, "Quantum-dot spin-photon entanglement via frequency downconversion to telecom wavelength", *Nature* **491**, 421–425 (2012).

[40] E. Purcell, H. Torrey, and R. Pound, "Resonance Absorption by Nuclear Magnetic Moments in a Solid", *Phys. Rev.* **69**, 37–38 (1946).

[41] S. M. Barnett, B. Huttner, R. Loudon, and R. Matloob, "Decay of excited atoms in absorbing dielectrics", *J. Phys. B: At. Mol. Opt. Phys.* **29**, 3763–3781 (1996).

[42] A. Auffèves, D. Gerace, J. M. Gérard, M. F. Santos, L. C. Andreani, and J. P. Poizat, "Controlling the dynamics of a coupled atom-cavity system by pure dephasing", *Phys. Rev. B* **81**, 245419 (2010).

[43] M. Yamaguchi, T. Asano, M. Fujita, and S. Noda, "Theoretical analysis of light emission from a coupled system of a photonic nanocavity and a quantum dot", *Phys. Status Solidi* **5**, 2828–2830 (2008).

[44] J. P. Reithmaier, G. Sęk, A. Löffler, C. Hofmann, S. Kuhn, S. Reitzenstein, L. V. Keldysh, V. D. Kulakovskii, T. L. Reinecke, and A. Forchel, "Strong coupling in a single quantum dot–semiconductor microcavity system", *Nature* **432**, 197–200 (2004).

[45] S. Reitzenstein, A. Löffler, C. Hofmann, A. Kubanek, M. Kamp, J. P. Reithmaier, A. Forchel, V. D. Kulakovskii, L. V. Keldysh, I. V. Ponomarev, and T. L. Reinecke, "Coherent photonic coupling of semiconductor quantum dots", *Opt. Lett.* **31**, 1738-1740 (2006).

[46] F. Albert, K. Sivalertporn, J. Kasprzak, M. Strauß, C. Schneider, S. Höfling, M. Kamp, A. Forchel, S. Reitzenstein, E. A. a Muljarov, and W. Langbein, "Microcavity controlled coupling of excitonic qubits", *Nat. Commun.* **4**, 1747 (2013).

[47] A. Laucht, J. M. Villas-Bôas, S. Stobbe, N. Hauke, F. Hofbauer, G. Böhm, P. Lodahl, M. C. Amann, M. Kaniber, and J. J. Finley, "Mutual coupling of two semiconductor quantum dots via an optical nanocavity", *Phys. Rev. B* **82**, 75305 (2010).

[48] A. Huggenberger, C. Schneider, C. Drescher, S. Heckelmann, T. Heindel, S. Reitzenstein, M. Kamp, S. Höfling, L. Worschech, and A. Forchel, "Site-controlled In(Ga)As/GaAs quantum dots for integration into optically and electrically operated devices", *J. Cryst. Growth* **323**, 194–197 (2011).

[49] S. Reitzenstein, S. Münch, P. Franeck, A. Löffler, S. Höfling, L. Worschech, A. Forchel, I. V. Ponomarev, and T. L. Reinecke, "Exciton spin state mediated photon-photon coupling in a strongly coupled quantum dot microcavity system", *Phys. Rev. B* **82**, 121306 (2010).

[50] M. Winger, T. Volz, G. Tarel, S. Portolan, A. Badolato, K. J. Hennessy, E. L. Hu, A. Beveratos, J. Finley, V. Savona, A. Imamoğlu, and A. Imamoğlu, "Explanation of photon correlations in the far-off-resonance optical emission from a quantum-dot-cavity system", *Phys. Rev. Lett.* **103**, 207403 (2009).

[51] A. Badolato, K. Hennessy, M. Atatüre, J. Dreiser, E. Hu, P. M. Petroff, and A. Imamoglu, "Deterministic coupling of single quantum dots to single nanocavity modes", *Science* **308**, 1158–1161 (2005).

[52] D. Press, S. Götzinger, S. Reitzenstein, C. Hofmann, A. Löffler, M. Kamp, A. Forchel, and Y. Yamamoto, "Photon antibunching from a single quantum-dot-microcavity system in the strong coupling regime", *Phys. Rev. Lett.* **98**, 117402 (2007).

[53] S. Strauf, K. Hennessy, M. T. Rakher, Y. S. Choi, A. Badolato, L. C. Andreani, E. L. Hu, P. M. Petroff, and D. Bouwmeester, "Self-tuned quantum dot gain in photonic crystal lasers", *Phys. Rev. Lett.* **96**, 127404 (2006).

[54] M. Kaniber, A. Laucht, A. Neumann, J. M. Villas-Bôas, M. Bichler, M. C. Amann, and J. J. Finley, "Investigation of the nonresonant dot-cavity coupling in two-dimensional photonic crystal nanocavities", *Phys. Rev. B* **77**, 161303 (2008).

[55] N. Chauvin, C. Zinoni, M. Francardi, A. Gerardino, L. Balet, B. Alloing, L. H. Li, and A. Fiore, "Controlling the charge environment of single quantum dots in a photonic-crystal cavity", *Phys. Rev. B* **80**, 241306 (2009).

[56] A. Majumdar, M. Bajcsy, A. Rundquist, E. Kim, and J. Vučković, "Phonon-mediated coupling between quantum dots through an off-resonant microcavity", *Phys. Rev. B* **85**, 195301 (2012).

[57] M. Maragkou, C. Sánchez-Muñoz, S. Lazić, E. Chernysheva, H. P. van der Meulen, A. González-Tudela, C. Tejedor, L. J. Martínez, I. Prieto, P. A. Postigo, and J. M. Calleja, "Bichromatic dressing of a quantum dot detected by a remote second quantum dot", *Phys. Rev. B* **88**, 75309 (2013).

[58] E. Gallardo, L. J. Martínez, A. K. Nowak, D. Sarkar, H. P. van der Meulen, J. M. Calleja, C. Tejedor, I. Prieto, D. Granados, A. G. Taboada, J. M. García, and P. A. Postigo, "Optical coupling of two distant InAs/GaAs quantum dots by a photonic-crystal microcavity", *Phys. Rev. B* **81**, 193301 (2010).

[59] M. Kaniber, A. Neumann, A. Laucht, M. F. Huck, M. Bichler, M. C. Amann, and J. J. Finley, "Efficient and selective cavity-resonant excitation for single photon generation", *New J. Phys.* **11**, 13031 (2009).

202

[60] M. Nomura, S. Iwamoto, T. Nakaoka, S. Ishida, and Y. Arakawa, "Cavity Resonant Excitation of InGaAs Quantum Dots in Photonic Crystal Nanocavities", *Jpn. J. Appl. Phys.* **45**, 6091–6095 (2006).

[61] D. Englund, A. Majumdar, A. Faraon, M. Toishi, N. Stoltz, P. Petroff, and Jelena Vučković, "Resonant Excitation of a Quantum Dot Strongly Coupled to a Photonic Crystal Nanocavity", *Phys. Rev. Lett.* **104**, 73904 (2010).

[62] M. Nomura, S. Iwamoto, T. Yang, S. Ishida, and Y. Arakawa, "Enhancement of light emission from single quantum dot in photonic crystal nanocavity by using cavity resonant excitation", *Appl. Phys. Lett.* **89**, 241124 (2006).

[63] Y. Ota, M. Nomura, N. Kumagai, K. Watanabe, S. Ishida, S. Iwamoto, M. Shirane, S. Kono, S. Yorozu, and Y. Arakawa, "Efficient excitation and emission of single quantum dot by simultaneous coupling to two different photonic crystal nanocavity modes", in *2008 Conference on Quantum Electronics and Laser Science Conference on Lasers and Electro-Optics, CLEO/QELS* (2008).

[64] S. M. Thon, M. T. Rakher, H. Kim, J. Gudat, W. T. M. Irvine, P. M. Petroff, and D. Bouwmeester, "Strong coupling through optical positioning of a quantum dot in a photonic crystal cavity", *Appl. Phys. Lett.* **94**, 111115 (2009).

[65] M. Winger, A. Badolato, K. J. Hennessy, E. L. Hu, and A. Imamoğlu, "Quantum dot spectroscopy using cavity quantum electrodynamics", *Phys. Rev. Lett.* **101**, 226808 (2008).

[66] A. Dousse, L. Lanco, J. Suffczyński, E. Semenova, A. Miard, A. Lemaître, I. Sagnes, C. Roblin, J. Bloch, and P. Senellart, "Controlled light-matter coupling for a single quantum dot embedded in a pillar microcavity using far-field optical lithography", *Phys. Rev. Lett.* **101**, 267404 (2008).

[67] A. Huggenberger, S. Heckelmann, C. Schneider, S. Höfling, S. Reitzenstein, L. Worschech, M. Kamp, and A. Forchel, "Narrow spectral linewidth from single site-controlled In(Ga)As quantum dots with high uniformity", *Appl. Phys. Lett.* **98**, 131104 (2011).

[68] C. Schneider, M. Strauß, T. Sünner, A. Huggenberger, D. Wiener, S. Reitzenstein, M. Kamp, S. Höfling, and A. Forchel, "Lithographic alignment to site-controlled quantum dots for device integration", *Appl. Phys. Lett.* **92**, 183101 (2008).

[69] C. Schneider, T. Heindel, A. Huggenberger, P. Weinmann, C. Kistner, M. Kamp, S. Reitzenstein, S. Höfling, and A. Forchel, "Single photon emission from a site-controlled quantum dot-micropillar cavity system", *Appl. Phys. Lett.* **94**, 111111 (2009).

[70] T. Sünner, C. Schneider, M. Strauss, A. Huggenberger, D. Wiener, S. Höfling, M. Kamp, and A. Forchel, "Scalable fabrication of optical resonators with embedded site-controlled quantum dots", *Opt. Lett.* **33**, 1759–1761 (2008).

[71] P. Gallo, M. Felici, B. Dwir, K. Atlasov, K. F. Karlsson, A. Rudra, A. Mohan, G. Biasiol, L. Sorba, and E. Kapon, "Integration of site-controlled pyramidal quantum dots and photonic crystal membrane cavities", *Appl. Phys. Lett.* **92**, 263101 (2008).

[72] M. Calic, P. Gallo, M. Felici, K. A. Atlasov, B. Dwir, A. Rudra, G. Biasiol, L. Sorba, G. Tarel, V. Savona, and E. Kapon, "Phonon-mediated coupling of InGaAs/GaAs quantum-dot excitons to photonic crystal cavities", *Phys. Rev. Lett.* **106**, 227402 (2011).

[73] E. Pelucchi, S. Watanabe, K. Leifer, B. Dwir, and E. Kapon, "Site-controlled quantum dots grown in inverted pyramids for photonic crystal applications", *Phys. E: Low-dimensional*

Syst. Nanostructures **23**, 476–481 (2004).

[74]   S. Watanabe, E. Pelucchi, K. Leifer, A. Malko, B. Dwir, and E. Kapon, "Patterning of confined-state energies in site-controlled semiconductor quantum dots", *Appl. Phys. Lett.* **86**, 243105 (2005).

[75]   E. Pelucchi, S. Watanabe, K. Leifer, Q. Zhu, B. Dwir, P. De Los Rios, and E. Kapon, "Mechanisms of Quantum Dot Energy Engineering by Metalorganic Vapor Phase Epitaxy on Patterned Nonplanar Substrates", *Nano Lett.* **7**, 1282–1285 (2007).

[76]   A. Mohan, P. Gallo, M. Felici, B. Dwir, A. Rudra, J. Faist, and E. Kapon, "Record-low inhomogeneous broadening of site-controlled quantum dots for nanophotonics", *Small* **6**, 1268–1272 (2010).

[77]   I. V. Kulkova, A. Lyasota, C. Jarlov, B. Rigal, A. Rudra, B. Dwir, and E. Kapon, "Emission wavelength control of ordered arrays of InGaAs/GaAs quantum dots", *J. Cryst. Growth* **464**, 69-74 (2016).

[78]   A. Surrente, "Epitaxial Growth and Optical Properties of Dense Arrays of Pyramidal Quantum Dots", PhD thesis, EPFL (2013).

[79]   A. Surrente, R. Carron, P. Gallo, A. Rudra, B. Dwir, and E. Kapon, "Self-formation of hexagonal nanotemplates for growth of pyramidal quantum dots by metalorganic vapor phase epitaxy on patterned substrates", *Nano Res.* **9**, 3279–3290 (2016).

[80]   K. A. Atlasov, K. F. Karlsson, E. Deichsel, A. Rudra, B. Dwir, and E. Kapon, "Site-controlled single quantum wire integrated into a photonic-crystal membrane microcavity", *Appl. Phys. Lett.* **90**, 153107 (2007).

[81]   J. W. Lee, M. W. Devre, B. H. Reelfs, D. Johnson, J. N. Sasserath, F. Clayton, D. Hays, and S. J. Pearton, "Advanced selective dry etching of GaAs/AlGaAs in high density inductively coupled plasmas", *J. Vac. Sci. Technol. A Vacuum, Surfaces, Film.* **18**, 1220 (2000).

[82]   K. A. Atlasov, P. Gallo, A. Rudra, B. Dwir, and E. Kapon, "Effect of sidewall passivation in BCl_3/N_2 inductively coupled plasma etching of two-dimensional GaAs photonic crystals", *J. Vac. Sci. Technol. B Microelectron. Nanom. Struct.* **27**, L21–L24 (2009).

[83]   K. A. Atlasov, M. Felici, K. F. Karlsson, P. Gallo, A. Rudra, B. Dwir, and E. Kapon, "1D photonic band formation and photon localization in finite-size photonic-crystal waveguides", *Opt. Express* **18**, 117-122 (2010).

[84]   B. Rigal, C. Jarlov, P. Gallo, B. Dwir, A. Rudra, M. Calic, and E. Kapon, "Site-controlled quantum dots coupled to a photonic crystal molecule", *Appl. Phys. Lett.* **107**, 141103 (2015).

[85]   K. A. Atlasov, K. F. Karlsson, A. Rudra, B. Dwir, and E. Kapon, "Wavelength and loss splitting in directly coupled photonic-crystal defect microcavities", *Opt. Express* **16**, 16255-16264 (2008).

[86]   C. F. Wang, A. Badolato, I. Wilson-Rae, P. M. Petroff, E. Hu, J. Urayama, and A. Imamoğlu, "Optical properties of single InAs quantum dots in close proximity to surfaces", *Appl. Phys. Lett.* **85**, 3423 (2004).

[87]   J. Johansen, B. Julsgaard, S. Stobbe, J. M. Hvam, and P. Lodahl, "Probing long-lived dark excitons in self-assembled quantum dots", *Phys. Rev. B* **81**, 81304 (2010).

[88]   J. P. Hoogenboom, E. M. H. P. van Dijk, J. Hernando, N. F. van Hulst, and M. F. García-

Parajó, "Power-law-distributed dark states are the main pathway for photobleaching of single organic molecules", *Phys. Rev. Lett.* **95**, 97401 (2005).

[89]   E. K. L. Yeow, S. M. Melnikov, T. D. M. Bell, F. C. De Schryver, and J. Hofkens, "Characterizing the fluorescence intermittency and photobleaching kinetics of dye molecules immobilized on a glass surface", *J. Phys. Chem. A* **110**, 1726–1734 (2006).

[90]   V. Protasenko, S. Gordeyev, and M. Kuno, "Spatial and intensity modulation of nanowire emission induced by mobile charges", *J. Am. Chem. Soc.* **129**, 13160–13171 (2007).

[91]   C. Bradac, T. Gaebel, N. Naidoo, M. J. Sellars, J. Twamley, L. J. Brown, A. S. Barnard, T. Plakhotnik, A. V Zvyagin, and J. R. Rabeau, "Observation and control of blinking nitrogen-vacancy centres in discrete nanodiamonds", *Nat. Nanotechnol.* **5**, 345–349 (2010).

[92]   M. Nirmal, B. O. Dabbousi, M. G. Bawendi, J. J. Macklin, J. K. Trautman, T. D. Harris, and L. E. Brus, "Fluorescence intermittency in single cadmium selenide nanocrystals", *Nature* **383**, 802–804 (1996).

[93]   G. Schlegel, J. Bohnenberger, I. Potapova, and A. Mews, "Fluorescence decay time of single semiconductor nanocrystals", *Phys. Rev. Lett.* **88**, 137401 (2002).

[94]   B. R. Fisher, H.-J. Eisler, N. E. Stott, and M. G. Bawendi, "Emission Intensity Dependence and Single-Exponential Behavior In Single Colloidal Quantum Dot Fluorescence Lifetimes", *J. Phys. Chem. B* **108**, 143–148 (2004).

[95]   P. Castrillo, D. Hessman, M.-E. Pistol, J. A. Prieto, C. Pryor, and L. Samuelson, "Spectroscopy, Imaging and Switching Behaviour of Individual InP/GaInP Quantum Dots", *Jpn. J. Appl. Phys.* **36**, 4188–4190 (1997).

[96]   M. Sugisaki, H. W. Ren, S. V. Nair, J. S. Lee, S. Sugou, T. Okuno, and Y. Masumoto, "Imaging and single dot spectroscopy of InP self-assembled quantum dots", *J. Lumin.* **87**, 40–45 (2000).

[97]   M. Pistol, P. Castrillo, D. Hessman, J. A. Prieto, and L. Samuelson, "Random telegraph noise in photoluminescence from individual self-assembled quantum dots", *Phys. Rev. B* **59**, 10725 (1999).

[98]   N. Panev, M.-E. Pistol, S. Jeppesen, V. P. Evtikhiev, A. A. Katznelson, and E. Y. Kotelnikov, "Spectroscopic studies of random telegraph noise in InAs quantum dots in GaAs", *J. Appl. Phys.* **92**, 7086 (2002).

[99]   X. Y. Wang, W. Q. Ma, J. Y. Zhang, G. J. Salamo, M. Xiao, and C. K. Shih, "Photoluminescence Intermittency of InGaAs/GaAs Quantum Dots Confined in a Planar Microcavity", *Nano Lett.* **5**, 1873-1877 (2005).

[100] F. Hu, Z. Cao, C. Zhang, X. Wang, and M. Xiao, "Defect-induced photoluminescence blinking of single epitaxial InGaAs quantum dots", *Sci. Rep.* **5**, 8898 (2015).

[101] M. Kuno, D. P. Fromm, H. F. Hamann, A. Gallagher, and D. J. Nesbitt, "Nonexponential 'blinking' kinetics of single CdSe quantum dots: A universal power law behavior", *J. Chem. Phys.* **112**, 3117 (2000).

[102] M. Kuno, D. P. Fromm, H. F. Hamann, A. Gallagher, and D. J. Nesbitt, "'On'/'off' fluorescence intermittency of single semiconductor quantum dots", *J. Chem. Phys.* **115**, 1028–1040 (2001).

[103] K. T. Shimizu, R. G. Neuhauser, C. A. Leatherdale, S. A. Empedocles, W. K. Woo, and M. G. Bawendi, "Blinking statistics in single semiconductor nanocrystal quantum dots", *Phys. Rev. B* **63**, 205316 (2001).

[104] R. Verberk, J. W. M. Chon, M. Gu, and M. Orrit, "Environment-dependent blinking of single semiconductor nanocrystals and statistical aging of ensembles," *Phys. E: Low-Dimensional Syst. Nanostructures* **26**, 19–23 (2005).

[105] A. Issac, C. von Borczyskowski, and F. Cichos, "Correlation between photoluminescence intermittency of CdSe quantum dots and self-trapped states in dielectric media", *Phys. Rev. B* **71**, 161302 (2005).

[106] P. Frantsuzov, M. Kuno, B. Jankó, and R. A. Marcus, "Universal emission intermittency in quantum dots, nanorods and nanowires", *Nat. Phys.* **4**, 519–522 (2008).

[107] S. Hohng and T. Ha, "Near-complete suppression of quantum dot blinking in ambient conditions", *J. Am. Chem. Soc.* **126**, 1324–1325 (2004).

[108] Y. Chen, J. Vela, H. Htoon, J. L. Casson, D. J. Werder, D. A. Bussian, V. I. Klimov, and J. A. Hollingsworth, "'Giant' multishell CdSe nanocrystal quantum dots with suppressed blinking", *J. Am. Chem. Soc.* **130**, 5026-5027 (2008).

[109] E. Zbydniewska, A. Duzynska, M. Popoff, D. Hourlier, S. Lenfant, J. Judek, M. Zdrojek, and T. Mélin, "Charge Blinking Statistics of Semiconductor Nanocrystals Revealed by Carbon Nanotube Single Charge Sensors", *Nano Lett.* **15**, 6349–6356 (2015).

[110] B. Alén, F. Bickel, K. Karrai, R. J. Warburton, and P. M. Petroff, "Stark-shift modulation absorption spectroscopy of single quantum dots", *Appl. Phys. Lett.* **83**, 2235 (2003).

[111] A. N. Vamivakas, Y. Zhao, S. Falt, A. Badolato, J. M. Taylor, and M. Atatüre, "Nanoscale optical electrometer", *Phys. Rev. Lett.* **107**, 166802 (2011).

[112] J. Houel, A. V. Kuhlmann, L. Greuter, F. Xue, M. Poggio, R. J. Warburton, B. D. Gerardot, P. A. Dalgarno, A. Badolato, P. M. Petroff, A. Ludwig, D. Reuter, and A. D. Wieck, "Probing single-charge fluctuations at a GaAs/AlAs interface using laser spectroscopy on a nearby InGaAs quantum dot", *Phys. Rev. Lett.* **108**, 107401 (2012).

[113] A. V. Kuhlmann, J. Houel, A. Ludwig, L. Greuter, D. Reuter, A. D. Wieck, M. Poggio, and R. J. Warburton, "Charge noise and spin noise in a semiconductor quantum device", *Nat. Phys.* **9**, 570–575 (2013).

[114] C. Arnold, V. Loo, A. Lemaître, I. Sagnes, O. Krebs, P. Voisin, P. Senellart, and L. Lanco, "Cavity-enhanced real-time monitoring of single-charge jumps at the microsecond time scale", *Phys. Rev. X* **4**, 21004 (2014).

[115] M. P. Bakker, T. Ruytenberg, W. Löffler, A. Barve, L. Coldren, M. P. Van Exter, and D. Bouwmeester, "Quantum dot nonlinearity through cavity-enhanced feedback with a charge memory", *Phys. Rev. B* **91**, 241305 (2015).

[116] S. a Blanton, M. a Hines, and P. GuyotSionnest, "Photoluminescence wandering in single CdSe nanocrystals", *Appl. Phys. Lett.* **69**, 3905–3907 (1996).

[117] S. Empedocles, D. Norris, and M. Bawendi, "Photoluminescence Spectroscopy of Single CdSe Nanocrystallite Quantum Dots", *Phys. Rev. Lett.* **77**, 3873-3876 (1996).

[118] R. G. Neuhauser, K. T. Shimizu, W. K. Woo, S. A. Empedocles, and M. G. Bawendi,

"Correlation between fluorescence intermittency and spectral diffusion in single semiconductor quantum dots", *Phys. Rev. Lett.* **85**, 3301–3304 (2000).

[119] J. Müller, J. M. Lupton, A. L. Rogach, J. Feldmann, D. V. Talapin, and H. Weller, "Monitoring surface charge movement in single elongated semiconductor nanocrystals", *Phys. Rev. Lett.* **93**, 167402 (2004).

[120] N. Panev, M.-E. Pistol, J. Persson, W. Seifert, and L. Samuelson, "Spectroscopic studies of random telegraph noise in small InP quantum dots in $Ga_xIn_{1-x}P$", *Phys. Rev. B* **70**, 73309 (2004).

[121] Y. Shen, L. Pang, Y. Fainman, M. Griswold, S. Yang, L. V. Butov, and L. J. Sham, "Photoluminescence spectral switching of single CdSeZnS colloidal nanocrystals in poly(methyl methacrylate)", *Phys. Rev. B* **76**, 85312 (2007).

[122] V. Türck, S. Rodt, O. Stier, R. Heitz, R. Engelhardt, U. W. Pohl, D. Bimberg, and R. Steingrüber, "Effect of random field fluctuations on excitonic transitions of individual CdSe quantum dots", *Phys. Rev. B* **61**, 9944–9947 (2000).

[123] V. Türck, S. Rodt, R. Heitz, O. Stier, M. Straßburg, U. W. Pohl, and D. Bimberg, "Interplay of surface charges and excitons localized in CdSe/ZnSe quantum dots," *Phys. E Low-Dimensional Syst. Nanostructures* **13**, 269–272 (2002).

[124] J. Seufert, R. Weigand, G. Bacher, T. Kümmell, A. Forchel, K. Leonardi, and D. Hommel, "Spectral diffusion of the exciton transition in a single self-organized quantum dot", *Appl. Phys. Lett.* **76**, 1872 (2000).

[125] T. Makino, R. André, J. M. Gérard, R. Romestain, L. S. Dang, M. Bartels, K. Lischka, and D. Schikora, "Time domain investigation on excitonic spectral diffusion in CdSe quantum dots grown on vicinal surface GaAs substrates", *Solid State Commun.* **130**, 63–66 (2004).

[126] R. Seguin, S. Rodt, A. Strittmatter, L. Reißmann, T. Bartel, A. Hoffmann, D. Bimberg, E. Hahn, and D. Gerthsen, "Multi-excitonic complexes in single InGaN quantum dots", *Appl. Phys. Lett.* **84**, 4023 (2004).

[127] J. H. Rice, J. W. Robinson, A. Jarjour, R. A. Taylor, R. A. Oliver, G. Andrew, D. Briggs, M. J. Kappers, C. J. Humphreys, G. A. D. Briggs, M. J. Kappers, and C. J. Humphreys, "Temporal variation in photoluminescence from single InGaN quantum dots", *Appl. Phys. Lett.* **84**, 4110–4112 (2004).

[128] M. Winkelnkemper, R. Seguin, S. Rodt, A. Schliwa, L. Reißmann, A. Strittmatter, A. Hoffmann, and D. Bimberg, "Polarized emission lines from A- and B-type excitonic complexes in single InGaN/GaN quantum dots", *J. Appl. Phys.* **101**, 113708 (2007).

[129] I. A. Ostapenko, G. Hönig, C. Kindel, S. Rodt, A. Strittmatter, A. Hoffmann, and D. Bimberg, "Large internal dipole moment in InGaN/GaN quantum dots", *Appl. Phys. Lett.*, **97**, 63103 (2010).

[130] K. Sebald, H. Lohmeyer, J. Gutowski, T. Yamaguchi, and D. Hommel, "Optical properties of single InGaN quantum dots up to 150 K", *Phys. Status Solidi* **3**, 3864–3868 (2006).

[131] K. Sebald, H. Lohmeyer, S. Herlufsen, J. Kalden, J. Gutowski, C. Tessarek, T. Yamaguchi, and D. Hommel, "Optical properties of single and multi-layer InGaN quantum dots", *Phys. Status Solidi* **5**, 1883–1885 (2008).

[132] R. Bardoux, T. Guillet, P. Lefebvre, T. Taliercio, T. Bretagnon, S. Rousset, B. Gil, and F.

Semond, "Photoluminescence of single GaN/AlN hexagonal quantum dots on Si(111): Spectral diffusion effects", *Phys. Rev. B* **74**, 195319 (2006).

[133] F. Rol, S. Founta, H. Mariette, B. Daudin, L. S. Dang, J. Bleuse, D. Peyrade, J.-M. Gérard, and B. Gayral, "Probing exciton localization in nonpolar GaN/AlN quantum dots by single-dot optical spectroscopy", *Phys. Rev. B* **75**, 125306 (2007).

[134] S. Sergent, S. Kako, M. Bürger, D. J. As, and Y. Arakawa, "Narrow spectral linewidth of single zinc-blende GaN/AlN self-assembled quantum dots", *Appl. Phys. Lett.* **103**, 151109 (2013).

[135] W. Bak, H. Noh, C. Stambaugh, Y. Arakawa, and W. Jhe, "Spectral fluctuations of excitonic transitions of InGaAs single quantum dots", *Appl. Phys. Lett.* **100**, 22105 (2012).

[136] S. Rodt, A. Schliwa, K. Pötschke, F. Guffarth, and D. Bimberg, "Correlation of structural and few-particle properties of self-organized InAs/GaAs quantum dots", *Phys. Rev. B* **71**, 155325 (2005).

[137] M. Abbarchi, F. Troiani, C. Mastrandrea, G. Goldoni, T. Kuroda, T. Mano, K. Sakoda, N. Koguchi, S. Sanguinetti, A. Vinattieri, and M. Gurioli, "Spectral diffusion and line broadening in single self-assembled GaAsAlGaAs quantum dot photoluminescence", *Appl. Phys. Lett.* **93**, 162101 (2008).

[138] R. Singh and G. Bester, "Effects of charged defects on the electronic and optical properties of self-assembled quantum dots", *Phys. Rev. B* **85**, 205405 (2012).

[139] L. O. Mereni, V. Dimastrodonato, R. J. Young, and E. Pelucchi, "A site-controlled quantum dot system offering both high uniformity and spectral purity", *Appl. Phys. Lett.* **94**, 223121 (2009).

[140] C. Schneider, A. Huggenberger, T. Sünner, T. Heindel, M. Strauß, S. Göpfert, P. Weinmann, S. Reitzenstein, L. Worschech, M. Kamp, S. Höfling, and A. Forchel, "Single site-controlled In(Ga)As/GaAs quantum dots: growth, properties and device integration", *Nanotechnology* **20**, 434012 (2009).

[141] A. Schramm, J. Tommila, C. Strelow, T. V Hakkarainen, A. Tukiainen, M. Dumitrescu, A. Mews, T. Kipp, and M. Guina, "Large array of single, site-controlled InAs quantum dots fabricated by UV-nanoimprint lithography and molecular beam epitaxy", *Nanotechnology* **23**, 175701 (2012).

[142] J. Tommila, A. Schramm, T. V Hakkarainen, M. Dumitrescu, and M. Guina, "Size-dependent properties of single InAs quantum dots grown in nanoimprint lithography patterned GaAs pits", *Nanotechnology* **24**, 235204 (2013).

[143] K. D. Jöns, P. Atkinson, M. Müller, M. Heldmaier, S. M. Ulrich, O. G. Schmidt, and P. Michler, "Triggered Indistinguishable Single Photons with Narrow Line Widths from Site-Controlled Quantum Dots", *Nano Lett.* **13**, 126–130, Jan. 2013.

[144] M. Bayer and A. Forchel, "Temperature dependence of the exciton homogeneous linewidth in $In_{0.60}Ga_{0.40}As$/GaAs self-assembled quantum dots", *Phys. Rev. B* **65**, 41308 (2002).

[145] U. Perinetti, N. Akopian, Y. B. Samsonenko, A. D. Bouravleuv, G. E. Cirlin, and V. Zwiller, "Sharp emission from single InAs quantum dots grown on vicinal GaAs surfaces", *Appl. Phys. Lett.* **94**, 163114 (2009).

[146] T.-P. Hsieh, H.-S. Chang, W.-Y. Chen, W.-H. Chang, T. M. Hsu, N.-T. Yeh, W.-J. Ho, P.-C.

208

Chiu, and J.-I. Chyi, "Growth of low density InGaAs quantum dots for single photon sources by metal–organic chemical vapour deposition", *Nanotechnology* **17**, 512–515 (2006).

[147] D. Richter, R. Hafenbrak, K. D. Jöns, W.-M. Schulz, M. Eichfelder, M. Heldmaier, R. Roßbach, M. Jetter, and P. Michler, "Low density MOVPE grown InGaAs QDs exhibiting ultra-narrow single exciton linewidths", *Nanotechnology* **21**, 125606 (2010).

[148] L. Besombes, K. Kheng, L. Marsal, and H. Mariette, "Charged excitons in single CdTe quantum dots", *Phys. E: Low-Dimensional Syst. Nanostructures* **13**, 134–138, 2002.

[149] G. Hönig, S. Rodt, G. Callsen, I. A. Ostapenko, T. Kure, A. Schliwa, C. Kindel, D. Bimberg, A. Hoffmann, S. Kako, and Y. Arakawa, "Identification of electric dipole moments of excitonic complexes in nitride-based quantum dots", *Phys. Rev. B* **88**, 45309 (2013).

[150] B. Patton, W. Langbein, and U. Woggon, "Trion, biexciton, and exciton dynamics in single self-assembled CdSe quantum dots", *Phys. Rev. B* **68**, 125316 (2003).

[151] C. Lobo, R. Leon, S. Marcinkevičius, W. Yang, P. C. Sercel, X. Z. Liao, J. Zou, and D. J. H. Cockayne, "Inhibited carrier transfer in ensembles of isolated quantum dots", *Phys. Rev. B* **60**, 16647–16651 (1999).

[152] R. Heitz, I. Mukhametzhanov, A. Madhukar, A. Hoffmann, and D. Bimberg, "Temperature dependent optical properties of self-organized InAs/GaAs quantum dots", *J. Electron. Mater.* **28**, 520–527 (1999).

[153] C. Jarlov, A. Lyasota, L. Ferrier, P. Gallo, B. Dwir, A. Rudra, and E. Kapon, "Exciton dynamics in a site-controlled quantum dot coupled to a photonic crystal cavity", *Appl. Phys. Lett.* **107**, 191101 (2015).

[154] C. Galland, Y. Ghosh, A. Steinbrück, M. Sykora, J. A. Hollingsworth, V. I. Klimov, and H. Htoon, "Two types of luminescence blinking revealed by spectroelectrochemistry of single quantum dots", *Nature* **479**, 203–207 (2011).

[155] T. Nakaoka, Y. Tamura, T. Saito, T. Miyazawa, K. Watanabe, Y. Ota, S. Iwamoto, and Y. Arakawa, "Competing influence of an in-plane electric field on the Stark shifts in a semiconductor quantum dot", *Appl. Phys. Lett.* **99**, 181109 (2011).

[156] T. Saito, T. Nakaoka, and Y. Arakawa, "Effect of lateral electric field on the transition energies of neutral and charged excitons in In$_{0.5}$Ga$_{0.5}$As/GaAs quantum dots", *Phys. Rev. B* **91**, 115306 (2015).

[157] L. Besombes, K. Kheng, L. Marsal, and H. Mariette, "Charged excitons in single CdTe quantum dots", *Phys. E: Low-dimensional Syst. Nanostructures* **13**, 134–138 (2002).

[158] M. Korkusinski, M. E. Reimer, R. L. Williams, and P. Hawrylak, "Engineering photon cascades from multiexciton complexes in a self-assembled quantum dot by a lateral electric field", *Phys. Rev. B* **79**, 35309 (2009).

[159] M. Kaniber, M. F. Huck, K. Müller, E. C. Clark, F. Troiani, M. Bichler, H. J. Krenner, and J. J. Finley, "Electrical control of the exciton-biexciton splitting in self-assembled InGaAs quantum dots", *Nanotechnology* **22**, 325202 (2011).

[160] M. E. Reimer, M. P. van Kouwen, A. W. Hidma, M. H. M. van Weert, E. P. A. M. Bakkers, L. P. Kouwenhoven, and V. Zwiller, "Electric Field Induced Removal of the Biexciton Binding Energy in a Single Quantum Dot", *Nano Lett.* **11**, pp. 645–650, 2011.

[161] M. T. Rakher, N. G. Stoltz, L. A. Coldren, P. M. Petroff, and D. Bouwmeester, "Externally mode-matched cavity quantum electrodynamics with charge-tunable quantum dots", *Phys. Rev. Lett.* **102**, 97403 (2009).

[162] A. Laucht, F. Hofbauer, N. Hauke, J. Angele, S. Stobbe, M. Kaniber, G. Böhm, P. Lodahl, M.-C. Amann, and J. J. Finley, "Electrical control of spontaneous emission and strong coupling for a single quantum dot", *New J. Phys.* **11**, 23034 (2009).

[163] B. D. Mangum, F. Wang, A. M. Dennis, Y. Gao, X. Ma, J. A. Hollingsworth, and H. Htoon, "Competition between auger recombination and hot-carrier trapping in PL intensity fluctuations of type II nanocrystals", *Small* **10**, 2892–2901 (2014).

[164] O. Gazzano, S. Michaelis de Vasconcellos, C. Arnold, A. Nowak, E. Galopin, I. Sagnes, L. Lanco, A. Lemaître, and P. Senellart, "Bright solid-state sources of indistinguishable single photons", *Nat. Commun.* **4**, 1425 (2013).

[165] A. K. Nowak, S. L. Portalupi, V. Giesz, O. Gazzano, C. Dal Savio, P.-F. Braun, K. Karrai, C. Arnold, L. Lanco, I. Sagnes, A. Lemaître, and P. Senellart, "Deterministic and electrically tunable bright single-photon source", *Nat. Commun.* **5**, 3240 (2014).

[166] C. Arnold, J. Demory, V. Loo, A. Lemaître, I. Sagnes, M. Glazov, O. Krebs, P. Voisin, P. Senellart, and L. Lanco, "Macroscopic rotation of photon polarization induced by a single spin", *Nat. Commun.* **6**, 6236 (2015).

[167] C. Jarlov, É. Wodey, A. Lyasota, M. Calic, P. Gallo, B. Dwir, A. Rudra, and E. Kapon, "Effect of Pure Dephasing and Phonon Scattering on the Coupling of Semiconductor Quantum Dots to Optical Cavities", *Phys. Rev. Lett.* **117**, 76801 (2016).

[168] F. Intonti, S. Vignolini, F. Riboli, A. Vinattieri, D. S. Wiersma, M. Colocci, L. Balet, C. Monat, C. Zinoni, L. H. Li, R. Houdré, M. Francardi, A. Gerardino, A. Fiore, and M. Gurioli, "Spectral tuning and near-field imaging of photonic crystal microcavities", *Phys. Rev. B* **78**, 41401 (2008).

[169] S. Vignolini, F. Intonti, M. Zani, F. Riboli, D. S. Wiersma, L. H. Li, L. Balet, M. Francardi, A. Gerardino, A. Fiore, and M. Gurioli, "Near-field imaging of coupled photonic-crystal microcavities", *Appl. Phys. Lett.* **94**, 151103 (2009).

[170] M. Gokten, A. Elsherbeni, and E. Arvas, "Multiresolution Frequency Domain Technique for Electromagnetics", *Synth. Lect. Comput. Electromagn.* **7**, 1–134 (2012).

[171] C. W. T. Jarlov, "Cavity quantum electrodynamics with systems of site-controlled quantum dots and photonic crystal cavities", PhD thesis, EPFL (2016).

[172] J. Kettler, M. Paul, F. Olbrich, K. Zeuner, M. Jetter, P. Michler, M. Florian, C. Carmesin, and F. Jahnke, "Neutral and charged biexciton-exciton cascade in near-telecom-wavelength quantum dots", *Phys. Rev. B* **94**, 45303 (2016).

[173] C. Jarlov, P. Gallo, M. Calic, B. Dwir, A. Rudra, and E. Kapon, "Bound and anti-bound biexciton in site-controlled pyramidal GaInAs/GaAs quantum dots", *Appl. Phys. Lett.* **101**, 191101, (2012).

[174] G. Muñoz-Matutano, I. Suárez, J. Canet-Ferrer, B. Alén, D. Rivas, L. Seravalli, G. Trevisi, P. Frigeri, and J. Martínez-Pastor, "Size dependent carrier thermal escape and transfer in bimodally distributed self assembled InAs/GaAs quantum dots", *J. Appl. Phys.* **111**, 123522 (2012).

[175] E. C. Le Ru, J. Fack, and R. Murray, "Temperature and excitation density dependence of the photoluminescence from annealed InAs/GaAs quantum dots", *Phys. Rev. B* **67**, 245318 (2003).

[176] L. Besombes, K. Kheng, L. Marsal, and H. Mariette, "Acoustic phonon broadening mechanism in single quantum dot emission", *Phys. Rev. B* **63**, 155307 (2001).

[177] A. Berthelot, I. Favero, G. Cassabois, C. Voisin, C. Delalande, P. Roussignol, R. Ferreira, and J. M. Gérard, "Unconventional motional narrowing in the optical spectrum of a semiconductor quantum dot", *Nat. Phys.* **2**, 759–764 (2006).

[178] K. Matsuda, K. Ikeda, T. Saiki, H. Tsuchiya, H. Saito, and K. Nishi, "Homogeneous linewidth broadening in a $In_{0.5}Ga_{0.5}As$/GaAs single quantum dot at room temperature investigated using a highly sensitive near-field scanning optical microscope", *Phys. Rev. B* **63**, 121304 (2001).

[179] W. Ouerghui, A. Melliti, M. A. Maaref, and J. Bloch, "Dependence on temperature of homogeneous broadening of InGaAs/InAs/GaAs quantum dot fundamental transitions", *Phys. E: Low-dimensional Syst. Nanostructures* **28**, 519–524 (2005).

[180] D. Valente, J. Suffczyński, T. Jakubczyk, A. Dousse, A. Lemaître, I. Sagnes, L. Lanco, P. Voisin, A. Auffèves, and P. Senellart, "Frequency cavity pulling induced by a single semiconductor quantum dot", *Phys. Rev. B* **89**, 41302 (2014).

[181] J. M. Smith, P. A. Dalgarno, R. J. Warburton, A. O. Govorov, K. Karrai, B. D. Gerardot, and P. M. Petroff, "Voltage control of the spin dynamics of an exciton in a semiconductor quantum dot", *Phys. Rev. Lett.* **94**, 197402 (2005).

[182] Q. Wang, S. Stobbe, and P. Lodahl, "Mapping the local density of optical states of a photonic crystal with single quantum dots", *Phys. Rev. Lett.* **107**, 167404 (2011).

[183] M. Feucker, R. Seguin, S. Rodt, A. Hoffmann, and D. Bimberg, "Decay dynamics of neutral and charged excitonic complexes in single InAs⁄GaAs quantum dots", *Appl. Phys. Lett.* **92**, 63116 (2008).

[184] K. Roy-Choudhury and S. Hughes, "Spontaneous emission from a quantum dot in a structured photonic reservoir: phonon-mediated breakdown of Fermi's golden rule", *Optica* **2**, 434 (2015).

[185] M. Yamaguchi, T. Asano, and S. Noda, "Photon emission by nanocavity-enhanced quantum anti-Zeno effect in solid-state cavity quantum-electrodynamics", *Opt. Express* **16**, 18067–18081 (2008).

[186] P. E. Barclay, C. Santori, K.-M. Fu, R. G. Beausoleil, and O. Painter, "Coherent interference effects in a nano-assembled diamond NV center cavity-QED system", *Opt. Express* **17**, 8081 (2009).

[187] T. Kojima, K. Kojima, T. Asano, and S. Noda, "Accurate alignment of a photonic crystal nanocavity with an embedded quantum dot based on optical microscopic photoluminescence imaging", *Appl. Phys. Lett.* **102**, 11110 (2013).

[188] L. Sapienza, M. Davanço, A. Badolato, and K. Srinivasan, "Nanoscale optical positioning of single quantum dots for bright and pure single-photon emission", *Nat. Commun.* **6**, 7833 (2015).

[189] G. Tarel and V. Savona, "Linear spectrum of a quantum dot coupled to a nanocavity", *Phys.*

Rev. B **81**, 75305 (2010).

[190] C. Jarlov, A. Lyasota, L. Ferrier, P. Gallo, B. Dwir, A. Rudra, and E. Kapon, "Exciton dynamics in a site-controlled quantum dot coupled to a photonic crystal cavity", *Appl. Phys. Lett.* **107**, 191101 (2015).

[191] N. W. L. Speijcken, M. A. Dündar, A. Casas Bedoya, C. Monat, C. Grillet, P. Domachuk, R. Nötzel, B. J. Eggleton, and R. W. van der Heijden, "In situ optofluidic control of reconfigurable photonic crystal cavities", *Appl. Phys. Lett.* **100**, 261107 (2012).

[192] F. Intonti, S. Vignolini, F. Riboli, M. Zani, D. S. Wiersma, L. Balet, L. H. Li, M. Francardi, A. Gerardino, A. Fiore, and M. Gurioli, "Tuning of photonic crystal cavities by controlled removal of locally infiltrated water", *Appl. Phys. Lett.* **95**, 173112 (2009).

[193] S. Vignolini, F. Riboli, D. S. Wiersma, L. Balet, L. H. Li, M. Francardi, A. Gerardino, A. Fiore, M. Gurioli, and F. Intonti, "Nanofluidic control of coupled photonic crystal resonators", *Appl. Phys. Lett.* **96**, 141114 (2010).

[194] B. Rigal, C. Jarlov, A. Rudra, P. Gallo, A. Lyasota, B. Dwir, and E. Kapon, "Site-controlled InGaAs/GaAs pyramidal quantum dots grown by MOVPE on patterned substrates using triethylgallium", *J. Cryst. Growth* **414**, 187–191 (2015).

[195] G. Rui, W. Chen, D. C. Abeysinghe, R. L. Nelson, and Q. Zhan, "Beaming circularly polarized photons from quantum dots coupled with plasmonic spiral antenna", *Opt. Express* **20**, 19297 (2012).

[196] D. V. Shenai-Khatkhate, R. L. DiCarlo, and R. A. Ware, "Accurate vapor pressure equation for trimethylindium in OMVPE", *J. Cryst. Growth* **310**, 2395–2398 (2008).

[197] M. Fulem, K. Růžička, V. Růžička, E. Hulicius, T. Šimeček, K. Melichar, J. Pangrác, S. A. Rushworth, and L. M. Smith, "Vapor pressure of metal organic precursors", *J. Cryst. Growth* **248**, 99–107 (2003).

Publications and conference contribution

Journal publications

- A. Lyasota, S. Borghardt, C. Jarlov, B. Dwir, P. Gallo, A. Rudra, and E. Kapon. 'Integration of multiple site-controlled pyramidal quatum dot systems with photonic-crystal membrane cavities'. Journal of Crystal Growth 414, 192-195 (2015)

- B. Rigal, C. Jarlov, A. Rudra, P. Gallo, A. Lyasota, B. Dwir, and E. Kapon. 'Site-controlled InGaAs/GaAs pyramidal quantum dots grown by MOVPE on patterned substrates using tri-ethylgallium'. Journal of Crystal Growth 414, 187-191 (2015)

- C. Jarlov, A. Lyasota, L. Ferrier, P. Gallo, B. Dwir, A. Rudra, and E. Kapon. 'Exciton dynamics in a site-controlled quantum dot coupled to a photonic crystal cavity'. Applied Physics Letters 107, 191101 (2015)

- C. Jarlov, É. Wodey, A. Lyasota, M. Calic, P. Gallo, B. Dwir, A. Rudra, and E. Kapon. 'Effect of Pure Dephasing and Phonon Scattering on the Coupling of Semiconductor Quantum Dots to Optical Cavities'. Physical Review Letters 117, 076801 (2016)

- I. Kulkova, A. Lyasota, C. Jarlov, B. Rigal, A. Rudra, B. Dwir, and E. Kapon. 'Emission wavelength control of ordered arrays of InGaAs/GaAs quantum dots'. Journal of Crystal Growth, 2016, 10.1016/j.jcrysgro.2016.11.022.

Conference presentations

- A. Lyasota, B. Dwir, P. Gallo, C. Jarlov, M. Calic, A. Rudra and E. Kapon. 'Integration of position- and spectrum- controlled InGaAs quantum dots in GaAs photonic crystal cavities'. The 17th International Conference on Metalorganic Vapour Phase Epitaxy, ICMOVPE 2014, Lausanne, Switzerland, July 2014 (Contributed oral presentation).

- A. Lyasota, B. Dwir, P. Gallo, C. Jarlov, M. Calic, A. Rudra and E. Kapon. 'Integration of site- and spectrum –controlled pyramidal quantum dots with photonic crystal membrane cavities'. 10th International ESPS-NIS Workshop on Epitaxial Semiconductors on Patterned Substrates and Novel-Indexed Surfaces, ESPS-NIS 2014, Traunkirchen, Austria, May 2014 (Contributed oral presentation).

- A. Lyasota, B. Dwir, P. Gallo, C. Jarlov, B. Rigal, A. Rudra and E. Kapon. 'Integration of site- and spectrum–controlled pyramidal quantum dots with photonic crystal membrane cavities' 5th International Topical Meeting on Nanophotonics and Metamaterials, NANOMETA 2015, Seefeld, Austria, January 2015 (Contributed poster presentation).

- <u>A. Lyasota</u>, C. Jarlov, B. Dwir, A. Rudra, P. Gallo and E. Kapon. 'Deterministic Coupling of Multiple Quantum Dots to Selected Modes of a Photonic Crystal Cavity'. Progress In Electromagnetics Research Symposium, PIERS 2015, Prague, Czech Republic, July 2015 (Contributed oral presentation).

Alexey A. Lyasota

Citizenship	Russian
Address	Route de Chavannes 66, Lausanne 1007, Switzerland
Phone	+41787665795
E-mail	alexey.lyasota@gmail.com
LinkedIn	https://ru.linkedin.com/in/alexei-lyasota-86915526

Education

09/2012 - 02/2017

PhD degree in Physics, Ecole Polytechnique Federale de Lausanne (EPFL), Lausanne, Switzerland. 'Interaction between site-controlled quantum dot systems and photonic cavity structures'.

- Nanofabrication and optical spectroscopy of nanostructures.
- Integrated 1-4 site-controlled pyramidal QDs with PhC cavities.
- Demonstrated coupling of four QDs with the same CM.
- Probed the CM field distribution with a single QD serving as a point dipole.
- Studied a Fano like interference effect between direct and indirect excitonic emission channels in the QD-PhC cavity system.
- Analyzed and simulated experimental data using Matlab and Mathematica.

09/2010 - 06/2012

Master degree in Applied Mathematics and Physics, **Moscow Institute of Physics and Technology (MIPT)**, Department of General and Applied Physics, Russia. 'Temperature transition and switching effects in excitonic spectra of GaAs/AlGaAs quantum wells'.

09/2006 - 06/2010

Bachelor degree in Applied Mathematics and Physics, **Moscow Institute of Physics and Technology (MIPT)**, Department of General and Applied Physics, Russia. 'Investigation of photoluminescence spectra of GaAs/AlGaAs heterostructures in magnetic field'.

Technical skills

Nanofabrication	ICP-RIE, wet etching; PECVD, spin-on polimer deposition.
Surface characterization	SEM, AFM and 2D profiling measurements
Optical laboratory	(μ-)PL and fiber optics setup; photoluminescence spectroscopy with time- and/or polarization- resolved modes; (qusi-) resonant, non-resonant or bichromatic optical excitation; photoluminescence excitation spectroscopy.
Cryogenic setup	He^4 bath- and flow- (magneto-) cryostats.
Vacuum setup	Diffusion and turbo-molecular based vacuum systems.
Software	Origin, Matlab, Mathematica, Adobe Illustrator CC, MS Office.

Language skills

Russian	Fluent (native)
English	Operational proficiency (C1)